Microtubules and Energy Metabolism:
Targets for Standard, Combination, and Novel Therapeutic Interventions and Monitoring of Cancer

by

Douglas Friesen

A thesis submitted in partial fulfilment of the requirements for the degree of

Doctor of Philosophy

in

Experimental Oncology

Department of Oncology
University of Alberta

Abstract

The challenge of understanding and treating cancer has proven to be exceedingly complex. At this juncture, understanding cancer from the perspective of a breakdown of a complex cooperative system using a biophysical analysis may aid in improved treatments and prevention of this disease. In any system, the following are crucial: the right raw materials and energy, the right vision and instructions, solid communication, and the right framework to hold everything together. In the biological system of an organism, these aspects roughly correspond to the right nutrition to fuel the organism, the proper genome to create the right proteins to create the organism, solid inter- and intra-cellular communication, and a robust structure involving the cytoskeleton of a cell and the extracellular matrix that keeps the organism ordered and stable. This thesis explores in depth the ideas of communication, structure, and energy, which are all crucial for a multicellular system to operate. My goal is that by providing insight into these aspects of an organism's optimal function, improved treatments for cancer may be developed.

The cytoskeleton of a cell is the component that provides the structure that the cell requires to maintain its shape under external forces. I explore in the most depth the properties of microtubules, which form the most rigid component of the cytoskeleton, that may be involved in intracellular electrical communication in addition to their more familiar structural role. Initially, I studied gamma-tubulin, which is a protein that forms a nucleating ring that nucleates microtubules. Using molecular dynamics simulations, I investigated the binding site of what were, to my knowledge, the first inhibitors found to interact with gamma-tubulin. This study could lead to more potent inhibitors of gamma-tubulin, which will allow for a more detailed exploration of the role gamma-tubulin plays

in maintaining the structure of the cell, and provide a possible chemotherapeutic target for glioblastoma multiforme, a form of brain cancer with one of the poorest prognoses of all human cancers where gamma-tubulin is upregulated.

Next, I investigated the role of energy metabolism in cancer, which may play a crucial role in maintaining the proper structure of the cytoskeleton. This investigation led to the possibility of improving our understanding of the cause of cachexia in late stage cancer patients, where these patients experience muscle wasting that is not able to be corrected through nutritional support. I present a mathematical framework for evaluating how an altered energy metabolism seen in cancer cells can help explain this muscle wasting that cancer patients experience. This model, if validated, could lead to improved treatment for cancer patients experiencing cachexia. I also evaluate the potential of the drug 3-bromopyruvate, which targets the altered energy metabolism in cancer cells, as a combination drug treatment for recurrent epithelial ovarian cancer. I initiated a study finding that 3-bromopyruvate is more cytotoxic to late stage ovarian cancer over early-stage ovarian cancer in a cell line progression model, which supports progressing to *in vivo* testing of the drug in a mouse model.

Finally, I explore the role of microtubules in the cell for intracellular electrical signaling. Microtubules have been hypothesized to be a component of an organism-wide electrical signaling network in the body, and I developed a microfabricated device to test electrical properties of microtubules in a physiological-like ionic solution. My preliminary results support the idea that microtubules are able to increase ionic conductivity, and provide an experimental system to facilitate testing microtubules' electrical effects in greater detail.

As a result of the work presented in this thesis, I have added insight into microtubules' role in electrical intracellular communication and how gamma-tubulin may be inhibited to understand its function in the cell more completely. I have also brought insight into how energy metabolism can both help explain cancer cachexia and be targeted for improved ovarian cancer therapy. These insights provide a greater framework for understanding cancer, through ideas of energy, electrical communication, and structure. I trust these insights will help the development of standard, combination, and novel treatments of cancer, as well as preventative measures to maintain an organism's order, structure, and proper energy metabolism.

Preface

The material presented in this thesis was completed in the Department of Oncology at the University of Alberta. This thesis contains material that was previously published.

Chapter 1 contains material that was previously published as Friesen DE, Craddock TJA, Kalra AP, Tuszynski JA "Biological wires, communication systems, and implications for disease," *BioSystems* 2015, 127:14-27, in the introduction. I primarily researched and wrote this manuscript. J. Craddock added insight into neurodegenerative disease, A. Kalra added insight into certain microtubule conductivity experiment, and J. Tuszynski added insight to the entire paper. Only text written primarily by myself from this publication is included in this thesis.

Chapter 2 contains material that was previously published as Friesen DE, Barakat KH, Semenchenko V, Perez-Pineiro R, Fenske BW, Mane J, Wishart DS, Tuszynski JA "Discovery of small molecule inhibitors that interact with gamma-tubulin," *Chem Biol Drug Des* 2012, 79:639-652. This was a collaborative effort. I performed molecular dynamics simulations, clustering, computer modelling, and analysis, and primarily wrote the manuscript. V. Semenchenko and R. Perez-Tineiro performed laboratory experiments and wrote the experimental sections of the manuscript. K. Barakat and B. Fenske performed docking. J. Mane, D. Wishart, and J. Tuszynski assisted with analysis. Special acknowledgment to Dr. Chih-Yuan Tseng for his assistance in repairing missing residues in the crystal structures, Dr. Travis Craddock for assistance with preparing Figure 2.1, and Mr. Philip Winter for assistance in preparing Tables 2.1 and 2.3.

Chapter 3 (primarily 3.2) contains material that was previously published as Friesen DE, Baracos VE, Tuszynski JA "Modeling the energetic cost of cancer as a result of altered energy metabolism: implications for cachexia," *Theor Biol Med Model* 2015, 12:17. I developed the model and drafted the manuscript. V. Baracos provided data and helped with manuscript edits. J. Tuszynski conceived of the study and helped with manuscript edits. Chapter 3 (primarily 3.1 and 3.3) contains material that was written for my PhD Candidacy grant proposal and PhD proposal. The text contains ideas published as Rietman EA, Friesen DE, Hahnfeldt P, Gatenby R, Hlatky L, Tuszynski JA "An integrated multidisciplinary model describing initiation of cancer and the Warburg

hypothesis," *Theor Biol Med Model* 2013, 10:39. E. Rietman, J. Tuszynski, and I developed the integrated theory. R. Gatenby contributed to experiments, and P. Hahnfeldt and L. Hlatky contributed insight into cancer and the model. Only text written primarily by myself from this publication is included in this thesis. Section 3.3 is unpublished work and contains a Cyquant cytotoxicity experiment that was designed by me and performed by K. Missaiaen. D. Moudgil assisted with performing the immunofluorescence staining using the Chan Lab protocol for tubulin staining.

Chapter 4 contains material that was previously published as Friesen DE, Craddock TJA, Kalra AP, Tuszynski JA "Biological wires, communication systems, and implications for disease," *BioSystems* 2015, 127:14-27, in the introduction. I primarily researched and wrote this manuscript. J. Craddock added insight into neurodegenerative disease, A. Kalra added insight into certain microtubule conductivity experiment, and J. Tuszynski added insight to the entire paper. Only text written primarily by myself from this publication is included in this thesis. The Chapter 4 introduction also contains material previously published as Friesen DE, Craddock TJA, Priel A, Tuszynski J "Cytoskeletal electrostatic and ionic conduction effects in the cell," in *Fields of the Cell*. Edited by Fels D, Cifra M, Scholkmann F. Kerala, India: Research Signpost; 2015. This book chapter was written by J. Tuszynski, T. Craddock, A. Priel, and myself, and was largely revised by me. Only sections written primarily by myself are included in this thesis. The experimental portion of Chapter 4 is unpublished work. Microfluidic work was assisted by A. Jemere. The original process to create nanofluidic channels with embedded nanoelectrodes was originally provided by W. Reisner, and modified by me to account for the available experimental equipment at the University of Alberta.

When something is important enough, you do it even if the odds are not in your favor.

– Elon Musk

Acknowledgments

First and foremost I would like to thank my supervisor, Dr. Jack Tuszynski, for his incredible supervision that has made my years as a graduate student joyful and tremendously rewarding. Jack, thank you for believing in me and giving me the freedom to explore the mysteries of biology and life. Thank you for providing such a stimulating group that is constantly at the forefront of biophysics. Thank you as well to Tuszynski group members past and present that made such a great research environment. In particular, thanks to Dr. Travis Craddock who was my closest collaborator in the group on information processing in microtubules and a great friend. As well, thanks to Dr. Khaled Barakat who was my mentor in molecular dynamics, and a great ally and friend. Thanks as well to Philip Winter who has always been completely dependable to help on projects and was the *de facto* social convenor of our research group. Thanks to Sara Omar, my fellow Oncology graduate student, for her kindness and friendship, and to Niloofar Nayebi and Francesco Gentile as well for their friendship and making such a positive environment for research. Thanks as well to all Tuszynski group members who have each been a source of friendship and ideas.

I'd like to thank the numerous people that helped me with my interdisciplinary research. Thanks to Dr. Michael Weinfeld, Dr. Michael Woodside, Dr. Michael Hendzel, and Dr. Manijeh Pasdar who have served on my supervisory committee for their excellent mentorship and insight into my research. Thanks to the Oncology department for supporting me, as a student with a theoretical biophysics background. Special thanks to Dr. Roseline Godbout for her support and assistance in helping me with her knowledge of everything about the oncology department. Thanks as well to members of the Godbout lab for assistance as I was learning experimental techniques, with special thanks to Dr. Matthew Hildebrandt and Dr. Devin Germaine for going out of their way to answer my numerous questions. Thanks as well to Dr. Michael Hendzel for allowing me to use his lab space at the Cross Cancer Institute, and for always challenging me to do my best research. Thanks to Gerry Barron for training me in cell culture and assistance with microscopy, and Dr. Xuejun Sun for support as well with microscopy. Thanks to the

Table of contents

List of Tables

List of Figures

Abbreviations

Common to all chapters

3BP	3-Bromopyruvate
ATP	Adenosine triphosphate
GBM	Glioblastoma multiforme (form of brain cancer)
GTP	Guanosine-5'-triphosphate
MT	Microtubule
SD	Standard deviation
SEM	Standard error of the mean

Chapter 1

APL	Acute promyelocytic leukemia
ATRA	All-trans retinoic acid
ECM	Extracellular matrix
GCP	γ-tubulin complex proteins
MDR	Multi-drug resistance
SMT	Somatic mutation theory
TIC	Tumor initiating cell
TOFT	Tissue organization field theory

Chapter 2

DBI	Davies-Bouldin index
FaSSIF	Solubility in simulated fasted state intestinal fluid
GDP	Guanosine-diphosphate
γTuRC	γ-Tubulin ring complex
MD	Molecular dynamics
MTOC	Microtubule organizing center
MW	Molecular weight
PDB	Protein Data Bank
RMSD	Root-mean-square deviation
SSR	Sum of squares of the regression
SST	Total sum of squares

T_PSA	Topological polar surface area

Chapter 3

ALDH	Aldehyde dehydrogenase
CA-125	Cancer antigen 125
CD44	Cluster of differentiation 44
CD117	c-Kit; Cluster of differentiation 117
CD133	Cluster of differentiation 133
CSC	Cancer stem cell
EOC	Epithelial ovarian cancer
FDG-PET	Fluorine-18 fluorodeoxyglucose positron emission tomography
FFL TIV	Firefly luciferase tumor initiating variant
FFM	Fat-free mass
FLC	Fibrolamellar hepatocellular carcinoma
GAPDH	Glyceraldehyde-3-phosphate dehydrogenase
HCC	Hepatocellular carcinoma
HIF	Hypoxia-inducible factor
HK-II	Type II hexokinase
IC50	Half maximal inhibitory concentration
L-CR	MOSE-L late stage, cisplatin resistant
MCT	Monocarboxylate transporter
MDR	Multi-drug resistance
MOSE	Mouse ovarian surface epithelial
MTS	(3-(4,5-dimethylthiazol-2-yl)-5-(3-carboxymethoxyphenyl)-2-(4-sulfophenyl)-2H-tetrazolium)
OCIC	Ovarian cancer initiating cell
qRT-PCR	Quantitative real-time polymerase chain reaction
REE	Resting energy expenditure
ROS	Reactive oxygen species
RNA	Ribonucleic acid
RPS6	Ribosomal protein S6
TIC	Tumor initiating cell

VDAC	Voltage dependent anion channel

Chapter 4

AC	Alternating current
Cr	Chromium
DC	Direct current
EBL	Electron beam lithography
EDA	Electrical Device A
EDB	Electrical Device B
EDC	Electrical Device C
EMF	Electromagnetic field
FITC	Fluorescein isothiocyanate
HPW	High-pressure wash
IPA	Isopropyl alcohol
I-V	Current-Voltage
PEM	Microtubule buffer solution (PIPES, EGTA, $MgCl_2$)
PLL	Poly-L-lysine
PMMA	Poly(methyl methacrylate)
PMT	Photomultiplier tube
Pt	Platinum
SEM	Scanning electron microscope
SWNT	Single-wall nanotube

Chapter 1

Introduction[*]

The current dominant theory of how cancer grows and develops is the somatic mutation theory (SMT), which focuses on genetic mutations as being the primary cause of cancer. The tissue organization field theory (TOFT) of cancer, that carcinogenesis takes place at the tissue level of biological organization, has recently been defended, citing numerous studies where tumor cells became normalized when placed within a normal morphogenetic field, such as when they were combined with normal mesenchyme, embryonic tissues, or normal extracellular matrices (ECMs) [1, 2]. The TOFT builds upon previous ideas from Szent-Györgyi [3, 4], that cancer is a disease of loss of order, akin to the cancerous cell reverting to a more primitive state of evolution characterized by lack of structure, fermentation, and unbridled proliferation [5]. The key difference in the SMT and TOFT theories of cancer is in defining the default state of cells in multicellular organisms; specifically whether the default state is quiescence or proliferation. The TOFT argues the default state is proliferation, and thus a loss of organization in the tissue leads to carcinogenesis. This aligns with Szent-Györgyi's previous ideas on cancer, where he wrote: "Not only were we too hasty in trying to cure cancer before understanding it, but we also may have asked the wrong question… The problem is not what makes cells proliferate, but what stops them from doing so in multicellular organisms, when proliferation is not needed. What is the brake?" [6].

Cancer can be viewed as a deregulation of the coordinated process that govern how cells are integrated into tissues, and thus cancer develops in the context of a loss of formation and developmental control [7]. It was found that progressive loss of the basement membrane may actively lead to neoplastic disorganization and tumor formation

---

[*] Chapter 1 contains material that was previously published as Friesen DE, Craddock TJA, Kalra AP, Tuszynski JA "Biological wires, communication systems, and implications for disease," *BioSystems* 2015, 127:14-27, in the introduction. I primarily researched and wrote this manuscript. J. Craddock added insight into neurodegenerative disease, A. Kalra added insight into certain microtubule conductivity experiment, and J. Tuszynski added insight to the entire paper. Only text written primarily by myself from this publication is included in this thesis.

[7]. Tumorigenesis is promoted when cells are isolated from neighbours by gap-junctional inhibition or physical barriers [8]. The morphogenetic field of the cell, being defined as the sum of patterning signals that carry information about the existing and future pattern of the organism, is key to embryonic development, regeneration after injury, and proper aging [8]. Bioelectric cues in this field are altered in cancer cells. For example, cancer cells have membranes that are typically depolarized [9], and this is associated with cell proliferation [10]. Indeed, artificial depolarization can make somatic cells have neoplastic-like properties [11]. Chronic inflammation increases the risk of carcinogenesis [12], and this may be due to the resulting disorganization of the tissue. That cancer is effected at the level of multicellular organization is apparent [8].

Cancer has been proposed to be impacted by a loss in the endogenous electrodynamic fields of cells, which affects structured water in cells and may lead to damping of MTs [13, 14]. A cancer detection device which emits 465 MHz waves, which is in use to detect prostate cancer, is theorized to detect these damped vibrations of MTs in cancer cells [15]. Nuclear magnetic resonance, used as a primary method in the detection of cancer, is theorized to detect the increased motional freedom of cancer water molecules [16]. Therefore, biophysical changes in cancer are being used to detect the disease.

When factors stimulating proper organization are reintroduced, cancer seems to be able to be remodelled into normal tissue [1, 2, 8, 17]. Cytokines are used to treat acute promyelocytic leukemia (APL), as all-trans retinoic acid (ATRA) induces differentiation of promyelocytes to mature cells [17]. The microenvironment of human embryonic stem cells can reprogram multipotent metastatic melanocyte cells to return to a melanocyte-like phenotype [18]. These examples demonstrate the crucial role organization and proper connection to the extracellular matrix have in mitigating cancer.

Forced biophysical changes also can suppress carcinogenesis. Artificial hyperpolarization of somatic cells can induce differentiation and suppress proliferation [11, 19]. Fusing cytoplasts from normal cells with karyoplasts from malignantly transformed cells is able to extinguish the tumorigenic phenotype [20]. Thus, a healthy cytoplasm, biophysical signals, and the microenvironment can trump genetic alterations [17].

Given these findings, the theory that cancer is primarily caused by genetic mutations may need to be expanded upon to include the role coherent structures play in the organism, and what disease the loss of coordination of these structures may lead to. Disorganization in the microenvironment for prolonged periods of time may lead to a phase transition to a diseased state where cells revert to an uncontrollably dividing state [21]. If submolecular signals, in addition to biophysical membrane potentials, are integral to organizational properties of the tissue, their measurement and characterization could be of insight to the carcinogenetic process, its detection, and its resolution.

This thesis will explore the role of structure in an organism using a multipronged approach. Microtubules (MTs) are a key element of the cytoskeleton of a cell, forming rigid cylinders in the cell that maintain a cell's shape. It was found that γ-tubulin, which is instrumental in nucleating microtubules, is overexpressed in glioblastoma multiforme (GBM) [22-26]. Our collaborators at the University of Alberta found compounds that interacted with γ-tubulin. We hypothesized the location of this binding, and I performed computational experiments to predict the binding location of these compounds to γ-tubulin. The goal of this project was the rational drug design of an effective small-molecular inhibitor of γ-tubulin, to pave the way forward to investigate γ-tubulin's biological roles in maintaining shape in the cell and its suitability as a cancer target.

Another aspect of maintaining structure is having the proper physical environment. Many physical properties of cells are generally altered in cancer. In many cancers it is found that cell membranes are depolarized [10, 27, 28], mitochondrial membrane potentials are hyperpolarized [29-31], intracellular pH is alkalized [32-35], and extracellular pH is acidified [32, 34, 35]. Additionally, as cancers become more transformed and metastatic, often they become more plastic [36-38], and the cytoskeleton becomes altered [36, 37, 39-42]. In effect, the cell's ability to maintain its order and proper function is potentially affected by these multiple changes, and key to these physical changes are the amount of ATP generated by oxidative phosphorylation by mitochondria and the amount of energy generated by glycolysis, which produces lactic acid. Mitochondria, in addition to producing ATP, are known to co-localize to microtubules in eukaryotes [43-47]. The cytoskeleton, made up of microtubules, actin, and intermediate filaments, plays a central role in several processes in the cell including

3

vesicle and organelle transport, cell polarization, and cell division [40, 48, 49]. Microtubules are theorized to oscillate mechanically [50] and obtain energy from possibly three main sources: hydrolysis of GTP, motor proteins, and liberated energy from mitochondria [14, 51]. It has been hypothesized that the greatest energy for microtubule oscillations comes from the approximately 60% unused energy liberated from mitochondria in the form of photons, heat, and chemical compounds other than ATP and GTP [51]. This could explain the need for co-localization of mitochondria to microtubules, which is shown in neurons and higher eukaryotic cells [43-46]. Thus, altered metabolism could affect the ability of microtubules to function normally should the energy they absorb be decreased. In Chapter 3, I investigate two main studies related to altered metabolism found in cancer. First, we hypothesized that changes in energy metabolism, which are characteristic of cancer cells, could lead to a high energetic cost of cancer to the body, especially in late stage cachexic cancer patients and be a primary cause of cancer cachexia [52]. Thus, I model how a tumor's high demand for glucose and glutamine combined with its high energetic cost contributes to muscle wasting seen in cachexic patients [52]. Second, I investigate targeting energy metabolism in order to target highly tumorigenic cells. The small molecular compound 3-bromopyruvate (3BP) has shown promise in targeting energy metabolism for the treatment of liver cancer with minimal side effects [53]. In epithelial ovarian cancer, tumor initiating cells (TICs) may play a central role in the relapse of patients undergoing current therapy [54-56]. Such TICs have been found to have high multi-drug resistance (MDR) properties to standard chemotherapeutic regimens [54]. In an ovarian epithelial cisplatin resistant cancer cell line displaying TIC properties, 3BP has been shown to resensitize the cells to cisplatin treatment [54, 57]. A cell line model of epithelial ovarian cancer at different stages of progression of the disease has been developed, which showed changes in cytoskeletal structure and metabolism [40, 58-60]. I hypothesize that 3BP targets late-stage ovarian cancer cells preferentially to early-stage cancer cells and report our findings. The goal of this study is to use energy metabolism to target the most tumorigenic and drug resistant ovarian cancer cells, which might be prevalent in recurrent ovarian cancer.

In Chapter 4, I review direct and indirect evidence indicating conductive properties of microtubules, actin, and collagen, which I refer to as bionanowires [61]. Through

connections made by integrins and connective proteins in the extra-cellular matrix, these bionanowires form an organism-wide matrix [62], which has been hypothesized to function as a communication system regulating the coordination of the organism [63]. If this is true, then each component of this signaling system should be able to support and facilitate electrical signaling. My goal is thus to develop a system to be able to detect and measure the electrical properties of these bionanowires. As a first step, my goal is to be able to characterize the electrical properties of MTs in a physiological-like ionic solution in a reproducible and robust system. Chapter 4 documents my findings on MT electrical properties in a physiological-like ionic solution, and the microfabrication and nanofabrication methods used to create my electrical measurement systems. I hypothesize that MTs making solid connections between platinum wires in physiological-like ionic solution will lead to improved measurements of ionic conductivity between the wires due to MTs.

As each chapter focuses on various aspects of microtubules and energy metabolism as targets of cancer treatment, the methods used in each chapter are distinct. Thus, each chapter contains its own methods section, as appropriate. Chapter 2 focuses on computational methods involving molecular dynamics simulations and drug-ligand binding. Chapter 3 uses mathematical modelling and cell culture based cytotoxicity assays. Chapter 4 details nanofabrication and microfabrication for use in novel electrical measurements of microtubules and eventually electrical measurements of other macromolecules such as actin and collagen.

The goal of this thesis is that the results and insights obtained by focusing on the biophysical aspects of cancer involving microtubules and energy metabolism will lead to improved treatment and prevention of cancer.

Chapter 2

Standard therapeutic intervention of cancer by targeting gamma-tubulin inhibition[*]

2.1 Introduction

This chapter describes my work to find a targeted inhibitor of γ-tubulin through *in silico* methods. Studies have shown an overexpression of γ-tubulin in human glioblastomas and glioblastoma cell lines [22-26]. As the two-year survival rate for glioblastoma is very poor (27.2% with radiotherapy and temozolomide [64]), potential benefit exists for discovering novel chemotherapeutic agents that can inhibit γ-tubulin [22], which is known to form a ring complex that acts as a microtubule nucleation center [65]. We present experimental evidence that colchicine and combretastatin A-4 bind to γ-tubulin, which are to our knowledge the first drug-like compounds known to interact with γ-tubulin. Molecular dynamics (MD) simulations and docking studies were used to analyze the hypothesized γ-tubulin binding domain of these compounds. The suitability of the potential binding modes were evaluated, and suggest the subsequent rational design of novel targeted inhibitors of γ-tubulin.

Microtubules, actin filaments, and intermediate filaments form the basis of the eukaryotic cytoskeleton. Microtubules are key to the correct functioning of the cell by providing structure, intracellular transport, and the creation of the mitotic spindle during

cell division. They are macromolecules consisting mainly of αβ-tubulin hetero-dimers and γ-tubulin at the nucleation site of the microtubule. γ-Tubulin is most known for its role as a nucleating agent for the creation of microtubules. In healthy dividing cells, γ-tubulin is associated at microtubule organizing centers (MTOCs) [66-68]. Current models suggest that γ-tubulin associates into a large γ-tubulin ring complex (γTuRC), where αβ-tubulin dimers then proceed to polymerize onto this template, creating a microtubule [69-72]. While α- and β-tubulin are abundant proteins, found in approximately equal amounts and making up approximately 2.5% of the total protein in a cell, γ-tubulin is decidedly less prevalent and makes up less than 1% of the total tubulin content of the cell [68].

In humans, there are two main isoforms of γ-tubulin denoted: TUBG1 and TUBG2. The isoforms are very closely related, with over 97% amino acid sequence identity [73], and it has been suggested that any chemical agent targeting one isoform would probably target the other [73]. The reason for two separate isoforms of γ-tubulin in humans has not yet been conclusively established [73, 74], and both isoforms were expressed in all tissues studied by Wise et al. [73]. In mice, it was found that TUBG1 was expressed ubiquitously, while TUBG2 was primarily found only in the brain [74]. Additionally, in mouse knockout studies it was found that TUBG1, as opposed to TUBG2, is critical to proper mitotic division, and thus it was concluded that TUBG1 corresponds to conventional γ-tubulin while TUBG2 has some still unknown function [74]. Although isoforms of γ-tubulin have been shown to have different expression levels and probably distinct functions in various species [74, 75], in mouse studies it was found that mouse γ-tubulin genes are orthologs of human TUBG1 and TUBG2 [74]. As both TUGB1 and TUBG2 are found to be over-expressed in human glioblastoma [22, 23], and in mouse knockout studies TUBG1 as opposed to TUBG2 was critical to proper mitosis [74], the present study is entirely focused on TUBG1 γ-tubulin.

Since microtubules play a pivotal role in mitosis by creating the mitotic spindle, tubulin has long been a natural target for chemotherapeutics [76, 77]. Chemotherapies targeting tubulin mainly involve the taxanes (ex. paclitaxel and docetaxel), and the vinca alkaloids (ex. vinblastine, vincristine). Paclitaxel is used as part of the treatment in breast, ovarian, prostate, non-small-cell lung cancer, and Kaposi's sarcoma [76]. Vinblastine is

used to treat leukemias and lymphomas [76]. Other drugs found to bind to tubulin include colchicine and, more recently, combretastatin, laulimalide, peloruside, and noscapine [78-81]. However, all of these drugs are thought to primarily target β-tubulin. At the time of this study, there were no known inhibitors of γ-tubulin.

Potential for therapeutic importance exists for a sufficiently specific and selective inhibitor of γ-tubulin. It has been shown that γ-tubulin is absolutely required for the assembly of mitotic spindle microtubules and an absence of functional tubulin leads to inhibition of mitosis [74, 82-84]. TUBG1 γ-tubulin has been found to be over-expressed in glioblastoma multiforme (GBM) [22, 24-26], the most prevalent and deadly form of brain cancer. While brain cancer is a relatively rare form of cancer [85], the prognosis for GBM is dismal, with a uniform survival of 3 months without treatment, and a median survival of only approximately 15.6 months with temozolomide treatment [86, 87], and 20.5 months with temozolomide and the novel treatment of tumor treating fields, involving applying low intensity 100-300kHz alternating electric fields to the tumor area, discussed in greater detail in Chapter 4 [88]. γ-Tubulin is also altered in breast cancer cells [89], and over-expressed in pre-invasive lesions and carcinomas of the breast [90, 91]. As γ-tubulin over-expression and altered cellular distribution is linked to tumor progression and anaplastic potential [22], a potent inhibitor of γ-tubulin would possibly halt mitosis in GBM, and lead to increased understanding for the altered expression of γ-tubulin in multiple cancers.

Thus, in this study, I have targeted the discovery of a ligand interaction with γ-tubulin. This is currently possible in view of the recent crystallographic studies of γ-tubulin [92, 93] that allow for a computational search of ligands with high binding affinities. Because γ-tubulin is structurally quite similar to β-tubulin [92], I concentrated our search on binding sites on γ-tubulin with homologous locations near binding sites of known β-tubulin inhibitors (see Figure 2.1). Our experimental results, using fluorescence spectroscopy and recombinant human γ-tubulin, indicate that colchicine and combretastatin A-4 bind to γ-tubulin (see Table 2.1 for compound structures). Computational studies identify both a possible binding site and a pose for these compounds bound to γ-tubulin.

Table 2.1. The structures of colchicine, colchicine derivatives, and combretastatin A-4.
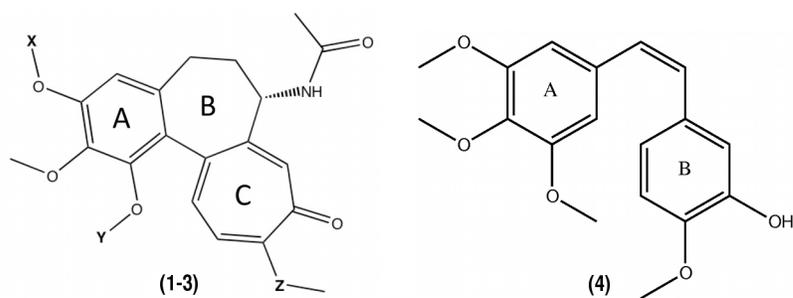
Ligands	X	Y	Z
1 (Colchicine)	CH_3	CH_3	O
2	CH_3	CH_2Ph, 3N	O
3a	H	CH_3	S
3b	CH_2CH_3	CH_3	S
3c	$CH_2CH_2CH_3$	CH_3	S
4 (Combretastatin A-4)			
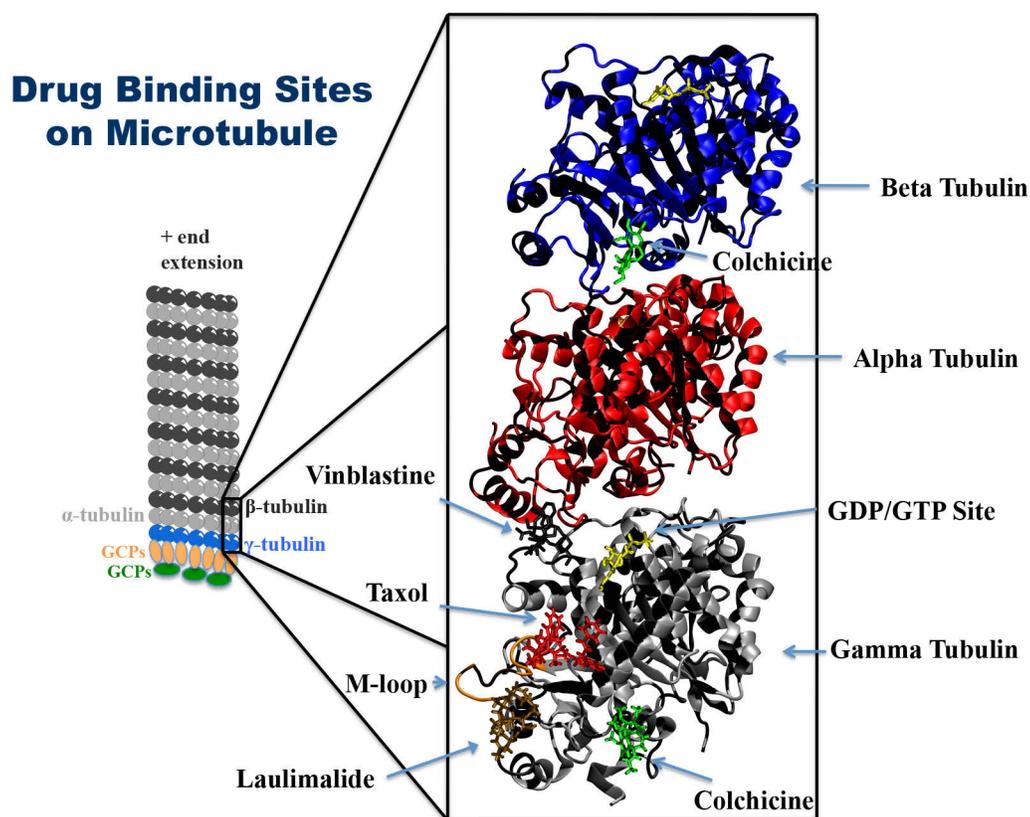
Figure 2.1. Homologous location of drugs known to target β-tubulin on γ-tubulin. This model was created using the crystal structure from Protein Data Bank (PDB) entry 1SA0, which contains two αβ-tubulin heterodimers bound together. The β-tubulin bound to the αβ-tubulin heterodimer was replaced with γ-tubulin in this model to illustrate hypothetical binding sites on γ-tubulin of ligands known to bind to β-tubulin. From this analysis, colchicine bound to γ-tubulin may bind in a region which might interfere with binding of γ-tubulin complex proteins (GCPs).

2.2 Experimental Methods

Experimental Apparatus and Reagents

The human TUBG1 gene was inserted into a pET15b vector between the *XhoI* and *HindIII* restriction sites (see Figure A.1 in Appendix A). The identity of the mutation and the correctness of gene insertion (location and orientation) were verified by DNA sequencing. The recombinant protein was expressed in *Eschericia coli BL21(DE3)* host cells in LB medium supplemented with 100 mg/ml ampicillin. The cultures were grown at 37 $^{\circ}$C until OD$_{600}$ reached a value of 0.8 and then induced with 1.0 mM IPTG for 18 hr at 25 $^{\circ}$C. Subsequently, the cells were harvested by centrifugation (6000 x *g* for 20 min in JS 7.5 rotor). The γ-tubulin protein was then isolated and purified from the inclusion

bodies via refolding by dilution with immobilized metal ion affinity chromatography (IMAC) using a Ni-NTA column.

More specifically, the cell pellet from 1L of culture with expressed γ-tubulin was resuspended in 25ml of lysis buffer and lyzed by sonication (using Fisher Scientific Ultrasonic Dismembrator Model 500 with microtip probe for 4 x 15 sec pulses at 45% power) on ice and centrifuged at 12,000 x g for 20 min (at 4 ^{o}C) in a JA 25-50 rotor. The supernatant was removed and inclusion bodies were cleaned by a series of washing procedures with buffer A (Buffer A: 50 mM Tris, 50 mM MgSO4, 50 mM NaCl, pH 8.8) containing 0.1% Triton X-100, 25% glycerol, 500mM NaCl and 2M Urea as separate additives for every next washing step. Inclusion bodies were centrifuged at 12,000 x g for 20 min (at 4 ^{o}C) in a JA 25-50 rotor after every wash and the supernatant was removed. Clean protein pellets were solubilized in a buffer B (Buffer B: 50 mM Tris, 50 mM NaCl, 1 mM CaCl2, 8 M Urea, 10 mM beta-mercaptoethanol, pH 8.8) and left for overnight incubation at room temperature with the next centrifugation at 33000 x g for 1 hr (25 ^{o}C) in a JA 25-50 rotor. The γ-tubulin protein was refolded by fast dilution (1:10) into the buffer C (Buffer C: 50 mM Tris, 50 mM NaCl, 10 mM MgSO4, 1 mM CaCl2, pH 8.8 and loaded onto a Ni-NTA column (12.5 mL bed volume) pre-equilibrated with buffer C. The loaded sample was incubated on a column for 1hr (at 4 ^{o}C) with rotation. The column was then washed with buffer D (Buffer D: 50 mM Tris, 50 mM NaCl, 10 mM MgSO4, 1 mM CaCl2, 10 mM imidazole, pH 7.2) and γ-tubulin was eluted with a linear gradient of 500 mM imidazole in buffer D. Fractions with protein were identified by SDS-PAGE mixed and dialyzed overnight (at 4 ^{o}C with two buffer changes) against 10 volumes of buffer E (Buffer E: 25 mM Tris, 25 mM NaCl, 10 mM MgSO4, 1 mM MgCl2, 1 mM CaCl2, pH 7.3). The protein concentration was determined using an extinction coefficient at 280nm of 47705 M^{-1}cm^{-1}. The extinction coefficient was calculated by Protparam program [94] based on recombinant γ-tubulin amino acid sequence. The TUBG1 protein was then concentrated using an Amicon Ultra-15 centrifugal device.

Fluorescence emission spectra were recorded on a PTI MODEL-MP1 spectrofluorometer using a 1 cm fluorescence cell in all measurements. The excitation wavelength of 295 nm was used and the scan range was 310-450 nm. The gene for human γ-tubulin was purchased from DNA2.0 Inc. USA. All reagents were purchased from

Sigma and Fisher. NI-NTA resin was purchased from Qiagen. The purity of colchicine was > 95% and it was determined by liquid chromatography-mass spectrometry (Agilent Eclipse plus C18 column, 250 mm × 4.6 mm, 5 μm particle size; mobile phase, water/acetonitrile (0.1% HCOOH) 80:20 to 5:95 over 5 min and then held for 1.5 min; flow rate 0.5 mL/min). The sample was dissolved in methanol.

Combretastatin A-4 was purchased from Sigma-Aldrich. The purity of combretastatin A-4 was ≥98%, determined by high-performance liquid chromatography.

Binding Experiments and Fluorescence Assays

In a 96-well microplate placed in a shallow tray with ice, γ-tubulin was mixed with the assay buffer to reach a final protein concentration of 2 μM. Guanosine 5'-Triphosphate (GTP) was added to the samples and control to keep a final concentration at 1 mM. The microplate was incubated on ice for 10 min then calculated amounts of stock solution of colchicine in DMSO were added to the samples to reach final ligand concentrations of 10 μM, 40 μM, and 80 μM, respectively. The control was ligand-free. The total volume of the sample was 100 μL. A glass bead was inserted in each well and the microplate was covered with protective film, sealed with a lid and incubated for 30 minutes at 25^0C. After that time the microplate was transferred to a rotating platform and it was vigorously rotated for 1 hour at room temperature. From each well 80 μL of samples and control were transferred to a 1 cm fluorescence cell. Fluorescence of the tubulin was monitored at 295 nm (excitation wavelength) and the scan range was 310-450 nm.

Estimation of the Binding Constant

Data from the fluorescence experiments were used to determine the apparent binding constant of γ-tubulin in the presence of the ligands according to the formula:

$$Fo/F = 1 + K_A[Q] \tag{1}$$

where $K_S = K_A$, the formation constant of the donor-acceptor (quencher-fluorogen) complex. The concentration of the quencher [Q] after titration was taken to be its ratio to γ-tubulin concentration [Pt]: [Q]/ [Pt] [95]. From the slope of the linear plot of Fo/F vs [Q]/ [Pt] the binding constant and dissociation constant ($1/K_A$) were estimated. The results were expressed as mean values ± S.D. (n=3). The inner filter effects were corrected empirically by measuring the change of fluorescence intensity of a tryptophan

solution equivalent to the γ-tubulin concentration in the presence of colchicine, and the corrected fluorescence intensities were used for all calculations [96].

Amine Cross-Linking Assay

In 1.5 ml Eppendorf tubes pre-chilled on ice, recombinant γ-tubulin (in 10 mM potassium phosphate, 1 mM MgSO4, 1 mM MgCl2, pH 7.6) was mixed with αβ-tubulin dimer (phosphocellulose purified from a bovine source, kindly provided by Dr. Richard Ludueña, University of Texas Health Science Center, San Antonio, TX) and 10 mM potassium phosphate buffer (pH 7.6) to reach the final protein concentration of 2 μM each. GTP was added at the same time to a final concentration of 1 mM. The protein mixture was incubated on ice for 5 min then calculated amounts of stock solution of disuccinimidyl glutarate (DSG) in DMSO were added to the samples to make cross-linking reagent/protein ratios of 1:1, 0.1:1 and 0.01:1, respectively. Two control samples were prepared for every DSG/tubulins combination. The first control sample included the cross-linking reagent and γ-tubulin only. The second control sample included the cross-linking reagent and the αβ-tubulin dimer only. The total volume of the sample was 100 μL. Samples were incubated for 30 minutes at room temperature. After that time the cross-linking reaction was quenched by addition of 1M Tris, pH 8.0 (50 mM final concentration) and samples were incubated at room temperature for an additional 15 minutes. 12% SDS-PAGE protein gel was used to visualize the amine cross-linking assay results.

Comparison Between β-Tubulin and γ-Tubulin Structures

The first X-ray crystal structure of γ-tubulin (bound to GTPγS) was reported by Aldaz et al. in 2005 at 2.7 Å resolution (Protein Data Bank (PDB) entries 1Z5V and 1Z5W) [92]. Rice et al. then reported a refined 2.3 Å crystal structure of γ-tubulin bound to GDP in 2008 (PDB entry 3CB2) [93]. It was found that the structure of γ-tubulin bound to GDP was in a curved conformation identical to that of γ-tubulin bound to GTPγS [93]. It was then concluded that γ-tubulin does not undergo a curved-to-straight domain change based on its nucleotide binding state [93]. Thus, while γ- and β-tubulin bind to GTP with similar affinity, and have a similar preference to bind to GTP over GDP as found by Aldaz et al. [92], we used the latest crystal structure from PDB entry 3CB2 of γ-tubulin

bound to GDP as the basis of our computation search for a γ-tubulin inhibitor because this structure would give us the highest resolution of γ-tubulin.

MD Simulations

MD simulations followed the procedure outlined by Barakat et al. [97] using NAMD [98]. PDB2PQR [99] and PTRAJ using the AMBER99SB force field [100] from Amber 10 [101] were used in setting up the system as described by Barakat et al. [97]. γ-Tubulin (residues 2-446) and the associated GDP from chain A were taken from PDB entry 3CB2 [93]. Swiss-PdbViewer 4.0 [102] was used to model the missing residues in the crystal structure (residues 1, 278-283, 311-312, 367-371, and 447-451). GDP was modeled using Amber 99 force field parameters developed by Meagher et al. [103]. A TIP3P water cube buffer that ensured 15 Å of water surrounded the system added 26,499 water molecules. Counter-ions were added to reproduce physiological ionic concentrations. The system was equilibrated for 519 ps by gradually releasing the constraints on the backbone atoms. The simulation, using period boundary conditions, then continued for 24 ns during which atomic coordinates were saved from the trajectory every 2 ps. To control the pressure at a standard atmospheric pressure value, a Langevin piston period of 300 fs was used.

Clustering

In order to generate a reduced representative sample of γ-tubulin conformations over the entire MD simulation trajectory, I followed the same method used by Barakat et al. [97, 104]. I examined the final 16 ns of our 24 ns MD simulation, when the root-mean-square deviation (RMSD) of the backbone atoms of the structure had stabilized (see Figure A.2 in Appendix A). RMSD and B-factor calculations were performed using PTRAJ in Amber 11 [105] (see Figure A.3 in Appendix A).

To extract representative structures for the colchicine binding site, I performed RMSD clustering on the 20 residues (excluding their hydrogens) that line the hypothesized colchicine binding site in γ-tubulin, namely: 242, 243, 248, 250-256, 258, 259, 321, 323, 334, 337, 341, 357-359. Clustering was performed on 4,001 structures every 4 ps in the final 16 ns of the MD simulation. As described below, using the DBI and SSR/SST metrics, an optimal number of 35 clusters was found, and the centroid of each cluster was chosen as the representative structure. These structures were later evaluated by our docking studies.

Docking

The colchicine ligand used for docking was the colchicine structure found from PDB entry 1SA0, chain B [106]. This colchicine in PDB entry 1SA0 was actually a colchicine derivative, with an added sulfur atom. The sulfur atom was removed, and the carbon previously bonded to the sulfur (C13) was modified to be located at 1.5046 Å from C12 in order to agree with the distance found in the colchicine structure from PubChem (CID_6167.sdf) and to generate a computational structure of the colchicine ligand.

All docking simulations were performed using AutoDock, version 4.0 [107]. Partial atomic charges were assigned to both the protein and docked ligands using the Gasteiger-Marsili method [108]. Atomic solvation parameters were assigned to the atoms of the protein using the AutoDock 4.0 utility ADDSOL. Docking grid maps with $54 \times 60 \times 126$ points and grid point spacing of 0.31 Å were then centered on the hypothesized colchicine binding site within γ- and β-tubulin using the AutoGrid 4.0 program [107]. Rotatable bonds of each ligand were then automatically assigned using the AUTOTORS utility of AutoDock 4.0. Docking was performed using the Lamarckian Genetic Algorithm (LGA) method with an initial population of 400 random individuals; a maximum number of 10×10^6 energy evaluations; 100 trials; 30,000 maximum generations; a mutation rate of 0.02; a crossover rate of 0.80 and the requirement that only one individual can survive into the next generation. Independent docking runs were performed for each protein structure and colchicine derivative with all residues of the receptors set being rigid during the simulations.

Colchicine Derivatives

The structures of colchicine and colchicine derivatives used in this study are given in Table 2.1. Elsewhere, we have described in detail the generation and characterization of colchicine derivatives based on the differences observed among the most commonly expressed human tubulin isotypes: βI, βII, βIII, βIV and βV [109]. The colchicine derivatives were modified at either the C1 or C3 methoxy position of the A-ring (see Table 2.1). Acylation of the common intermediates 1 or 3-demethylcolchicine afforded ester derivatives while alkylation gave ether derivatives. The general synthetic schemes for the ester and ether derivatives of colchicine were based on previously published schemes [110]. The modification to the first analog was done by replacing the $-OCH_3$ in

15

the $C13$ position of the A-ring of colchicine by different $-OX$ groups. In the second analog, the $-OCH_3$ in the $C11$ position of the A-ring and the $-OCH_3$ in the C-ring of colchicine were replaced by different $-OY$ groups and $-SCH_3$, respectively. All of these resulting derivative structures including colchicine were constructed using the MOLDEN program [111]. In constructing the models we used colchicine derived from PDB entry 1SA0 as the starting structure (see "Docking" section above) [106].

Equivalent Binding Site Energies

Given the AutoDock predicted binding energies (ΔG) in kcal/mol, we used the formula: $\Delta G = RT \ln(K_D)$ to calculate the equivalent K_D value.

Figure Representations

All figures representing proteins were generated using VMD [112], and were aligned using the RMSD Trajectory Tool plugin for VMD. Electrostatic calculations for figures were done using APBS Plugin for VMD [113].

2.3   Results

Discovery of Colchicine and Combretastatin A-4 Binding to γ-Tubulin

Identification of a potent small molecule inhibitor of γ-tubulin first requires finding a molecule that binds to γ-tubulin. The crystal structures of both γ-tubulin (TUBG1) and β-tubulin (TUBB2B) are presently available (PDB entries 3CB2 [93] and 1SA0 [106], respectively), and comparison of the two yields a very similar tertiary structure, discussed by Aldaz et al., with an RMSD of only 1.18 Å in the intermediate β-sheets (see Figure 2.2) [92]. There is a 33% sequence identity and a 75% structure similarity of the two structures [114]. Given this similarity of these structures, we tested colchicine, combretastatin A-4, and paclitaxel, all known to bind to β-tubulin, using a fluorescence spectroscopy assay with recombinant human γ-tubulin, and discovered evidence that colchicine and combretastatin A-4, both inhibitors of β-tubulin, also binds to γ-tubulin. Paclitaxel showed no evidence of binding to γ-tubulin (data not shown). Colchicine and combretastatin A-4 are known to bind to the same binding site on β-tubulin [115].

16
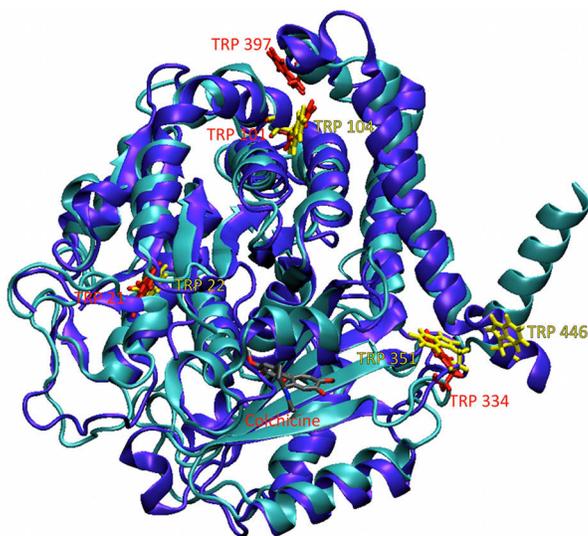
Figure 2.2. β-tubulin from PDB entry 1SA0 (cyan) and γ-tubulin from PDB entry 3CB2 (purple) are aligned, showing tertiary structure similarity. Colchicine docked to β-tubulin is shown. Tryptophans from β-tubulin are shown in red, and tryptophans from γ-tubulin are shown in yellow.

The tubulin hetero-dimer, which contains four tryptophan residues in both the α- and β- monomer, has intrinsic fluorescence of which can be used to detect ligand binding and to monitor conformational changes of the protein associated with binding [116-118]. Fluorescence quenching as a result of colchicine binding to tubulin has been extensively observed and analyzed [117, 118]. Given that γ-tubulin contains four tryptophan residues in three of the same areas (see Figure 2.2), and has a high tertiary structure similarity to β-tubulin, fluorescence spectroscopy was selected as a reasonable method to detect a binding event of colchicine to γ-tubulin. The fluorescence spectrum of human γ-tubulin in the presence of colchicine is shown in Figure 2.3A. The final fluorescence value was corrected for any possible inner filter effect. A notable quenching of the tryptophan fluorescence of γ-tubulin was observed upon addition of increasing concentration of colchicine as a result of ligand binding. According to the graph shown in Figure 2.3B the addition of 80 µM of the ligand quenched more than 70 percent of the fluorescence of the protein expressed as the percentage of fluorescence extinction of the tubulin tryptophans (denoted as F/Fo, %). Similar to the results found previously for other tubulin isoforms [119], colchicine induces structural changes in the γ-tubulin upon binding since a blue shift of the maximum emission wavelength ($\Delta\lambda$em = 11nm) was observed (see Figure

17

2.3A), which suggests a change in the polarity of the environment surrounding one or more of the emitting tryptophan residues. The Stern-Volmer plot of the fluorescence data obtained from the colchicine binding is linear in the range of concentrations tested for this ligand. From this graph the value of the apparent dissociation constant was estimated as, K_D=13.9 ± 0.4 μM (see Figure 2.3C), which is equivalent to a binding energy of -6.9 ± 0.03 kcal/mol at 310 K. This K_D value is higher than our to our experimental results of colchicine binding to $α_I β_I$-tubulin with a K_D of 5.40 μM [120], which suggests colchicine has a higher affinity to β-tubulin over γ-tubulin. This direct comparison of fluorescence quenching data of colchicine interacting with both γ-tubulin and $α_I β_I$-tubulin is found in Figure A.4 in Appendix A. Published K_D values of colchicine binding to bovine tubulin yield K_D values of 1.1-1.4 μM [115, 121-123], is less than our experimental results, but may be due to experimental conditions and differing methods of measurement.
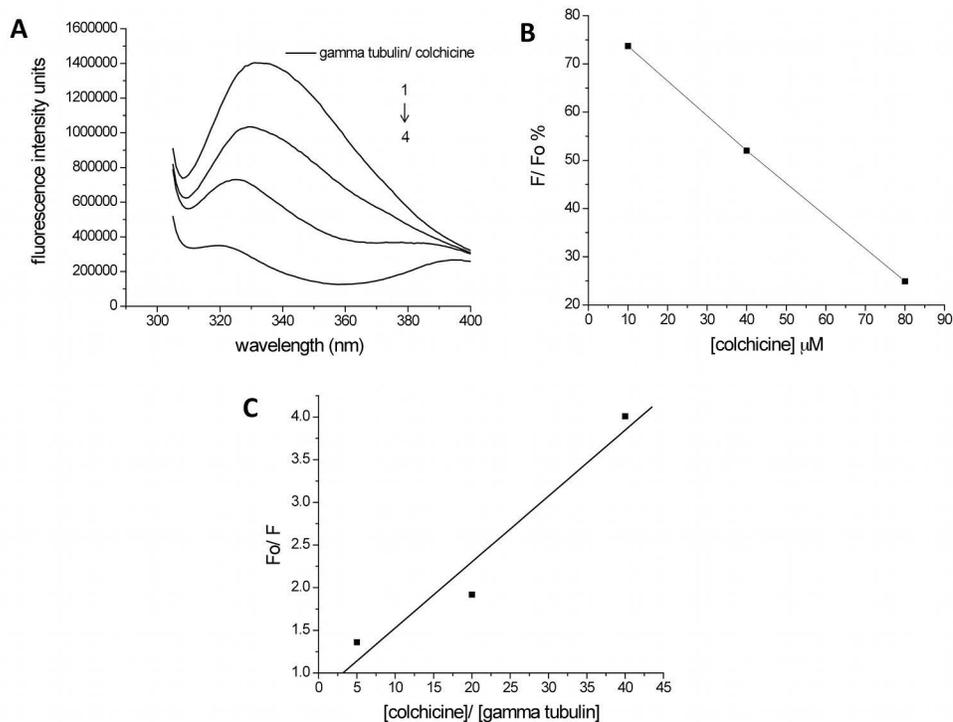
Figure 2.3. Fluorescence emission spectra of γ-tubulin (2 μM) in the presence of colchicine: 0 μM (1), 10 μM (2), 40 μM (3), 80 μM (4). λexcit= 295 nm, slit width 5 nm (A). Tryptophan fluorescence quenching of γ-tubulin (2 μM) plotted as extinction of tubulin tryptophans (F/Fo, %) in the presence of increasing concentrations of colchicine (B). The Stern-Volmer plots of fluorescence quenching of γ-tubulin by colchicine (C). The value of the K_D estimated from this plot by using equation 1 is 13.9 ± 0.4 μM.

The fluorescence spectrum of human γ-tubulin in the presence of combretastatin A-4 is shown in Figure 2.4. This shows combretastatin A-4 binding to γ-tubulin in a concentration-dependent fashion. However, the ligand has a strong fluorescence emission (450 nm) at the same excitation wavelength of the tryptophan (295 nm) that interferes with the protein quenching. Thus, a quenching effect as shown for the colchicine-γ-tubulin interaction has not been clearly demonstrated yet, and thus K_D values were not calculated. We plan to perform more careful measurements for combretastatin and its analogs in the future. Published results show combretastatin binds to tubulin with a K_D of 0.40 ± 0.06 μM, making it a stronger binder than colchicine to the colchicine binding site on β-tubulin [124].
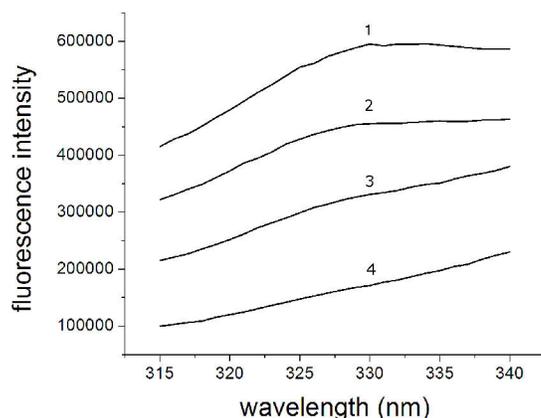
Figure 2.4. Fluorescence emission spectra of γ-tubulin (2 μM) in the presence of different concentrations of combretastatin A-4: 0 μM (1), 10 μM (2), 40 μM (3), 80 μM (4). λexcit= 295 nm, slit width 3 nm.

Validation of the Quality of γ-Tubulin Created

As recombinant γ-tubulin studied in isolation is a relatively novel construct, we performed an αβ-tubulin dimer and γ-tubulin amine cross-linking assays to assess if the γ-tubulin created was in a functionally correct conformational state. In theory, if we have an αβ-tubulin dimer and functional γ-tubulin, these proteins would combine to make a trimer. Each tubulin monomer is ~55 KDa. Our 12% SDS-PAGE gel showed evidence of the expected trimer of γ-tubulin bound to the αβ-tubulin dimer in the 130-170 kDa molecular weight range, in the assay involving the reactive mixture of αβ-tubulin, γ-tubulin, and disuccinimidylglutarate (DSG) (see Figure A.5 in Appendix A). Controls of

reactive mixtures with just γ-tubulin and just αβ-tubulin combined with DSG showed no bands in the 130-170 kDa molecular weight range as expected (see Figure A.5 in Appendix A). This suggests our prepared γ-tubulin binds as expected to the αβ-tubulin dimer, which is consistent with it being in a functional state. A more comprehensive analysis of γ-tubulin functionality was beyond the scope of this project but we intend to perform appropriate assays in a future study. Multiple preparations of γ-tubulin showed the same fluorescence quenching in the presence of colchicine (see Figure A.6 in Appendix A).

Additionally, we have used the same methods for expressing recombinant tubulin in the case of β-tubulin single residue mutants and tested their products by performing binding affinity assays with a host of ligands known to bind to α/β tubulin dimers. The results obtained for binding colchicine to γ-tubulin closely reproduced the known values of the binding kinetics constants of colchicine to β-tubulin giving us a level of confidence that the method produces a protein that is properly folded.

Binding Site Prediction of Colchicine to γ-Tubulin

Given the experimental information that suggest colchicine and combretastatin A-4 bind to γ-tubulin, we used computational methods to predict the binding pose and location of these compounds bound to γ-tubulin. The crystal structure of γ-tubulin from PDB entry 3CB2 (TUBG1) was used for the computational docking process [93]. This structure was missing 19 residues that were repaired using Swiss-PdbViewer 4.0 (see Methods) [102]. An MD simulation of γ-tubulin bound to GDP in explicit water solvent was performed for 24 ns. The last 16 ns of this simulation were identified to have a stable RMSD from the initial reference structure for residues not in the N- and C-termini, i.e. residues 2 to 438 (see Figure A.2 in Appendix A). Fluctuation analysis shows the movement of each residue in the simulation, and clearly identifies the N- and C-termini (see Figure A.3 in Appendix A). The homologous region on γ-tubulin corresponding to the binding site of colchicine on β-tubulin was selected for investigation as to whether there was computational support for colchicine binding to this region. Combretastatin A-4 is known to bind to the same location as colchicine on β-tubulin so the same site on γ-tubulin was investigated for combretastatin A-4 binding as well.

20

Protein Flexibility in Docking

Proteins are structurally dynamic biomolecules in solution. This behavior is essential for recognition and binding to other molecules inside the cell. Although many attempts have been made to take into account the flexibility of the target with docking algorithms, there are many challenges to find a computationally efficient way of dealing with this flexibility. One solution is to use the relaxed complex scheme [125-128], which is an approach to accommodate receptor flexibility and allows for the use of accurate docking scoring techniques in order to implement a hybrid between static docking and MD simulations. I utilized this method by running a 24 ns MD simulation to explore the conformational space of the target, and then we subsequently docked the ligand to our representative ensemble of 35 receptor conformations.

By extracted structures every 2 ps from our MD simulation, the final 16 ns of the trajectory that yielded a stable RMSD that had 8000 resulting (snapshot) structures. To reduce this set to a manageable number of representative structures, I used average-linkage clustering which has been documented to be effective in this task [129]. This clustering method yields several metrics that help reveal the optimal number of clusters to be created and their population size. The metrics are the Davies-Bouldin index (DBI) [130] and the ratio of the sum of squares of the regression (SSR) to the total sum of squares (SST) [129]. A high-quality clustering is associated with a local minimum DBI value. As well, the percentage of variance explained by the data, shown by the SSR/SST curve, is expected to plateau for cluster counts exceeding the optimal number of clusters [129]. Using these metrics, by varying the number of clusters, I looked for adequate clustering by selecting a local minimum for DBI and for a leveling off of the line for the percentage of variance explained by the data, shown by the SSR/SST curve, which is known as the "elbow criterion" [129]. Using this methodology, I reduced the 8000 MD trajectory structures into just 35 target structures (see Figure A.7 in Appendix A) to represent the conformational space of the binding site within γ-tubulin (see Figure A.8 in Appendix A).

Docking Colchicine to γ-Tubulin

Colchicine (denoted as colchicine derivative **1**: see Table 2.1) was docked to the 35 representative structures of γ-tubulin created from our clustering method, which we refer

to as targets 1 through 35. The targets were ordered based on the percentage of the trajectory that they represented, i.e. Target 1 represented the target representing the greatest proportion of the trajectory (at 33%). A binding mode resulting from the docking procedure was considered a hit if its presence in the results presented by AutoDock was more than or equal to 20% of the found poses. This indicates that it is a well-defined mode of binding and could be used for further analysis. Using a cutoff of docking cluster size of 20%, target 3 (which comprised 6.5% of the trajectory), gave the computational docking result with the greatest binding energy of -7.9 kcal/mol. However, colchicine docking to target 34 (comprising 0.1% of the trajectory) had the overall greatest binding energy of -8.7 kcal/mol but with a docking cluster size of only 6%. Both these targets had colchicine oriented deep within the binding pocket with the A-ring deepest in the pocket, similar to that of colchicine binding to β-tubulin (see Figure 2.5).
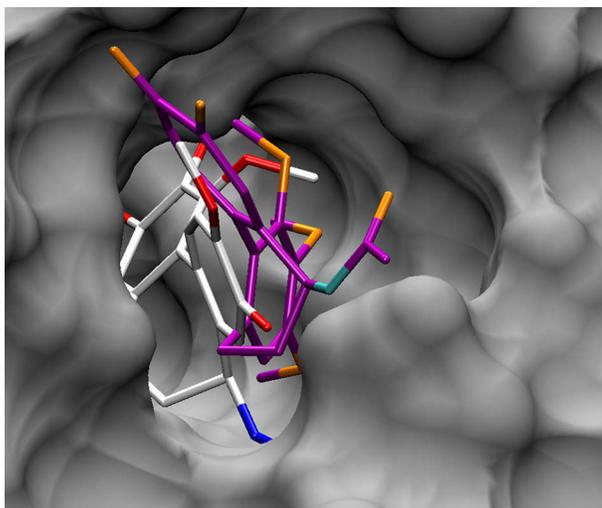
Figure 2.5. Colchicine bound to γ-tubulin in target 3 (white), and the relative position of colchicine bound to β-tubulin (purple). γ-Tubulin from target 3 is displayed (silver) and is aligned with β-tubulin to indicate the relative position of colchicine bound γ-tubulin versus β-tubulin. These computational findings suggest colchicine bound to γ-tubulin may be able to penetrate deeper than colchicine bound to β-tubulin. Both structures have the colchicine A-ring penetrating deepest into the protein.

Colchicine derivatives **2**, **3a**, **3b**, and **3c** (see Table 2.1) were also docked to the 35 representative structures to determine whether these derivatives had any potential to preferentially bind to γ-tubulin over β-tubulin. Results showed that all these derivatives had a best binding energy between -8.0 and -8.6 kcal/mol (although many of these cluster sizes were below 20%), which was comparable in binding energy to the results of

colchicine binding to γ-tubulin. It is worth mentioning as a cautionary note that the standard error in binding energies given from our docking software, AutoDock, is empirically on the order of ± 2.5 kcal/mol [107]. The binding energies of colchicine and the corresponding derivatives that had the greatest binding energy are summarized in Table 2.2.

Table 2.2. Best AutoDock binding energies compared for colchicine and colchicine derivatives docked to 35 representative structures of γ-tubulin. Best AutoDock binding energy of combretastatin A-4, which was docked to targets 3, 33, and 34, is also shown for comparison.

Compound	γ-Tubulin Target Structure (except first entry)	Binding energy (kcal/mol)	Equivalent K_D (μM)	Cluster size (%)
1	β-tubulin	-6.8	15	41
1	Target 3	-7.9	2.6	23
1	Target 34	-8.7	0.77	6
2	Target 3	-8.2	1.6	4
3a	Target 33	-8.0	2.3	96
3a	Target 3	-8.0	2.3	28
3a	Target 34	-7.9	2.6	15
3b	Target 3	-7.6	4.6	2
3b	Target 33	-7.0	11	16
3b	Target 34	-8.3	1.4	8
3c	Target 34	-8.6	0.83	3
4	Target 33	-5.9	69	58

Docking Colchicine to β-Tubulin

As a positive control for our AutoDock docking studies, we computationally docked colchicine to β-tubulin, and I compared our computational results with the experimental result seen in PDB entry 1SA0 [106]. Colchicine bound in the same orientation as in the crystal structure shown in Figure 2.6. Colchicine bound to β-tubulin with an AutoDock binding energy of -6.8 kcal/mol, which compares well with our experimental fluorescence quenching binding energy estimate of -6.9 ± 0.03 kcal/mol. This is also within the error of AutoDock's energy calculating function and is comparable to other experimental binding energy estimates of -8.4 kcal/mol for colchicine bound to bovine

tubulin (calculated from a K_D of 1.1 μM) [121, 122]. This AutoDock binding energy result is summarized in Table 2.2.
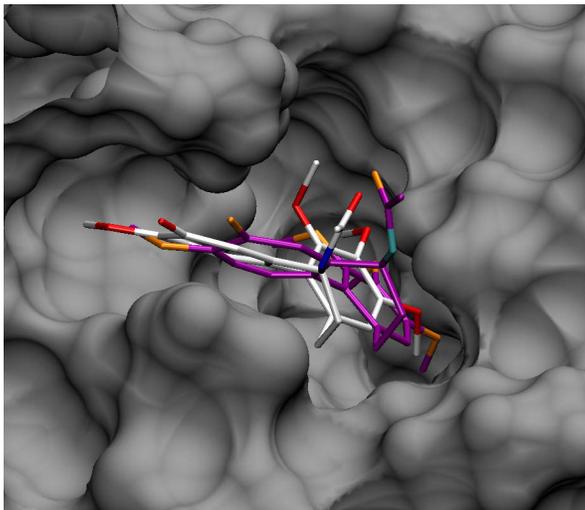
Figure 2.6. Colchicine docked to β-tubulin (white) and colchicine from PDB entry 1SA0 (purple) in β-tubulin from PDB entry 1SA0. Distance between nitrogens in the two colchicines is 2.3 Å, indicating good agreement in the docked pose generated from AutoDock and the known pose given from crystal structure (PDB entry 1SA0).

Docking Combretastatin A-4 to γ-Tubulin

Combretastatin A-4 was docked to targets 3, 33, and 34, which were the targets found most amenable to colchicine and colchicine derivative binding. Computationally, combretastatin A-4 bound to γ-tubulin with a best AutoDock binding energy of -5.9 kcal/mol and a significant cluster size of 58% (see Table 2.2. Best AutoDock binding energies compared for colchicine and colchicine derivatives docked to 35 representative structures of γ-tubulin. Best AutoDock binding energy of combretastatin A-4, which was docked to targets 3, 33, and 34, is also shown for comparison.). Its computational binding pose is shown in Figure 2.7. This pose is deep inside the hypothesized colchicine binding pocket and shows promise for subsequent design of targeted derivatives that bind to this site.
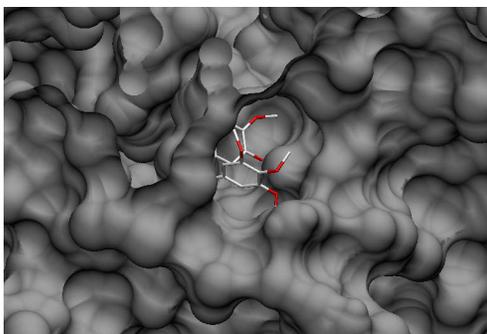
Figure 2.7. Combretastatin A-4 bound to γ-tubulin in target 33. This pose is deep inside the γ-tubulin hypothesized colchicine binding site.

Computational Results Overview

Our AutoDock binding energies were comparable between colchicine binding to γ-tubulin and β-tubulin, with binding energies of -7.9 and -6.8 kcal/mol respectively (see Table 2.2). It should be noted that the primary strength of AutoDock is in determining binding positions and not in calculating an accurate binding energy. The best docking trials of colchicine binding to γ-tubulin, in terms of binding energy, had colchicine consistently binding to γ-tubulin in a pose similar to that of colchicine binding to β-tubulin, with the A-rings of colchicine penetrating furthest into the protein (see Figure 2.5) [106]. The electrostatic characteristics of these binding poses are shown in Figure 2.8 and Figure 2.9. It is seen that colchicine binds to a predominantly electropositive region of β-tubulin, but our hypothesized binding location on γ-tubulin has both positive and negative electrostatic regions. This is not surprising given β-tubulin and γ-tubulin have different electrostatic profiles, which may alter their preference to bind laterally or longitudinally [131]. The different electrostatic profiles of the hypothesized γ-tubulin binding pocket suggest opportunities to derivate targeted colchicine and combretastatin derivatives to bind specifically to γ-tubulin which is our intention for future work. The similarity of the binding poses and binding energies between our computational and experimental work for colchicine give added probability that our computationally predicted binding poses are indeed accurate. However, ultimately direct experimental validation of the binding poses of colchicine and combretastatin A-4 to γ-tubulin are required.
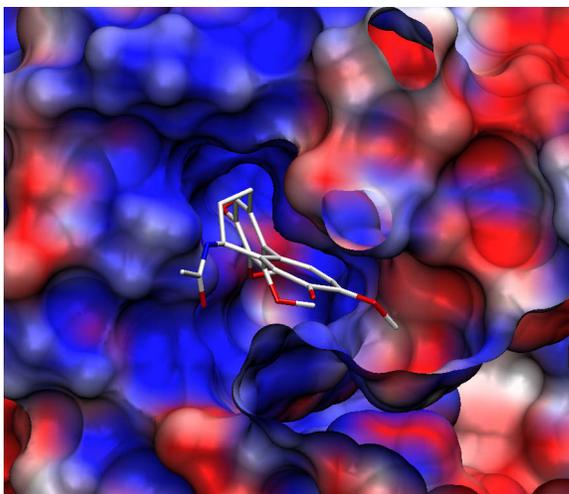
Figure 2.8. Colchicine binding pocket from β-tubulin (PDB entry 1SA0). Colors of protein convey electrostatics: positive (blue) and negative (red). This binding region is predominantly positive electrostatically.
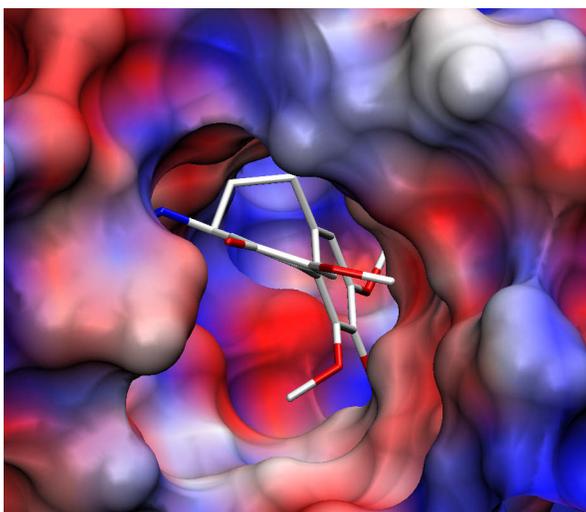
Figure 2.9. Colchicine binding pocket hypothesized in γ-tubulin. Colors of protein convey electrostatics: positive (blue) and negative (red). This binding region contains both positive and negative regions.

Colchicine derivatives that were earlier investigated for their isoform-specific binding to β-tubulin [109] were analyzed here for their hitherto unknown potential to target γ-tubulin (see Table 2.2). The fact that the docking of colchicine derivatives yielded similar binding energies as colchicine itself neither indicates their potential for utilization as specific targets of γ-tubulin inhibition nor discounts their effectiveness in this regard. Further characterization of the binding site is needed for any definitive conclusions to be

made as to whether an appropriate colchicine derivative can be designed with a sufficiently high affinity for the investigated γ-tubulin binding site.

Pharmacokinetic Properties of Ligands

The pharmacokinetic properties of colchicine, its derivatives, and combretastatin A-4 were analyzed in order to gauge their potential as chemotherapeutics for GBM (see Table 2.3). Colchicine and its derivatives had predicted partial coefficient (Log P) values from 1.37-2.55, human jejunal permeability (P_{eff}) from 1.03-1.29 cm/second x 10^4, and solubility in intestinal fluid (FaSSIF) of 0.071-0.559 mg/ml. Combretastatin A-4 is importantly smaller and has a decreased polar surface area (57.15 $Å^2$) compared to that of colchicine and colchicine derivatives (73.86-95.98 $Å^2$), making derivatives of combretastatin A-4 more amenable to passing the blood-brain barrier in a possible treatment for GBM.

Table 2.3. Selected properties for compounds. Log P: octanol-water partition coefficient. P_{eff}: human jejunal effective permeability. FaSSIF: solubility in simulated fasted state intestinal fluid. MW: molecular weight. T_PSA: topological polar surface area. These results were generated by ADMET Predictor™ 5.5 software provided by Simulations Plus, Inc., Lancaster, California, USA.

Compound label	Log P	P_{eff} (cm/s × 10^4)	FaSSIF (mg/mL)	MW (g/mol)	T_PSA ($\bar{Å}^2$)
1 (Colchicine)	1.37	1.03	0.559	399.45	83.09
2	1.44	1.09	0.146	476.53	95.98
3a	2.42	1.09	0.207	401.48	84.86
3b	2.34	1.09	0.113	429.54	73.86
3c	2.55	1.29	0.071	443.57	73.86
4 (Combretastatin A-4)	2.57	5.35	0.041	316.36	57.15

2.4   Discussion

As γ-tubulin is over-expressed in GBM, and is required to nucleate microtubules that divide a cell in mitosis, it is a potential target for a novel chemotherapeutic agent. A potential inhibitor of γ-tubulin would ideally be highly specific for γ-tubulin and not have as great an affinity to the structurally similar α- and β-tubulin proteins. This is because γ-tubulin, being involved in nucleating the microtubule and not in the microtubule's polymerization, is less abundant than the more prevalent α- and β-tubulins. Thus, any

inhibitor that binds with similar affinity to both β- and γ-tubulin, for instance, might act with an effect similar to an inhibitor binding only to β-tubulin. Based on our fluorescence spectroscopy results that show colchicine having a similar affinity to both γ- and β-tubulin, this may indeed be the situation with colchicine. It is notable that colchicine did not pass clinical trials as a β-tubulin inhibitor due to toxicity. Therefore, a more targeted inhibitor of γ-tubulin might be able to have therapeutic window at a lower dosage and thus provide a higher therapeutic index. It is also possible to speculate that inhibiting γ-tubulin results in extreme toxicity and that colchicine may in addition to inhibiting β-tubulin, may also be inhibiting γ-tubulin, leading to its extreme toxicity. Further studies are required to test the therapeutic value of a γ-tubulin inhibitor. However, even if inhibiting γ-tubulin results in a chemotherapeutic agent that is too toxic for a general therapy, it could possibly be used in the future as a chemotherapeutic agent in a targeted delivery system, for example being conjugated with a protein or an antibody. In addition, a targeted inhibitor of γ-tubulin could provide an additional tool to discover the protein's precise role in various cellular processes other than nucleation [22], such as affecting the dynamics of microtubules [65] or inactivation of the anaphase-promoting complex at the end of mitosis and G_1 [84].

It is our hope that the experimental results presented here showing that colchicine and combretastatin A-4 bind to γ-tubulin *in vitro* are a promising first step in the creation of an effective inhibitor of γ-tubulin that could be further developed as a chemotherapeutic agent for the treatment of GBM. My computational work has confirmed that there is a potential binding pocket on γ-tubulin in the homologous location to the known binding site of colchicine on β-tubulin, and our analysis below suggests there is sufficient potential for rational drug design to develop an effective inhibitor of γ-tubulin at this *in silico* predicted binding location.

Binding Energy Calculations for an Effective γ-Tubulin Inhibitor

It is estimated that γ-tubulin is 250-500 times less abundant than either α- or β-tubulin in cultured toad cells and frog eggs [68]. Given this range, I calculate the binding affinity needed for an inhibitor to bind with equal probability to both γ-tubulin and β-tubulin. I use the Boltzmann distribution, given by

$$e^{-\frac{\Delta\Delta G}{K_B T}} = \frac{N_\beta}{N\gamma}$$

(2)

where $\Delta\Delta G$ is the change in binding energy of the inhibitor to γ-tubulin versus β-tubulin (i.e. $\Delta G\gamma$ - $\Delta G\beta$), N_β is the number of β-tubulin proteins available to bind and Nγ is the number of γ-tubulin proteins available to bind. Given γ-tubulin is 250-500 times less abundant than β-tubulin, $\Delta\Delta G$ = -3.4 to -3.8 kcal/mol. Thus targeted inhibitors of γ-tubulin in order to be effective would ideally have increased binding affinity to γ-tubulin over β-tubulin by at least 3.8 kcal/mol. We have experience finding comparable differences for derivatives of colchicine and noscapine binding to various isoforms of tubulin [132, 133].

Colchicine Binding Site Analysis

From the crystal structure found in PDB entry 1SA0, the colchicine binding site on β-tubulin is well characterized [106]. It is surrounded by two β-sheets below-right (S8 and S9), a loop on the left (T7), alpha helix H7 below-left and alpha helix H8 above-left (see Figure 2.10). Analysis of the residues immediately surrounding the site shows residues that are predominantly short and non-polar. Most notably, colchicine sits between T7 Leu 246 and H8 Leu 253.
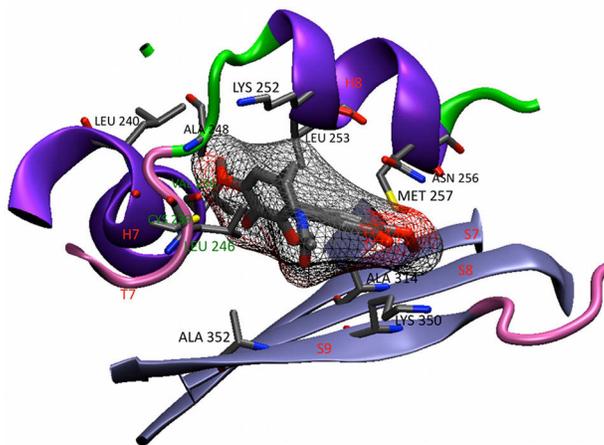
Figure 2.10. Colchicine bound to β-tubulin from PDB entry 1SA0. Residues surrounding the binding site are shown.

The homologous γ-tubulin region contains a binding pocket also surrounded by predominantly short and non-polar residues, and lies surrounded by β-sheets S8 and S9, alpha helix H8, and loop T7 (see Figure 2.11). The predominant exception is that Asn

251 and Tyr 248 are large residues, which in many of the conformations of γ-tubulin observed, blocked penetration of colchicine into the hypothesized binding pocket. The structure shown in Figure 2.11 has Asn 251 and Tyr 248 residues in the T7 loop oriented in a manner that allows an open pocket for colchicine to penetrate deep into the protein. Trp 22, Trp 446, and Trp 351 are located 1.9 nm, 2.0 nm, and 2.2 nm respectively from the approximate center of the hypothesized colchicine binding site in complex 3. Thus, while these tryptophans are not immediately adjacent to the hypothesized binding site, as shown in Figure 2.2 they are in similar locations to the tryptophans in β-tubulin and possibly similarly altered by colchicine binding, which would suggest we would obtain similar results of fluorescence quenching of colchicine interacting with β-tubulin and γ-tubulin, which is what was in fact observed [134].
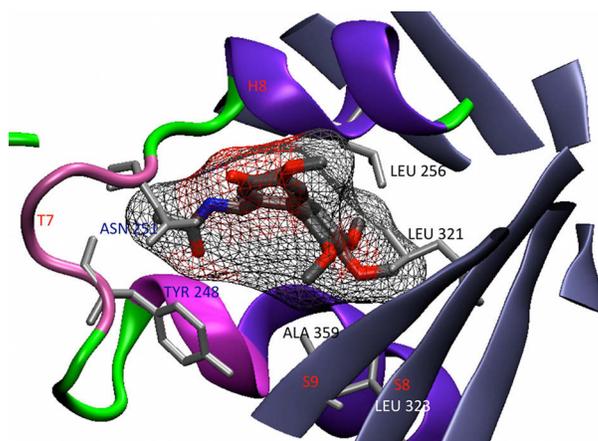
Figure 2.11. *In silico* predicted colchicine binding site on γ-tubulin target 3. Asn 251 and Tyr 248 are large residues in T7, which in certain configurations of our MD simulation of γ-tubulin prevent a large enough space for colchicine to enter this site.

Recent work has characterized the crystal structure of the γ-tubulin complex protein 4 (GCP 4) and has found that it binds directly to γ-tubulin [135]. The study suggests that the H7-H8 (or T7) loop, helix H8, and strand S9 interact with GCP2 and GCP3 [135, 136], which are regions all associated with the hypothesized γ-tubulin binding pocket. Thus the hypothesized colchicine binding pocket in γ-tubulin is in a position that might directly interfere with the binding of γ-tubulin to GCPs.

The recent work on combretastatin derivatives has yielded progress in finding water-soluble derivatives of combretastatin A-4 [124]. As combretastatin derivatives have lower surface area than colchicine derivatives, they may also be promising targets to design an

effective inhibitor of γ-tubulin that can penetrate the blood-brain barrier, and thus investigation of this is underway. Our finding that combretastatin A-4 binds to γ-tubulin may also explain its anti-mitotic effects, although this as well must be further investigated.

2.5   Conclusion

Our combined experimental and computational results suggest that colchicine and combretastatin A-4 bind to γ-tubulin. These results provide the first evidence of a drug-like ligand interaction to γ-tubulin. Further work is still required to experimentally confirm the binding location of these compounds to γ-tubulin, so that focused virtual screening and derivitization can proceed to find a highly specific and selective inhibitor of γ-tubulin. Such an inhibitor may eventually yield therapeutic benefit to treat GBM. These studies might also explain an additional mode of action of these compounds biologically, namely, their possible inhibition of γ-tubulin. A potential inhibitor could also be of benefit to study various biological functions of γ-tubulin.

Since the publication of this work [137], a research group has performed a further screen of compounds that bind to the colchicine-binding site on β-tubulin, to see if these compounds bind to γ-tubulin [138]. They synthesized derivatives of compounds that bound best to γ-tubulin and through tryptophan fluorescence quenching, and found a compound, gatastatin, that binds to γ-tubulin with a K_d of 3.6 ± 1.3 µM versus a K_d of 42.5 ± 36.7 µM to a tubulin dimer [138]. Thus, they have evidence of a ligand that binds preferentially to γ-tubulin over β-tubulin [138]. In comparison, we found colchicine binds to γ-tubulin with a K_d of 13.9 ± 0.4 µM, while they report using their method a higher (but with large standard deviation) K_d of 196.4 ± 47.9 µM for colchicine bound to γ-tubulin. With either K_d value, their finding of gatastatin binding to γ-tubulin with a K_d of 3.6 ± 1.3 µM (binding energy: -7.7 kcal/mol) marks an advance of a strong binding greater than that of colchicine to γ-tubulin. Computational analysis of the bound pose would be of further interest in a docking study.

Supporting Information Available: Additional supporting figures are available.
Figure A.1 in Appendix A. Human γ-tubulin construct sequence

Chapter 3

Energy metabolism of cancer cells: Implications for cachexia and targeted combination treatment[*]

3.1 Introduction

As discussed in Chapter 2, the prognosis for glioblastoma multiforme (GBM) is bleak, with only about 16% of patients surviving for at least 36 months [64]. Clearly, improved treatment is needed for GBM and other cancers with five-year relative survival ratio below 50%, such as ovarian, liver, and pancreatic cancer [139]. It is now recognized that the great majority of cancers have increased glycolysis [140-145], even in the presence of oxygen [143, 144, 146, 147]. Thus, a metabolic switch has occurred in the great majority of cancers, and so Hanahan and Weinberg, who originally proposed the six hallmarks of cancer [148], now suggest that altered energy metabolism be considered as an emerging hallmark of cancer [149]. With my interest in understanding biophysical aspects of cancer to develop better cancer treatments, I investigated whether energy metabolism could be targeted to improve cancer treatment.

---

[*] Chapter 3 (primarily 3.2) contains material that was previously published as Friesen DE, Baracos VE, Tuszynski JA "Modeling the energetic cost of cancer as a result of altered energy metabolism: implications for cachexia," *Theor Biol Med Model* 2015, 12:17. I developed the model and drafted the manuscript. V. Baracos provided data and helped with manuscript edits. J. Tuszynski conceived of the study and helped with manuscript edits. Chapter 3 (primarily 3.1 and 3.3) contains material that was written for my PhD Candidacy grant proposal and PhD proposal. The text contains ideas published as Rietman EA, Friesen DE, Hahnfeldt P, Gatenby R, Hlatky L, Tuszynski JA "An integrated multidisciplinary model describing initiation of cancer and the Warburg hypothesis," *Theor Biol Med Model* 2013, 10:39. E. Rietman, J. Tuszynski, and I developed the integrated theory. R. Gatenby contributed to experiments, and P. Hahnfeldt and L. Hlatky contributed insight into cancer and the model. Only text written primarily by myself from this publication is included in this thesis. Section 3.3 is unpublished work and contains an experiment that was designed by me and performed by K. Missaiaen. D. Moudgil assisted with performing the immunofluorescence staining using the Chan Lab protocol for tubulin staining.

Targeting energy metabolism for cancer treatment has been an idea that stemmed from Otto Warburg's investigation of cancer in the 1920s. Warburg found that cancer tissue fermented glucose to produce energy at a high rate regardless of the availability of oxygen [146]. Thus, the "Warburg Effect" is described as the observation that cancer cells use increased glycolysis to produce energy even in the presence of oxygen [150]. Warburg as a result of his research hypothesized that the prime cause of cancer is an irreversible injury of respiration, where mitochondria have been impaired leading the cell to upregulate glycolysis to survive [146]. Criticism of this theory by Weinhouse [151, 152] on the basis that not all cancer cells showed decrease in oxygen consumption, along with interest in genetic investigations of cancer led to Warburg's theory of carcinogenesis largely being abandoned [153, 154].

The Warburg Effect, which is described as the observation that cancer cells use increased glycolysis to produce energy even in the presence of oxygen, has gained renewed interest in the past decade due to the success of fluorine-18 fluorodeoxyglucose positron emission tomography (^{18}FDG PET) imaging in identifying cancer [155-159]. ^{18}FDG PET uses the tracer fluorodeoxyglucose, which is an analog of glucose and measures glucose uptake by cells. Since most cancers are characterized by an accelerated rate of glucose uptake compared to normal tissue [140-142, 146, 158, 160, 161], tumors are detected using this imaging process. High profile reviews have documented the current state of research in targeting energy metabolism for cancer treatment [154, 162-164].

It is now recognized that the great majority of cancers have increased glycolysis [140-145], even in the presence of oxygen [143, 144, 146, 147]. It appears that cancer cells use glycolytic metabolism even before exposure to hypoxic conditions [161]. Frieden and Gatenby suggest that cancer cells have undergone an information phase change from a maximum to a minimum information content condition [165]. They hypothesize that the initiation of mutations that give rise to carcinogenesis are the result of energy restriction in the cell, and thus, energy restriction arising from a change in metabolism in the cell may be the critical first step that triggers the genetic mutations that drive cancer tumorigenesis [165, 166]. They suggest this may be possible through loss of mitochondrial function, suggested by the "Warburg hypothesis" [146], or through chronic

hypoxia [165, 167, 168]. As well, mitochondrial dysfunction could lead to increased reactive oxygen species (ROS) or decreased DNA repair capacity [169]. This question, whether altered metabolism is a driver of tumorigenesis or simply a by-product of oncogenes and other primary genomic and epigenomic changes [149, 170] is still an open issue. However, it has ramifications for therapy, for if altered metabolism is a driver of cancer, then targeting this pathway could provide broad therapeutic relief to many cancers [171].

In light of the numerous avenues to explore to improve cancer therapies based on biophysical changes in cancer cells, in this chapter I focus on two main topics. The first topic relates to investigating whether the altered metabolism in cancer cells can explain cancer cachexia, which is the uncontrollable muscle wasting seen in the majority of late stage cancer patients. I develop a mathematical model to detail the energetic requirements and energy substrate requirements of cancer cells to see if this can explain the phenomenon of late stage patients catabolising their muscle leading to cachexia [52]. This model is presented as a basis for experimental validation, which will be more feasible once details on the energy metabolism and substrate utilization of cancer cells in human tumors as opposed to cell lines is better characterized [172], and simultaneously tumor burden and total energy consumption are monitored.

The second topic involves a specific investigation to target energy metabolism for cancer treatment. The glycolytic inhibitor, 3-bromopyruvate (3BP), has been found to be promising to treat liver cancer, which is a highly glycolytic form of cancer in both rat studies and an initial human case study [53, 173]. 3BP was initially tested in immunocompetent female Sprague-Dawley rats [173]. Like liver cancer, ovarian cancer has a low survival rate. Ovarian cancer is usually only detected at late stages [174], with approximately 75% of patients having advanced stage (III/IV) tumors when they are detected, and the 5 year survival rate for these patients is 30% [175]. A mouse ovarian surface epithelial (MOSE) cell progression model has been developed, to model ovarian cancer at early, intermediate, and late stages. MOSE cells at each stage are available for analysis, and the MOSE cell lines show metabolic changes toward an increased glycolytic phenotype [60]. I was interested to see if 3BP was effective against this MOSE cell line, especially in late stage MOSE cells. I hypothesized that 3BP would preferentially target

late stage MOSE cells, and that this investigation could be a basis for translating the use of 3BP as a combination therapy for recurrent ovarian cancer, using 3BP to target the most invasive and stem-cell like cancer cells, as has been seen in other cell lines [54].

3.2 Modeling the energetic cost of cancer as a result of altered energy metabolism: implications for cachexia[*]

Cachexia affects most patients with incurable cancer. I hypothesize that in metastatic cancer the mass of the tumor as well as its level of anaerobic energy metabolism play a critical role in describing its energetic cost, which results in elevated resting energy expenditure and glucose utilization, leading to cachexia. Prior models of cancer cachexia may have underestimated the specific energetic cost of cancer as they have not taken the range of tumor mass and anaerobic energy metabolism fully into account.

I therefore modelled the energetic cost of cancer as a function of the percentage of energy the cancer produces anaerobically, based on resting energy expenditure, glucose turnover, glucose recycling, and oxygen consumption in cancer patients found in previous studies.

Data from two clinical studies where tumor burden was estimated and resting energy expenditure or oxygen consumption were measured lead to a broad range of estimates of tumor cost from 190 to 470 kcal/kg tumor/day. These values will vary based of the percentage of energy the cancer produces anaerobically (from 0% to 100%), which in and of itself can alter the cost over a 2 to 3-fold range. In addition to the tumor cost/kg and the degree of anaerobic metabolism, the impact on a given individual patient will depend on tumor burden, which can exceed 1 kg in advanced metastatic disease. Considering these dimensions of tumor cost I was able to produce a 2-dimensional map of potential values, with an overall range of 100-1400 kcal/day.

Quantifying the energetic cost of cancer may benefit an understanding of the tumor's causation of cachexia. Our estimates of the range of tumor cost include values that are

higher than prior estimates and suggest that in metastatic disease the tumor cost could be expected to eclipse attempts to stabilize energy balance through nutrition support or by drug therapies. Tumor mass and the percentage of anaerobic metabolism in the tumor contribute to the cost of the tumor on the body and potentially lead directly to negative energy balance and increased muscle wasting.

3.2.1 Background

Cancer cachexia affects over 1.3 million people in the United States annually [176]. It is associated with severe muscle wasting and reduced survival that cannot be fully reversed by nutritional support [177]. The causes of cachexia are complex and not well understood [178], although its consequences are well documented. Cachexia is associated with reduced caloric intake, inflammation, metabolic change, and fatigue [179]. It affects the majority of late stage cancer patients [180]. Cachexia results from a variable combination of decreased food intake and altered metabolism. This reduction in food intake can arise from primary anorexia as well as symptoms arising from the tumor or side effects from cancer treatment [181], although reduced food intake does not completely explain the weight loss seen in cachexic patients [182]. In attempting to find the primary cause of cancer cachexia, it has been suggested that cancer induces abnormalities in lipid, carbohydrate, and protein metabolism, reduces the efficiency of energy metabolism, and this elevates resting energy expenditure (REE), which may be a major determinant in patients developing cachexia [183]. Our paper builds upon the investigation of the contribution of cancer on REE by investigating in greater depth the energy usage and substrate usage of tumors in order to quantify the energy cost of cancer to the patient, to develop a better understanding of the cause of cancer cachexia from an energetic perspective. The challenge in arriving at a cost estimate of cancer is that while in many studies the REE of cancer patients is measured [183-185], uncoupling the energetic usage of the body and that of the cancer is difficult. If the cancer is dispersed at several locations its entire volume or mass is difficult to quantify, and the measurement of the specific metabolic rate (i.e. energy cost/kg of tissue) of a tumor mass *in vivo* is technically challenging in human subjects [172].
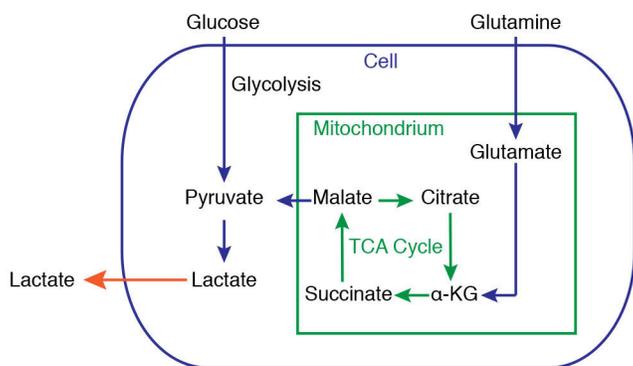
Figure 3.1. Metabolic pathways that convert glucose and glutamine into lactate. Glucose is converted via glycolysis to lactate, and glutamine through a truncated TCA cycle is able to be converted to lactate as well via glutaminolysis. α-KG stands for alpha-ketoglutarate.

Tumors generally have a high uptake of glucose relative to most normal tissues, and this is exploited clinically in the use of FDG-PET to detect cancer [159]. This upregulated glycolysis in cancer cells is a hallmark of cancer [149]. The high demand for glucose, even in the presence of adequate oxygen, has been termed the Warburg effect. To what extent a tumor generates adenosine triphosphate (ATP) based on the glycolytic pathway converting glucose to pyruvate and then to lactate (an anaerobic process) versus oxidative phosphorylation (an aerobic process) is difficult to ascertain *in vivo* and likely varies considerably [172, 186]. I refer to glycolysis as the pathway that converts glucose to lactate, generating 2 net ATP for the cell (Figure 3.1). Warburg estimated that highly glycolytic tumors may make as much as 50% of their ATP from glycolysis [146], although other researchers have found wide ranges of values *in vitro* (0.31% to 80%) [187, 188]. *In vitro* studies have limitations, as cells may have increased glycolysis due to the artificial environment conducive to proliferation [189]. More relevant are recent studies examining the energy metabolism of tumors *in situ*, obtained by infusing uniformly labeled ^{13}C-glucose into cancer patients and then performing surgical resection of the tumor followed by ^{13}C nuclear magnetic resonance spectroscopy [172, 190, 191]. In brain tumors glycolysis was activated, though oxidative phosphorylation (oxphos) was still intact [190]. In lung tumors glycolysis was elevated compared to surrounding non-cancerous tissues [191]. Cancer patients exhibit increased whole body glucose turnover [192-195], increased Cori cycle activity, where lactate is recycled to glucose [192-194, 196], and increased gluconeogenesis [193, 196], suggesting that *in vivo* glycolysis is

elevated in many tumors. Additionally, microcalorimetric measurements of isolated tumor and non-tumor tissue samples removed from humans showed tumors having a higher metabolic rate, with increasing malignancy correlated with a higher metabolic rate [197].

Glutamine is also converted into lactate in cancer cells *in vitro*, and in glioblastoma cells it was found that ~60% of glutamine was metabolized through glutaminolysis to lactate [198] (Figure 3.1). Anaerobic metabolism of glucose and glutamine in the tumor is potentially a direct driver of muscle protein catabolism, as muscle is the major metabolic source of carbon for gluconeogenesis and glutamine biosynthesis.

The clinical approach to abnormalities of human body weight is framed in the concept of energy balance. A discrepancy between energy intake and energy expenditure results in cancer-associated weight loss, and to stop this (i.e. achieve weight maintenance) or to reverse it and achieve weight gain, requires a quantitative understanding of both the energy costs of the body and those of the tumor. While it might be important to know if total tumor cost was likely to be 10, 100 or 1000 kcal/day, we have no clearly defined theoretical framework to determine this cost and therefore no clear clinical guideline of how much energy intake is required to achieve the desired body weight goals. I therefore propose a quantitative theoretical model to estimate the energetic cost of a tumor *in situ* based on the percentage of energy generated by the tumor anaerobically. I estimate the energetic cost of cancer based on resting energy expenditure (REE), glucose turnover, glucose recycling, and oxygen consumption in cancer patients. REE is assessed by indirect calorimetry, which measures oxygen consumption, carbon dioxide production, and urea excretion to derive the energy usage of the body [199]. This analysis can help explain how tumors directly impact elevated REE seen in cancer patients [185], which may lead to cancer cachexia.

3.2.2   The Model

Mathematical model of tumor cost based on tumor energy metabolism

In order to quantify a possible cost of cancer based on the energy metabolism of tumors in patients, I formulate a model of the energetic cost of cancer based on its level of anaerobic energy production. Confusion has reigned on how to quantify the energetic cost of cancer in cachexic patients due to the complexity of correctly accounting for the

recycling of glucose when it is converted to lactate by the tumor and then recycled primarily in the liver [200, 201]. I attempt to clarify this with our model, illustrated in Figure 3.2.
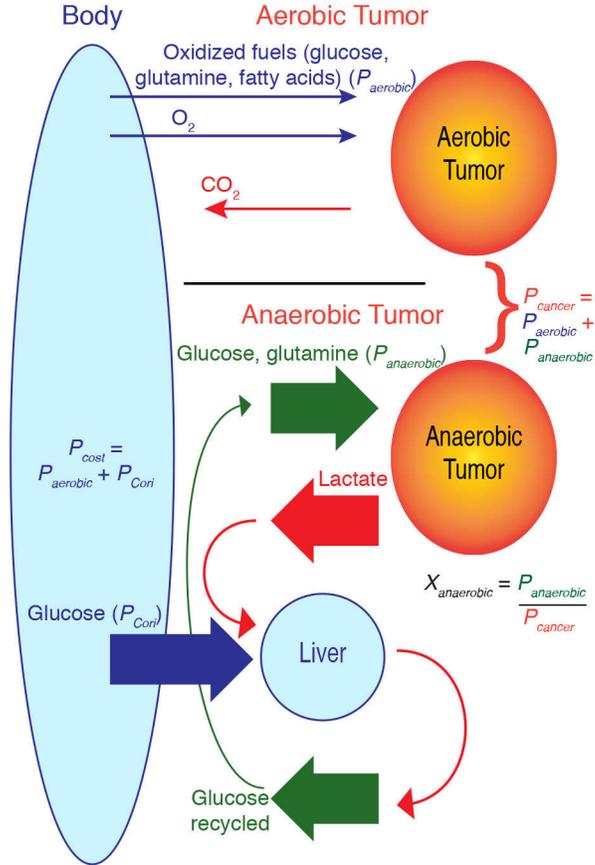
Figure 3.2. The cost of aerobic and anaerobic metabolism of the tumor on the body. A tumor will consume substrates both aerobically and anaerobically. The substrate usage of both an aerobic and an anaerobic tumor is described. Anaerobic metabolism costs the body three times more energy due to the cost of recycling lactate back into the glucose lost to the tumor (see Appendix B.1 and equation (5)). The substrate usage is equivalent to describe the metabolic rates of the aerobic and anaerobic tumor, which leads to the definitions of the metabolic cost of the cancer on the body, P_{cost}, and the metabolic rate of the tumor, P_{cancer}. The percentage of energy produced anaerobically by the tumor, $X_{anaerobic}$, is also illustrated.

A cancer patient may be considered a system comprising the host and tumor mass. P denotes metabolic rate in kcal/day and K denotes the corresponding specific metabolic rate, in kcal/day per kg patient, tumor or other specified mass. The cancer's energetic demand and growth will induce a cost on the normal body, and thus,

$$P = P_{normal} + P_{cost} \qquad (1)$$

where P_{normal} is the metabolic rate of the person free of cancer, and P_{cost} is the energetic cost (in kcal/day) on the normal body caused by the cancer. P_{cost} is due to the metabolic requirements of the tumor, an elevated Cori cycle with increased gluconeogenesis, an activated immune system, an acute phase response, and increased substrate turnover [202-204]. In this paper, I investigate in detail the energetic cost of the tumor by focusing on the metabolic requirements of the tumor and the resultant elevated Cori cycle (Figure 3.2). Normally, metabolic rates are determined based on oxygen consumption, and it is assumed that all food (protein, carbohydrates, and fat) is completely oxidized when the body is at rest. However, this is not the case for a tumor. I model a tumor having an anaerobic component of its energy metabolism. Thus:

$$P_{cancer} = P_{aerobic} + P_{anaerobic} \qquad (2)$$

where $P_{aerobic}$ is the aerobic component of a tumor's metabolic rate, and $P_{anaerobic}$ is the anaerobic component of a tumor's metabolic rate (Figure 3.2). Now, I introduce:

$$X_{anaerobic} = P_{anaerobic} / P_{cancer} \qquad (3)$$

where $X_{anaerobic}$ is the percentage of ATP energy generated anaerobically by the tumor cell. $X_{anaerobic}$ is a measure of how anaerobic the tumor is, and will be used extensively in the analysis of how a tumor with a higher level of anaerobic metabolism will cost the body more energy.

While theoretically aerobic metabolism generates 38 ATP per glucose, when accounting for energy loss in the respiratory chain, current estimates indicate around 30 ATP are produced per glucose in oxidative phosphorylation [205]. Thus aerobic metabolism generates 15 times the ATP that anaerobic metabolism generates per glucose (30 ATP vs. 2 ATP). When energy is generated anaerobically by the tumor via glycolysis, 2 net ATP are generated per glucose converted to lactate, and then 6 ATP are needed by the body to reconvert the resulting lactate to glucose.

In a tumor producing energy 100% aerobically, glucose from the body would be converted into 30 ATP for use by the tumor, and CO_2 would return to the host. Other oxidized fuels from the body (such as glutamine and fatty acids) would also be obtained from the bloodstream and these tumor-oxidized fuels would be lost to the body. Thus, the cost of the tumor on the body, P_{cost}, would be $P_{aerobic}$. However, a tumor that produces

41

energy 100% anaerobically from glucose and glutamine produces only lactate, which will be recycled back into glucose in the liver and kidneys by the body via the Cori cycle [201]. Thus, all the glucose consumed by the tumor would be recovered, at a cost of 6 ATP per glucose used by the tumor. If a tumor consumed only glucose, a 100% anaerobic tumor would consume 15 times the glucose that a 100% aerobic tumor would consume, but the glucose would be recycled in the Cori cycle. In the anaerobic case, the Cori cycle takes 6 ATP to generate 2 ATP for the tumor, and so the energetic cost of the tumor is 3 times greater in the anaerobic case (see Appendix B.1 for a more detailed derivation) (Figure 3.2). Thus:

$$P_{Cori} = 3P_{anaerobic} \tag{4}$$

P_{Cori} is the energetic cost of Cori cycling lactate back into glucose (in kcal/day).

The energetic cost of cancer increases linearly as the percentage of energy derived anaerobically by the tumor, $X_{anaerobic}$, increases. This can be expressed as follows:

$$P_{cost} = P_{aerobic} + P_{Cori} \tag{5}$$
$$= P_{cancer}\left(1 + 2\,X_{anaerobic}\right)$$

where P_{cost} is the metabolic cost of the cancer on the body due to the cancer's metabolism and the resultant Cori cycling that occurs to recycle the lactate produced by the cancer (see Appendix B.1 for a complete derivation). P_{cost} can be rewritten as:

$$P_{cost} = K_{cancer}M_{cancer}\left(1 + 2\,X_{anaerobic}\right) \tag{6}$$

This gives the total energetic cost of cancer as a function of the specific metabolic rate of cancer (K_{cancer}), the mass of cancer (M_{cancer}), and the percentage of ATP generated by the tumor anaerobically ($X_{anaerobic}$). I attempt to estimate a range of tumor specific metabolic rates (K_{cancer}) from several previous studies using measurements of REE and glucose turnover and Cori cycling activity, with the understanding that K_{cancer} may vary greatly between patients and tumors due to tumor heterogeneity of the disease, and in various microenvironment conditions, which may change rapidly in terms of glucose and oxygen availability.

Measurements currently performed when evaluating REE by indirect calorimetry, REE_{IC}, will determine the following:

$$REE_{IC} = P_{normal} + P_{cost} \qquad (7)$$
$$= P_{normal} + P_{aerobic} + P_{Cori}$$

Measured REE reportedly increases with increasing tumor burden [203, 206], which will be used to estimate P_{cost}. Cancer will tend to have effects on the body in terms of weight loss, energy intake, cytokine production and an immune response, which may cause some systems to consume less energy than normal, such as that for digestion and movement, and some systems like the immune system to consume more energy. This has led to conflicting results on whether cancer leads to increased REE or not [182, 185, 207]. These values are not incorporated into P_{cost} in this analysis, and further studies would need to be done to control for these variables.

3.2.3   Results

Estimates of energetic cost of cancer based on REE studies

The energetic cost of the tumor, P_{cost}, can be estimated by the increase in REE_{IC} caused by the tumor. There are currently limited studies that concurrently measure REE_{IC} as well as estimate tumor burden. Study A [206] evaluated a metastatic colorectal cancer patient cohort (n=18), with REE measurements and estimated mass of the combined liver and metastases located in the liver, determined by computed tomography image analysis. Patient fat-free mass (FFM) was measured as well. There is a primary correlation between REE and FFM, leading to the generalized prediction equation: REE = 370 + 21.6 × FFM (Cunningham equation) [208]. Healthy patients would also have liver mass primarily proportional to their fat free mass (FFM) [209], and so an increased (liver+metastases)/FFM value may be primarily due to increased cancer metastases. Thus I plotted the given patient REE compared to their estimated combined liver and metastases mass, adjusted for patient fat free mass (Figure 3.3).

REE/FFM vs (Metastases/FFM + Liver/FFM)
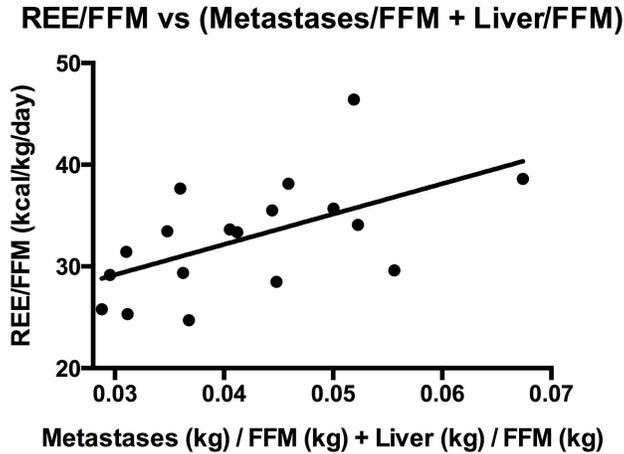
Figure 3.3. Impact of increased tumor mass on resting energy expenditure. Plot of resting energy expenditure (REE) and liver & metastases mass from the prospective colorectal cancer patient cohort (n=18) found in [206]. The values have been adjusted for variations in fat free mass (FFM) of the patient cohort. Simple linear regression found: REE/FFM (kcal/kg/day) = (300 ± 110) * (Liver+Metastases mass) (kg)/FFM (kg) + 30 (r^2 = 0.32, p = 0.01). Future studies to reduce the standard deviation of this result are recommended.

I found:

$$REE \ (kcal/day) \ / \ FFM \ (kg) \ assessed \ by \ indirect \ calorimetry \qquad (8)$$
$$= 300 \pm 110 \times (liver + metastases \ mass, \ in \ kg) \ / \ FFM \ (kg) + 20$$
$$(r^2 = 0.32, \ p = 0.01)$$

It is important to note that there is a large standard deviation in this result. Ideally additional studies would be conducted to measure tumor mass and REE for patients over a time course in order to test more precisely how tumor mass might correlate with REE. As the liver's metabolic rate is approximately 200 kcal/kg liver/day [210], a slope in Figure 3.3 of 300 kcal/(kg liver+metastases)/day would potentially indicate the energetic cost of metastases is higher than 200 kcal/kg metastases/day. If I assume the increased REE after controlling for LBM is primarily due to metastases, then, as in our model, from equation (7) the specific total cost of the tumor from this study is (to 2 significant figures):

$$K_{cost} = 300 \pm 110 \ kcal/kg \ tumor/day \ (Study \ A) \qquad (9)$$

Again, this value must be used with caution due to the large standard deviation and imprecision in measuring tumor mass. However, I use this result to illustrate how our model may estimate the specific metabolic rate of the cancer using this slope of 300 kcal/kg tumor/day (Figure 3.3), provided we know the percentage of ATP generated by

glycolysis from the tumor. I make the initial assumption that 25% of ATP is generated by glycolysis ($X_{anaerobic}$ =0.25), as this is in line with *in vitro* estimates from cell lines derived from metastatic adenocarcinoma of the colon [211] and other cell lines where many estimates range from 20% to 75% [142, 212, 213]. A value of 25% anaerobic ATP synthesis is also consistent with preliminary *in situ* reports and *in vivo* data on glucose turnover and Cori cycling [194]. This corresponds to 50% of the tumor-associated REE, K_{cost}, due to Cori cycling and 50% due to the aerobic component of tumor energy metabolism, if we neglect other factors that might increase REE as a result of the tumor (Appendix B.2: Table S1 displays the relative $P_{aerobic}$ and P_{Cori} based on $X_{anaerobic}$). Thus:

$$K_{aerobic} = 150 \pm 55 \ kcal/kg \ tumor/day \qquad (10)$$

$$K_{Cori} = 150 \pm 55 \ kcal/kg \ tumor/day \qquad (11)$$

From this I obtain:

$$K_{anaerobic} = 50 \pm 18 \ kcal/kg \ tumor/day \qquad (12)$$

$$K_{cancer} = 200 \pm 73 \ kcal/kg \ tumor/day \qquad (13)$$

As these results are calculated scalar multiples of K_{cost} (see Appendix B.2), the standard deviation in these values are multiples of the standard deviation of K_{cost}. This value of K_{cancer} is higher than the previous assumption used by Hall of K_{cancer} = 150 kcal/kg/day [202], and is roughly equal to the metabolic rate of liver (Table 3.1) [210].

Table 3.1. Estimates of the energetic costs of cancer and comparable tissues

Organ	$K_{aerobic}$ (kcal/kg/day)	$K_{anaerobic}$ (kcal/kg/day)	K_{cancer} or K_{organ} (kcal/kg/day)	K_{Cori} (kcal/kg/day)	K_{cost} (kcal/kg/day)
Cancer: Study A [206]	150 ± 55	50 ± 18	200 ± 73	150 ± 55	300 ± 110
Cancer: Study B [203]	200 to 230	50 to 80	270 to 310	200 to 230	400 to 470
Liver [210]	200	0	200	0	200
Heart [210]	440	0	440	0	440
Kidney [210]	440	0	440	0	440
Brain [210]	240	0	240	0	240
Skeletal muscle [210]	13	0	13	0	13

The specific energetic cost of cancer, with $X_{anaerobic}$ = 25%, are compared with various other organs. Typical organs are assumed to have complete oxidation. Cost is rounded to two significant figures. Study A was a study of n=18 metastatic colorectal cancer patients [206]. Study B was a study of n=85 cancer patients studied preoperatively, with a majority of patients having solid tumors of the gastrointestinal tract,

retroperitoneum, or limbs [203]. Ranges of cost were given due to patient mass in the studies not being provided. Details of calculations involved in K_{cost} for Study B are detailed in Appendix B.3, and were based on the plot of oxygen consumption of patients and their tumor bulk with $r^2 = 0.79$. Estimates of energetic costs of cancer should be taken with caution, as they could be highly variable due to the type of cancer studied.

The specific energetic cost of cancer, with $X_{anaerobic} = 25\%$, are compared with various other organs. Typical organs are assumed to have complete oxidation. Cost is rounded to two significant figures. Study A was a study of n=18 metastatic colorectal cancer patients [206]. Study B was a study of n=85 cancer patients studied preoperatively, with a majority of patients having solid tumors of the gastrointestinal tract, retroperitoneum, or limbs [203]. Ranges of cost were given due to patient mass in the studies not being provided. Details of calculations involved in K_{cost} for Study B are detailed in Appendix B.3, and were based on the plot of oxygen consumption of patients and their tumor bulk with $r^2 = 0.79$. Estimates of energetic costs of cancer should be taken with caution, as they could be highly variable due to the type of cancer studied.

Another study related tumor mass with whole body oxygen consumption over a wide variety of types of cancers (Study B) [203]. Tumor mass was assessed by reviewing dimensions of tumors in resected specimens, as well as estimating volumes from ultrasound and computed tomographic scanning. Oxygen consumption was measured by indirect calorimetry. Their data corresponds to an oxidative metabolic increase of 6.67 kcal/kg tumor/day/kg patient, with $r^2 = 0.79$ (see Appendix B.3 for detailed calculations) [214]. Patient body mass data was not provided in Study B; however, assuming average patient weight between 60 and 70 kgs, the K_{cost} in Study B is estimated between 400 and 470 kcal/kg tumor/day (see Appendix B.3). If again, ATP from glycolysis is estimated at 25% for the tumor, this corresponds to K_{cancer} in the range of 270 to 310 kcal/kg/day (equation (5)). This estimate for specific metabolic rate of cancer falls within the range of previous estimates (150 to 406 kcal/kg/day [202, 206, 215]) (Table 3.1).

Estimates of energetic cost of cancer based on substrate usage

Another method to estimate specific tumor metabolic cost is to analyze glucose turnover in the body (i.e. rate of glucose entering and exiting the bloodstream) and the rate of Cori cycling (Figure 3.4).

46
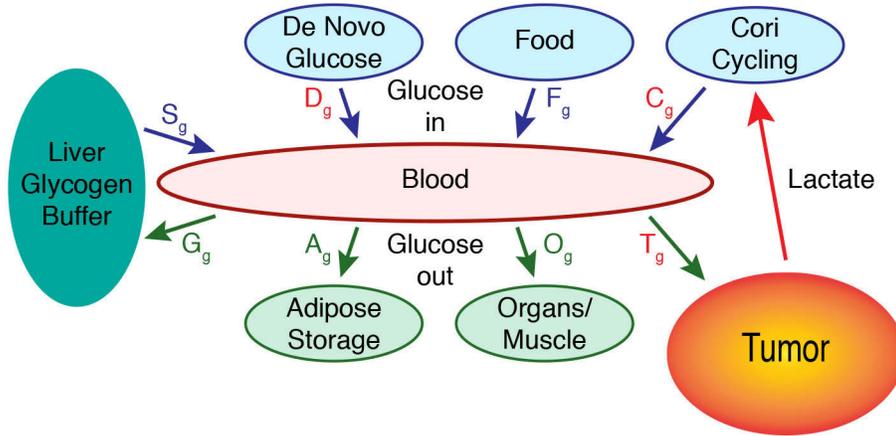
Figure 3.4. A model of glucose turnover in the bloodstream. The tumor, by consuming glucose at an elevated rate, T_g, may lead to increased *de novo* glucose production, D_g (ie. muscle and fat catabolism), in fasting periods. This may be a large contributor to cachexia. As well, the Cori cycling rate, C_g, a function of how much glucose is recycled in the liver from lactate generated from the body, leads to increased energy demand on the body when the tumor exports lactate due to its high rate of glycolysis. The liver glycogen buffer stores approximately 100-120g of glucose.

Glucose is one of the primary sources of fuel for a tumor cell [213], and so estimating the glucose usage of the tumor will provide an estimate of a percentage of the total energy usage of the tumor. Glucose enters the bloodstream primarily from food (F_g), glycogen stores (S_g), de novo gluconeogenesis (D_g), and Cori cycling (C_g). Glucose is used by the body's organs (O_g), and may be stored as glycogen in the liver (G_g), converted to triglyceride and stored in adipose tissue (A_g), or used by a tumor (T_g). The rate of all of these processes, at any given time, is

$$F_g + C_g + D_g + S_g = O_g + T_g + A_g + G_g \tag{14}$$

if we assume a static level of glucose in the blood. In a healthy person in the fed state, F_g will be high, C_g, D_g, and S_g will be essentially zero and storage (G_g, A_g) will occur. During early fasting, liver glycogen is mobilized to maintain blood glucose levels, and after a fast of 4-6 hours, gluconeogenesis from the catabolism of muscle protein and glycerol from triglyceride will increasingly sustain blood glucose levels.

In the case of a patient with a tumor, T_g will be high continuously. Consider

$$T_g = T_{anaerobic} + T_{aerobic} \tag{15}$$

where $T_{anaerobic}$ is the rate of glucose uptake by the tumor converted to lactate and $T_{aerobic}$ is the rate of glucose that is used by the tumor to generate energy by oxidative phosphorylation. I will assume that $T_{anaerobic} = C_g$ [216]. Then our rate equation becomes:

$$F_g + D_g + S_g = O_g + T_{aerobic} + A_g + G_g \qquad (16)$$

$T_{aerobic}$ will provide a constant drain on overall glucose supply, necessitate additional gluconeogenesis and correspondingly deplete gluconeogenic precursors, as O_g, A_g, and G_g will be reduced. All these factors may result in reduced liver glycogen stores, which have been reported in cachexic patients [193] and mice with cachexia-inducing C26 colon adenocarcinoma [217]. During fasting, C_g will supply some of the needed glucose, but as F_g is zero, and glycogen stores may be low, the tumor may increasingly rely on glucose originating from *de novo* gluconeogenesis, D_g.

While a tumor has multiple fuels including glucose, glutamine, and fatty acids, if we analyze glucose turnover and glucose recycling, we can estimate the component of P_{cost} due to tumor glucose consumption, which I define as $P_{cost\_glucose}$ (see Appendix B.4 for details on these calculations). Multiple studies gave measurements of glucose turnover and glucose recycling in cachexic patients, leading to our computation of estimates of $P_{cost\_glucose}$ in Table 3.2. Study C [194] compared patients with metastatic carcinoma who had progressive weight loss or were weight stable, and I calculate a $P_{cost\_glucose} = 200$ kcal/day. Study D [193] compared cachexic metastatic colorectal cancer patients versus an age-related control group without cancer, with a calculated $P_{cost\_glucose} = 94$ kcal/day. Study E [192] compared malnourished cachexic cancer patients versus malnourished patients without cancer, where all patients had lost ~14-15% of their normal body weight, with a $P_{cost\_glucose} = 240$ kcal/day.

Table 3.2 Cost estimates of tumors based on increased glucose turnover and increased glucose recycling

Study	Additional glucose turnover in cancer patients	p_{cancer}, probability glucose in bloodstream consumed by tumor	$X_{anaerobic}$, % ATP generated from glycolysis in tumor	Cost estimate of tumor based on glucose turnover and glucose recycling (for 70kg patient)
C [194]	2.06 g/kg patient/day	44%	26%	$P_{cost\_glucose} = 200$ kcal/day
D [193]	0.850 g/kg patient/day	26%	19%	$P_{cost\_glucose} = 94$ kcal/day
E [192]	1.19 g/kg patient/day	27%	4%	$P_{cost\_glucose} = 240$ kcal/day

Additional information about the calculation of p_{cancer}, $X_{anaerobic}$, K_{cost}, and $P_{cost\_glucose}$ are found in Appendix B.4. Cost is rounded to two significant figures. Study C [194] compared patients with metastatic carcinoma who had progressive weight loss or were weight stable. Study D [193] compared cachexic metastatic colorectal cancer patients versus an age-related control group without cancer. Study E [192] compared malnourished cachexic cancer patients versus malnourished patients without cancer, where all patients had lost ~14-15% of their normal body weight.

The average of the studies C, D, and E gives an estimate of $P_{cost\_glucose}$ of 180 kcal/day for a 70 kg patient while fasting, although an estimate of the size of the tumors in these studies is not provided and so $K_{cost\_glucose}$ of the cancer cannot be calculated from these studies. Study B [203] related plasma glucose appearance to estimated mass of tumor in 85 cancer patients. From their data I calculate $K_{cost\_glucose}$ in the range of 220 to 260 kcal/kg tumor/day based on increased plasma glucose appearance dependent on tumor mass, and the assumption that 25% of tumor ATP was generated anaerobically (see Appendix B.4 for details on this calculation). This equates to $K_{cost\_glucose}$ being 55% of K_{cost} in Study B.

Tumor energetic cost

Table 3.3 Estimates of K_{cost} and K_{cancer}

Study and parameter measured in study	Estimated cost of cancer, K_{cost} (kcal/kg/day)	Equivalent K_{cancer} assuming $X_{anaerobic}$ = 25% (kcal/kg/day)
A [206]: REE increase	300 ± 110	200 ± 73
B [203]: increased oxygen consumption	400 to 470	270 to 310

Estimates are summarized of tumor cost on body per kg tumor. The equivalent K_{cancer} using $X_{anaerobic}$ = 25% is shown (calculated from equation (5)). Study A derives this estimate from increased resting energy expenditure (REE) per kg (liver+metastases) adjusted for variations in fat free mass (FFM) in a prospective colorectal cancer patient cohort (n=18) found in [206], and Study B derives this estimate from increased oxygen consumption per kg tumor (see Appendix B.3), in a study of n=85 cancer patients studied preoperatively [203]. Ranges of cost in Study B were given due to patient mass in the studies not being provided. Cost is rounded to two significant figures. Estimates of energetic costs of cancer should be taken with caution, as they could be highly variable due to the type of cancer studied.

Table 3.3 summarizes estimates of the cost of the tumor on the body, K_{cost}. The range of costs from REE and oxygen consumption is 190 to 470 kcal/kg tumor/day. This is a large range and further studies must incorporate estimates of tumor mass in order to derive more accurate values for K_{cost}. However, analyzing this energetic cost, even with its current large uncertainty, is instructive in appreciating the potential importance of understanding this energetic cost of the tumor. Kleiber's formula for estimating the reference man's basal metabolic rate simplifies to [218]:

49

$$P_{normal} = 69.6M^{0.75} \qquad (17)$$

Thus, in our model, using the representative value of K_{cost} being 300 kcal/kg tumor/day from Study A, this leads to the metabolic rate of a cancer patient to be:

$$P = P_{normal} + P_{cost} = 69.6M^{0.75} + 300M_{cancer} \qquad (18)$$

where $M = M_{normal}$. I note the high coefficient based on tumor mass, and the fact that the cost scales linearly to the tumor mass.

To assess the range of values of the cost of the tumor, P_{cost}, I plot equation (6),

$$P_{cost} = K_{cancer}M_{cancer}(1 + 2X_{anaerobic}) \qquad (19)$$

using $K_{cancer} = 200$ kcal/kg tumor/day calculated from Study A, and a range of clinically plausible values of the mass of the cancer, M_{cancer}, and the percentage of ATP generated anaerobically by the tumor, $X_{anaerobic}$ (Figure 3.5).
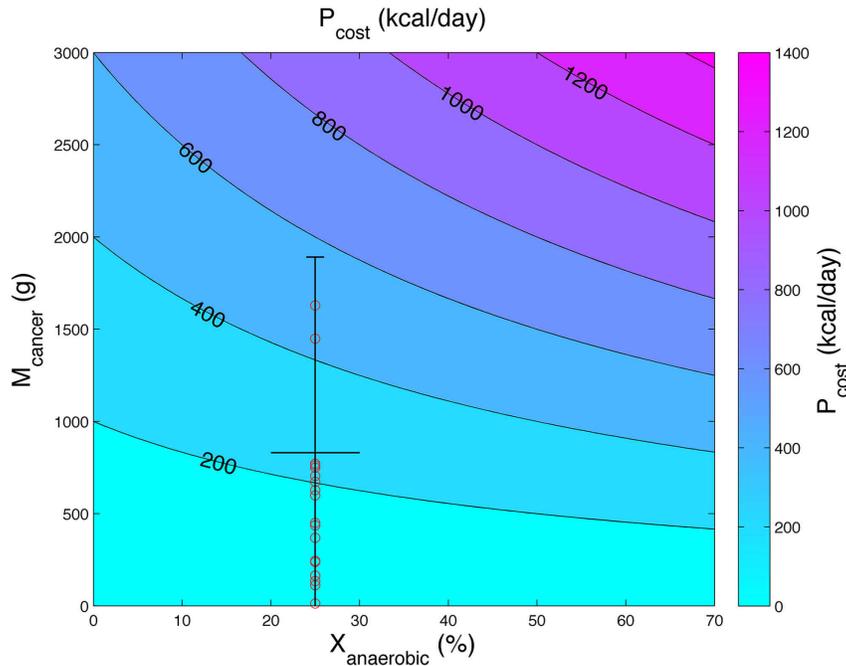
Figure 3.5. Contour plot of the estimated energetic tumor cost based on energy metabolism and tumor mass. The estimated energetic cost of the tumor, P_{cost}, in kcal/day, is plotted based on its mass, M_{cancer}, and the percentage of ATP the tumor generates anaerobically through glycolysis, $X_{anaerobic}$. The plot uses equation (6), with $K_{cancer} = 200$ kcal/kg tumor/day found in Study A (see Table 3.3). Early stage tumors may not present a high cost, but as tumors grow and become more glycolytic, their cost will increase and may induce a catabolic, cachexic state. Patients from the retrospective colorectal cancer cohort in [206], n=30 (Study A) are plotted in red, with assumed 25% ATP generated by glycolysis, where tumor mass is estimated by taking their final (liver+metastases) mass and subtracting the initial (liver+metastases) mass in the time course of their disease. This is to provide an illustration of where cachexic patients may fit within this map and should

only be considered as a very rough estimate of tumor energetic cost. For the thirty patients, the mean tumor burden is 0.83 kg (equivalent to a cost of 250 kcal/day), standard deviation is 1.06 kg, and a patient with estimated tumor mass of 4.7 kg, outside the axis of the figure, is not shown.

Study A [206] provided an analysis of a retrospective colorectal cancer cohort (n=30) of patients, tracking their liver+metastases mass over the time course of their disease. As liver mass was assumed to be constant, I could provide an estimate of metastases mass at the endpoint of the disease, and these masses are plotted in red in Figure 3.5, where I use the previous assumption that $X_{anaerobic}$=0.25 for these patients. In early stage cancers, the cost of the tumor will likely be in the lower-left quadrant of Figure 3.5 but for extensive metastatic disease, the tumor cost would extend towards the upper-right quadrant [143, 203, 219]. The potentially large energetic cost of the tumor may help explain cachexia in advanced metastatic disease. A disseminated metastatic tumor weighing 1.8 kg which makes 25% of its ATP from glycolysis could plausibly cost ~540 kcal/day, i.e. 32% of the basal metabolic rate of the reference man. Such high levels of tumor energy expenditure, often in the context of profound anorexia, would drive proteolysis and lipolysis. This model of cachexia is summarized in Figure 3.6.
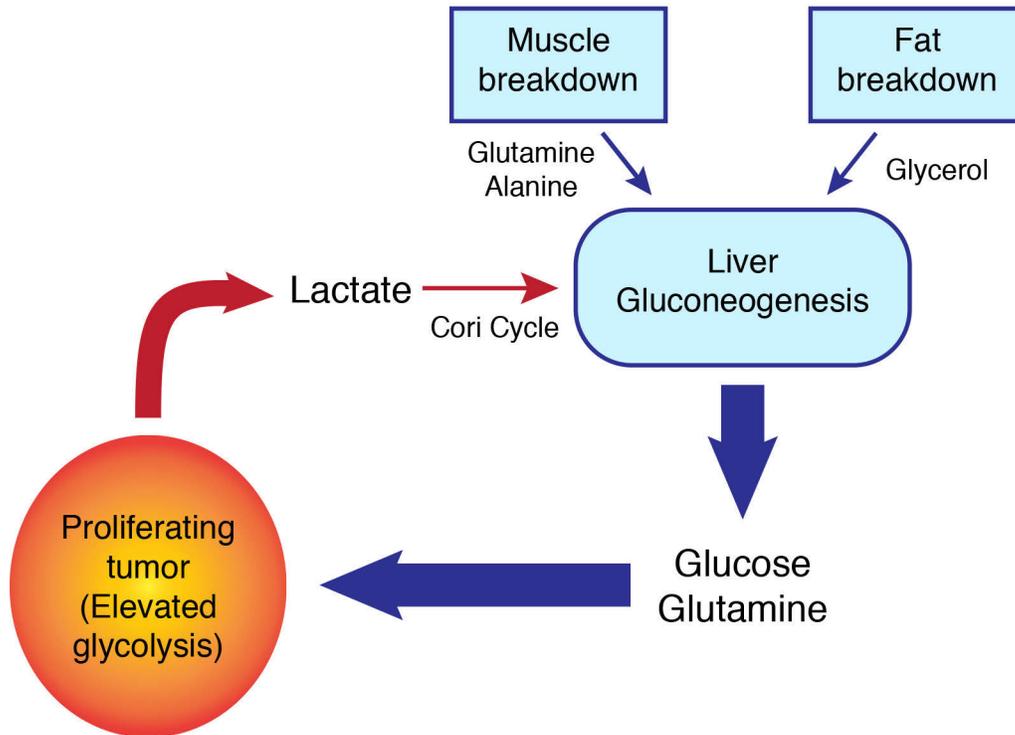
Figure 3.6. The proposed model of the tumor causing an energy deficit leading to cachexia. The tumor's large consumption of glucose and glutamine, and conversion of these substrates to lactate which then require energy from the body to convert back to glucose, creates a vicious cycle of lost energy. Muscle breakdown would provide glucose and glutamine to feed the tumor, especially in a fasting state.

Percentage of energy from glucose lost to the tumor

While a tumor may have a high energetic cost, its cost may not be readily apparent as measured by indirect calorimetry, because while a tumor might have a high energy usage, owing to depletion of lean and fat tissues the body may be correspondingly consuming less energy. By analyzing glucose turnover and Cori cycling I can estimate the percentage of energy from glucose lost to the tumor, which may be a parameter better suited to predict cachexia based on tumor energetic cost.

The probability that glucose is consumed by a tumor, p_{cancer}, can be estimated as the increased glucose turnover in cancer patients compared to the glucose turnover of the patient:

$$p_{cancer} = (t_{cancer} - t_{control}) / t_{cancer} \tag{20}$$

where t_{cancer} is the glucose turnover rate in cancer patients and $t_{control}$ is glucose turnover rate in healthy controls. p_{cancer} ranged from 26% to 44% in studies C-E (Table 3.2). The estimate of the percentage of glucose converted to lactate by tumors, $p_{anaerobic}$, can be estimated as the increased Cori cycling in cancer patients (indicating the amount of glucose used by the tumor anaerobically) compared to the increased glucose turnover (indicating the amount of glucose used by the tumor):

$$p_{anaerobic} = (C_{cancer} - C_{control}) / (t_{cancer} - t_{control}) \qquad (21)$$

where C_{cancer} is the Cori cycling rate of glucose in cancer patients and $C_{control}$ is the Cori cycling rate of glucose in healthy controls. $p_{anaerobic}$ ranged from 40% to 84% in studies C-E (Table 3.2). These values of $p_{anaerobic}$ correspond to 4 to 26% of ATP generated from glycolysis ($X_{anaerobic}$) (Table 3.2 and Appendix B.4). A tumor has a much higher $p_{anaerobic}$ than $X_{anaerobic}$ as the ATP generated anaerobically per glucose is 15 times less than that of ATP generated aerobically from glucose (see Appendix B.4 for the exact conversion formula).
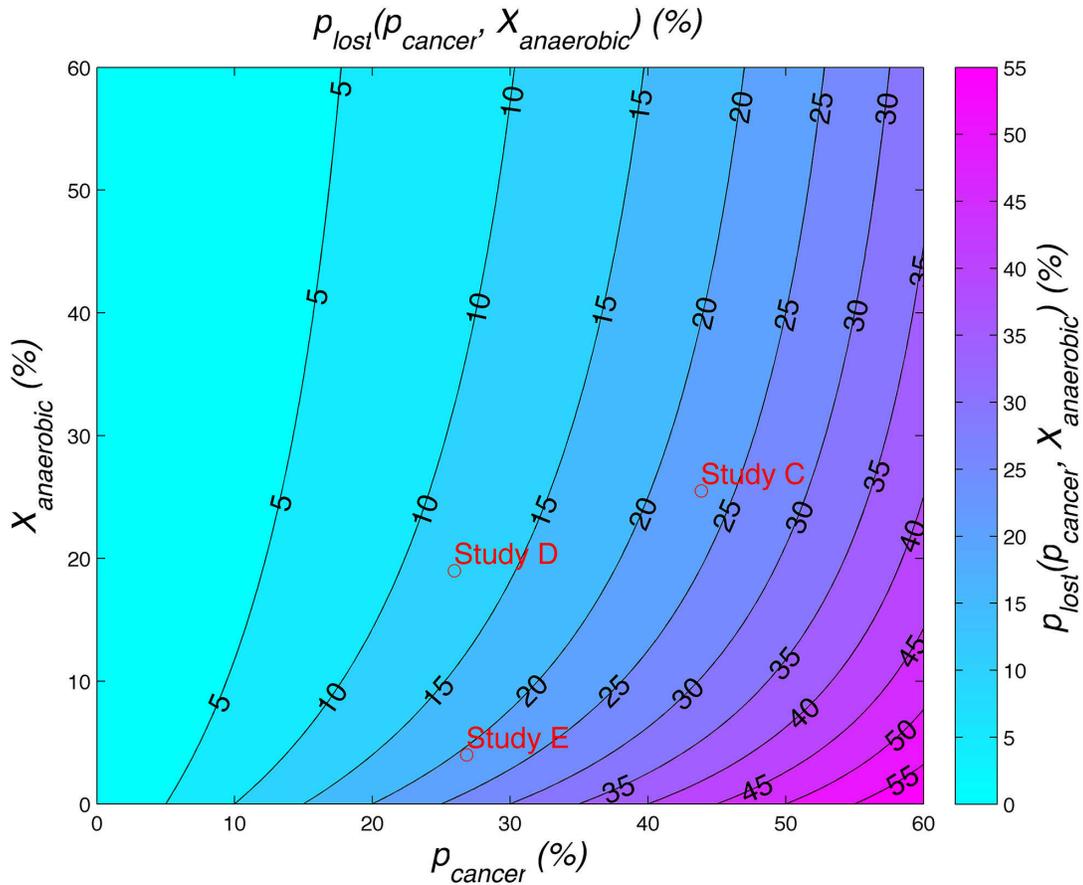
Figure 3.7. Contour plot of the percentage of glucose energy lost to tumor, p_{lost}. p_{lost} is indicated on the graph for studies C-E based on the probability the glucose in the bloodstream enters the tumor, p_{cancer}, and the percentage of ATP derived by glycolysis in the tumor, $X_{anaerobic}$. Study C compared cachexic cancer patients versus weight-stable cancer patients. Studies D and E compared cachexic cancer patients versus normal controls. In study E both cachexic cancer patients and normal controls were 14-15% under their normal weight.

The expected ATP generated for the body per glucose entering the bloodstream (energetic payout of a glucose), $g(p_{cancer}, p_{anaerobic})$, can be estimated by assuming that 30 ATP will be generated per glucose consumed by the body [205], and that 6 ATP will be consumed to recover a glucose used by tumor anaerobically, and 0 ATP will be generated if the glucose is lost to the tumor aerobically (see Appendix B.5 for more information on the definition of $g(p_{cancer}, p_{anaerobic})$). The percentage of energy lost to the body per glucose entering the bloodstream, p_{lost}, is then determined from $g(p_{cancer}, p_{anaerobic})$ (see Appendix B.5). p_{lost} is plotted in Figure 3.7. The values of p_{cancer} and $X_{anaerobic}$ are

calculated for studies C-E in order to find p_{lost} for these studies (see Table 3.2). Study C compared cachexic cancer patients to weight-stable cancer patients and showed an additional 23% of energy from glucose lost. Studies D and E, which compared cancer patients to normal controls showed 12% and 21% of energy from glucose lost to the tumor, respectively.

3.2.4   Discussion

I used a variety of currently available evidence for REE, glucose turnover, Cori cycling rate, and tumor burden to obtain our main result to estimate a tumor's energy cost on the body, P_{cost}, based on tumor mass (M_{cancer}), the percentage of ATP synthesized anaerobically in the tumor ($X_{anaerobic}$), and the specific metabolic rate of the cancer (K_{cancer}) (Figure 3.5). The first dimension of the map (M_{cancer}) encompasses a range of clinically plausible tumor burdens up to 3 kg [203, 220]; the second dimension is $X_{anaerobic}$ over a range primarily seen in cancer cell lines [146, 186, 187], and I use a base value of K_{cancer} = 200 kcal/kg tumor/day estimated from Study A [206]. This map provides a range of estimates, which may be considered within the limitation that data sets which include all of the relevant parameters: M_{cancer}, $X_{anaerobic}$, and K_{cancer}, with known REE values over the time course of the disease, are not readily available. In future studies, M_{cancer} and insight into glucose utilization could be aided by combined positron emission tomography/computed tomography (PET/CT) scan analysis [221]. $X_{anaerobic}$ and K_{cancer} are difficult to evaluate empirically in a direct manner, with current efforts involving *in vivo* isotope labelling, primarily with ^{13}C-glucose [172]. In human cancers, $X_{anaerobic}$, could be lower or higher than the base value I used in our model (25%), and could also vary over time and even within a tumor [172]. Within those caveats, estimates of P_{cost} are higher than previously considered [202, 206]. Consider a metastatic colon cancer patient with the average tumor burden of the sample in Figure 3.5, for which the energetic cost of the tumor would likely fall in the range of 180-500 kcal/day, depending on the proportion of ATP synthesized anaerobically within that tumor mass. At the distal ends of the tumor mass distribution in the patient sample, there are individuals whose tumor cost would be < 200 kcal/day in any instance, and others whose tumor cost could be in excess of 400 kcal/day and potentially over 800 kcal/day if largely anaerobic. These estimates of tumor energy demand are useful in achieving understanding of the scope of potential tumor

55

contribution to the body's energetic deficit. The absolute cost of a tumor will have a variable impact on patients depending on their REE which is largely dependent on body mass. For instance, a tumor cost of 300 kcal/day will be 25% of REE of a patient with a normal REE of 1200 kcal/day, but only 15% of REE for a patient with a normal REE of 2000 kcal/day.

The estimate of % ATP synthesis generated anaerobically, $X_{anaerobic}$, is a large assumption of our model, and further information on tumor metabolism *in situ* in humans is needed to refine this number for various cancers and at various stages of disease progression [172]. Drug-resistant, aggressive tumors found in late stage cancer patients may have a higher rate of glycolysis [197, 222]. A study to investigate energy consumption in the resting versus proliferating state, using mitogen-activated rat thymocytes, found cells in the proliferating state consumed 4.9 times the ATP as those in the resting state, with 86% of ATP generated from glycolysis in the proliferating state versus only 12% of ATP generated from glycolysis in the resting state [223]. Thus, rapidly proliferating tumors may have increased $X_{anaerobic}$ and K_{cancer}, which would drive P_{cost} higher according to equation (6). This is consistent with findings of elevated REE for newly diagnosed stage IV cancer patients compared with newly diagnosed stage I-III cancer patients [183].

Analyzing glucose turnover and glucose recycling also approximated the energetic cost of cancer where glucose is the energy substrate, $P_{cost\_glucose}$, in Table 3.2. These calculations, perhaps more importantly, allow us to approximate the percentage of energy taken from the body from glucose by the cancer. Approximately 10-25% of energy derived from glucose is lost to the tumor in cachexic cancer patients (Figure 3.7). This may lead to muscle wasting to generate more glucose to make up for this loss of energy. It also suggests a further avenue of study to test for a critical percentage of energy from glucose lost, p_{lost}, which overloads the body's ability to maintain adequate glucose to the body without resorting to excessive gluconeogenesis and muscle wasting. In effect, I hypothesize this parameter, p_{lost}, may be a predictor for the onset of cachexia.

Our model develops further the previous model of Hall and Baracos [202] by refining estimates of the cost of the tumor because of the tumor's increased glucose consumption, and incorporates the possibility that a tumor may vary in the proportion of oxidative and

glycolytic metabolism. Hall et al. [202] modeled the change in lipolysis, proteolysis, gluconeogenesis and Cori cycle rates during progressive tumor growth and their effects on resting metabolic rate and gluconeogenesis. The model incorporated the cost of elevated glycogen, fat, and protein turnover and lipolysis and proteolysis. It also incorporated the cost of the tumor in terms of Cori cycling cost, which was estimated to start at 16 kcal/day and increased to 64 kcal/day, and assumed a specific metabolic cost of the tumor at 150 kcal/kg/day based on experimental studies [224]. Our model refines this to a base estimate of $K_{aerobic}$ = 150 kcal/kg/day, and K_{Cori} based on the level of glycolysis in the cancer, with a base estimate of 150 kcal/kg/day, for a combined total cost, K_{cost}, of 300 kcal/kg/day (Study A). Based on this K_{cost}, and assuming $X_{anaerobic}$ is 25%, the actual specific metabolic rate of cancer, K_{cancer}, here is estimated at 200 kcal/day.

Implications of tumor anaerobic metabolism for skeletal muscle loss

Anaerobic metabolism may drive additional gluconeogenesis, due to the increased usage of glucose and glutamine. Cancer is suggested to act as a "glutamine trap," leading to a transfer of nitrogen from muscle to the tumor [225]. Cultured tumor cells require ten times as much glutamine as any other amino acid [198] and more than 90% of the body's glutamine stores are in the muscle [226]. It is now recognized that glucose and glutamine are the main sources of energy for cancer cells [198, 213], although this has yet to be conclusively established *in vivo*. Since skeletal muscle–derived amino acids are the major precursors of glutamine synthesis as well as the main source of carbon for gluconeogenesis, muscle protein catabolism may be driven by tumor consumption of these substrates.

Clinical implications

A dilemma in treating patients with cachexia is that an increase in caloric consumption reduces or slows weight loss but does not typically lead to weight gain [227, 228]. This raises the question as to exactly how much energy intake would be required to result in weight stability or restore positive energy balance. Improved volitional energy intake that is achieved with dietary consultation and oral nutritional supplements can reach between 500 and 600 kcal/day [229, 230]. This type of intervention has documented clinical benefits and is most successful during radiation and chemotherapy with curative intent,

while the tumor is responding to treatment. Indications for non-volitional (artificial enteral/parenteral) feeding are specified within published clinical practice guidelines [231, 232], according to their potential benefits and risks. The reference range of tumor energy expenditure (Figure 3.5) should help frame clinical expectations. For the patient with limited tumor burden or whose disease is controlled by anticancer therapy, reduced weight loss or weight stability could be achievable within a realizable set of nutritional goals. Patients undergoing an objective tumor response during treatment (tumor shrinkage) would be expected to have a reduced tumor energy demand compared to a rapidly proliferating tumor. Aligned with the concept of refractory cachexia [177] for the patient whose cancer is metastatic, very large and growing in spite of cancer therapy, the tumor cost would be expected to eclipse attempts to stabilize energy balance through volitional food intake, or even by means of artificial nutrition. Additionally, any proposed treatment for cachexia, such as reducing the activity of catabolic mediators (ie. cytokines, myostatin) that activate proteolysis and lipolysis, without addressing the energetic burden of the cancer will potentially have limited impact.

3.2.5 Conclusions

I have calculated the energetic cost of cancer based on the cancer's specific metabolic rate and level of anaerobic energy production, and estimated this cost based on clinical data, reaching the conclusion that tumor cost may be considerably higher than previously assumed in patients with metastatic disease. High glucose turnover as a result of anaerobic energy production has the potential to result in cachexia due the high constant demand for glucose from the tumor, especially in the fasting state. Our models in Figure 3.2 and Figure 3.4 provide a framework for better understanding the role of anaerobic energy production in cancer in affecting the energy balance in cancer patients. Our estimates of the energetic cost of tumors as a function of anaerobic energy production in the tumor in Figure 3.5 and equation 6 suggest that reduction in anaerobic tumor ATP synthesis may mitigate tumor cost. At present we do not have a means of convincing a tumor to switch to aerobic metabolism, although this becomes a topic of interest now that we understand that such an intervention could have a quantitatively important impact on energy balance. While it is generally understood that hypermetabolism is common in advanced cancer patients [185, 233], future studies should attempt to estimate tumor

burden, tumor energy consumption through indirect calorimetry, tumor substrate utilization, and ideally liver glycogen reserves at different stages of cancer disease progression in order to better understand the tumor's energy consumption as a cause of hypermetabolism and weight loss.

3.3   The Effects of Metabolic Inhibitor 3-Bromopyruvate in an Ovarian Surface Epithelial Cancer Progression Model[*]

Ovarian cancer is the fifth leading cause of cancer deaths among women in the U.S., causing 14,600 deaths in 2009 [234-237]. Epithelial cancer is the most common form of ovarian cancer, accounting for approximately 90% of ovarian cancers [238, 239]. Current treatment for ovarian cancer consists of surgery followed by platinum and taxane based chemotherapy. However, 80% of cases using this treatment relapse [240, 241] contributing to a 5-year survival rate of only 40-50% [54, 238]. In epithelial ovarian cancer, tumor initiating cells (TICs) may play a central role in the relapse of patients undergoing current therapy [54-56]. Such TICs have been found to have high multi-drug resistance (MDR) properties to standard chemotherapeutic regimens [54]. It has been observed that cancer cells in general have upregulated glycolysis, even in the presence of oxygen, which is termed the Warburg Effect, and that they may rely upon this for survival [242]. The drug 3-bromopyruvate (3BP), a small-molecule analogue of pyruvate and lactate, has been found to have preferential uptake in cancer cells and a minimal toxicity profile [243]. In an ovarian epithelial cisplatin resistant cancer cell line displaying TIC properties, 3BP has been shown to resensitize the cells to cisplatin treatment [54, 57]. After preclinical trials for treating liver cancer in rat and rabbit models

[173, 243], 3BP has been used in treatment in the first human case published in 2012 with promising results [53]. Questions remain as to the exact cause of 3BP's apparent low toxicity profile, and only a few studies have tested 3BP in ovarian cancer cells [54, 57]. A report suggests that the expression of monocarboxylate transporter 1 (MCT1), which is thought to be used by 3BP to enter the cell, is the key determinant of 3BP's toxicity [244]. As the mouse ovarian surface epithelial (MOSE) model was known to display changes in morphology and possibly changes in energy metabolism at the start of the study, my goal was to characterize 3BP's effect on MOSE cells in order to develop optimal treatment strategies for ovarian cancer, which is often only discovered at a late stage, and to bring such treatments into the clinic.

Thus, I investigated 3BP toxicities to mouse ovarian surface epithelial (MOSE) early stage, intermediate stage, and late stage cancer cell, and collaborated with the developers of the MOSE cell model, who investigated 3BP on their late stage cisplatin-resistant, and firefly luciferase tumor initiating variant (FFL TIV) cell lines, in normoxic and hypoxic conditions.

3.3.1   Overview

Current cancer treatments consist of surgery, radiation, and chemotherapy. However, in ovarian cancer, mortality statistics have changed very slightly over the last 30 years [238]. One of the central issues in treating ovarian cancer is that after surgery and chemotherapy, after initial response of the tumor, drug resistance and/or a more malignant phenotype of cancer results, and the cancer recurs, metastasizes, and kills the patient [219, 240, 245]. Improved strategies to combat chemoresistant ovarian cancer are required. In general, cancer cells are known to change their energy metabolism, with an upregulation of glycolysis, and this is emerging as a hallmark of cancer [140-147, 149]. Thus, an emergent new avenue of treatment is termed metabolic therapy, which seeks to use the observed increased glycolysis, even in the presence of oxygen, of tumors (aka the "Warburg Effect"), to create a targeted therapy and prevent metastasis [219]. Upregulated glycolysis has been proved to be a robust property of tumors, as it is used effectively by fluorine-18 fluorodeoxyglucose (FDG-PET) imaging to detect tumors in general [155-158] and in recurrent ovarian cancer [246]. An open question is whether a cancer cell, and especially TICs, are dependent on increased glycolysis for their survival. If so,

inhibitors targeting glycolysis may be effective treatments for cancer [171]. One of the most promising anti-metabolic drugs being developed to date has been 3BP (see Figure 3.8), an analogue of lactate and pyruvate [53]. Importantly, this drug has been found to be effective on chemoresistant cell lines [54, 57, 247]. Our goal was to test the effect of 3BP in an ovarian cancer progression model, in order to gain insight as to this drug's effect in both cancer cells which are non-tumorigenic and those which are highly tumorigenic. Such knowledge could lead to optimal therapies using 3BP that lead to the destruction of tumor initiating cells, and potentially to treatments which guard against multi-drug resistance and increased malignancy. This approach could lead to beneficial treatments, regardless of the multitude of heterogenic genetic and epigenetic modifications present in ovarian and other cancers [240], should malignant cells be reliant on increased glycolysis and elevated MCT1 expression. While it is known that 3BP has great tumor killing potential on multiple cancer types [248], and more specifically with chemo-resistant ovarian cancer cell lines in combination with cisplatin, [54] 3BP to my knowledge had not been tested in a cancer progression model. My studies were done in order to test the drug's ability to not only be effective at killing a tumor, but to preferentially kill the most aggressive and malignant tumor cells thought to be the prime generators of relapse and malignancy.

Figure 3.8. 3BP as an analogue to pyruvic acid and lactic acid. From Ko et al. *Biochem Biophys Res Commun* 2004, **324:**269-275 [173]. Reproduced with permission from Elsevier. Copyright © 2004.

3.3.2 Background

3.3.2.1 Epithelial Ovarian Cancer (EOC)

Ovarian cancer is an extremely lethal disease, as it is usually only detected at late stages [174]. Approximately 75% of patients have advanced stage (III/IV) tumors when they are detected, and the 5 year survival rate for these patients is only 30% [175]. The vast majority of ovarian cancers (approximately 90%) are epithelial ovarian carcinomas, and this subset of ovarian cancer will be the focus of our investigation [238, 249].

Treatment for EOC has been difficult due to the difficulties of early detection of this disease. Symptoms often only arise once the disease has metastasized [240], and there is a lack of reliable biomarkers. Annual screening with transvaginal ultrasound and cancer antigen 125 (CA-125) have not resulted in earlier stage diagnosis or reduced mortality [250, 251]. The survival rate of women with epithelial ovarian cancer has not changed much since the advent of platinum-based chemotherapy over 30 years ago, with the Canadian relative survival ratio of ovarian cancer increasing by roughly 5% from 1992-1994 to 2006-2008 [139, 252]. The treatment for advanced stage epithelial ovarian cancer is surgery followed by chemotherapy. Chemotherapeutic regimens have traditionally combined platinum-based therapy with a taxane (currently a carboplatin-paclitaxel combination) [253], and more recently, liposomal doxorubicin has been used with carboplatin [252]. Unfortunately, while clinically complete remissions occur in over 70% of patients, relapse follows in over 90% of those responders [240, 241], where the cancer is often drug-resistant, and second-line treatments have been largely ineffective, with conventional second-line chemotherapy response rates of between 5 and 15% [253]. Platinum-resistant ovarian cancer is considered uniformly fatal [254]. Thus, new therapies specifically able to target late-stage epithelial ovarian cancer would be beneficial. Developing therapeutic targets has been challenging, as EOC is heterogeneous [255, 256]. EOC has with widespread gene expression and DNA copy number changes in serous carcinoma, the most common invasive histotype of ovarian cancer, allowing for adaptation and development of resistance [240, 252, 257]. Other approaches have included dose dense chemotherapy which increased response rates to drug resistant ovarian cancer to up to 65% [253]. In addition, epigenetic resensitization therapies, using hypomethylating agents are being researched with promising results in phase II clinical trials [254, 258]. Tumor-initiating cells have been implicated in ovarian cancer as being highly chemoresistant and causing relapse after initial chemotherapeutics [54-56]. Cisplatin-resistant SKOV-3 ovarian cancer cells displaying stem cell properties have been shown to be sensitive to 3BP, and particularly to combination treatment of cisplatin and 3BP [54, 57]. Thus, it has been suggested that 3BP may be able to target malignant TIC ovarian cancer populations [54].

3.3.2.2 MOSE Cell Lines

In order to develop new treatment regimens for epithelial ovarian cancer, animal models that are able to model the progression of ovarian cancer are important [238]. Dr. Roberts and colleagues have developed a syngeneic mouse ovarian cancer cell model, applicable to evaluate chemotherapeutic treatment regimens at multiple stages of the disease [58]. This model has the advantage of ultimately testing new therapeutic regimens in an immunocompetent mouse, allowing for evaluation of immune surveillance on the potential therapy [58]. In addition, *in vitro* work can be done, as cell lines have been captured at various time points in the disease progression. The cell lines are named mouse ovarian surface epithelial (MOSE) cells, and arose from the spontaneous transformation of MOSE cells isolated from female breeder mice (C57BL/6) in culture. With increasing passage number, the cells gradually transformed their phenotype from being benign, non-tumorigenic cells to highly malignant, tumorigenic cells. The malignant phenotype is defined here as the ability to form colonies in soft agar, to grow as multicellular tumor nodules on organotypic raft culture, and to be tumorigenic in immunocompetent mice [58]. The cells are classified as early (MOSE-E), early/intermediate (MOSE-E/I), intermediate (MOSE-I), and late (MOSE-L), and this is based on ranges of passage numbers where the growth rates and anchorage-independent growth efficiencies are similar (see Table 3.4) [58]. Most recently, a subpopulation of highly tumorigenic cells from MOSE-L cells has been isolated and transfected with the firefly luciferase gene for detection, and is referred to as FFL TIV cells. These FFL TIV cells are highly aggressive and tumorigenic, able to initiate a tumor in syngeneic mice with as few as 100 cells administered. Cisplatin-resistant MOSE-L cell lines (L-CR) have also been developed by Dr. Roberts, by culturing the cells in the presence of increasing concentrations of cisplatin. MOSE-E cells are characterized by a slow growth rate, contact inhibition of growth, inability for anchorage-independent growth, and non-tumorigenicity in immunocompetent, syngeneic mice [58]. However, these cells have undergone significant genetic changes [58]. In contrast, MOSE-L cells are rapidly dividing, have enhanced capacity for anchorage-independent growth, and have rapid tumorigenic potential *in vivo* [58]. Major chromosome structural abnormalities were not found, although progressive aneuploidy was observed as MOSE cells transitioned to this stage [58]. This cell

progression model provides the ideal opportunity to test the effects of 3BP and combination treatments in an *in vitro* and eventually *in vivo* system that mimics the progression of ovarian cancer and has varying properties of energy metabolism, structure, malignancy, and tumorigenicity. My goal is to help bring treatments tested in this model to the clinic.

Table 3.4. Growth Characteristics of MOSE Cells at various stages, indicated by passage numbers. From Roberts et al. *Neoplasia* 2005, **7:**944-956 [58]. Reproduced with permission from Elsevier. Copyright © 2005.

Table 1. Growth Characteristics of MOSE Cell Lines.

MOSE Classification (Passage Number)		Doubling Rate (in Hours; ±SEM)	% CFU* (±SEM)	Spheroid Growth[†]	Raft Culture[‡]	*In Vivo* Tumorigenicity[§]
MOSE-E	p4−p15	26.51 (±1.52)	0.4 (±0.2)	∓	S	0/3 mice
MOSE-E/I	p20−p35	18.4 (±0.95)	0.8−2.1 (±0.4)	++	S/I	ND
MOSE-I	p40−p80	15.55 (±0.74)	2−5.4 (±0.6)	+++	M/I	ND
MOSE-L	p90−170	13.8 (±0.51)	13.7−16 (±1.1)	++++	M/I	6/6 mice (33−38 days)
ID8		15.08 (±0.46)	11.8 (±1.6)	∓	M/I	2/2 mice (60 days)

E=Early; E/I=Early/Intermediate; I=Intermediate; and L=Late passage MOSE cells and passage range.
*Percent CFU (percent colony forming units in soft agar assay) = mean of the number of colonies per well/number of cells seeded per well × 100.
[†]Spheroid growth defined as: (∓) little to no growth; (++) spheroids < 50 μm; (+++) spheroids > 50 < 200 μm in diameter; and (++++) spheroids > 200 μm in diameter.
[‡]Organotypic collagen raft culture: S = single monolayer growth; I = invasion of collagen; and M = multilayered growth.
[§]Number of mice with detectable ascites or macroscopic evidence of peritoneal tumor formation. Days until death or sacrifice are reported in parenthesis.

3.3.2.3 Tumor energy metabolism – upregulated glycolysis

With the advent of FDG-PET imaging to reliably detect tumors due to the increased glucose uptake of tumors, interest in metabolic therapies has intensified in the last decade [259]. FDG-PET / CT scans are used in detecting suspected recurring ovarian cancer [246, 260]. Genetic profiling shows glycolysis ubiquitously overexpressed in 24 cancer classes [141] and oxidative phosphorylation reduced in metastatic tumors [219], which also supports the notion that a change in energy metabolism is an emerging hallmark of cancer [149]. A primary goal of cancer therapies is to effectively target cancer cells and not normal cells. As cancer cells have been shown to rely on upregulated glycolysis, metabolic targeting is a possible novel therapeutic approach [29, 154, 160-162, 171, 173, 186, 242, 261-280]. Cancer cells are thought to benefit from upregulated glycolysis as this allows them to live in conditions of fluctuating oxygen levels, proliferate quickly, avoid apoptosis, and create an environment providing them with a proliferative advantage [34, 143, 264, 267, 277]. Much controversy has existed whether cancer cells have upregulated glycolysis because of defects in mitochondrial ability to generate ATP through oxidative phosphorylation (the Warburg hypothesis), or simply because it provides them with the aforementioned advantages [153, 171, 277]. Metabolic therapies

aim to target upregulated glycolysis in order to negate the proliferative advantage and protection from apoptosis that this phenotype allows. Many metabolic inhibitors have been investigated [242, 281], and 3BP is a leading candidate for successful translation to clinical use [53]. As stem cells are also known to have increased glycolysis [282, 283], any metabolic therapy should also be tested against toxicity to normal stem cells.

3.3.2.4 3-Bromopyruvate

3-Bromopyruvate is a small-molecule analogue of lactate and pyruvate (Figure 3.8). Historically, it was known to alkylate cysteine residues [284] and inhibit many metabolic enzymes [285]. More recently, it was found to be a potent anti-cancer compound. In an initial study, 3BP targeted a highly glycolytic cancer cell line (AS-30D) compared with fresh hepatocytes [173]. As a follow-up study with rats, hepatocellular carcinoma cells seeded in two different locations in young rats had advanced cancers (2-3 cm) develop in all animals, and upon treatment with 3BP, all treated animals had their tumors eradicated without apparent toxicity or recurrence [173]. A subsequent rabbit biodistribution study also showed limited toxicity of 3BP, and importantly 3BP did not appear to cross the blood-brain barrier [243]. Finally, 3BP has been used in an initial case study with a human patient with promising results [53]. The patient with fibrolamellar hepatocellular carcinoma (FLC) underwent ten treatments of 3BP over ten months, and effective killing of the FLC was observed [53]. No major cytotoxicities were observed in the patient treated at concentration of 2-3.5 mg/kg body weight [53]. Liver regeneration was not inhibited, and the rate of tumor necrosis due to 3BP seemed to exceed all known cytostatic drugs [53]. The patient eventually passed away due to overload of liver function [53]. Thus, 3BP holds promise in treating liver cancer, which displays a high level of glycolysis (ie. Warburg effect), once optimal dosing and detoxification strategies are in place. 3BP has subsequently been approved by the FDA as an investigational new drug in 2013 [286].

3BP targets the cancer cell's energy metabolism by inhibiting ATP energy production through both glycolysis and mitochondrial oxidative phosphorylation, resulting in rapid depletion of energy reserves and cancer cell death [53]. It was originally believed that 3BP's primary target was type II hexokinase (HK-II). HK-II catalyzes the first step in the glycolytic pathway, and rests on the outside of mitochondria, binding to the voltage

dependent anion channel (VDAC) of the mitochondria [265]. HK-II is found to be highly expressed in tumors (>100-fold in liver hepatocytes), and initiates a high rate of glycolysis, and promotes cell growth and survival [265, 287, 288]. HK-II protects against cell death by its binding to the mitochondrial outer membrane and inhibiting Bax-induced cytochrome *c* release and apoptosis [289]. Its location allows it to have first access to mitochondrial generated ATP which, along with glucose, is the substrate that produces glucose-6-phosphate and commits the incoming glucose to the glycolytic cascade [264, 290, 291]. Its location also allows it to escape the inhibitory effect of its product glucose 6-phosphate [264, 290, 291]. Inhibiting HK-II by alkylation and triggering dissociation from the mitochondria then might inhibit glycolysis which is upregulated in tumors, and cease blocking the cell's apoptotic machinery [288, 292].

Recently, 3BP has been found to primarily target glyceraldehyde-3-phosphate dehydrogenase (GAPDH) through alkylation [293-296]. GAPDH is involved in the central step of glycolysis, and as multiple pathways to generate ATP from carbohydrates all converge at the GAPDH step, this makes GAPDH an ideal target for complete inhibition of glycolysis [293]. In addition, GAPDH has been implicated in influencing cell survival and apoptosis [293, 297-301]. Other metabolic pathways such as the pentose phosphate pathway and fatty acid synthesis indirectly are affected as they are interdependent on glycolysis where GAPDH catalyzed reactions are required [293]. 3BP also promotes cellular stress, leading to endoplasmic reticulum stress and the blockage of protein synthesis, and promotes increases in the level of intracellular reactive oxygen species (ROS) [293, 302, 303]. The multi-pronged attack of blocking glycolysis, protein synthesis, and inducing cellular stress and ROS levels potentially provides the combination effect able to kill cancer cells, and resistance strategies such as utilizing autophagy or MDR are suggested to not be able to prevent the effects of 3BP [293, 295].

Increased investigation has focused on the drug's apparent non-toxicity, especially to the brain and to the liver [53, 173, 243, 304], as its ability to inhibit both glycolysis and oxidative phosphorylation would presumably be toxic to normal cells as well, which traditionally rely more on oxidative phosphorylation. Initial research postulates that it is due to tumor cells' upregulated glycolysis leading to increased lactate production and upregulated monocarboxylate transporter (MCT) transporters that allows 3BP to enter

tumor cells preferentially due to these upregulated MCT transporters [244, 296, 305, 306]. Indeed, it is suggested that MCT1 (SLC16A1) mRNA levels are the best predictor of 3BP sensitivity and are most elevated in glycolytic cancer cells [244]. MCT4 has also been implicated in 3BP uptake [306].

3.3.2.5 Tumor initiating cells

With the propensity of cancer cells to become more malignant and tumorigenic in response to current chemotherapy, and observing high heterogeneity in cancer genomes even within the same tumor, an hypothesis that certain tumor cells (named tumor initiating cells (TICs), or cancer stem cells), are central to a tumor's ability to recur and metastasize has been under high levels of investigation [307-309], and therapies to target such TICs are sought after [310-312]. Evidence exists that stem cell transformation can be the underlying cause of ovarian cancer [55].

Human embryonic stem cells have been found to have increased glucose uptake and increased levels of HK-II [313]. Indeed, a reliance on glycolysis has been documented to allow maintenance of stem cells in the pluripotent state, while oxidative metabolism appears integral for the metabolic demands of differentiation [282, 283]. It has been found that human pluripotent cells rely mostly on glycolysis to meet their energy demands, and overexpress HK-II compared to differentiated cells, with increased localization of HK-II in mitochondrial fractions suggesting increased binding of HK-II to the outer mitochondrial membrane [314]. Glioblastoma stem-like cancer cells are suggested to prefer a low oxygen microenvironment and actively use glycolysis for ATP generation [315]. They have showed low mitochondrial respiration and high glycolytic activity, resistance to standard drugs such as carmustine and temozolomide, but they were highly sensitive to a derivative of 3BP especially under hypoxic conditions [247]. In initial investigations, 3BP has been found to be effective on treating epithelial ovarian cancer cisplatin resistant TIC-like cells [54].

3.3.2.6 Hypoxic environments

Hypoxic environments promote tumor progression and resistance to therapy [316, 317]. The transcription factors primarily responsible for the response to hypoxia are hypoxia-inducible factors (HIFs), which can alter cellular metabolism and stimulate

angiogenesis [307, 318]. HIFs have also been shown to activate signalling pathways such as Notch and the expression of transcription factors such as Oct4 that may inhibit differentiation and promote generation of cancer stem cells [307]. In ovarian cancer, HIF-1α mediates epidermal growth factor induced Snail and Slug expression and cell invasion [319], and its overexpression is associated with a poor prognosis [320, 321]. Ovarian cancer cell lines were shown to survive hypoxia by upgrading their stem-like properties (stronger CD44 expression), and they behaved more aggressively when returned to a normoxic environment [322]. Thus, 3BP's effect on MOSE cells in hypoxic conditions were planned to be investigated by Dr. Roberts. Pancreatic cell lines were found to be more sensitive to 3BP under hypoxia [323].

3.3.2.7 Drug combinations synergistic with 3BP

When combined with 3BP, cisplatin has been shown to lead to massive cell death [303]. The mechanism remains unclear but is hypothesized to be partly due to decreased DNA repair due to decreased available ATP [303]. In ovarian cancer cell lines (SKOV-3), cisplatin combined with 3BP leads to substantially increased cell death [54, 57].

Citrate is a natural organic acid found in citrus fruits that can inhibit glycolysis by targeting phosphofructokinase, which catalyzes the third step in glycolysis (see Figure 3.9) [324]. It has found to be synergistic with 3BP in decreasing viability of C6 glioma cells and spheroids, and does not seem to be toxic except at very high doses [325, 326]. Moreover, it has been found to be synergistic with cisplatin in toxicity to malignant mesothelioma cells, possibly due to inhibiting DNA repair as a result of lowered ATP, or through inhibiting the anti-apoptotic activity of Bcl-2 family proteins [327].
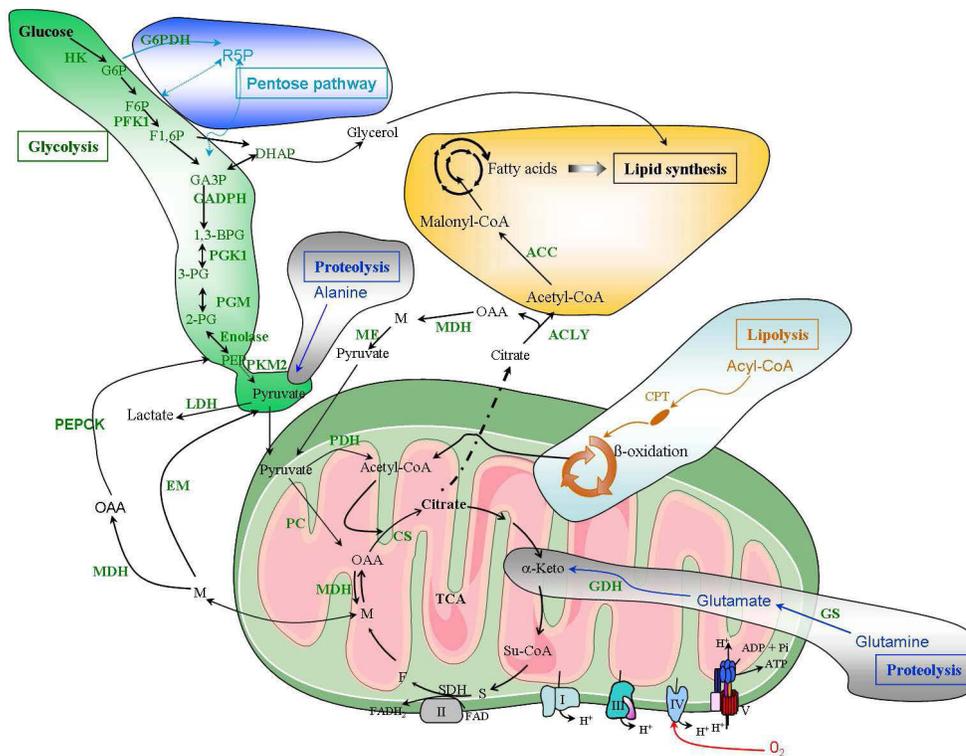
Figure 3.9. Energy metabolism in the cell. 3BP targets HK and GAPDH in the glycolysis pathway. Citrate inhibits phosphofructokinase (PFK1) in the glycolysis pathway. From Icard et al. Why Anti-Energetic Agents Such as Citrate or 3-Bromopyruvate Should be Tested as Anti-Cancer Agents: Experimental In Vitro and In Vivo Studies. In *Mesotheliomas - Synonyms and Definition, Epidemiology, Etiology, Pathogenesis, Cyto-Histopathological Features, Clinic, Diagnosis, Treatment, Prognosis.* Edited by Zubritsky A: InTech; 2012: 225-244 [325]. Reproduced under CC BY 3.0 license (http://creativecommons.org/licenses/by/3.0/legalcode). Copyright © 2012.

3.3.3 Methods

MOSE cells were grown as a monolayer in high-glucose DMEM (Dulbecco's modified Eagle's medium), supplemented with 4% (v/v) FBS in a humidified incubator at 37 °C with 5% CO_2.

AlamarBlue® cytotoxicity assay

AlamarBlue (ThermoFisher) contains resazurin, which is an indicator dye of a reducing environment indicative of metabolic cells. Measuring fluorescence corresponds to the cells' metabolic activity and so this is usually proportional to the number of living cells. Cells were plated in 96 well plates and after 24 hours, 3BP was administered, with plain media as a control. Cell viability was measured with AlamarBlue after 24h and 48h.

Fluorescence was measured by Fluostar Optima with excitation/emission of 544/590 nm, (v. 1.32 R2).

3BP was prepared freshly. 3BP (Sigma-Aldrich, 16490) was added to PBS, then NaOH added to pH 7.4. 3BP solution was filtered through 0.22 μm filter, then added to media at desired concentrations.

Trypan blue cytotoxicity assay

Trypan blue is a dye exclusion method, where viable cells have intact cell membranes, and thus exclude the trypan blue dye from entering them. When this dye is mixed with cells, the live cells are unstained, small, and round, while the dead cells are stained and swollen. Thus, cell viability can be measured by counting the live versus dead cells.

Cells were plated in 24 well plates and after 24 hours, 3BP was administered, with plain media as a control. After 24 and 48 hours, cell suspension was diluted 1:10 with 4% trypan blue (Sigma-Aldrich, 19812-9, 25g in PBS, filtered 0.45 μm) to a 0.2ml final volume, gently mixed and left for 5min at room temperature, then loaded in a hemocytometer chamber. After 1-2 minutes, the cells were counted, by manually counting the number of live and dead cells in each 1mm x 1mm corner square of the hemocytometer.

CyQuant Cytotoxicity assay protocol

Cells were seeded in 96 plate wells @ ~3000/well (50uL) and incubated for 24 hours, along with media as a control. 3BP was prepared freshly at 2x final concentration needed in plate. 3BP (50uL) added to the wells, for 3BP concentrations of 0, 10, 30, 50, 75, 100, and 200 μM, followed by further 24 hour incubation. CyQuant Direct (Invitrogen, C35011) added following manufacturer's protocol (100uL/well), followed by 1 hour incubation. Cyquant Direct is based on a green fluorescent nucleic acid stain and background suppression dye, which leads to fluorescent intensity linearly dependent on cell number (peak excitation is 508nm, peak emission is 527 nm). The fluorescent intensity was scanned on a Typhoon 9400, excitation 488nm, emission filter 526nm and acquired data through ImageQuant Software. Fluorescent intensity was controlled by area scanned and media fluorescence, then taken as a percent of control cells (no drug added). This was plotted as cell viability as a percent of control cells. 3BP in these CyQuant experiments was not neutralized with NaOH.

Immunofluorescence

100,000 MOSE-E and MOSE-L cells were seeded onto 22 mm^2 coverslips in 35-mm diameter dishes for 48 hours, and 170,000 MOSE-I cells were seeded onto 22 mm^2 coverslips in 35-mm diameter dishes for 24 hours. Cells on coverslips to be imaged were fixed with 3.5% (w/v) paraformaldehyde in PBS with 10mM Pipes (pH 6.8) for 7min. Then the cells were permeabilized in KB (50mM Tris/HCL, pH 7.4, 150mM NaCl and 0.1% BSA) + 0.2% Triton X-100 for 5min, followed by rinsing in KB buffer for 5min (all at room temperature). Monoclonal mouse anti-α-tubulin (Sigma B512), dilution 1:2000 applied, with Alexa Fluor® 488-conjugated anti-mouse secondary antibody, 1:1000 dilution, for green MT visualization. Rabbit polyclonal to COX IV, 1:1000 dilution (Abcam 16056) and Alexa Fluor® 555-conjugated goat anti-rabbit secondary antibody 1:400 (Invitrogen, A-21428) applied, for red mitochondria visualization. DAPI also applied for blue nucleus visualization.

Images were taken on a Zeiss Laser Scanning Microscope 710 with a plan-Apochromat 63x (NA 1.4) oil immersion lens, with Zen software v 7.0.4.287. Images were processed using Imaris 7.6.5 and Adobe Photoshop CS6 v. 13.0.

3.3.4   Results: 3-Bromopyruvate cytotoxicity of MOSE cells

In preliminary work, AlamarBlue was used to assess the half maximal inhibitory concentration (IC_{50}) values of 3BP on MOSE-E, MOSE-I, and MOSE-L cell lines (Figure 3.10). In our context, IC_{50} is the concentration that results in 50% cell viability as compared to control. Results at 3BP concentrations above 1 mM indicated increasing viability with increased concentration of 3BP administered. This paradoxical effect was also observed with another cytotoxicity assay, MTS [328], and so it was determined that 3BP likely interferes with the AlamarBlue assay. This is because the AlamarBlue assay is based on measuring resazurin, a non-fluorescent indicator dye that is cell permeable, that is converted into red fluorescent resorufin by reduction reactions in viable cells. As 3BP interferes with cell metabolism, it may be interfering with the correct function of the assay.
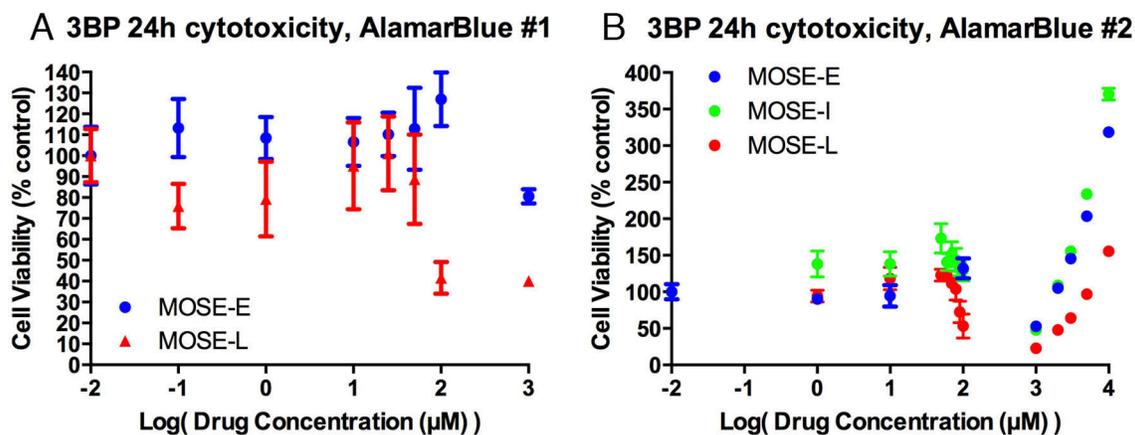
Figure 3.10. Semi-log plot of 3BP cytotoxicity profiles using AlamarBlue assay. (A) MOSE-E and MOSE-L initial cytotoxicity assay. Results suggest MOSE-L more sensitive than MOSE-E, although a high cytotoxicity concentration was not established. (B) MOSE-E, MOSE-I, and MOSE-L second cytotoxicity assay, again suggesting MOSE-L cells most sensitive to 3BP. Increased fluorescence signal past 1mM suggests the Alamar Blue assay is unreliable, especially at concentrations of 3BP greater than 1mM.

I then performed a dye exclusion method (trypan blue) for determining viability, which is not based on metabolism (Figure 3.11). I found that at 100 µM concentration of 3BP (2.0 on the log x-axis), the majority of MOSE-E cells live, and approximately half or more of MOSE-L cells die at both 24 and 48h (see Table 3.5). MOSE-I sensitivity to 3BP was between MOSE-E and MOSE-L sensitivity, as expected, but more data points would be needed to show this conclusively.
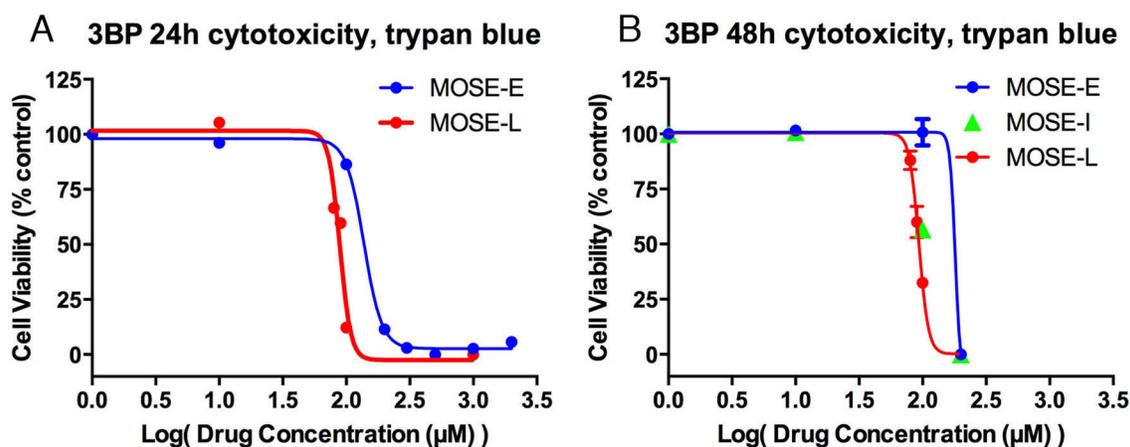
Figure 3.11. Semi-log plot of trypan blue assay of 3BP cytotoxicity to MOSE cells. Data suggests MOSE-L cells are more sensitive to 3BP than MOSE-E cells. (A) Cytotoxicity after 24h exposure to 3BP, n=1, 1 replicate. (B) Cytotoxicity after 48h exposure to 3BP,

n=1, 2 replicates for MOSE-E and MOSE-L, 1 replicate for MOSE-I. No living cells were recorded after 48h exposure with 200μM 3BP for all cell lines.

Table 3.5. Cell viability (% control) of 3BP at 100 μM concentration for multiple experiments

	AlamarBlue 24h #1	Alamar Blue 24h #2	Trypan Blue 24h	Trypan Blue 48h
MOSE-E	127 ± 13	132 ± 14	86 *	101 ± 6 **
MOSE-I	N/A	130 ± 15	N/A	57 *
MOSE-L	42 ± 8	53 ± 16	12 *	32 ± 0.03 **

At 3BP concentration of 100 μM, using multiple cytotoxicity assays and multiple time points, it is repeatedly shown that this concentration is more toxic to MOSE-L cells than MOSE-E cells. SD given for six replicates, unless otherwise noted (* one data point; ** two data points).

I then sought to obtain the IC_{50} value of the MOSE cell lines using the Cyquant Direct Cell Proliferation Assay Kit, which measures DNA content and has been validated to measure cytotoxicity [329], and is applicable for high-throughput cytotoxicity assays [329]. This assay has been previously reported to be used with 3BP [244]. Performing this assay was used to assess cell viability at multiple 3BP concentrations (Figure 3.12). Unexpectedly, 3BP was most toxic to MOSE-I cells; however, 3BP was more toxic to MOSE-L cells than MOSE-E cells (p=0.02, unpaired t test, two-tailed) (Figure 3.13 and Table 3.6). The IC_{50} value of the MOSE cell lines are plotted in Figure 3.13 and given in Table 3.6.
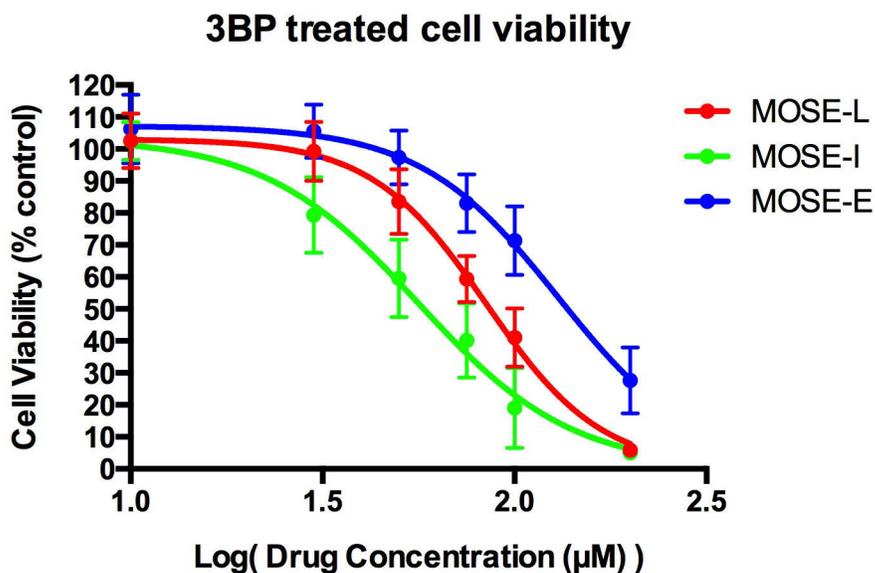
Figure 3.12. Semi-log plot of cytotoxicity of 3BP on MOSE cell lines (Cyquant assay), n=4. Error bars are SD.
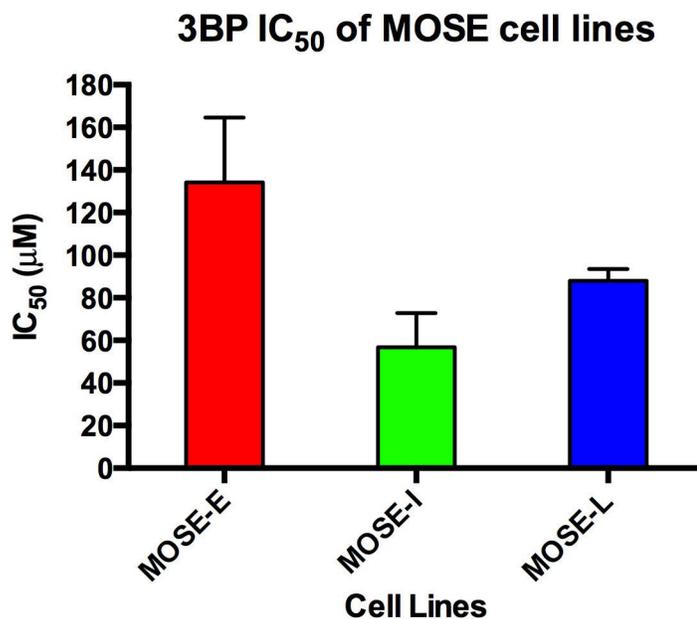
Figure 3.13. Cytotoxicity of 3BP on MOSE cell lines (Cyquant assay), n=4. Error bars are SD.

Table 3.6. 3BP IC$_{50}$ (μM) of Cyquant cytotoxicity assays (n=4).

Cell line	3BP IC$_{50}$ (μM)
MOSE-E	134 $\pm$ 31
MOSE-I	57 $\pm$ 16
MOSE-L	88 $\pm$ 5

MOSE-L and MOSE-I increased sensitivity to 3BP over MOSE-E cells are as expected as microarray data indicate upregulation of MCT1 RNA levels as cells progress to late stage (Figure 3.14), and we hypothesize 3BP activity is correlated with MCT1 levels, and energy metabolism studies of MOSE cells indicate an upregulation of glycolysis in MOSE-L cells as compared to MOSE-E [60], another probable indicator of 3BP sensitivity as rate of glycolysis and MCT1 levels tend to be correlated [244]. Our MCT1 antibody (Santa Cruz, sc-14917) was non-functional, and so future studies will need to be done to test the relationship between MCT1 expression and 3BP sensitivity of MOSE cells.
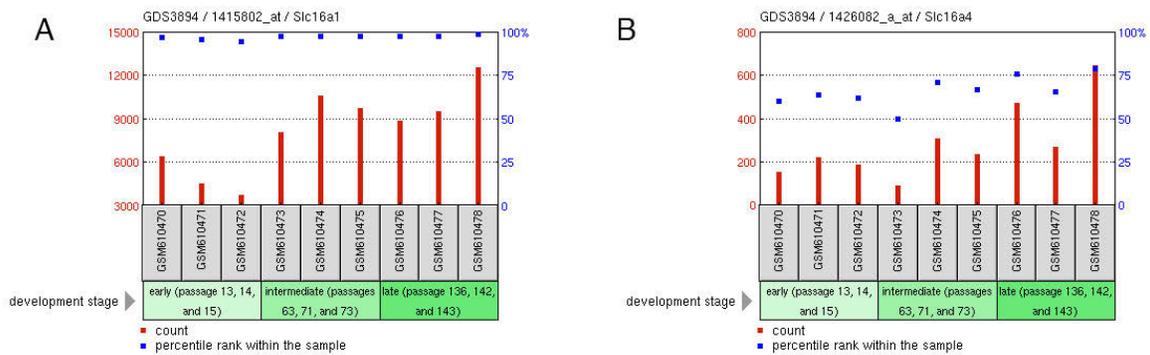
Figure 3.14. Microarray gene expression RNA data of MOSE cells, with MCT1 on the left (A) and MCT4 on the right (B). MCT1 tends to be elevated starting at the intermediate passage stage, and MCT4 tends to be elevated at the late stage. Data from [40]. Data accessible at NCBI GEO database, accession GDS3894. Image from (A): http://www.ncbi.nlm.nih.gov/geo/tools/profileGraph.cgi?ID=GDS3894:1415802_at. Image from (B): http://www.ncbi.nlm.nih.gov/geo/tools/profileGraph.cgi?ID=GDS3894:1426082_a_at.

We performed immunofluorescence to observe and confirm the alterations in cytoskeletal profiles of the various cell lines [40], and to prepare for further analysis of 3BP's effect on these cells, should this be required to test our hypotheses. Cells at early stage had a population of extremely large cells, with lengths spanning greater than 200 µm, while MOSE-I cells typically were between 20 and 60 µm long, and MOSE-L cells were typically under 20 µm long (Figure 3.15).
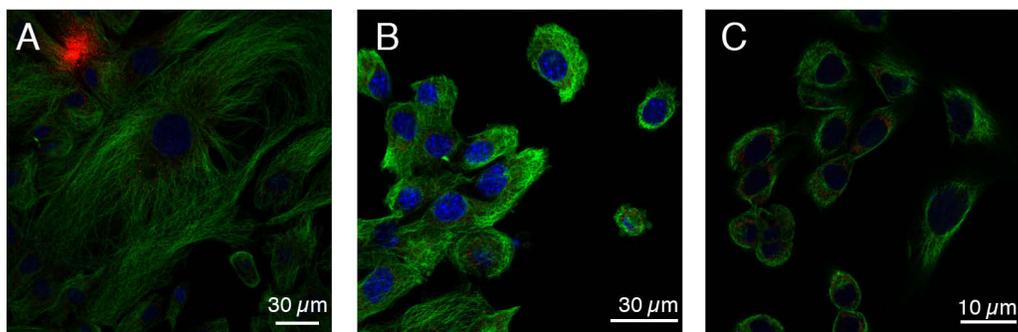
Figure 3.15. Immunofluorescence image of MOSE-E, MOSE-I, and MOSE-L cells confirming changes in size of cells during progression. Cells were fixed and immunostained for DNA (DAPI, blue), microtubules (α-tubulin, green), and mitochondria (COX-IV, red). (A) MOSE-E cells. (B) MOSE-I cells. (C) MOSE-L cells.

Our collaborators, Dr. Roberts and Dr. Schmelz who supplied us with the MOSE cell lines, also tested 3BP cytotoxicity on their highly aggressive MOSE cell line subpopulation and drug (paclitacel and cisplatin) resistant cell lines. They found the IC_{50} for 3BP on the highly aggressive MOSE cell line to be ~20µM and that this sensitivity is retained in their drug (paclitaxel and cisplatin) resistant cell lines (personal communication). Thus, they planned to move the investigation of 3BP to *in vivo* experiments with an immunocompetent syngeneic mouse model, although this has not yet to my knowledge been done.

3.3.5   Discussion and Conclusions

We demonstrated that late stage ovarian cancer cells were more susceptible to 3BP than early stage ovarian cancer cells (p=0.02) and that intermediate stage ovarian cancer cells were most susceptible to 3BP of the three cell lines tested. Dr. Roberts indicated that his lab's results showed that his highly aggressive MOSE cell line was highly sensitive to 3BP (~20µM IC_{50}). This led Dr. Roberts to recommend moving to mouse models to test 3BP in an immunocompetent system (personal communication). This would be a similar test to that previously done to evaluate 3BP for liver cancer [173]. 3BP is, as of 2015, approved by the FDA as an investigational new drug and the company PreScience Labs is planning to move to Phase I clinical evaluation for liver [286], and eventually pancreas [323], breast, lung, and ovarian cancer [330].

3.3.6 Future Work

3BP toxicity in both hypoxic and normoxic conditions at various stages of malignancy in the MOSE epithelial ovarian cancer progression model is likely correlated with MCT1 expression, as suggested in [244]. Further, as 3BP tends to target more tumorigenic cells in the MOSE cell line based on Dr. Roberts' and my results, repeated 3BP treatment may be able to select for a less malignant phenotype and halt progression of this disease in this model due to the elimination of the most malignant cells. Also, determining an optimal combination of 3BP, cisplatin, and citrate to lead to tumor elimination without recurrence in the corresponding immunocompetent *in vivo* mouse model is worthy of further study.

The following objectives are proposed:

Objective 1: Investigate 3BP toxicities to mouse ovarian surface epithelial (MOSE) early stage, intermediate stage, late stage, late stage cisplatin-resistant, and firefly luciferase tumor initiating variant (FFL TIV) cell lines, in normoxic and hypoxic conditions, as they compare to MCT1, MCT4, and HK-II expression, and rate of glycolysis.

Objective 2: Determine if repeated 3BP treatment on MOSE cells selects for a less malignant phenotype (contrary to most chemotherapy), and halts progression of the disease.

Objective 3: Optimize 3BP treatment for epithelial ovarian cancer by testing combination treatments *in vitro* and in a syngeneic immunocompetent mouse model.

As a result of objective 1, it would be determined if MCT1 is a primary indicator of 3BP toxicity in our model of epithelial ovarian cancer at various stages of progression, in both normoxic and hypoxic conditions, and in TIC subpopulations. This would help explain 3BP's effect in a heterogeneous tumor and its applicability as a combination treatment in epithelial ovarian cancer and possibly other cancers. As well, objective 2 would determine if 3BP has an opposite effect of most chemotherapeutic drugs, where it selectively kills the most malignant cells and prevents progression of ovarian cancer, selecting for a less malignant and drug sensitive phenotype, as opposed to a more malignant, drug resistant phenotype. If this is the case, it will possibly aid in the use of 3BP as a combination drug in cancer therapeutics. Finally, objective 3 experiments would determine if 3BP, alone or in combination with cisplatin and/or citrate, is able to have an

improved result than cisplatin treatment alone in an immunocompetent mouse model. If so, this will suggest its applicability to the clinic, especially where in ovarian cancer, intraperitoneal administration of chemotherapy shows improved survival benefit, but it results in increased toxicity of standard of care carboplatin and paclitaxel [331]. As 3BP shows promise of being able to decrease the amount of cisplatin/carboplatin needed in treatment, with a synergistic and less toxic effect, its introduction in the clinic could provide tremendous benefit.

There are several aspects to be aware of when considering developing 3BP as a cancer treatment. One is that 3BP is not stable in solution and so it must be prepared freshly, as in [304]. Additionally, recently it has been found that 3BP should be neutralized to pH 7.0 with a weak base such as $NaHCO_3$ as opposed to NaOH, in order to prevent 3BP rapidly losing its bromide to a hydroxide ion [332]. The specific half-life of 3BP in solution, and possible ways for longer, stable storage of 3BP, are discussed in [332].

Also of note is that 3BP as an "off-the-shelf" drug is not patentable. However, its delivery method has been patented under US patents: **7,547,673**, **7,754,693**, and **8,119,116**. A subset of these patents is believed to form the basis of the company PreScience Labs, which is in the process of beginning clinical trials using 3BP [330], under Dr. Geschwind's expertise of optimal drug delivery. The lack of patentability of the compound 3BP, as well as a possible patent dispute involving the origin developers of 3BP as a cancer treatment may have impeded progress to translate 3BP to the clinic. Efforts have been made to use an ester derivative of 3BP that upon entering the cells, gets metabolized and becomes 3BP, in order to develop a more stable form of 3BP [247].

3.4   Conclusions

Energy metabolism remains an active target for new drugs to enter the clinic as complementary drugs to current standard of care [162]. The potential of 3BP to target the most tumorigenic, multi-drug resistant, and hypoxic cells by its selective entry in cells uptaking large amounts of glucose make it an attractive drug to translate into the clinic [53, 244], if it were not for patent issues related to the drug. According to my initial results, enough data exists for 3BP to be evaluated in immunocompetent syngeneic mouse models developed by Dr. Roberts. The end goal would be for 3BP to be translated as a combination therapy in recurrent epithelial ovarian cancer, due to its ability to

preferentially target highly tumorigenic cells in the MOSE model studied. If effective, 3BP may be targeted to other cancers showing altered metabolism with high uptake of glucose.

With improved methods to measure energy metabolism pathways of cancer cells [190], my model suggesting that upregulated glycolysis of cancer cells may have a profound energetic cost to the body and lead to cachexia will be able to be more effectively evaluated [52]. This could lead to improved understanding of cachexia which is common in late stage cancer patients and leads to much clinical suffering [180]. If the cause of cachexia is better understood, better targeted therapies could be developed.

In summary, a biophysical analysis of cancer, especially in regards to cancer cell energy metabolism, has potential to bring increased understanding to unresolved effects of cancer, such as cachexia, and lead to new targeted therapies. In the next chapter, my analysis of biophysical factors that can be taken advantage to improve cancer therapies will be expanded to analyse electrical factors at play in cancer and the role of microtubules in electrical effects in the cell.

Chapter 4

Novel therapeutic intervention and monitoring of cancer: Microtubule electrical effects[*]

4.1 Introduction

In this chapter, I explore the possibilities of novel detection and monitoring of cancer through examining the possibility of electrical inter- and intra-cellular signaling. The goal of this chapter is improve our understanding of the electrical properties of microtubules as a building block for understanding possible electrical signaling systems in an organism, which may be perturbed in cancer with altered energy production and cytoskeletal organization in a cancer cell.

4.1.1 Submolecular signals in non-excitable cells

Explaining the mechanism of coordination of the organism as a whole is still a major challenge in the field of biology. Methods of communication in the human body are commonly thought to include electrical signalling by the central nervous system, chemical signalling through blood plasma with hormones, and cytokine chemical signalling. Additionally, inter- and intra-cellular connections in the body, which form a structurally and mechanically connected link between the cytoskeleton, the nuclei of cell,

---

[*] Chapter 4 contains material that was previously published as Friesen DE, Craddock TJA, Kalra AP, Tuszynski JA "Biological wires, communication systems, and implications for disease," *BioSystems* 2015, 127:14-27, in the introduction. I primarily researched and wrote this manuscript. J. Craddock added insight into neurodegenerative disease, A. Kalra added insight into certain microtubule conductivity experiment, and J. Tuszynski added insight to the entire paper. Only text written primarily by myself from this publication is included in this thesis. The Chapter 4 introduction also contains material previously published as Friesen DE, Craddock TJA, Priel A, Tuszynski J "Cytoskeletal electrostatic and ionic conduction effects in the cell," in *Fields of the Cell*. Edited by Fels D, Cifra M, Scholkmann F. Kerala, India: Research Signpost; 2015. This book chapter was written by J. Tuszynski, T. Craddock, A. Priel, and myself, and was largely revised by me. Only sections written primarily by myself are included in this thesis. The experimental portion of Chapter 4 is unpublished work. Microfluidic work was assisted by A. Jemere. The original process to create nanofluidic channels with embedded nanoelectrodes was originally provided by W. Reisner, and modified by me to account for the available experimental equipment at the University of Alberta.

and the extracellular matrix indicate the possibility for mechanotransduction with much faster speeds than traditional chemical signalling [333]. These structures involve microtubules (MTs), actin, and collagen, which are bionanowires that form a mechanical tensegrity matrix throughout the body potentially capable of high-speed electrical, protonic, and ionic signalling. Bioelectrical signalling is involved in regeneration and ordering of the organism [11, 334], and as chemical message passing systems have limited speeds, this introduction reviews the evidence that an organism takes advantage of these bionanowires to attain faster message passing speeds.

The main theories for a body-wide information network based upon bionanowires come from the tensegrity work of Donald Ingber [62], as well as the theories of James Oschman [63, 335, 336] and Mae-wan Ho [337], who have previously theorized submolecular (electronic, protonic, and ionic) communication systems in the body, and the work of Albert Szent-Györgyi [338, 339] concerning the idea that proteins in organisms possess semiconducting properties. We take an in-depth look at information transfer possibilities involving MTs, actin, and collagen in the organism. In essence, we extend the Dendritic Cytoskeleton Information Processing Model describing the role of MTs and actin in information processing in the brain [340-342] to investigate the potential for a fully interconnected submolecular messaging passing system in the body as a whole. This communication could be integral to an organism's organization and thus be perturbed in cancer.

4.1.1.1   Intercellular Message Passing

Conventional message passing systems include chemical and electrical signals passed through synapses and gap junctions, and autocrine, paracrine, and endocrine chemical signalling. However, it is becoming apparent that the entire organism is mechanically connected in an interconnected 'tensegrity' matrix that allows for long-range mechanotransduction [62, 333]. The extracellular matrix, which defines the space between cells, forms connections to the cell's interior through integrins, which connect to the intracellular cytoskeleton. The cytoskeleton, in turn, connects to the nuclei of cells forming a continuous mechanical linkage (Figure 4.1).
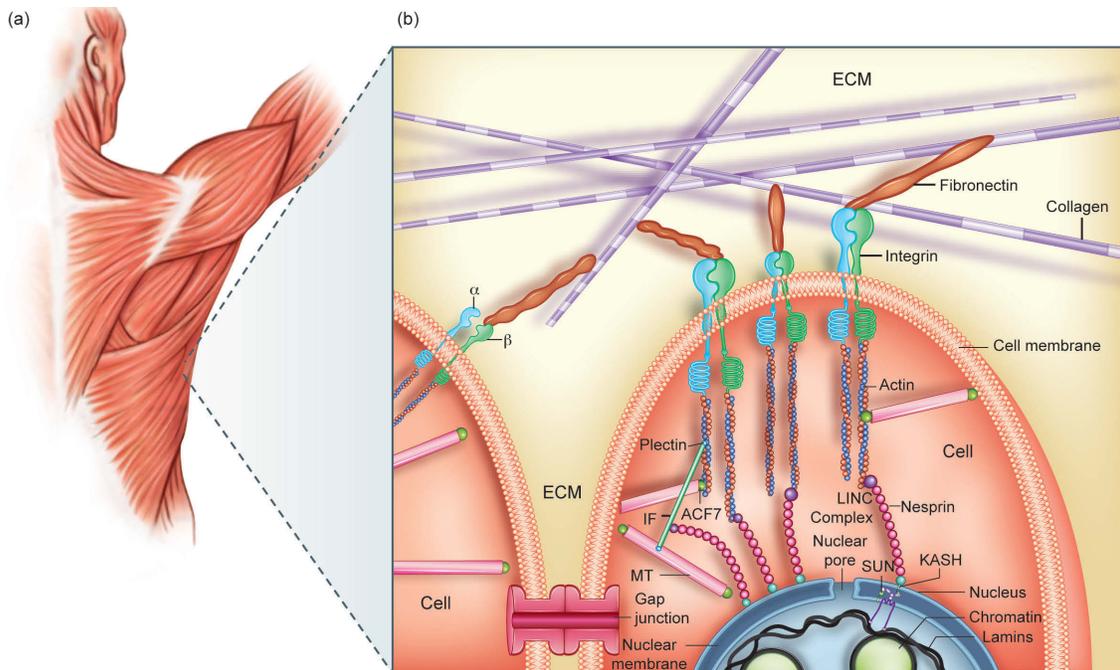
Figure 4.1. The interconnected matrix of bionanowires. (a) Connective tissue forms a continuous network throughout the body. (b) Much of connective tissue is composed of a web-like collagenous matrix that forms an extracellular matrix between cells. Collagen, connected to fibronectin, integrins, the cytoskeleton, and the nucleus, form a mechanically coupled system. Mechanotransduction, as well as ionic, electronic, and protonic signals, are hypothesized to be transmitted through this matrix.

Mechanical stress-wave propagation through this structure can create signals that travel at least 40 times faster [343] and potentially thousands of times faster than chemical signals that use diffusion or translocation [333]. This connective matrix suggests the possibility of high-speed communication systems at work in the organism.

Non-chemical message passing systems include those supported by electrons, ions, protons, excitons, mechanical vibrations [15], solitons, phonons, and photons [344, 345]. Developments in these fields have largely been slow due to the challenge of probing electromagnetic and nanoscale events in biological systems. Sub-cellular biological signalling research has developed rapidly in recent years through the use of modern experimental tools such as fluorescence imaging, confocal microscopy, scanning tunnelling microscopy, transmission electron microscopy, and atomic force microscopy. The interest into conductive properties of cells and their components was largely initiated by Albert Szent-Györgyi [338] with the claim that proteins may be semiconductors, but developments in this field have remained hampered by the significant experimental

challenges of measuring electric fields and currents at a sub-cellular level. The advent of nanotechnology, more precise instruments, and the interest in developing biological circuits promise to lead to rapid developments in this field [346, 347]. The domain of electromagnetic effects in biology is large and reviewed elsewhere [334, 348-350]. Here we focus on electrical communication systems involving MTs, actin, and collagen, and review current understanding of message passing using submolecular signals.

4.1.1.2 Components of a Biological Electrical Communication System

Albert Szent-Györgyi [338] pioneered the notion that proteins act as semiconductors. While organisms conduct electricity, as evidenced by medical equipment such as electrocardiograms, electroencephalograms, and transcutaneous electrical nerve stimulation, questions remain as to what are the charge carriers in living systems, and what are all the functions of these electrical signals. Well known are the action potentials that allow for neural firing and the control of the nervous system. A closer examination of the body reveals the exquisite role of membrane potentials, ionic currents, and endogenous electromagnetic fields in cellular proliferation, morphogenesis, and regeneration [334]. Also emerging in investigation is the potential crucial role of water in the proliferation of biological signals due to the structure imparted by hydrophilic surfaces [351].

Charge carriers under investigation in relation to protein semiconduction have largely been electrons and protons [352]. Electron tunnelling involved in enzymes has been studied [353, 354]. Evidence for protonic conduction in proteins has been found for collagen, keratin, cytochrome c and hemoglobin [355]. MTs are theorized to be involved in numerous forms of information processing, theoretically transferring ionic [356, 357], mechanical [358], photonic [359], and possibly quantum communication messages [360, 361]. MTs have also been theorized to support kink-like soliton waves which theoretically travel at 2-100 m/s [362, 363]. Mechano-electric vibrations of MTs have been studied theoretically [364]. In regard to the roles of these signal propagation effects, perhaps the most interesting and well developed is the possible connection between MTs and memory storage and retrieval in neurons using solitonic-like waves [365].

4.1.1.3   Microtubule Conductivity

MTs have been investigated for their potential to support various methods of submolecular message passing (Figure 4.2).
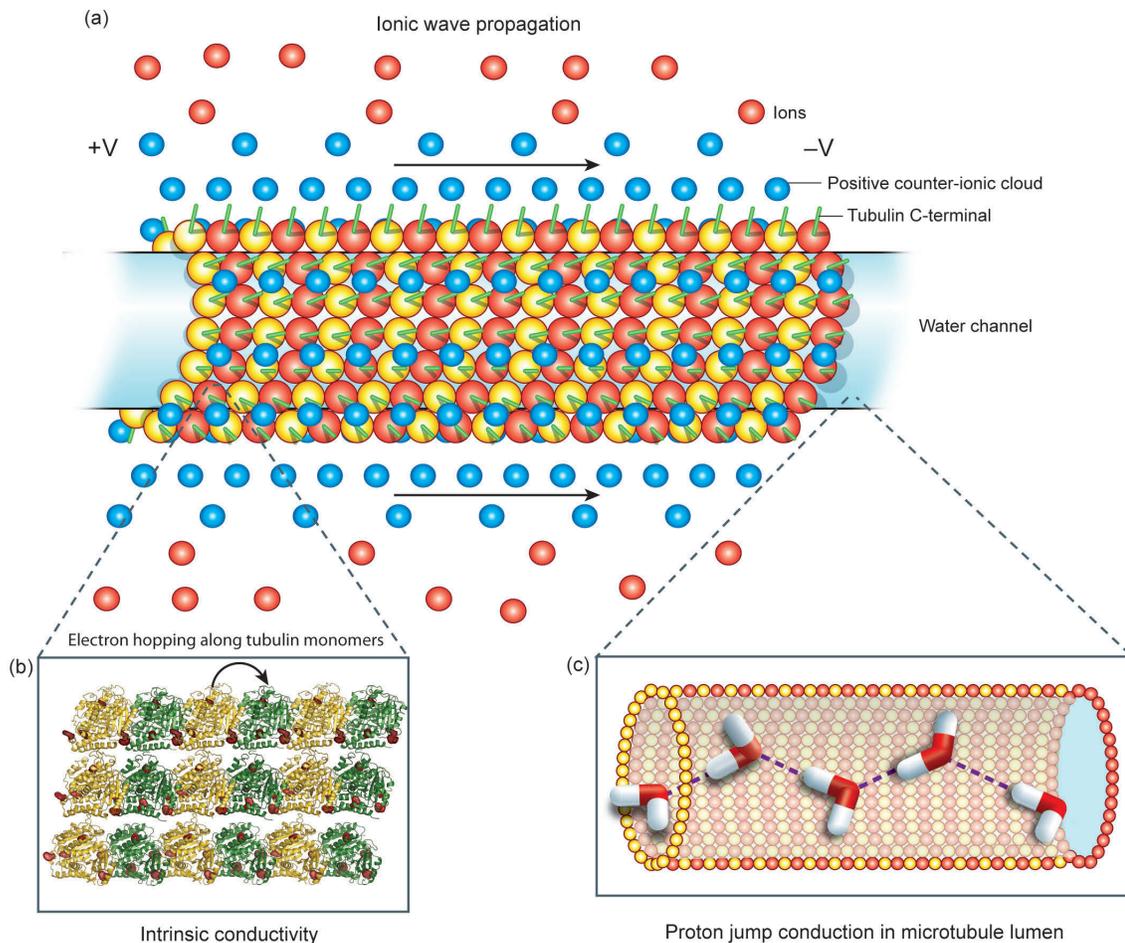
Figure 4.2. Conductivity Pathways along Microtubules. Experiments have probed microtubule conductivity based on (a) ionic wave propagation along the outside of MTs (positive ions are blue; negative ions are red), and (b) Intrinsic conductivity through the macromolecular structure itself, based on electron hopping along the tubulin monomers, and (c) Proton jump conduction, or intrinsic conductivity facilitated by structured water inside the MT, have been hypothesized.

MTs are part of the cell's cytoskeleton, and are macromolecular structures made from polymerized tubulin, which is abundant and makes up approximately 2.5% of the protein of a cell [68]. In multicellular organisms, their main roles are in maintaining the structure of the cell, providing tracks for intracellular transport, and in creating the mitotic spindle in cell division. MTs have also been theorized to be involved in information processing [366]. As well, MTs have been hypothesized to support intrinsic conductivity, which is

electronic conductivity through the protein itself, with electrons hopping through the hypothesized semiconducting bands of tubulin [341]. MTs have highly electronegatively charged C-terminal tails, resulting in a cloud of positive counter-ions surrounding the protein. In the presence of a voltage difference this cloud may propagate along the MT as an ionic signal [357]. It has been experimentally suggested and theoretically explained that ionic waves are propagated along MTs [341, 367]. MTs themselves are cylindrical in shape. The inner hollow volume of the MT has also been theorized to have special conducting properties [347, 359]. Many studies have been performed to examine the conducting properties of MTs. Table 4.1 summarizes the experiments performed to measure the various conductivities of MTs, with results largely dependent on the experimental method applied, and the type of conductivity detected. Conductivities in this table are estimated when exact values are not given.

Table 4.1. Conductivity data for microtubules and reference solutions

Paper	Type of experiment	Conductivity type	Conductivity (S/m)
[368]	Electro-orientation	Ionic	0.15
[369]	AC electrokinetics	Ionic	0.25
[370]	Cytoplasm	Ionic	2.5
[371]	Dry MTs	Intrinsic	Less than 3
[372]	Axoplasm	Ionic	3.4
[373]	Sea water	Ionic	4.8
[374]	TMR-coated, 4-point probe	Ionic	~40
[375]	DC MTs	Intrinsic	0.6 to 136
[376]	Gold electrodes, channel	Ionic/Intrinsic	Less than 80
[356]	Patch-pipette	Ionic	367
[347]	AC MTs. Water inside.	Intrinsic/Water channel	$10^3 - 10^5$
[377]	RF reflectance spectroscopy	Ionic/Intrinsic	$1\text{-}5 \times 10^6$ (they reported same as lead or stainless steal)

Ionic conductivity experiments largely show that the presence of MTs increases conductivity compared to simple solution. Minoura and Muto [368] found the conductivity to be increased by as much as 15x compared to that of the surrounding solution, although the ionic concentration, at ~1mM was lower than physiological ionic concentrations of just over 0.1 M. Priel et al. [356] confirmed a MT's ability to increase ionic charge conductivity, with current transmission increasing 69% along the MT length. In this case the buffer used was close to that of the intracellular ionic concentration, using 135 mM KCl. Increased ionic current along MTs is explained by the positive counter-

ionic cloud surrounding the MT surface [356]. From Priel et al.'s [356] conductance data, I approximate the conductivity of their result to be 367 S/m.

Uppalapati et al. [369], similar to Minoura and Muto [368], exposed an MT solution to an AC field, and observed electro-osmotic and electrothermal flow, as well as MT dielectrophoresis. At 5 MHz, where electrohydrodynamic flows were minimal, they estimated the conductivity of MTs to be 0.25 S/m. An investigation into measuring the conductivity of nanogold-coated MTs also measured tetramethylrhodamine labeled MTs as a control, and found the conductivity to be ~40 S/m [374], which is an order of magnitude less than that found by Priel et al. [356], but 2 orders of magnitude greater than Minoura and Muto [368] and Uppalapati et al. [369].

Intrinsic conductivity of MTs has been challenging to measure. This is due to the difficulties of measuring the conductivity of MTs in solution. It is known that hydration of proteins can drastically affect their conductivity [355]. However, when measuring MT conductivity in solution, only the increased ionic conductivity due to the counterion cloud formed around the highly electronegative surface of MTs is routinely measured [347]. Fritzsche et al. [371] have attempted to measure dry protein conductivity, but their setup is far removed from MTs native environment and so any results from these experiments may not be indicative of the intrinsic conductivity of MTs in their biological environment. MTs adsorbed to a glass substrate yielded an intrinsic conductivity of less than 3 S/m. Umnov et al. [376] attempted to measure intrinsic conductivity of MTs by putting MTs in an ultra-pure water solution, bridging gold electrodes. As the setup used only two probes, and the conductivity was estimated from the difference in conductance of buffer solution, MT+buffer, and pure water, using an estimated 50 MT contacts between electrodes, the calculation in effect theorizes ionic conductivity indirectly, much like Minoura and Muto [368], and Uppalapati et al. [369], and their result yields is consistent with MTs having a conductivity less than 80 S/m.

Sahu et al. [347, 375] have attempted to resolve the problem of measuring ionic conductivity along the periphery of MTs instead of intrinsic conductivity, as well as the problem that MTs likely require hydration layers inside of them in order to support high conductivity. They have adsorbed MTs onto glass and highly ordered pyrolytic graphite substrates and performed four-probe measurements of direct current (DC) and alternating

current (AC) conductivities. The DC intrinsic conductivities of MTs, from a 200 nm gap, were found to be in the range of 10^{-1} to 10^2 S/m, consistent with the previous findings of ionic and intrinsic conductivity mentioned. Surprisingly, they found that MTs at certain AC frequencies become approximately 1000 times more conductive, exhibiting conductivities in the range of 10^3 to 10^5 S/m [347, 375]. They claimed that it is in fact the water channel inside the MT that is responsible for the high conductivity of the MT at specific AC frequencies [347]. This importance of the water channel has previously been theorized by Jibu et al. [359], as well as by studies of carbon nanotubes that show proton conductivity increasing 40 fold inside the carbon nanotube channel [378]. Additionally, very thin films of water adsorbed onto a solid surface have been found to show surprisingly high conductivity using a scanning tunneling microscope (STM) [379], similar to the experimental setup of Sahu et al. [347]. Sahu et al. [347] report intrinsic conductivities along MTs are not length dependent. However, they also note that these experiments are the first of their kind to be done, and replication, as well as controls, such as investigating properties of similar biological wires such as actin and collagen, are badly needed to see if indeed the properties found for MTs generalize to other biological wires.

Another attempt to measure the conductivity of MTs was done by Goddard and Whittier [377]. They used radio frequency reflectance spectroscopy, and concluded the conductivity of MTs was similar to that of lead or stainless steel, which would be on the order of 10^6 S/m. This number is very high compared to other studies, and only solutions of MTs were studied by these authors and thus without more precise measurements on single MTs and validation of their method in measuring conductivities of biological wires, the significance of these results is unclear.

Several theoretical models of conductivity through MTs have been proposed, as shown in Table 4.2.

Table 4.2. Theoretical models of microtubule conductivity

Paper	Type	Result
[341]	Theoretical, Intrinsic	Conductivity 0.18-1.6 x 10^5 S/m using various assumptions

[357]	Theoretical, Ionic	Ionic pulse velocity: 0.26 m/s
[380]	Theoretical, Ionic, MT C-termini	Importance of C-termini and MAP2 in transmitting ionic signals

The work of Tuszynski et al. [341] builds on previous research done theoretically aimed at calculating the conductivity of MTs using the Hubbard model with electrons hopping between tubulin monomers (Figure 4.2B), with the two tubulin monomers forming a double well, given assumptions favorable to MT conductivity [381]. The results, in the range of $10^4 – 10^5$ S/m, correspond well to Sahu et al.'s [347] maximum AC conductivity numbers.

The ionic conductivity (Figure 4.2A) has been modelled further, and it is estimated that solitons transferring an ionic pulse would travel at 0.26 m/s, and the range of their propagation would be 3.2 μm [357]. MTs are often cross-linked together and with intermediate filaments by MT-associated protein 2 (MAP2). The physical properties of tubulin's highly electrostatically negative C-termini in transmitting signals, relevant to the transmission of signals along MTs and transferring signals through MAP2 to other MTs were also modeled [380].

Hameroff et al. [360] reviewed theoretical models of information processing involving MTs in 2002. Updates to these models continue to be developed based on additional experimental results, listed in Table 4.3.

Table 4.3. Theoretical models of information processing involving MTs

Paper	Type
[382]	Electro-mechanical vibrations
[365]	Memory, information processing
[383]	Quantum coherence in MTs
[361]	Consciousness

Havelka et al. [382] have modelled the generation of electromagnetic fields as a result of longitudinal vibrations of MTs, as a possible mechanism for ultra-fast electrodynamic signalling. Craddock et al. [365] have theorized information storage in MTs is due to phosphorylation sites on tubulin, which would support a theory of memory and information storage in neuronal MTs. The reports of quantum coherence in biological systems, specifically in photosynthesis [384, 385], have given support to ideas of

quantum coherence in MTs [383] since MTs exhibit uncanny similarity of the arrangement of tryptophan rings in their structure compared to photosynthetic systems [366]. The recent experimental findings on MTs reported by Sahu et al. [347, 375] have led to updates on previous quantum mechanical properties of MTs as they relate to quantum coherence and consciousness [361].

The multiple mechanisms of MT conductance provide ample possibility to explain the varied reports on MT conductivity given. Ionic conductivity along the outer rim of the MT (Figure 4.2A), intrinsic conductivity through the MT itself (Figure 4.2B), and possible proton jump conduction and conductivity through the inner MT lumen (Figure 4.2C) have all been theorized. The experimental challenge to simulate *in vivo* conditions, and the possible significance of structured water, ionic, pH and temperature conditions, as well as different messages being carried over different time scales, at different frequencies, and with different mechanisms, makes the need to evaluate the experimental results especially acute. This is clear in view of the large range of conductivities reported, in the context of various possibilities of information transfer known to be available. Like many other biological proteins and macromolecular structures, MTs may have multiple functions, and the diversity of theories of MT information transfer suggest several different mechanisms may be at play depending on the prevailing circumstances. With the advent of nanotechnology, further experiments designed to decipher the role of MTs in information processing will be instrumental in elucidating these issues.

4.1.1.4 Actin Message passing

F-actin forms microfilaments, which are approximately 7nm in diameter, with a helix repeating every 37nm. They have a high electrostatic charge density [386], and experiments indicate that they are able to conduct ionic signals through the counterionic cloud surrounding them [386, 387], similar to the ionic conduction effects observed for MTs [356]. Actin is typically the most abundant protein in a eukaryotic cell, and typically accounts for 1-5% of cellular protein, and up to 10% of cellular protein in muscle cells [388]. Actin filaments have been modelled as electrical transmission lines for ion flows and it has been estimated these flows have a velocity of propagation between 1 and 100 m/s [389], which gives a realistic model of actin that can support soliton-like ionic traveling waves [341]. This model has been updated by Sataric et al. [390] with a more

plausible estimation of model parameters. Calcium ionic condensation along actin in particular has been suggested as having a role in signal transduction within the cell [391]. Like MTs [392], actin filaments can be manipulated by external electric fields [393]. These properties have led to the theory that actin filaments may be an integral part of message passing in neurons [341], and the connection of actin filaments to integrins in the cell membrane, which in turn connect to the extracellular matrix, has resulted in speculations of actin's role in mechanotransduction signaling [62], and message passing throughout the organism, as is discussed below.

4.1.2 Extracellular wires

Collagen is the main component of connective tissue, in bones, tendons, ligaments, cartilage, and fascia, and thus is the most abundant protein in mammals, constituting over 30% of whole-body protein content [394]. Investigations into its conductivity show a high correspondence to its level of hydration [395, 396]. Its conductivity has been theorized to occur from protons which hop from highly adsorbed water molecules on the surface of the collagen [395-397]. Its conductivity at 13°C and 45% water content was measured as 2.0×10^{-3} S/m, which is 800 times higher than that when the water content was 22% [395]. Water has been found to be tightly adsorbed as a monolayer around collagen [398]. Collagen's maximum conductivity in biological ranges peaks around 310K [399]. The property of delayed luminescence (DL) has been found to depend significantly on the water content in the collagen [400]. The phenomenon of DL may be linked with coherent electron states of macromolecules [401]. Collagen with bound water has been proposed to form a semi-conducting, highly responsive network that links to cells through integrins, forming an excitable electrical matrix throughout the body [335-337]. This proposal is still quite speculative, and the conductivity measurements of collagen in physiological-like conditions are still being awaited. Initial attempts in this regard have found that collagenous bands are significantly associated with lower electrical impedance in human subjects [402].

4.1.3   Communication system connections

4.1.3.1   Integrins

The discovery of integrins connecting the interior of the cell with the extracellular matrix allows for the tensegrity model of the organism to be developed. This model has been developed in Donald Ingber's lab, who showed that integrins act to transmit mechanical signals to the cell [358]. Pulling on integrins results in the cytoskeleton reorienting, and the nuclei distorting [403]. It was reported that these effects were specific to integrins [403].

Signal transduction involving integrins currently centre on outside-in signalling, which is described as integrins affecting chemical signalling inside the cell, as well as inside-out signalling, which is where integrins change their affinity for extracellular ligands [404]. Ligation of integrins signals transduction events that modulate aspects of cell behavior such as proliferation, survival/apoptosis, shape, polarity, motility, gene expression, and differentiation, and this suggests integrins are full-fledged signal transduction receptors [405]. Most integrins connect to the actin-based microfilament system, which integrins regulate and modulate [405].

Several proteins in the plakin family of proteins, BPAG1e and plectin, have been shown to connect the cytoskeleton to integrin proteins [406]. BPAG1e associates with BPAG2, a transmembrane protein with an extracellular collagenous domain, as well as to the cytoskeletal keratin intermediate filaments (IFs) [406]. Plectin associates with β4 integrin and keratin IFs and actin [406]. Talin is a protein that provides a direct link between integrins and the actin cytoskeleton [407], and is key in activating integrins by changing integrins' affinity for their extracellular ligands [404].

Integrins then connect to collagen, for example by fibronectin [408]. These integrin-mediated cell adhesions are crucial to cell migration, morphogenesis, as well as regulation of extracellular-matrix assembly, cell proliferation, differentiation, and death [409].

How bionanowires, such as MTs, actin, and collagen are connected may give an idea of how they may transfer information through the organism. Tensegrity studies show that integrins connect the extracellular matrix to the cytoskeleton, and the cytoskeleton is connected to the nucleus of cells, forming an integrated system [62]. We further explore

these connections to understand if these bionanowires may transfer submolecular signals in addition to mechanical signals.

4.1.3.2 Connections between MTs and Actin

MTs and actin appear to be coordinated during cell motion [406] and neuromorphogenic processes [410]. Several proteins are involved in the connection between these cytoskeletal components [411]. MT-actin crosslinking factor 1 (MACF1/ACF7), MT-associated proteins 1B and 2 (MAP1B and MAP2) have all been found to cross-link actin and MTs [341, 406, 412]. Proteins that crosslink the cytoskeleton are enormous in terms of molecular weight in the protein world [406]. MACF1, for example, is 620 kDa, while tubulin which makes up MTs is only 55 kDa.

In neurons, actin has been hypothesized to connect to MTs by MAP2, and MAP2 has been hypothesized to be able to conduct ionic signals [380], in order to process information and regulate ion channels and thus synaptic strengths [341].

4.1.3.3 Connections between cytoskeleton and nucleus

Pulling integrins results in a reorientation of the cytoskeleton and the nucleus of a cell [403]. Actin and IFs were involved in mediating the force transfer to the nucleus [403]. This direct mechanical linkage of integrins to the nucleus indicates regulatory information could be rapidly passed to the nucleus using this pathway [403]. Indeed, these type of mechanical signals from integrins could be passed to ion channels, nuclear pores, nucleoli, chromosomes, and potentially genes [403]. Examples of this type of signalling, such as the neurotransmitter release from motor nerve terminals within 10-20 msec after cell surface integrins are mechanically stressed, are discussed [403]. It remains to be determined whether electrical signalling systems, using the same system of interconnected bionanowires, are being used by the organism.

4.1.3.4 Gap Junctions

Fast intercellular communication is important for multi-cellular organisms, and gap junctions play a pivotal role in this function. Gap junctions allow conduits between cells where voltage, pH and specific ionic concentrations are equalized [413]. Interestingly, gap junctions have also been theoretically shown to allow tissues to be increasingly sensitive to electromagnetic field effects [414]. Gap junctions are expressed in nearly all

tissues of the body and allow fast electrical synchronization. This is easily seen in the heart, where gap junctions allow heart muscle cells to coordinate in contraction [415]. Gap junctions have also been postulated to allow for brain 30- to 90-Hz gamma synchrony electroencephalography, which exists when humans are conscious, but disappears under anesthesia [416]. Their role in proliferating intercellular ionic signals is crucial, and it remains to be seen if electronic and protonic signals are also proliferated using gap junctions.

4.1.3.5   Tunnelling nanotubes

Recently it has been discovered that multicellular organisms create tunnelling nanotubes (TNTs), which are membranous channels of diameter between 50-200nm that form connections between cells up to a distance of several cell diameters [417, 418]. The channels contain actin and in some cases MTs, and provide electrical coupling, exchange of small molecules, organelles, and pathogens, and mechanical signals [417, 419]. Ionic flow, including calcium signalling, is thought to be transported passively through the channels, and compared to neuronal axons and dendrites, the electrical signal is of lower amplitude [417, 419]. However, these TNTs provide a selective electrical signalling that is much faster than chemical signalling [417]. This electrical coupling is thought to facilitate a fast and selective information transfer to coordinate cell migration [419] and other developmental processes such as wound healing, limb development, left-right patterning, regeneration, and morphogenesis [8, 9, 11, 28, 413]. The existence of TNTs suggests the importance of creating a high-speed intercellular communication medium using actin in specific circumstances when a gap junction network does not already exist.

4.1.4   Body-wide Theoretical Message Passing System

The dendritic cytoskeleton information processing model proposed by Tuszynski et al. [341] has previously assumed that the neural cytoskeleton constitutes the backbone for ionic wave propagation by regulating ion channels to effectively control synaptic connections. We hypothesize here that this type of framework could be extended throughout the organism to help explain the high-speed coordination of the organism. As outlined in section 2, there is a mechanical tensegrity system formed by connections from the extracellular matrix through the integrins to the cytoskeleton and nuclei of cells. This

system is primarily made up of bionanowires such as collagen, actin, and MTs, and is connected by integrins through the cellular membrane, and other supporting linking proteins such as MAP2 and fibronectin. As hypothesized by Oschman [335] and Ho [420], this system creates a "living matrix" of semiconducting macromolecules that are able to transmit, store, and process information involved in regulation.

The motivation for extending the theory of intercommunication between organisms arises from the fast coordination needed for a multi-cellular organism to function. Table 4.4 lists the speeds of message passing of different systems.

Table 4.4. Message passing systems suggested to be used by an organism

Message type	Typical speed	Function	Time to traverse 1m	References
Diffusion (protein)	100 μm^2/s	Passive transport	317 years	[421], 110.
Diffusion (K^+ ion)	2000 μm^2/s	Ion channel	12 ms to traverse 5nm ion channel	[421], 112
Diffusion (proton)	9310 μm^2/s	Proton channel	3.4 years	[422], 143.
Diffusion (proton in carbon nanotubes, theoretically)	17000 μm^2/s	Proton pumps	1.9 years	[378]
Kinesin (along MT)	10^{-6} m/s	Organelle transport	12 days	[421], 111
Calcium wave through astrocytes	13.9x10^{-6} m/s	Pathological event signaling	20 hours	[423]
Electrostatic guided phosphorylated messenger proteins in the cytoskeleton	2x10^{-4} m/s	Theoretical intracellular message passing	1.4 hours	[424]
Hormones (arterial blood flow)	0.4 m/s	digestion, metabolism, respiration, tissue function, etc.	2.5 s	[425]
Cardiac impulse propagation (action potential along gap junctions)	0.43 m/s	Coordinated heart beat	2.3 s	[426]
Unmyelinated nerve (ionic action potential)	1 m/s	Dull pain, temperature, itch	1 s	[427]
Mechanical (tensegrity) stress propagation along tensed cytoskeletal filaments	30 m/s	Stress propagation	33 ms	[343]
Myelinated nerve – A-beta (saltatory conduction)	55 m/s	Touch, pressure	18 ms	[427]
Myelinated nerve – A-alpha (saltatory conduction)	100 m/s	Muscle, position, spatial awareness	10 ms	[427]

Hydrogen jump conduction (protons)	~10^8 m/s	Theoretical coordination	10 ns	[428]
Semiconducting through biopolymers (electrons)	~10^8 m/s	Theoretical information processing	10 ns	[347]
Photons	~10^8 m/s	Theoretical coordination	10 ns	[350]

Simple diffusion is much too slow to be effective at translating messages for multicellular organisms such as mammals, which span up to meters in length. Active transport of organelles along molecular motors such as kinesin, which traverse MTs is much faster, but still would take 12 days for a payload to travel a meter. Calcium waves travelling through astrocytes, which are connected by gap junctions, are an order of magnitude faster, but still would take 20 hours to travel a meter. Electrostatic effects within cells have been postulated to aid in directional transport of messenger proteins [424, 429], and this again would increase message speeds several orders of magnitude over diffusion, but again this system would take approximately 1.4 hours to travel a meter. Hormone signalling can impact the entire body but is spread through the circulatory system, requiring only seconds to spread throughout the body. The neural action potential system is much faster, which is needed to coordinate movement. Speeds of myelinated nerves are typically on the order of 100 m/s in humans, thus requiring 0.02 seconds to extend from head to toe of a 2m person. While this is fast enough to coordinate movement, perhaps it is not fast enough to account for the coordination of an entire organism [63].

To create faster communication speeds, smaller carriers of information are needed. Chemical diffusion is too slow for a high-speed communication system, and thus ionic, electric, and protonic signals, and the methods by which they could be transmitted, are of interest. As the body is largely conductive, and as nature would naturally tend to take advantage of high speed messaging systems, from a survival standpoint taking advantage of high-speed communication would be of a survival benefit [63]. To support electron and proton charge carriers, a certain degree of order would be expected. Interest in the properties of water in living systems to support this type of order has increased in the last decade.

4.1.4.1   Importance of structured water

While the body is approximately 65% water by mass, a re-examination of the properties of water in living systems has been occurring extensively in the last decade. Water, rather than simply behaving like bulk liquid water, inside an organism may be gel-like [430, 431]. Proteins with hydrophilic surfaces create structured interfacial water [351]. This interfacial layer has been found to extend beyond the 1 to 2 layers previously expected [351]. The cytosol of cells is a packed volume of proteins, and thus the water in a cell is likely structured to a large degree [432]. Innovative imaging techniques using polarized light microscopy has shown organisms have liquid crystalline domains [433, 434]. This structured water, absorbed to collagen for example [398], could then theoretically support proton jump conduction [355, 397, 435]. Interfacial water along membranes has also been found to support rapid migration of protons [436, 437].

In contrast to this, several reports seem to confirm the historical assumption that the majority of water in the cell is bulk water [438-440], although these studies involved high-speed centrifugation of cell samples. Cameron et al. [441] also reviewed the controversy over the state of water in a cell with evidence in support that a substantial portion of water is not bulk-like, and their experimental protocol avoids high speed centrifugation due to this potentially altering the structured water properties of the cell.

Water has also been theorized as being necessary for protein electronic conductivity, as hydration resulted in albumin conductivity increasing by eight orders of magnitude [355, 442, 443]. Water has been suggested to support short and long range hopping motions of protons [355, 443, 444].

4.1.4.2   Proton Jump Conduction

The conductivity of collagen was found to be related to the degree of hydration of the protein [397]. Tightly bound water has been documented surrounding collagen [441]. This has led to the proposal that proton jump conduction occurs along collagen, and that this could facilitate rapid intercommunication in organisms, allowing them to have exceptional coordination [435]. Proton mobility in water is 9.31 cm^2/s, and is approximately five times that of Na$^+$ [445]. Its mobility is enhanced by the Grotthuss mechanism, which is the proton hopping that occurs along water chains without the need for hydrodynamic diffusion [446, 447]. Theoretically, proton diffusion in a carbon

nanotube can reach 40 times that of ordinary proton diffusion in water [378]. Mae-wan Ho [428] hypothesizes that proton jump conduction along one dimensional collagen wires allows for very rapid signal propagation, which still requires experimental testing.

4.1.4.3 Semiconduction

Robert Becker in the 1960s was examining currents in salamanders generated as a result of wounds, and performed an experiment to determine whether the charge carriers were ionic or semiconductive [448]. Hall voltages are proportional to the degree of mobility of the charge carriers. Ions in solution are large and not very mobile, and free electrons in metallic wire are abundant, but have low mobility. However, electrons in semiconductors are quite mobile, and measurable Hall voltages were recorded with Becker's equipment [448]. Becker [449] took his detection of Hall voltages, whose magnitude varied inversely with the level of anesthesia in the salamanders, to indicate that semiconductive properties existed along the nerves or related components. There has been a lack of follow-up studies in this area, and Borgens [450, 451] has criticized Becker's claims that the nervous system being the source of surface-detected bioelectric potentials. These differences are reviewed by Smith [452]. Given the data suggestive of semiconductive properties in organisms reviewed here, follow-up studies to detect Hall voltages in organisms would be indicated.

4.1.4.4 Ionic Conduction

Ionic signalling has been extensively studied, as ion flows result in the action potential that gives rise to rapid messages utilized by the central nervous system. Calcium signalling is also involved in a multitude of processes, including proliferation, development, learning and memory, and contraction and secretion [453]. Ions, and ion transport play a large role in cellular membrane potentials. A wound has been shown to depolarize the wound area, resulting in a "current of injury." This is due to damage in the epithelial layer, which maintains a transcutaneous voltage [450, 454].

Levin [8] has extensively studied ionic signals in regards to morphogenesis and cancer. Currents of injury and associated electrical signals have been shown to be both necessary and sufficient for regeneration [9]. Patterning information during embryogenesis and regenerative repair are influenced by bioelectric ionic signals [8].

97

Ionic signalling and endogenous voltage gradients affected by ionic flow regulate proliferation and cell cycle progression, apoptosis, migration and orientation, and differentiation and de-differentiation [455]. Thus, ions allow for message passing orders of magnitude faster than molecules. An open question in biology is whether signals propagated by electrons and protons are integral to biological function due to the signals propagating even faster than those from sodium, potassium, and calcium ions.

4.1.4.5 Photons

Endogenous photons, which are produced by organisms, have also been suggested to transmit biological information. Albrecht-Buehler [456] has done extensive work on cellular infrared detection, and concludes that the centrosome appears to be able to detect infrared signals. Additional research on photons has been reviewed elsewhere, listing studies showing ultra-weak, endogenous coherent light, termed biophotons, impacting mutual cellular interactions and proliferation [345, 350, 457, 458]. Red and near-infrared light involved in growth, development and cell metabolism has also been suggested [459]. However, the feasibility of photon signal detection by cells, due to the weak intensity of endogenous emissions and an unfavourable signal-to-noise ratio, remains low [460]. Photons and electromagnetic field propagation would make the fastest ideal signal propagation currently known, and so further studies in this area would be encouraged for a complete picture of biological communication systems.

4.1.4.6 Mechanical

The integrated connections between extracellular matrix, integrins, the actin cytoskeleton, and the nuclei of cells allows for a mechanical tensegrity system which allows for high-speed message passing, at approximately 30 m/s [333]. This system which has provided evidence of high speed mechanical signalling has also been theorized to support protonic and electronic signalling [336], and requires testing.

4.1.4.7 Messages and Message types

An organism works coherently at many time and distance scales. Human development into an adult takes decades. Cell division takes a day. Protein synthesis takes half a second. Gating of an ion channel takes 2 ms. Fast enzyme catalysis takes 1 μs. The speed of message passing depends on the distance and time requirements of the message, which

are listed in Table 4.4. In this review, we are most interested in the messages that require high speeds over 1 m/s. For example, muscle activation involves relatively large distances, and time scales in the milliseconds. Thus, myelinated axons exist to provide message passing on the order of 100 m/s, using flow of ions and propagating electric fields. Cardiac muscle contraction also requires fast coordination, and this is made possible by ionic action potentials travelling through gap junctions. Mechanical tensegrity networks allow for fast mechanotransduction, the process of physical forces creating cellular biochemical responses [62].

4.1.5 Theoretical high-speed message passing

A key question in biology is whether an organism is in need of a high-speed communication system above the well-studied systems using chemical diffusion, hormone distribution, and action potential and ionic signal cascades found in the nervous system, and if there is any evidence of such high-speed signals in organisms. It is known that organisms conduct electricity, and electrical forces play a key role in organisms as a whole [349], with membrane potentials allowing for action potentials, and providing morphogenetic information [9, 455]. With evidence suggesting MTs, actin, and collagen may form conductive wires throughout the organism, we discuss if and how the organism would benefit from these systems.

Two systems that might benefit from high-speed electricity are information processing in the brain, and signals to synchronize and coordinate the entire organism, for example in morphogenesis. The dendritic cytoskeleton information processing model has already been developed to describe how these bionanowires would assist in information processing in the brain [340, 341]. Recent findings of kilohertz, megahertz, and gigahertz quantum vibrations in MTs support the orchestrated objective reduction (Orch OR) theory of consciousness in the brain, that depends on orchestrated coherent quantum processes in collections of MTs within the brain neurons [361]. Cytoskeletal elements of the axon such as MTs may also help explain the increased action potential message speeds above theoretical calculations [461], by providing a reduction in resistance along the axon compared to axoplasm resistivity assumptions, as preliminary evidence suggests MTs facilitate ionic conduction [356, 368].

The question of maintaining order in a system without high-speed communication has been posed, and quantum field theory has been proposed to explain the collective behavior of ensembles of microscopic units [462]. Ho has provided evidence that organisms have liquid crystalline domains which may be key for biological organization and function [434]. She proposes liquid crystalline water aligned with collagen forms high-speed intercommunication networks throughout the body [428]. This assertion is strengthened by findings of a change in the quantum ground state of nano-confined water, which may lead to enhanced proton conductivity along proton exchange membranes, or nanochannels [463]. As carbon nanochannels are a simple model of biological channels, the result that protons delocalize in carbon nanochannels relative to bulk water [463] may have implications for understanding proton conduction along collagen filaments [428]. Molecular dynamics simulations also predict proton mobility along confined water chains to exceed that of bulk water by a factor of 40 [378], which supports the idea of biological wires such as collagen and MTs facilitating proton message passing. While there is a strong theoretical basis for electronic and proton jump conduction signals throughout the body, the experimental evidence thus far largely remains indirect, and so quantification of the information transfer and fidelity of these signals remains to be determined.

4.1.6 External application of electromagnetic fields for cancer treatment

Applications for cancer treatment have emerged using external electromagnetic fields (EMFs), which provide compelling evidence to further study electrical effects in non-excitable cells (ie. non-neuronal cells). Many findings indicate that electromagnetic fields may directly modulate the regulation of cellular growth and differentiation, including the growth of tumors [464, 465]. Both static magnetic and electric fields can alter the mitotic index and cell cycle progression of a number of cell types in various species [465, 466]. Gagliardi [467] has done work to explain all stages of mitosis as controlled by electric fields acting on charges.

The impact of external electric fields on a cell theoretically depends on the cell's shape. Calculations of the electric field strength in a spherical cell indicate that, assuming the conductivities of the extracellular and intracellular fluids of the cell are the same, due to the small conductivity of the membrane versus these fluids, the electric field strength inside a typical cell is approximately 5 orders of magnitude less than that outside the cell

[461]. Thus, given an applied electric field in air of 300 V/m, a cell with diameter 10 microns would theoretically experience a field of 5.4×10^{-10} V/m [461], thereby making the intracellular space shielded to a large degree from extracellular electric fields. King and Wu's [468] theoretical calculations for a spherical cell agree that the electric field in the protoplasm of the cell is negligibly small compared with the saline tissue around the cell, again approximately 5 orders of magnitude smaller.

A more interesting picture emerges when the cell is not spherical, as becomes the case increasingly when cells enter mitosis. King and Wu [468] have calculated the shielding occurring in elongated cells such as those found in muscle and long nerve cells by calculating the theoretical electric field inside a cell modelled as a cylinder. They found that in sufficiently elongated cells, no shielding occurs [468]. Extending their analysis, they found that in bundles of elongated cells such as those in muscle, still no shielding occurs [469]. Brown and Tuszynski [470] note that the DNA contents in the nucleus will still be protected from external fields due to being enclosed in the spherical nuclear membrane. However, during mitosis, when cell elongation typically occurs, external electric field effects may be much more relevant to cellular processes. Kirson et al. [471] have demonstrated this in their study of applying alternating electric fields for cancer therapeutics. In 2004, Kirson et al. [471] discovered that low-intensity, intermediate frequency (100-300 kHz), alternating electric fields (named tumor-treating fields (TTF)) had a profoundly inhibitory effect on the growth rate of various human and rodent tumor cell lines. The effects included both arrest of cell proliferation due to interference of proper formation of the mitotic spindle and destruction of cells undergoing division. This work has been shown to be effective in increasing survival rates as an adjuvant treatment to chemotherapy in glioblastoma multiforme [472, 473], and has subsequently been approved by the United States Food and Drug Administration (FDA). This work has led to the company, NovoCure, to be formed, which as of 2015 has over 265 global treatment centres. A Phase III clinical trial has shown including TTF treatment along with standard of care increases median survival of GBM patients from 15.6 months to 20.5 months [88]. The alternating fields are postulated to interfere with polymerizing and depolymerizing electrostatics of MTs, due to the force of the alternating fields acting on the tubulin dimers that make up the MTs. The tubulin dimers' dipole moment [362, 467]

could be affected by these external fields, possibly especially in mitoses due to decreased shielding as explained by King and Wu. Theoretical calculations done by Gagliardi [467] in explaining how electrostatic forces generated by MTs are at work during mitosis and influence chromosomal motion, suggest other effects could be at work when alternating fields are applied to cells in mitosis. Kirson et al. [471] also note that during mitosis, instead of the electric field in the cell being uniform, the field gets focused to the cleavage furrow. This may have the effect of attracting any dipoles toward the furrow, and causing cell membrane rupture and post-mitotic apoptotic cell death [471, 474]. Interestingly, Kirson et al. [473] postulate that dividing cells of the hematopoietic system are not affected by these alternating fields due to muscles surrounding the bone marrow serving as a shield to the external electric field effects. It is known that in the presence of an external electric field, the field aligns cell division, making a high proportion of cells having their cleavage plain orthogonal to the electric field [475]. Put together, there is reasonable evidence that especially during mitosis, electric field effects are relevant toward cell functioning, especially in the creation of the mitotic spindle and effects on MTs. The success of the Novocure clinical trials is a success story of investigation into electrical effects on non-excitable cells leading to a novel approved utilized treatment of cancer.

4.1.7   Forced membrane depolarization for cancer suppression

Another example pointing to the importance of electrical effects in non-excitable cells in terms of cancer is that involving the importance of cell membrane potential. In many cancers it is found that cell membranes are depolarized [10, 27, 476], mitochondrial membrane potentials are hyperpolarized [29-31], intracellular pH is alkalized [32-35], and extracellular pH is acidified [32, 34, 35]. Recent work has investigated whether this property of cancer cells being depolarized can be utilized to develop a novel cancer treatment strategy. In general, differentiated cells tend to be strongly polarized, while more plastic cells such as stem cells and cancer cells tend to be relatively depolarized [28]. Forced hyperpolarization, by misexpressing hyperpolarizing ion channels, has been found to make cells resistant to cancer transformation [19]. More remarkably, hyperpolarization of cells distant to the cancer site was able to suppress tumorigenesis

[477]. These results suggest the bioelectrical effects at play in non-excitable cells, and in between non-excitable cells has potential to lead to novel cancer treatment strategies.

4.1.8 Experiments to characterize electrical properties of macromolecules

Given that electrical effects in non-excitable cells are emerging to be able to be targeted for cancer suppression and treatment, and may be involved in key intercellular signals, additional understanding of these electrical signals, and the methods of electrical signal propagation are potentially key missing aspects of our understanding of cancer and intercellular organization as a whole. To gain insight into this realm, I hypothesize that MTs are involved in electrical signaling in the cell. I therefore used micro- and nanofabrication to build devices to probe MT electrical effects in physiological solutions in two ways. First, I created a flow cell device to measure electrical effect of MTs in solution. I hypothesized that:

MTs making solid connections between platinum wires will lead to increased ionic conductivity between the wires.

Second, I created a nanofluidic channel to isolate MTs to characterize their electrical properties. Several attempts have been made to characterize the conductivity of macromolecules such as DNA and MTs. Studies have used microfabrication in order to pattern electrodes in flow cells [368, 369, 374] and on substrates [376], and my flow cell experiments were modeled on these methods, as well as other previous work involving electrophoresis on MTs in microchannels [392, 478]. My flow cell experiments are intended to build upon the work of Priel et al. [356], who showed MTs are able to increase ionic conductivity along MTs, with an easily reproducible experimental system that is able to test ionic conductivity using multiple electrical measurement techniques (four point probe, two electrode measurement, capacitance-voltage testing, pulsed I-V measurements) under various ionic conditions. My flow cell experiments vary from Umnov et al.'s previous work [376] by exploring MT effects in physiological-like ionic solutions.

In order to create precise electrical characterization of single MTs, I built upon the methods to make nanofluidic channels integrated with nanoelectrodes for use in measuring transverse conductivity of DNA base pairs [479-483]. These efforts led to building a nanofluidic channel with nanoelectrodes regularly embedded on one side of

the channel and tubulin entering the nanofluidic channel; however, further work needs to be done to optimize the design for easy introduction of MTs into the nanofluidic channel.

4.2 MT electrical effects in solution in a flow cell

4.2.1 Methods

4.2.1.1 Device fabrication

For electrical characterization, Platinum (Pt) electrodes were fabricated on a square 10cm borofloat wafer (Swiftglass) using standard photolithography processes. Photoresist (HP504) was spincoated (500 rpm – 10s, 4000rpm – 40s) and patterned as a mask for subsequent metal evaporation and liftoff (see Appendix C for Matlab code which generated the mask pattern). Microwires of thickness 55nm (10nm Ti / 45nm Pt) were evaporated, followed by acetone liftoff. Fisher coverslips (#1 18mm x 18mm; Fisher 12-542A) were mounted on the wafer using Scotch double-sided sticky tape (3M) to create a flow cell.

Electrical Device A (EDA): EDA consisted of five electrode wires, designed to be 4µm wide, separated by 6µm.

Electrical Device B (EDB): EDB consisted of two electrodes 30µm wide, separated by 14µm. EDA 5-7 were tested in preliminary experiments to gain experience with the measurement system (data not shown), and then four of these devices were tested in one experiment: EDA 1-4. The devices were fabricated with the same design as EDA, except the wires were designed to be 3µm wide, separated by 4µm. Due to these dimensions being at the limit of the microfabrication equipment, the electrode wires were not successfully fabricated.

Electrical Device C (EDC): EDC consisted of five electrode wires, designed to be 3µm wide, separated by 4µm. In this one device, the wires were successfully fabricated. The device was tested in preliminary experiments to gain experience with the measurement system and optimize measurement parameters (data not shown).

4.2.1.2 Solution preparation

Rhodamine-labeled fluorescent MTs were polymerized from 5μL of porcine brain tubulin (Cytoskeleton kit #BK004R). Tubulin (Cytoskeleton, Kit #BK007R) was prepared following the protocol for the Fluorescent MTs Biochem Kit, with parameters used to obtain long MTs. Briefly, one aliquot of rhodamine tubulin was resuspended in 4.25 µl G-PEM (100 mM GTP (Cytoskeleton, BST06) + microtubule buffer solution (PEM) (Cytoskeleton, BST01)) and 0.75 µl MT Cushion Buffer to yield 4 mg/ml fluorescent tubulin. 16 µl of unlabeled tubulin (5 mg/ml) was added to the 5 µl of fluorescent tubulin (4 mg/ml), leading to 21 µl of tubulin (1 rhodamine : 3 unlabelled; 4.76 mg/ml). Four 5 µl aliquots were made per rhodamine tubulin aliquot.

MT solution was prepared by polymerizing 5 µl fluorescent tubulin (1 rhodamine : 3 unlabelled; 4.76 mg/ml) at 35ºC for 45min, followed by adding 100 µl PEM solution containing Taxol (10μM), yielding a 2mM tubulin solution of fluorescent MTs. 1x Antifade (Cytoskeleton, BSM02), with beta-mercaptoethanol (Sigma, M6250) added to MT solutions to be imaged.

Poly-L-lysine (PLL) (0.1 mg/ml; 70-150 kDa; 0.6-1.4μM) (Sigma, P1274) was prepared in general tubulin buffer (PEM) (Cytoskeleton, BST01), consisting of: 80 mM PIPES pH 6.9, 2 mM $MgCl_2$ and 0.5 mM EGTA. At this pH, PEM contains roughly ~46mM PIPES2-, ~36mM PIPES-, ~68mM Cl-, ~160mM Na+, and ~2mM Mg2+ [392]. Cytoskeleton reports adjusting PEM pH to 6.9 using NaOH, as opposed to KOH (personal communication). PLL is a positively-charged amino acid polymer that is used to promote cell adhesion to a culture surface. As it has multiple positively-charged sites available to bind, it is also used to promote binding of MTs to a glass surface [374, 376].

4.2.1.3 EDA Experimental setup

Four-point collinear probe measurements were performed with the Keithley 4200-SCS on the first four wires from the left of the EDA device, with 1nA applied current (the current range recommended by Keithley to give a voltage drop of about 10mV) between wire 1 and 4. Wires 2 and 3 both measure the voltage respective to ground wire 4. Reported mean voltages reported with SD error. The current source range to determine the input impedance of wires 2 and 3 was set to be in the 1nA range. Tungsten probe tips, with 5.0 µm tip diameter (Signatone, SE-T) were used. The Keithley settings used were

Sampling mode, normal speed, interval 0.25s, hold time 1s (Keithley software v. 8.2). In this mode, the 1nA bias is applied and held during the entire time of the execution, which consists of an initial hold time of 1s, to allow the system to settle after initial application of the 1nA current. Then ten measurements are taken, with a settling time for the sourced current to stabilize (approximately 0.13s), then the 0.25s interval time, then the measurement time. The measurements from wires 2 and 3 are synchronized. This entire measurement execution with 1nA sourced current takes approximately 4.44s.

4.2.1.4 EDB Experimental setup

Current-voltage measurements were performed using a semiconduction characterization system (Keithley 4200-SCS) with a probe station. Range of applied voltage was ±1 V with 0.2 V step, from -1V to 1V. Keithley settings were sweeping mode, normal speed, sweep delay 0s, hold time 0s (Keithley software v. 8.2). Linear regression was applied on the -0.6 to 0V points to report a conductance. The slope calculated from linear regression is the conductance, and the inverse is the resistance. Multiple voltage sweeps were performed in each experimental situation (the number of sweeps done is reported in the figures). Tungsten probe tips, with 5.0 μm tip diameter (Signatone, SE-T) were used. Capacitance-voltage (C-V) sweeps were also done, from -2V to 2V and then 2V to -2V, with 0.0635V step size, at 3kHz, 100kHz, 1MHz, and 8MHz alternating current frequencies (data not shown). For EDB 1-3, after all I-V measurements were taken, 3 C-V sweeps followed by I-V measurements were performed for each frequency: 100kHz, then 8MHz, then 3kHz, then 1MHz. Keithley settings were quite speed (delay factor 1.3), sweep delay 0s, hold time 0s (Keithley software v. 8.2). For EDB 4, these C-V measurements were performed after I-V measurements of PEM solution were done, as well as all I-V measurements of MT solutions were done (data not shown).

4.2.1.5 Imaging

Fluorescence imaging was performed by an upright microscope (Imager.Z.1, Carl Zeiss, Inc.), using a 10x EC Plan-Neofluor objective (NA=0.3), 40x Plan-Apochromat objective (NA=1.4), and 66x Plan-Apochromat objective (NA=1.4). Images were acquired by SensiCam (Cooke) charge-coupled device camera (PCO-TECH Inc.) with

Metamorph software 7.8.12.0 (Universal Imaging Corp.). Images were processed using Adobe Photoshop CS6 v. 13.0.

4.2.1.6 Calculations

Conductance reported is the mean of the slope of the linear regression of each voltage sweep using data points -0.6 to 0V, which is an approximate of the conductance at the equilibrium voltage (voltage where current is 0A) ie. x-intercept [376]. Error is standard deviation. Conductance reported for PEM for wire 2 4 is taken from points -0.6 to -0.2 V, due to large variance of the 0V data point. Error reported is SD. Wire 2 4 PEM linear regression taken from -0.6 to -0.2 V data points due to large variance of 0 V data point.

4.2.2 Results and Discussion

4.2.2.1 Resistance effects of MTs in solution: Four-point probe

I created electrical devices, made of 55nm high Pt wires attached to a glass substrate in a flow cell, to test electrical changes due to MTs in physiological-like solution. The electrical devices were constructed on a 10cm square wafer as designed in Figure 4.3.
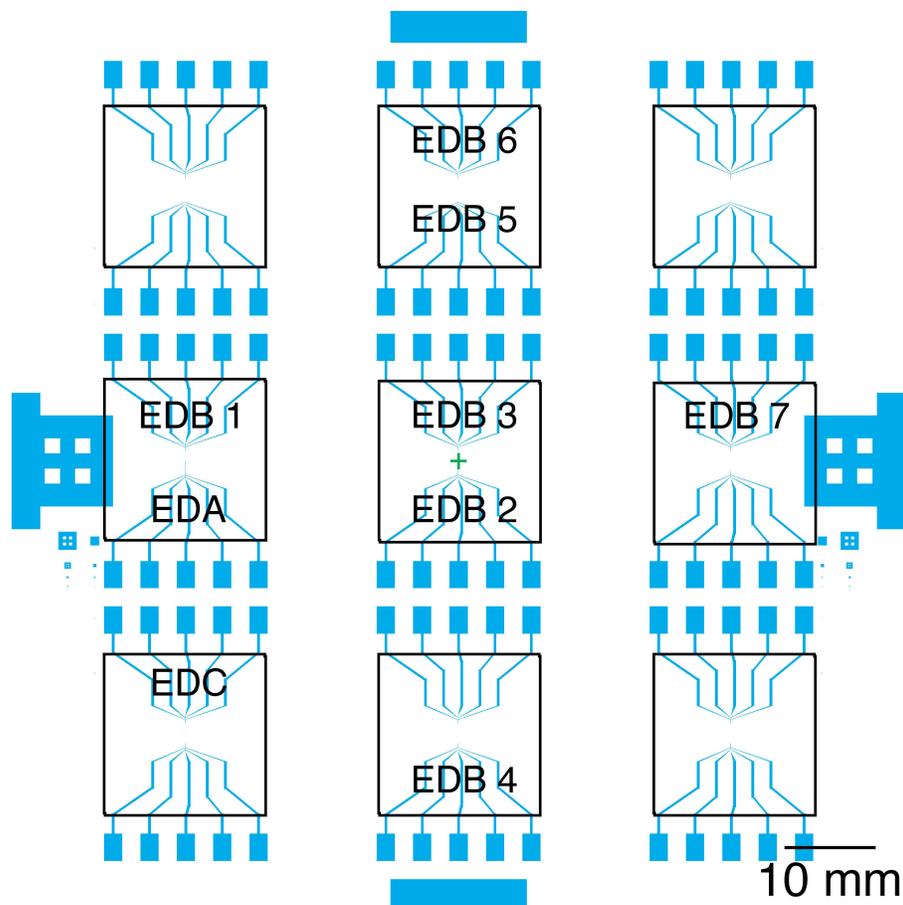
Figure 4.3. Design of nine flow cells, with two measurement devices per flow cell. Pt wires are defined in blue, and the locations of coverslips of flow cells are black squares. The locations of electrical devices A, B1-7, and C (EDA, EDB, and EDC) are marked.

Electrical devices A (EDA), B (EDB), and C (EDC) were fabricated as shown in Figure 4.3. The devices not labelled in Figure 4.3 were not fabricated correctly, with the wires not being continuous. The wires of devices in the outer corners of the square substrate were not fabricated correctly probably due to uneven height of photoresist when spinning the photoresist on the square substrate. Using a circular Borofloat substrate may improve device yield due to more uniform photoresist height after photoresist spinning. The results of experiments performed on EDA are reported in this section. The constructed substrate with flow cells is shown in Figure 4.4.

Figure 4.4. Flow cell substrate, featuring nine locations for flow cells. Device is rotated 180º from the design in Figure 4.3. Four probe tips in a probe station on a Pt test contact pad are shown. The probe tips are connected to a Keithley 4200 semiconductor characterization system. Square glass substrate shown is 10 cm x 10 cm.

The design of the devices, created in Matlab, is shown in Figure 4.5. Each device design has five wires, with contact pads large enough to be attached with probe tips to the Keithley 4200 semiconducting characterization system (Keithley 4200-SCS) (Figure 4.5A). The region where the wires converge (top red rectangle in Figure 4.5B) has the five wires extending for 500 µm where the MTs can cross all 5 wires. In EDA, the wires were fabricated to be 4 µm wide, with 6 µm between wires (10 µm apart centre-to-centre) (Figure 4.5C).
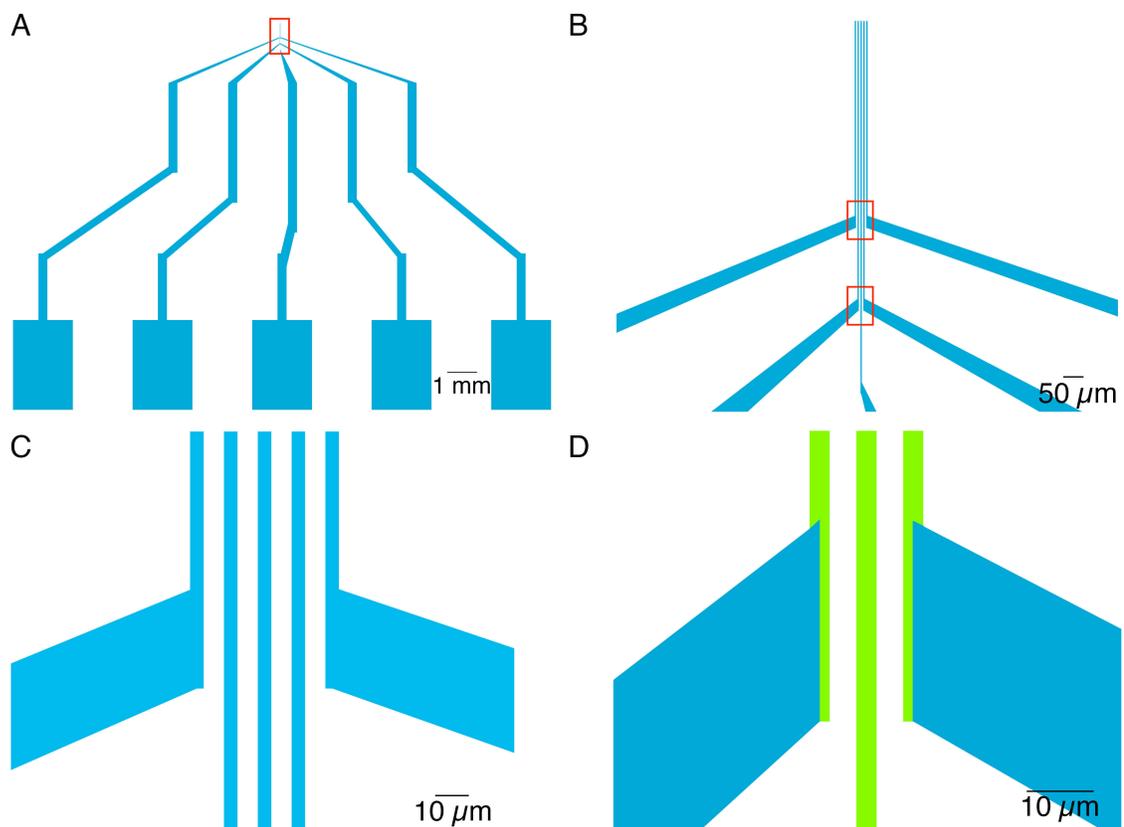
Figure 4.5. Matlab design of flow cell electrical wires, with platinum wires designed in blue. (A) Flow cell electrical measurement device. The region of interest (red rectangle) is zoomed in, in (B). (B) Five electrode wires merging. The top red rectangle is zoomed in, in (C). The bottom red rectangle is zoomed in, in (D). (C) In one device, the wires were fabricated to be thicker than the other devices: 4 µm wide, with 6 µm between wires. These wires were fabricated correctly, and the device is named EDA. (D) In most devices made, the wires were designed to only be 3 µm wide, with 4 µm between wires, as shown in green. However, in most cases, the wires were not successfully fabricated, leaving the device shown in blue with no fine wires, known as EDB.

These wires in EDA (Figure 4.5C) were fabricated correctly, although the Pt wires were thinner than designed, measuring 1.5µm wide and with 8.8µm spacing between wires (Figure 4.6). By visual inspection of fluorescence images, these appears to be 2, 3, 10, and 7 MTs making solid connections between wires 1 and 2, 2 and 3, 3 and 4, and 4 and 5, respectively. This allowed me to prepare a four-point probe experiment to ascertain the electrical changes caused by MTs in solution.
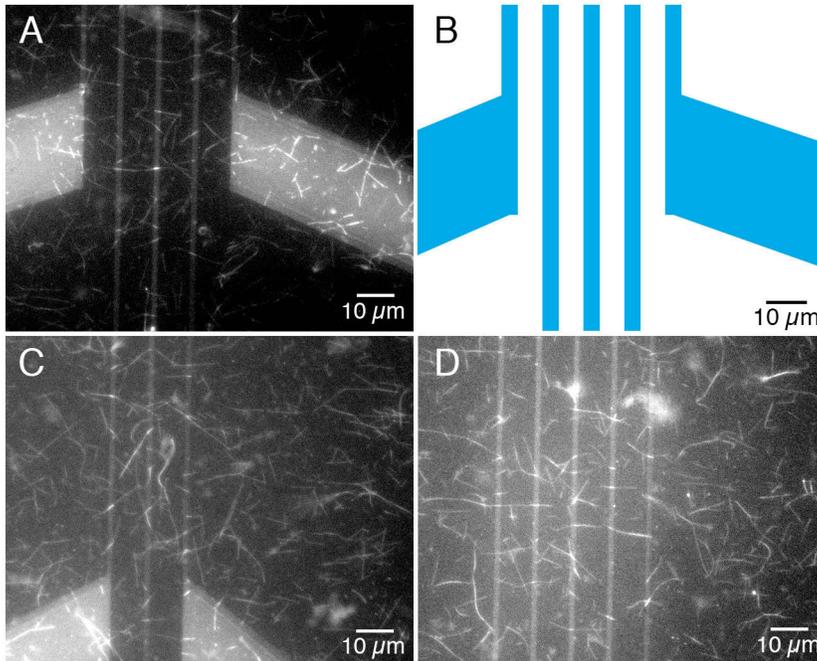
Figure 4.6. EDA device. (A), (C), and (D) are red fluorescence (Cy3), 40x magnification. (A) EDA device shows MTs adhered to substrate. The MTs also appear to be making contact on the thin Pt wires. This area corresponds to the top red rectangle in Figure 4.5B. This is where wires 1 and 5 merge (B) The design of the device, corresponding to (A). The Pt wires are thinner than designed, measuring 1.5µm wide and with 8.8µm spacing between wires. (C) The area of the device corresponding to the lower red rectangle in Figure 4.5B. This is where wires 2 and 4 merge (D) The five wires extending higher than that imaged in (A). MTs which appear to span pairings of wires shown. The left 4 wires are used for 4 point probe measurements.

Two concentrations of rhodamine-labeled (fluorescent) MTs were prepared (41nM and 82nM) in PEM (MT buffer solution). PLL in PEM (0.1 mg/ml) was introduced into the flow chamber as it is used to coat the flow chamber glass substrate. MTs stick to the PLL coating, due to the PLL's positively charged binding sites, and I-V characteristics were measured after 14min. Then PEM was flushed through the flow cell to remove any unadsorbed PLL in the flow cell, and I-V characteristics where again measured immediately and after 28min. Then MTs (41nM) were introduced, and I-V characteristics measured after 6min. Then MTs (82nM) were introduced, and I-V characteristics measured after 35min. Then MTs were imaged following all I-V measurements in a separate facility. Figure 4.6 shows MTs appearing to be adsorbed to the substrate, as they were not moving while imaging, and they appear to be spanning the electrode wires, as

the focus while taking the image is in line with the electrodes. The electrode wires are thinner than designed, imaged at 1.5 μm compared to their 4 μm design (Figure 4.6).

A four-point probe experiment is used to accurately measure the resistance of a material by avoiding contact resistance of the probes to the material being studied to a large extent [484]. It involves four probes usually in contact with a material of known thickness and unknown resistance. The material is usually semiconducting. In my case, the material is an ionic solution, which presents unknowns in terms of correction factors needed to convert voltage measured into resistivity of the solution. The electrodes (wires) are numbered 1-4 from the left and are equally spaced. The setup using the Keithley 4200-SCS to perform a four-point collinear measurement is displayed in Figure 4.7. Wire 4 serves as the ground wire. Wire 1 sources 1nA of current, which was chosen in order to get measured voltage drops of around 10mV, as per the Keithley 4200-SCS documentation [485]. Wires 2 and 3 both measure the voltage respective to ground wire 4, which are referred to as V_{23} and V_{24}, and in each measurement execution, V_{23} and V_{24} are measured 10 times over approximately 4.44s of the 1nA current being applied (see methods). The voltage between wire 2 and 3 is the difference between the measured voltages from wires 2 and 3. i.e. $V_{23} = V_{24} - V_{34}$ (Figure 4.7). The reported results are of the first measurement recorded after 1.38s of the 1nA current being applied. The results of this experiment, with V_{23} plotted, are shown in Figure 4.8. This data showed PLL and PEM in solution has similar values compared to that of MTs.
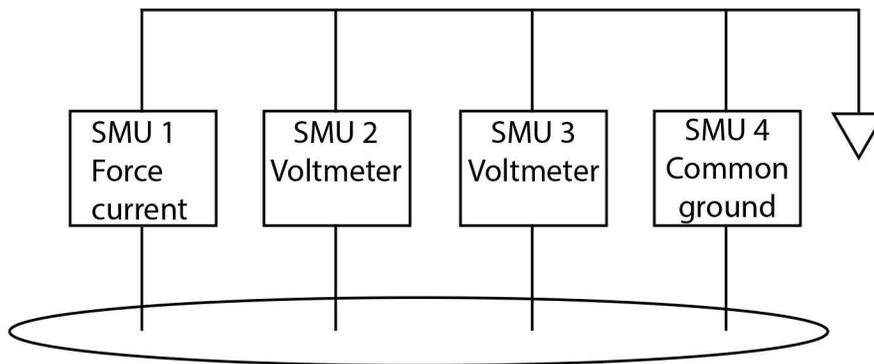
Figure 4.7. Design of four-point collinear probe measurement. Current bias of 1nA set between source-measure units (SMU) 1 and 4. SMU 2 and 3 measure voltage, respective to the common ground (SMU 4), which are referred to as V_{24} and V_{34}. Settings follow the recommended four-point collinear probe measurement settings for Keithley 4200-SCS [485].

Four-point probe measured voltage, V_{23} (1nA applied current)
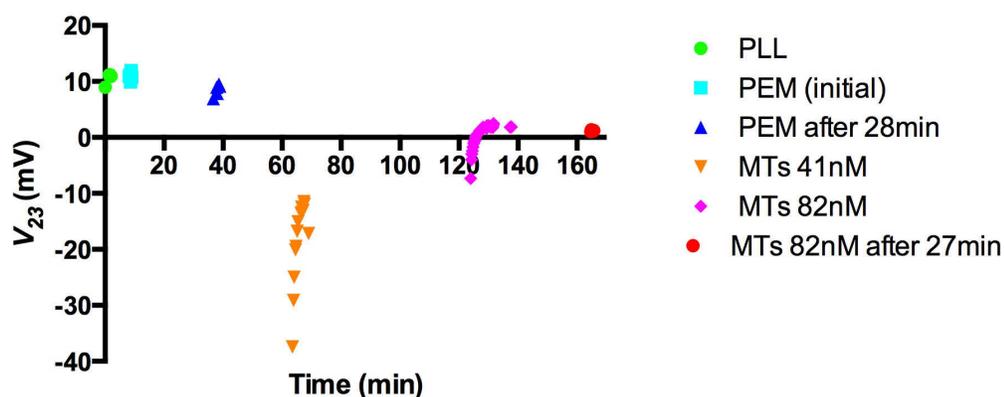
Figure 4.8. Four-point probe measured voltage V_{23} (in mV) with 1nA applied current over time. PLL was injected into the flow cell, followed by PEM, then MT solution (41nM tubulin), then MT solution (82nM tubulin). The large drop of measured voltage with the initial addition of MT solution was unexpected.

To analyze Figure 4.8, PLL initially adsorbs onto the substrate and coverslip surfaces, and when PEM is added, the adsorbed PLL will remain and most of the unadsorbed PLL will flow out of the flow cell. Thus, the only difference in the flow cell between the PLL and PEM recordings should be that the PLL solution would have much more unadsorbed PLL, and PLL concentration initially is only 0.6 – 1.5 µM, so no major change in measured voltage was expected, which was what was observed. The slight drop of resistivity between the initial PEM and final PEM readings could be explained by reduced numbers of unadsorbed PLL after the PEM had sufficient time to flush the unadsorbed PLL out of the flow cell and equilibrate.

Upon addition of MTs (41nM tubulin) in PEM solution, and after over 6 minutes of equilibration time, the measured voltage was substantially lower at -37mV (Figure 4.8). Over four minutes, it increases rapidly to a maximum of -11.5mV and then two measurements after show it decreasing again to -17.2mV. After addition of MTs at additional concentration (82nM tubulin), the measured voltage is still negative at -7.3mV and again rises asymptotically to a maximum of 2.5mV. After a rest period of 27 min, measurements were 1.2 ± 0.2 mV (n=4).

A negative voltage drop when then MT solution (41nM tubulin) was added, and an applied current of 1nA was provided was unexpected. To analyze this further, V_{24} and V_{34} are plotted in Figure 4.9.

113
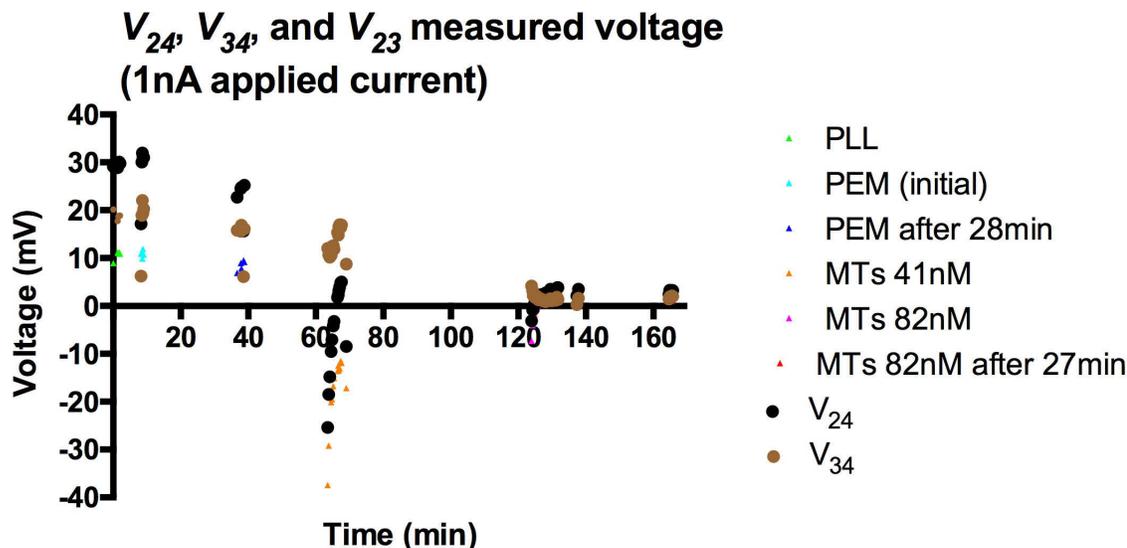
Figure 4.9. Voltage between wires 2 and 4 (V_{24}) and voltage between wires 3 and 4 (V_{34}) plotted in mV with 1nA applied current over time. Plot of $V_{23} = V_{24}$-V_{34} also shown, which was plotted in Figure 4.8. PLL was injected into the flow cell, followed by PEM, then MT solution (41nM tubulin), then MT solution (82nM tubulin). V_{24} drops over 40mV upon addition of MT 41nM solution.

As expected, V_{24} is larger than V_{34}, and both are positive, for the PLL and PEM solutions. When the low concentration MT solution is added, V_{24} drops 50.6 mV while V_{34} only drops 4.1 mV. This could be due to the effects of MTs, which are negatively charged, creating this negative voltage. The substrate surface, where the 55nm electrodes rest on, in the case of the PLL and PEM solution environments, have PLL adsorbed to the surface creating a positive charged surface. MTs adhered to this surface may create a negatively charged surface, potentially leading to different electro-osmotic effects and altered positive and negative charge carrier mobility for the counter-ions adsorbed to the surface and providing a screening layer for the charged surface [367, 369]. As the connection between wires 1 and 4 is through an ionic solution with positive and negative ions with negatively-charged MTs on the surface of the device, the system is more complex than a simple resistor model between wires 1 and 4. It must be cautioned that this experiment must be replicated in order to come to concrete conclusions. Longer and shorter microelectrode wires (now 500 µm long) could be used to gauge the effect of the number of MTs spanning the electrodes. As well, an electric field could be applied within the flow cell while introducing the MTs to the flow cell to bias the MTs to span the electrodes, to induce more MTs to directly interface the electrodes, and see if this

114

modifies the result. To test whether the effects seen are unique to MTs, other macromolecules such as single-wall nanotubes (SWNTs), and actin could be tested. Also, using subtilisin-treated MTs, which are able to have the negatively charged C termini removed, could be used, as these MTs would have less charge and therefore less capacitance. Also, the applied current was only 1nA, which is on the range of current needed to make a voltage measurement V_{23} and V_{24}. Therefore, higher applied current, such as 10-100nA, would be recommended to be tested.

Another effect seen is that with repeated measurements, V_{24} rapidly increased to a positive voltage, although still less than V_{23} with the MT (41nM) solution. Additionally, in the time period of almost an hour between MT (41nM) and MT (82 nM) measurements, the measured V_{23} hardly changed, then with subsequent measurement, increased rapidly. This suggests there is a measurement effect going on, and would be understood better once the cause of the negative voltage was deduced, from the aforementioned additional proposed experiments to deduce what effect MTs may be having electrically. In terms of understanding the amount of current applied compared to that held by MTs, during a measurement execution, a 1nA current is supplied for approximately 4.44s, which corresponds to 2.77e10 elementary charges. A 10μm long MT has approximately 7.6e5 negative elementary charges (assuming 47 negative charges on a tubulin dimer 8.0nm in length). Thus, the charge applied during each measurement is approximately equivalent to that held by 36,000 MTs. Solution flow in the flow cell might be causing the changes in measurements, due to electro-osmotic flow or temperature gradients [369]. Applying the 1nA current will lead to electro-osmotic flow, which is the flow that results from ion movement as a result of the electric field causing fluid flow [369]. Temperature gradients may be caused by Joule heating, which is the heating caused by the current applied through the electrodes. This may also cause electrothermally induced fluid flow around the microelectrodes, which has been previously analyzed theoretically to cause on the order of 0.004 °C heating for a similar experimental setup (thin microelectrodes 25μm apart, 200μm wide in water on glass, with 5V applied) [486].

When the high concentration MT solution (82nM tubulin) was further added, V_{34} was lower than previous measurements and V_{24} with subsequent measurements became

positive again and eventually greater than V_{34}, as would be expected. Both V_{24} and V_{34} were much less than when measured in PLL and PEM solutions. Further experimentation must be done to see if this is directly due to MTs. Another experiment to perform would be to apply current pulses between electrode wires to test whether MTs increase the signal between wires, which is possible with the Keithley 4200-SCS used, and similar to the experiment performed by Priel et al. [356].

The voltages reported for each measurement execution are the first of ten measurements as the 1nA current was applied over 4.44s. The V_{24} and V_{34} voltages tended to increase or decrease monotonically over the 10 measurements as the 1nA current was applied and then on the next measurement execution, after the applied current was discontinued for several seconds, reverted to largely the same measurements. This effect must be studied in further detail to determine the effects of charge build-up in the system, induced electro-osmotic and electrothermal flow, and the length of time the system takes to equilibrate with an applied 1nA current.

The measured V_{23}s, corresponding to the PLL, initial PEM, PEM after 28min, and final MTs (82nM tubulin) after 27min solutions (Figure 4.8) are graphed in Figure 4.10. A higher measured voltage corresponds to higher resistivity of the solution. The MT 82nM solution final measured voltage is significantly smaller than the voltage measured by the PLL and PEM solutions (p<0.0001). This implies the resistance in the system has lowered, and must be reproduced to determine if MTs are causing this effect. The effect is consistent to Priel et al.'s report [356] that MTs are able to increase electrical conductivity signals.

116
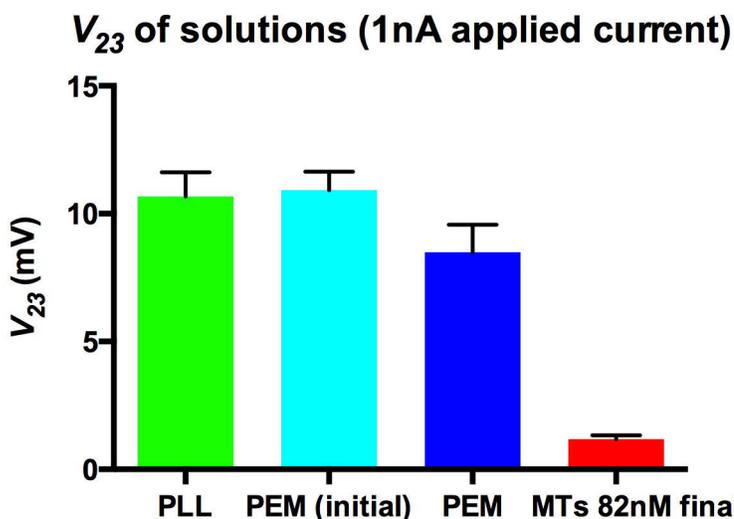
Figure 4.10. Average of the measured voltages using the four point probe measurement system where 1 nA current bias is applied. Error is standard deviation. If replicated, the lower measured voltage observed with MT solution may indicate high ionic conductivity of MTs.

Priel et al's report [356] used 5-10 ms voltage pulses in the range of ±200 mV which led to the evoked current increasing from 1.91 ± 0.13 nA to 2.78 ± 0.17 nA ie. an increase of 0.87nA [356]. I used a 1 nA current bias, which is the same order of current evoked by Prel et al.'s voltage pulse [356], which is useful for comparison between experiments. If MTs are able to increase ionic conductivity, then MTs, which as shown in Figure 4.6 appear to be in contact with the electrical wires, could increase ionic conductivity between the wires, leading to reduced measured voltage when the 1nA current bias is applied. Based on the measured voltage, MTs, which appear to be in contact between electrodes, are able to make the solution 7.2 times as conductive, potentially due to the ionic conductivity properties of MTs. The same experiments proposed to ascertain the V_{24} negative drop upon addition of MTs would apply to understand if ionic conductivity properties of MTs are at play. As previously mentioned, performing pulsed I-V measurements between wires to test whether MTs increase conductivity between wires would be recommended. To test whether the effects seen are unique to MTs, other macromolecules such as SWNTs, and actin could be tested. Voltage measurements of PEM alone without the previous addition of PLL, which contains positively charged polymers, could also be tested to measure the voltage measurement corresponding to the PEM buffer solution alone.

To convert a four-point probe measurement to measure the resistivity of the sample, for an arbitrary shaped sample,

$$\rho = 2\pi s F \frac{V}{I} \tag{1}$$

where ρ is resistivity, s is the length between the probes (10µm), F is a correction factor for probe location near sample edges, for sample thickness, probe width, probe separation, and sample temperature [484]. The correction used for thin samples where the thickness of the layer, t, is much less than the probe spacing, s, i.e. $t \ll s$ leads to the following equation:

$$\rho = \frac{\pi}{\ln(2)} t \frac{V}{I} \tag{2}$$

where V is the measured voltage, and I is the source current (I is 1nA) [484]. I use t as the thickness of the electrodes, 55nm.

As the relative values are most important, Table 1 illustrates the result of the four-point probe experiment in terms of measured voltage, and calculated conductivity, for device EDA. As my experimental setup is different from traditional four-point probe measurements of solid semiconductors, I also use a correction factor to correct to the previous reported conductivity of PEM solution which is 1.08 S/m [376], and the thin sample approximation is only a factor of 2.25 different that this empirical calculation.

Table 4.5. EDA Four point probe conductivity.

4-Point Probe Solution	Mean Measured Voltage, V_{24} (mV)	Conductivity, σ (S/m) (thin sample estimation)	Conductivity, σ (S/m), corrected to PEM reported conductivity
Air (n=3)	283 ± 15	0.014 ± 0.0007	0.03 ± 0.002
PLL (n=5)	10.7 ± 1.0	0.38 ± 0.04	0.85 ± 0.09
PEM (initial) (n=5)	10.9 ± 0.7	0.37 ± 0.02	0.83 ± 0.06
PEM (n=5)	8.5 ± 1.1	0.48 ± 0.07	1.08 ± 0.15
MTs 41nM solution (initial value, n=1)	-37.4	-0.11	-0.25
MTs 82nM solution (final) (n=4)	1.2 ± 0.2	3.4 ± 0.4	7.7 ± 1.00

Voltage drop measured by wires 2 and 3 of EDA device. Conductivity is given as both an approximation using the thin sample approximation, and corrected to known PEM conductivity [376]. Air indicates the flow cell is empty and no solution exists between the

probes. As there is a forced current of 1nA, this result for air would not be considered reliable. Error given is standard deviation.

The result showing that MTs in a physiological-like ionic solution, PEM (~160mM Na$^+$ at pH 6.9 [392]), potentially in direct contact between electrode wires, yields more conductivity than PEM solution, is worthy of further study. The cytosol of cells has similar strong ionic concentrations (~155mM K$^+$) [421], and it is of interest to test whether MTs, in this crowded, structured environment may be propagating fine ionic signals. By inspection, between wires 2 and 3, three MTs appear to make a solid contact between the wires (Figure 4.6A shows two of these MTs). Therefore, a simplified parallel resistor model between wires 2 and 3 can be used to estimate the resistance of a MT (Figure 4.11).
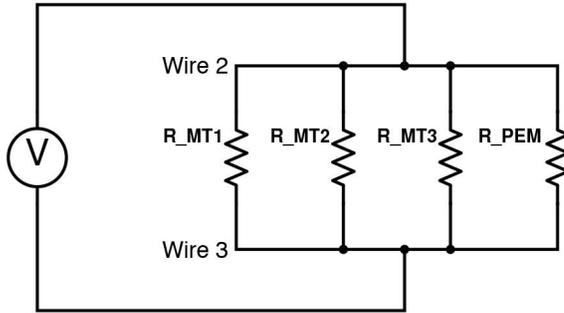
Figure 4.11. Simplified parallel circuit diagram of resistance between wire 2 and 3 of EDA device. There are three MTs making direct contact between wire 2 and 3, each with resistance R_{MT}, and there is the resistance of the buffer solution, R_{PEM}. This model does not take into account the effect of MTs not making direct contact between the two wires (Figure 4.6D).

Using Ohm's Law, with:

$$R = \frac{V}{I}$$

(3)

we assume initially the entire 1nA current is flowing between wires 2 and 3, to get the resistance between wires 2 and 3 for the PEM solution, R_{PEM}, and the final MT solution, R_{eff}. The final MT solution is PEM solution with 3 MTs in contact with the wires in parallel, as shown in Figure 4.11. Therefore:

$$\frac{1}{R_{eff}} = \frac{1}{R_{PEM}} + \frac{3}{R_{MT}}$$

(4)

119

The definition of electrical resistivity, ρ, is:

$$\rho = R\frac{A}{l} \tag{5}$$

where A is the cross-sectional area, and l is the length, and R is the resistance. A_{MT} is 4.9e-16 m^2, using the radius of a MT to be 12.5nm, and l_{MT} is 8.8µm. Conductivity, σ, is:

$$\sigma = \frac{1}{\rho} \tag{6}$$

The conductivity of a MT in ionic solution (intrinsic+ionic), σ_{MT}, is thus calculated to be 4400 S/m, which is an order of magnitude greater than Priel et al. [61, 356], and similar to values suggested by Sahu et al. [61, 347, 375]. The value could be greater than that of Priel et al. [356] due to better electrical contact between the electrode wires and the MTs. Also, Priel et al. [356] measured one MT precisely, while my measurements potentially are measuring a bulk effect of multiple MTs, which might explain the difference. The value is lower than the theoretically predicted value of between 18,000 to 160,000 S/m with favourable assumptions towards conductivity [341]. However, the value is much higher than the conductivity values reported with indirect methods, which give conductivities in the order of 0.15 to 0.25 S/m [368, 369].

4.2.2.2 Resistance effects of MTs in solution: 2 Electrode EDB resistance

In most devices, such as EDB 1-7 (shown in Figure 4.3), the fine 3 µm wires were not fabricated correctly, giving instead a region (Figure 4.5D) of two electrodes, 30µm wide, separated by 14µm, which we refer to as EDB 1-7 (see Figure 4.3). A bright-field image of EDB 4 (Figure 4.12A), shows the distance between the 30 µm wide electrodes to be 14µm, as predicted by the design. Of the nine locations for flow cells, six had usable electrode wires, and flow cells were created in these six locations (see Figure 4.3 and Figure 4.4). Preliminary experiments were performed using EDB 5-7, and then an experiment (n=4) was performed on EDB 1-4 (see Figure 4.3).
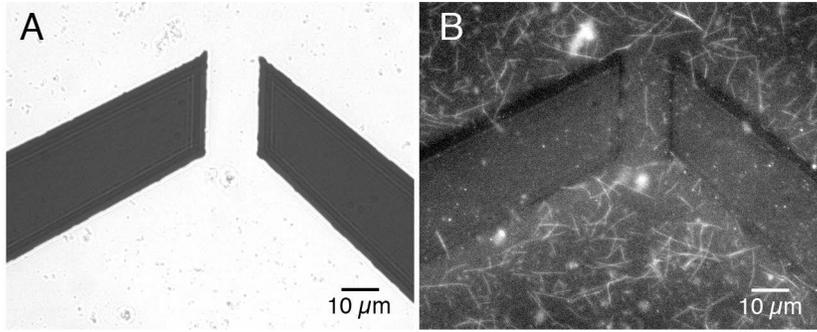
Figure 4.12. EDB 4, 40x image, taken with bright-field and red fluorescence (Cy3). (A) Bright-field image of EDB 4. The distance separating the electrodes is 14μm, consistent with the Matlab design in Figure 4.5C without the fine wires patterned. (B) Red fluorescence image (Cy3), showing MTs adhered to PLL on substrate surface. Electrodes are 55nm high, and not many MTs adhere to the electrode, probably because PLL does not adhere to Pt.

Two concentrations of rhodamine-labeled MTs were prepared (41nM and 82nM) in PEM (MT buffer solution). PLL in PEM (0.1 mg/ml) was introduced into the flow chamber as it is used to coat the flow chamber glass substrate, and MTs stick to the PLL coating, due to PLL's positively charged binding sites, and I-V characteristics were measured. Then PEM was flushed through the flow cell to remove any unadsorbed PLL in the flow cell, and I-V characteristics where again measured. Then MTs at 41nM were introduced, and I-V characteristics measured. Then MTs at 82nM were introduced, and I-V characteristics measured. These resistance measurements were performed on four EDA devices. Then the devices were imaged using fluorescence and bright-field microscopy in a separate facility. Figure 4.12B shows MTs, which appear to be adhered to PLL on the substrate surface as while imaging, the MTs did not move. Electrodes are 55nm high, and not many MTs appear adhered to the electrode, in contrast to EDA (Figure 4.6A). All EDB devices are shown in Figure 4.13 at 10x. At this resolution, and depending on the focus employed, MTs are not clearly visible, but they are present as they can be most clearly seen over the Pt wires. All EDB devices are also shown in Figure 4.14 at 40x. An improper focus was used to image EDB 1-3, and so the state of MTs adhered to the substrate in the interface between the electrodes is not known for certain. However, from this image (Figure 4.14) it appears that MTs are sparse between electrodes in EDB 2 and 3, and plentiful between electrodes in EDB 1 and 4. As there is a 14 μm gap between the

electrodes, it is doubtful that there is a solid connection of an MT across the electrodes. Nevertheless, we test if MTs in solution have an effect on the resistance of the solution.
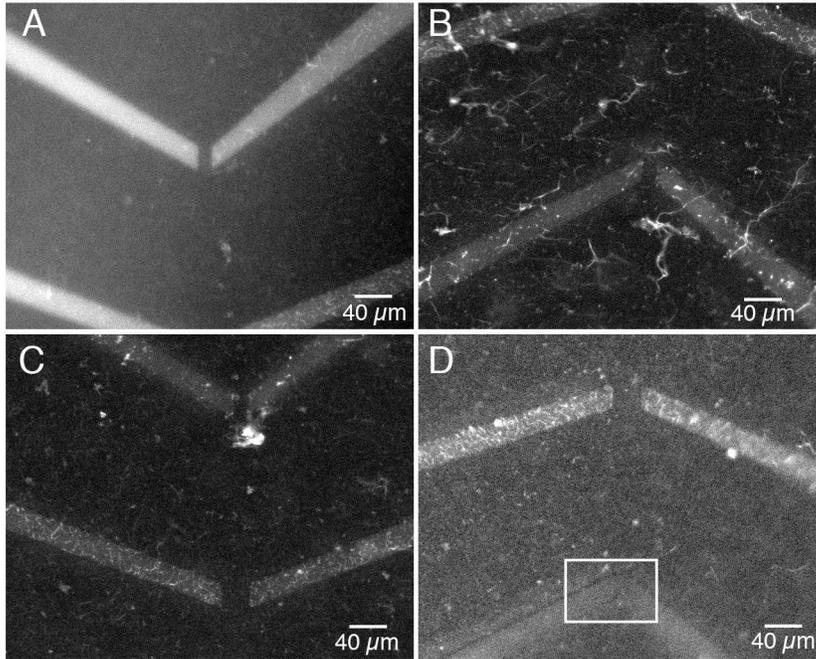
Figure 4.13. All EDB devices at 10x with red illumination (Cy3). At this magnification, MTs are difficult to observe. However, they can be seen above the Pt wires. (A) EDB 1. (B) EDB 2. (C) EDB 3. (D) EDB 4. The equivalent 40x image of the region indicated by the rectangle can be seen as Figure 4.12B.
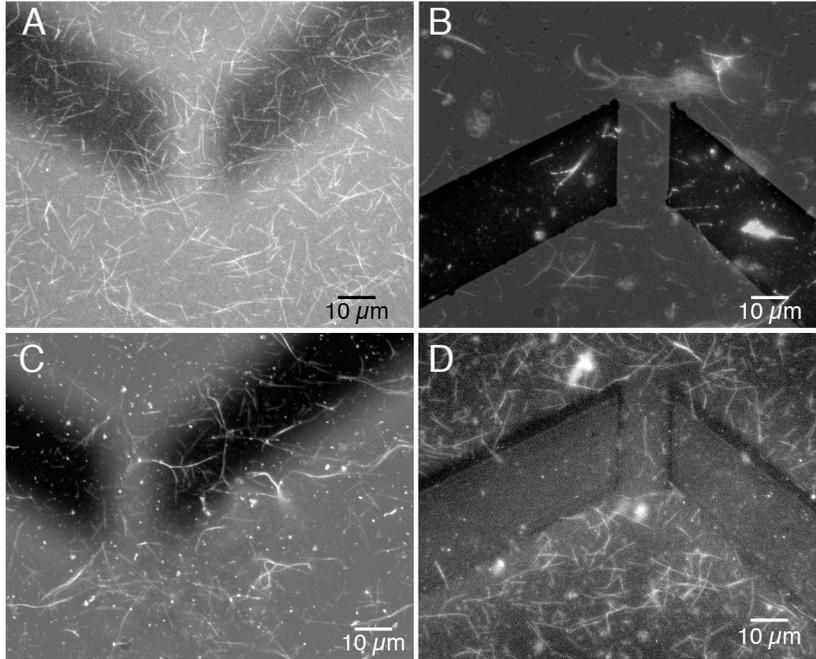
Figure 4.14. All EDB devices at 40x. Figures (A)-(C) are overlay images of 40x image using red (Cy3) and bright-field illumination. These images are not exactly focused on the electrodes; therefore the MTs seen may not be attached to the device surface. (A) EDB 1. (B) EDB 2. MTs do not seem to be plentiful in this region, but this may be due to focus. (C) EDB 3. MTs do not seem plentiful in this region, but with faintly seen MTs, this may be due to focus. (D) EDB 4 is image is exclusively from red fluorescence (Cy3), and in focus with the electrodes.

Multiple voltage sweeps were performed on each device over time, with the current plotted as a function of voltage. The slope of this plot is equivalent to the conductance following Ohm's Law, where G is conductance:

$$G = \frac{1}{R} \tag{7}$$

That is:

$$G = \frac{I}{V} \tag{8}$$

where G is conductance, I is current, and V is voltage.

The results of the voltage sweeps on EDB devices 1-4 for PEM and MT 82nM solutions are displayed in Figure 4.15. To explore the large error in PEM solutions for data points above 0V, the individual voltage sweeps are investigated. Figure 4.16 shows EDB 1-4 PEM solution individual voltage sweep results. Typically, measurements taken within 10s of each other are similar with slightly higher current measured at the final data

point of 1V applied (Figure 4.16 (E)-(H)). This could be due to increased charge carriers attracted to the region, or electrothermal effects [486]. EDB 2, 3, and 4 PEM I-V data shows unexpected negative slops (Figure 4.16 (B)-(D)). This may be due to charge accumulation at the electrodes, as the current applied was direct current (DC). To test this, applying alternating current (AC), similar to that done with electrical conductivity meters, would be recommended to be applied to counter the effect of charge accumulation.

EDB 1: PEM voltage sweep (n=12)

A

EDB 1: MT 82nM voltage sweep (n=12)

E

EDB 2: PEM voltage sweep (n=21)

B

EDB 2: MTs 82nM voltage sweep (n=7)

F

EDB 3: PEM voltage sweep (n=24)

C

EDB 3: MT 82nM voltage sweep (n=11)

G

EDB 4: PEM voltage sweep (n=36)

D

EDB 4: MT 82nM voltage sweep (n=11)

H

Current (μA)

Applied Voltage (V)
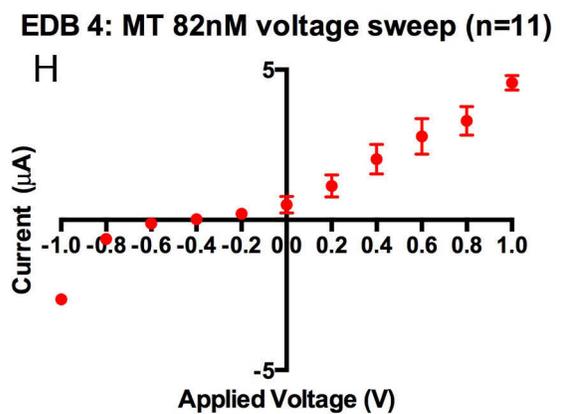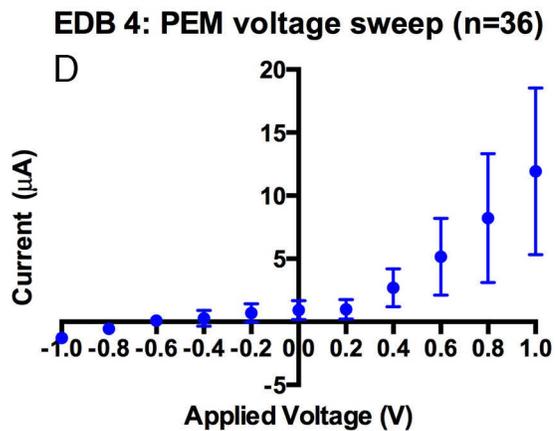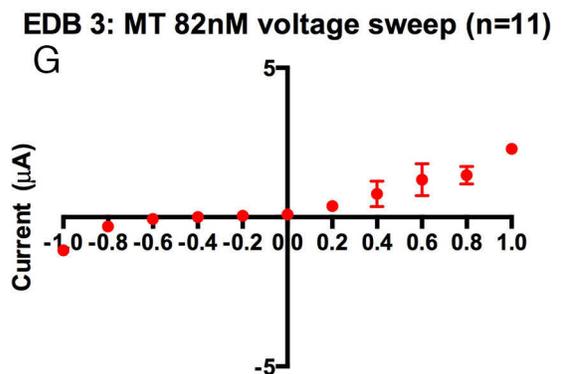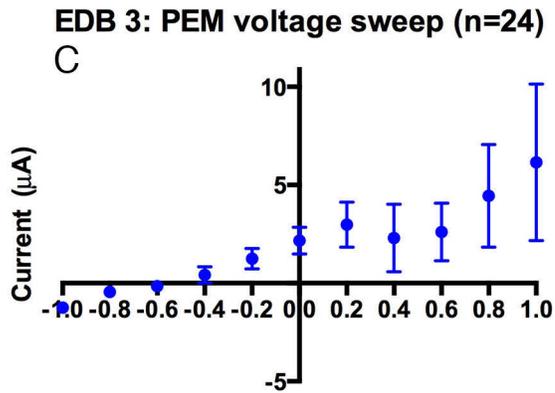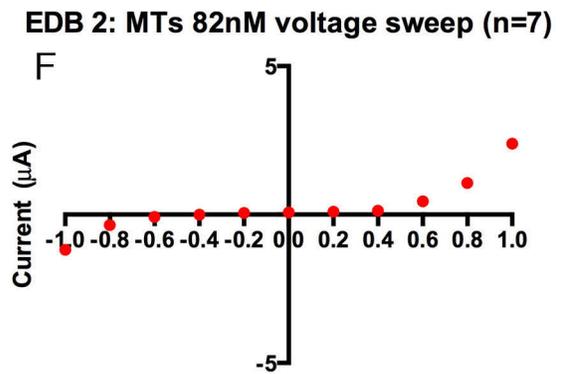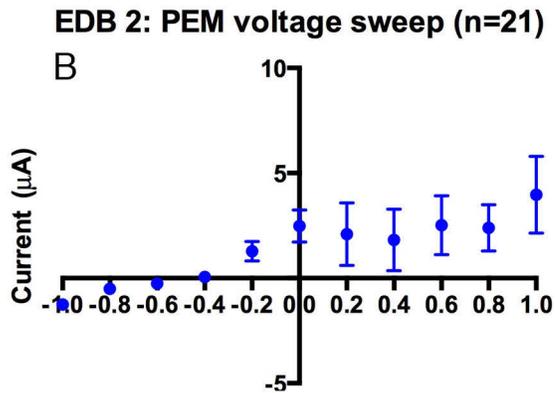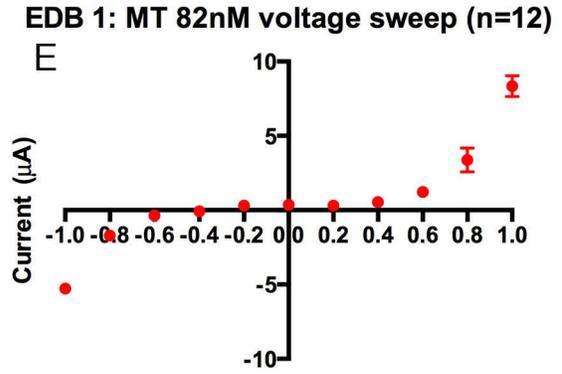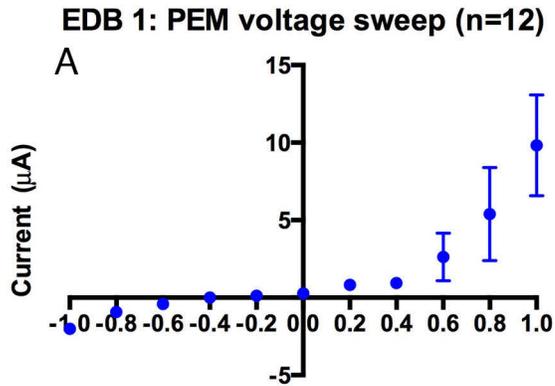
Figure 4.15. Multiple I-V voltage sweeps (±1V, 0.2 step size) of PEM and MT 82nM solutions in EDB devices 1-4. The I-V curves were nonlinear. (B) and (C) show unexpectedly negative slopes in the 0.0 – 0.6V range.

EDB 1: PEM voltage sweep (n=12)

A

EDB 1: PEM current vs time (1V applied)

E

EDB 2: PEM voltage sweep (n=21)

B

EDB 2: PEM current vs time (1V applied)

F

EDB 3: PEM voltage sweep (n=24)

C

EDB 3: PEM current vs time (1V applied)

G

EDB 4: PEM voltage sweep (n=36)

D

EDB 4: PEM current vs time (1V applied)

H
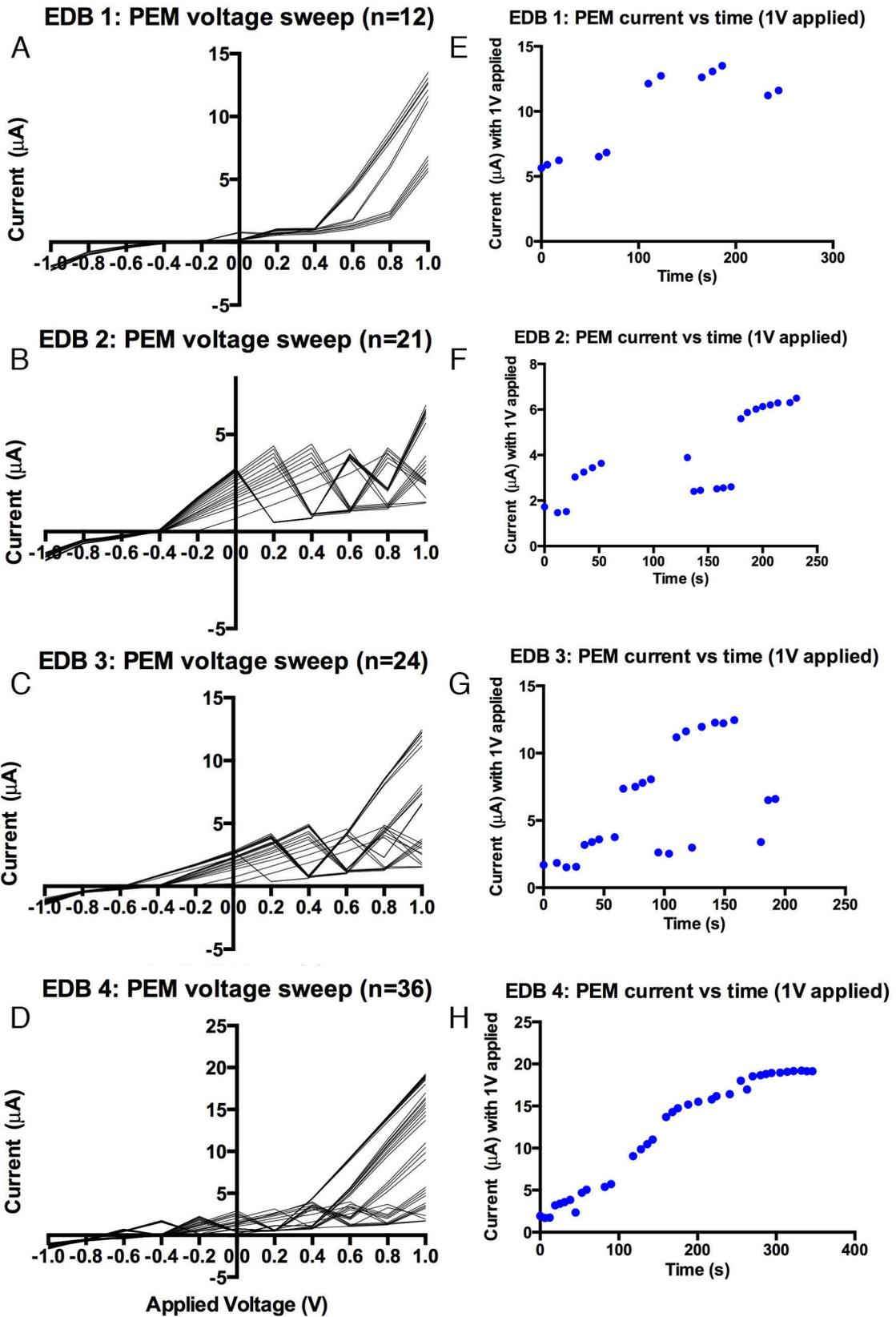
Figure 4.16. (A)-(D) Individual voltage sweeps of EDB devices 1-4 with PEM solution. (E)-(H) The current measured when 1.0 V applied is plotted over the time of the voltage sweep measurements, in order to visualize how the voltage sweeps are changing over time. As time goes on, the critical voltage applied that results is a large increase in conductance (large positive slope in (A)-(D)) changes from 0.8V to -0.4V.

The results of the voltage sweeps on EDB devices 1-4 for PLL and MT 41nM solutions are displayed in Figure 4.17. To explore the large error in the PLL solutions for data points above 0V, the individual voltage sweeps are investigated (Figure 4.18). The trend is the same as with the PEM data. Over time, the critical voltage after which a large linear slope appears (high conductance) becomes smaller. Eventually, there appears to be a current (~4-5µA) after which a negative slope appears, potentially due to charge accumulation.

As well, the voltage sweeps showed non-symmetrical plots about the y-axis, where in absolute value, current measured with negative voltage was less than that using positive voltage. This effect was more apparent for solutions without MTs (Figure 4.15 and Figure 4.17). This could be a result of a DC sweep from negative voltage to positive voltage. Sweeping back from positive voltage to negative voltage (cyclic voltammetry) would be recommended to test this, as well as using AC frequency in the 1-3kHz range similar to electrical conductivity meters.

EDB 1: PLL voltage sweep (n=9)

A

EDB 1: MTs 41nM voltage sweep (n=10)

E

EDB 2: PLL voltage sweep (n=18)

B

EDB 2: MTs 41nM voltage sweep (n=13)

F

EDB 3: PLL voltage sweep (n=21)

C

EDB 3: MTs 41nM voltage sweep (n=8)

G

EDB 4: PLL voltage sweep (n=12)

D

EDB 4: MTs 41nM voltage sweep (n=13)

H
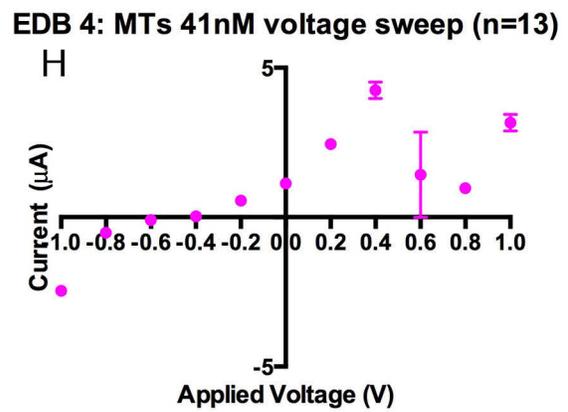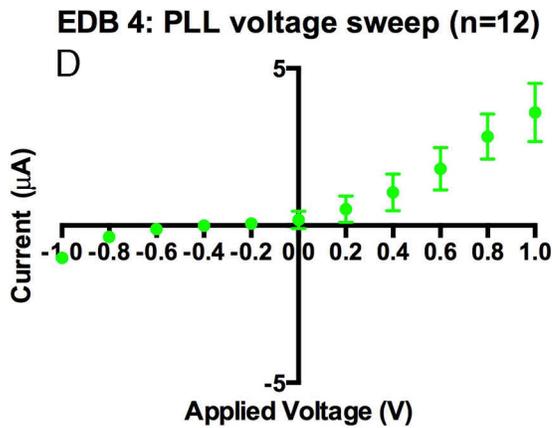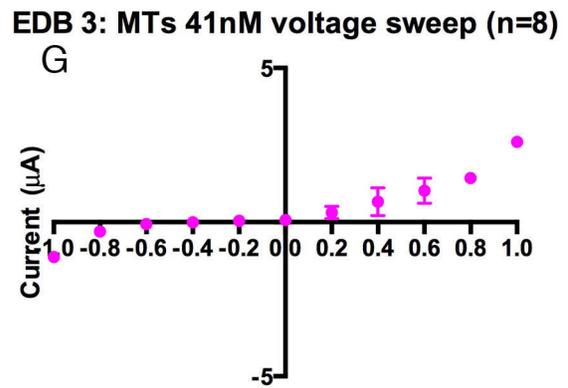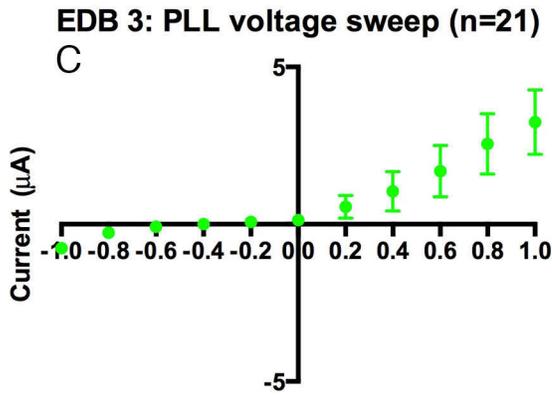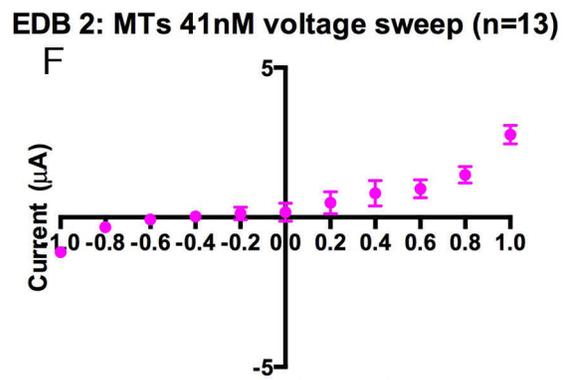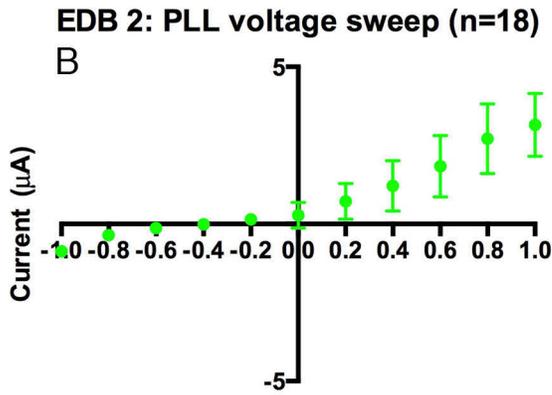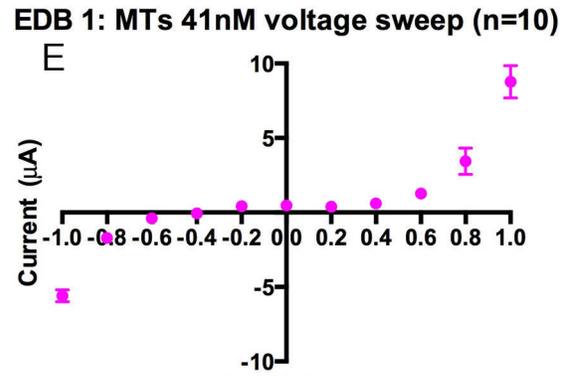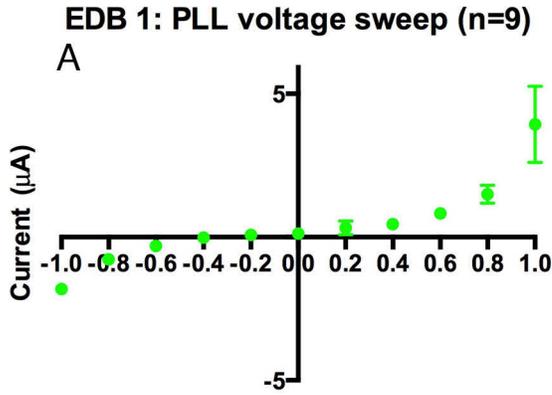
Figure 4.17. Multiple I-V voltage sweeps (±1V, 0.2 step size) of PLL and MT 41nM solutions in EDB devices 1-4. The I-V curves were nonlinear. (H) showed unexpectedly negative slopes in the 0.4 – 1.0 V range.
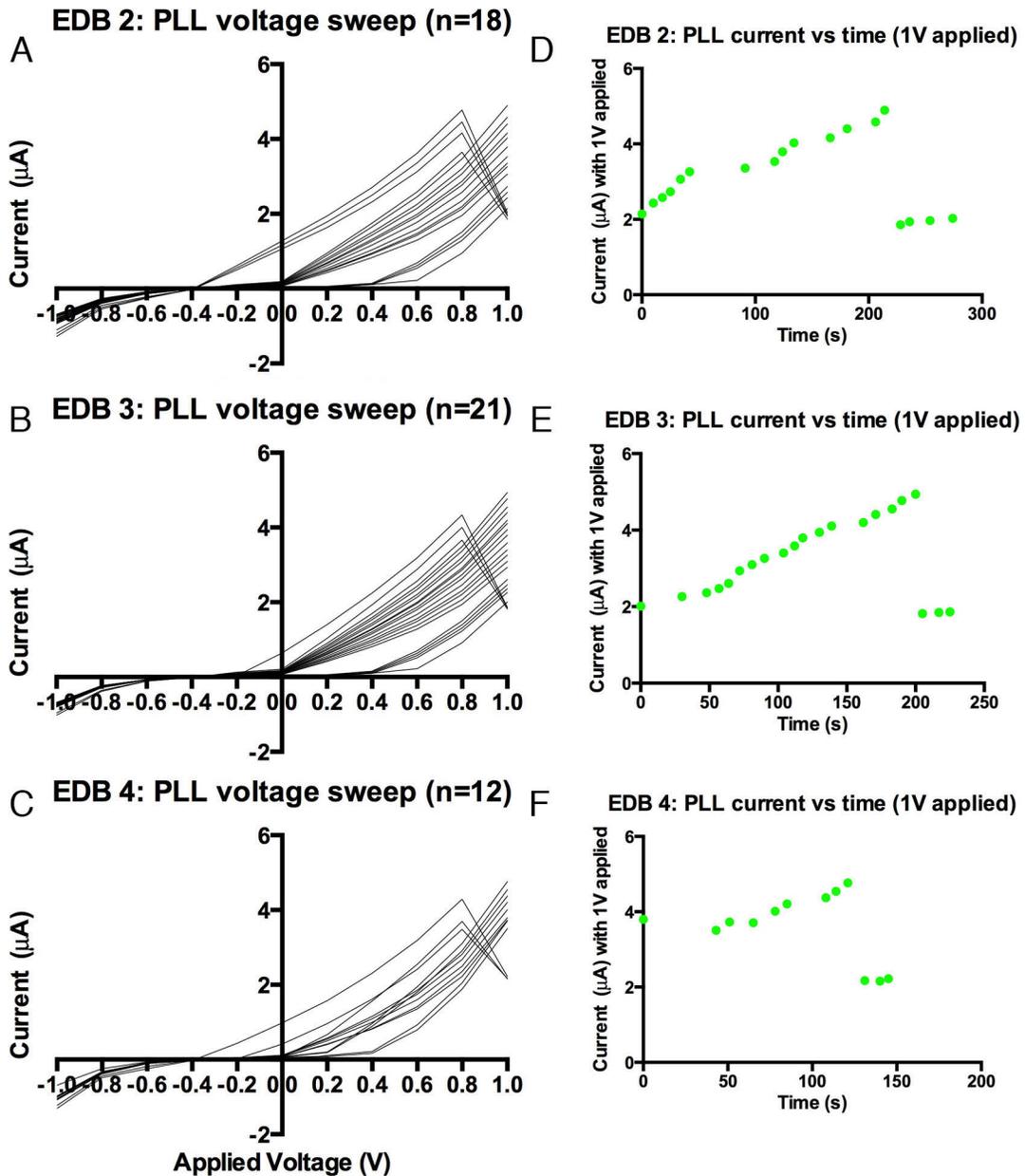
Figure 4.18. (A)-(C) Individual voltage sweeps of EDB devices 2-4 with PLL solution. (D)-(F) The current measured when 1.0 V applied is plotted over the time of the voltage sweep measurements, in order to visualize how the voltage sweeps are changing over time. As time goes on, the critical voltage applied that results is a large increase in conductance (large positive slope in (A)-(C)) changes from 0.6V to -0.4V.

The I-V plots are summarized in Figure 4.19, with a common vertical axis, so that comparisons between the solutions can be seen. The I-V relationship was not linear (ie. not ohmic). The variability between devices appears smallest with the PLL solution, which makes sense as this is the first solution introduced into the flow cell. The variability of PEM devices increases as the voltage sweep progresses from negative voltage to positive voltage (Figure 4.16), which may as well be indicative of charge accumulation on the electrodes. This underscores the need in future experiments to use alternating current to mitigate charge build-up effects. Overall, PEM solution appears most conductive, while PLL solution and MT solutions appear similar. This suggests that both PLL and MTs interfere with ionic conductance especially in the 0-1V range. The variability with MT solutions may be due to altered number and orientation of MTs in measurement area.
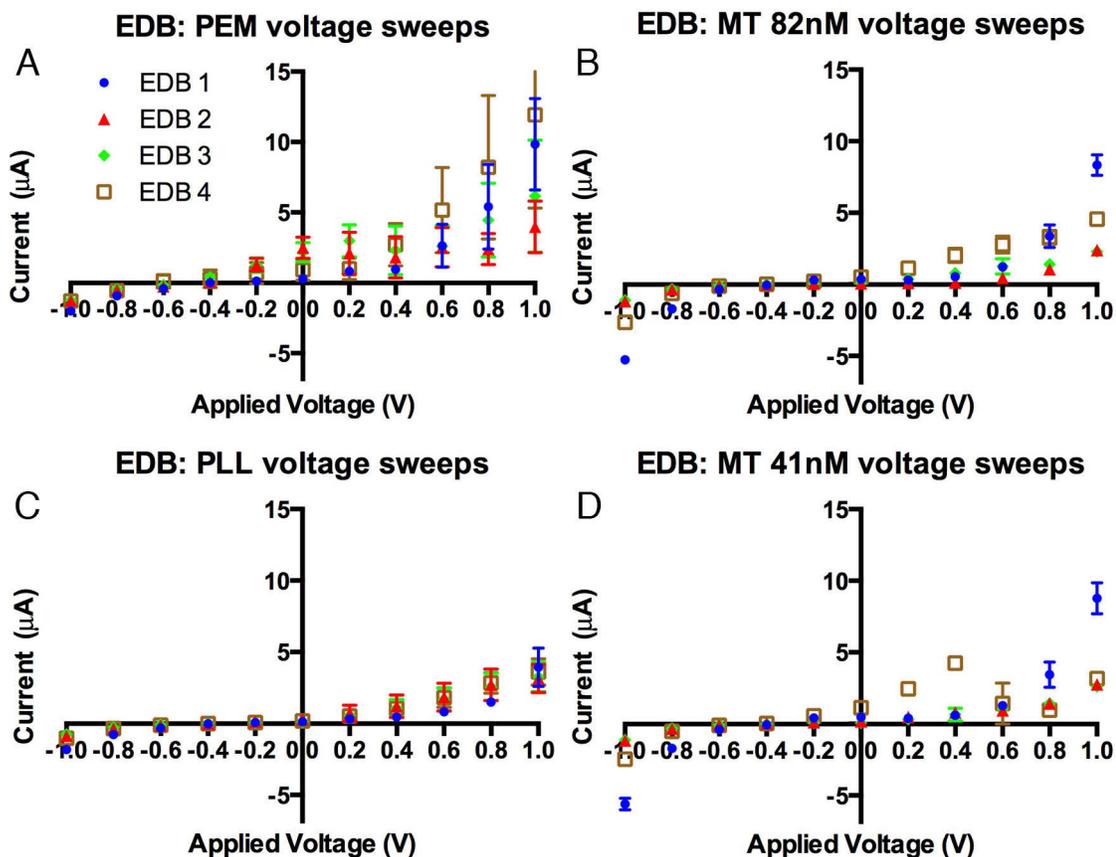
Figure 4.19. Grouped summary of voltage sweep plots of solutions for EDB devices. (A) PEM solution voltage sweeps. (B) MT 82nM solution voltage sweeps. (C) PLL solution voltage sweeps. (D) MT 41nM solution voltage sweeps.

The region from -0.6 V to 0 V was close to linear (ohmic) in all devices, and included the equilibrium voltage, which is the voltage where the current was 0 µA, ie. the x-intercept [376]. To estimate the conductance at this equilibrium voltage (similar to [376]), we estimate the slope of the I-V curves as the linear regression of the -0.6 to 0 V points (4 points) (Figure 4.20). In essence, voltage sweeps where added voltage does not increase the current dramatically have lower conductance, so a flatter slope in the voltage sweep curves is a reported lower conductance. In EDB 2 and 3, PEM solution appears to be the most conductive, and solutions with PLL and MTs tend to have less conductance. In EDB 1, MTs may facilitate conductance, and in EDB 4, MTs seem to have similar conductance than PEM but more than PLL. Inspecting the devices (Figure 4.14) indicated that MTs likely are more prevalent and potentially making better contact between electrodes in EDB 1 and 4, consistent with the hypothesis that they facilitate conductance at low current, as supported by data in 4.2.2.1.

Figure 4.20. Conductance of PLL, PEM, MT 41nM and MT82nM solutions using linear regression of points of voltage sweeps from -0.6 to 0V (conductance is the slope of a linear I-V plot). EDB devices did not see significant increased conductance in this range, and in EDB 2 and 3 seemed to reduce conductance. There is large variability in the devices in PEM, potentially due to charge buildup effects with DC applied and time dependence of measurements seen. Large variability with MT solutions may be due to altered number and orientation of MTs in measurement area.

The mean conductance and standard deviation of the four solutions in the flow cell for the four flow cells is reported in Figure 4.21. The standard deviation is too large to reveal any definitive conclusions from this experiment. To improve this experiment, the voltage sweeps would contain more data points (step size 0.01V, and 0.001V for voltages less than 20mV and around the equilibrium voltage), and AC current and forward and backward DC sweeps would be done. The large variability in PEM data, as seen in Figure 4.16, is after the -0.6V data point. This suggests that AC is important especially for results in simple buffer solution (PEM). The variability of conductance of solutions with MTs may be due to numbers and placement of adhered MTs between the electrodes, if indeed MTs have an effect. As well, testing a solution of unpolymerized tubulin (that has not formed MTs) would be useful as a control, to see whether there is a different effect of tubulin (the building blocks of MTs) vs. MTs on solution conductivity.

Conductance between electrode 2 and 4 (-0.6 to 0 V)
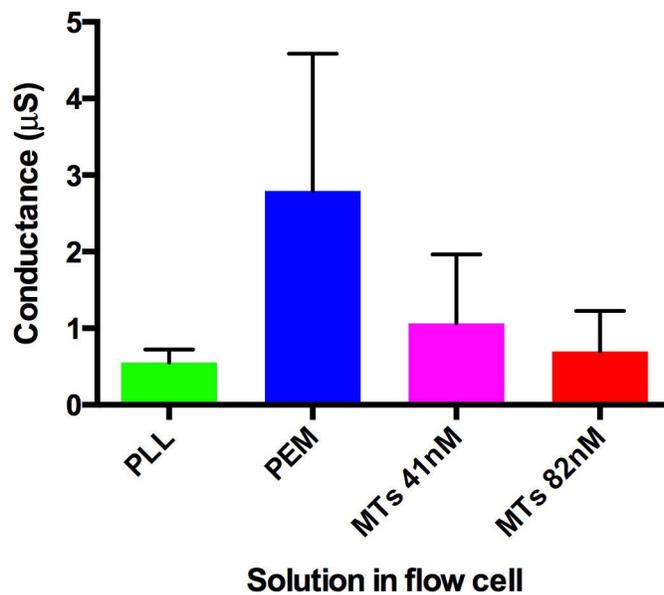
Figure 4.21. Mean conductance of the various solutions between electrode 2 and 4 of EDB devices (14 μm spacing), from results in Figures 10 and 11 (n=4). Error is standard deviation. There was a large variability of results between EDB devices, indicating improvements are needed for experiments with EDBs.

Table 2 presents the conductance results and the equivalent conductivity, assuming a simplified model of the standard equation (Pouillet's Law):

$$G = \sigma \frac{w \bullet h}{l} \qquad (9)$$

where G is conductance, σ is conductivity, l is length between the electrodes, w is the width of the electrodes, and h is the height of the electrodes. In the case of our system, we take $l = 14$ μm, $w = 30$ μm, and $h = 55$ nm. This simplified model is not entirely accurate as the ionic solution is not limited to being between the two electrodes. Accurate conductivity measurements of solutions are typically done by measuring AC resistance 1-3 kHz range, used primarily in order to avoid effects of ion charge build-up, and then correcting to solutions of known conductivity. Table 2 also scales the conductivity result to the reported conductivity of PEM, 1.08 S/m [376].

Table 4.6. Mean conductance, and corresponding conductivity of four 2 electrode device systems.

2 Electrode	Conductance (μS)	Conductivity (S/m) Pouillet's Law	Conductivity (S/m) Corrected to known conductivity of PEM
PLL	0.6 ± 0.2	4.7 ± 1.5	0.2 ± 0.1
PEM	2.8 ± 1.8	23.7 ± 15.2	1.1 ± 0.7
MTs 41nM solution	1.1 ± 0.9	9.0 ± 7.6	0.4 ± 0.4
MTs 82nM solution	0.7 ± 0.5	5.9 ± 4.5	0.3 ± 0.2

The calculations of conductivity are calculated using Pouillet's Law and should not be taken as absolute. A correction factor is also applied to correct to the reported conductivity of PEM solution, 1.08 S/m [376]. Error is standard deviation. Additional data is required to reduce the error in conductance calculations to obtain statistical significance.

The results suggest at higher voltages MTs decreases the conductance of the buffer solution in this system where MTs likely do not make electrical contact between electrodes. There are several possible explanations for this.

Hypothesis 1: MTs adsorb ions, leaving less charge carriers to freely flow between electrodes.

As an analysis of this possibility, our solution contained MTs made up of 41 nM tubulin, followed by 82nM tubulin. As a calculation of how many ions MTs could adsorb, tubulin has a negative charge of 47e per dimer [392] at pH 6.9 (that of PEM). After counter-ion screening, its effective charge is negative 23e per dimer [392]; thus it traps 24e positive charges. As an upper bound, with 41+82 = 123nM tubulin, the positive

charges trapped are 3.0 µM. In PEM, there is approximately 160mM Na+ at pH 6.9 [392] and ~2 mM Mg^{2+}, and thus the trapped ions are expected to be less than 1/1000 of the total ions. Therefore, this explanation does not seem very plausible. To test this, subtilisin-treated MTs, which are able to have the negatively charged C termini removed, could be used, as these MTs would have less charge (although the removal of C termini may as well affect the ability of MTs to adsorb onto the PLL coating).

Hypothesis 2: MTs attached to the substrate physically impede charge carriers.

As shown in Figure 4.12B, MTs may be adhered onto the substrate surface between electrodes, where the strongest electric field strength will be when voltage is applied [369], and around the electrodes. The electrode height is 55nm and MT height is ~25nm with possible C-terminal tail of the MT extending another 4-5nm. Thus, 45-55% of the cross-sectional area of the electrodes may be blocked. This might explain the decrease in conductance. This could be tested by replacing the addition of PLL with casein, which has the opposite effect of ensuring MTs do not stick to the glass substrate [392]. If a decrease in conductance is still detected, this might favor hypothesis 1 as an explanation.

Hypothesis 3: Free tubulin in solution may interfere in a similar way as PLL with free-flowing charges.

The impact of MT solution was similar to that of PLL in voltage sweep data. The MT solution contains free tubulin, which has a similar molecular weight as PLL, around 110kDa. These proteins may similarly interfere with free-flowing charge, and MTs may not have an effect at all. This could be tested by adding a solution of free tubulin as a control after PEM to test the effect of free tubulin versus MTs.

4.2.2.3 Resistance effects of MTs in solution: 2 Electrode EDA resistance

From imaging EDA, which has five 1.5µm wide wire electrodes, MTs appeared to make connections between wires 1 to 5 (Figure 4.6). Four-point probe measurements indicated when 1nA was applied from wire 1 to 4, the voltage drop was lower (and initially negative) between wire 2 and 3 when MTs were present, and typically in the 10mV range (Figure 4.7), indicating MTs may increase ionic conduction similar to Priel et al. [356] who found increased ionic conduction using 100mV pulses. Additionally, voltage sweeps were performed, with voltage in the ±1V range and with the lowest voltage applied being 200mV.

As detailed in 4.2.2.1, PLL in PEM (0.1 mg/ml) was introduced, and I-V characteristics were measured. Then PEM was flushed through the flow cell to remove any unadsorbed PLL in the flow cell, and I-V characteristics where again measured. Then MTs (41nM) were introduced, and I-V characteristics measured. Then MTs (82nM) were introduced, and I-V characteristics measured. Then MTs were imaged following I-V measurements in a separate facility. The flow cell was brought back to the probe station for further characterization. I-V characteristics were measured of the MT (82nM) solution, which we refer to as measurements of the MT (82nM) post-image solution; however, it was unclear if the MT (82nM) post-image solution remained completely surrounding the electrodes in the flow cell, due to evaporation or leakage. Therefore, a second injection of MT solution (82nM), which I refer to as MT (82nM) x2 solution, was added into the flow cell and I-V characteristics were measured.

The results of these voltage sweeps are reported in Figure 4.22 and Figure 4.23 and Figure 4.24. The voltage sweeps were predominantly between adjacent wires and between wires 2 and 4, where the large 30μm wide electrodes are only 14μm apart (Figure 4.6C). The voltage sweeps with the EDA device with MT solutions commonly had an outlier at 0.4V, 0.6V and/or 0.8V, with a measured current in the voltage sweep less than that of the previous data point and 1.0V (similar to Figure 4.17H). Figure 4.15B and Figure 4.15C for voltage sweeps of PEM also had outliers at 0.4V and 0.6, so these outliers are not exclusive for MTs. Thus voltage sweeps with a smaller step size, such as 0.01 V, as well as additional data points in the 100mV range would be recommended in future experiments. Analyzing the large standard deviation of EDA PEM current between wires 2 and 4 (Figure 4.22D), showed that after a critical voltage applied, the conductance became large and linear, and this critical voltage decreased over time (Figure 4.25). This conductance was over 20 μS, and was the largest conductance measured in all EDB and EDA voltage sweep measurements.
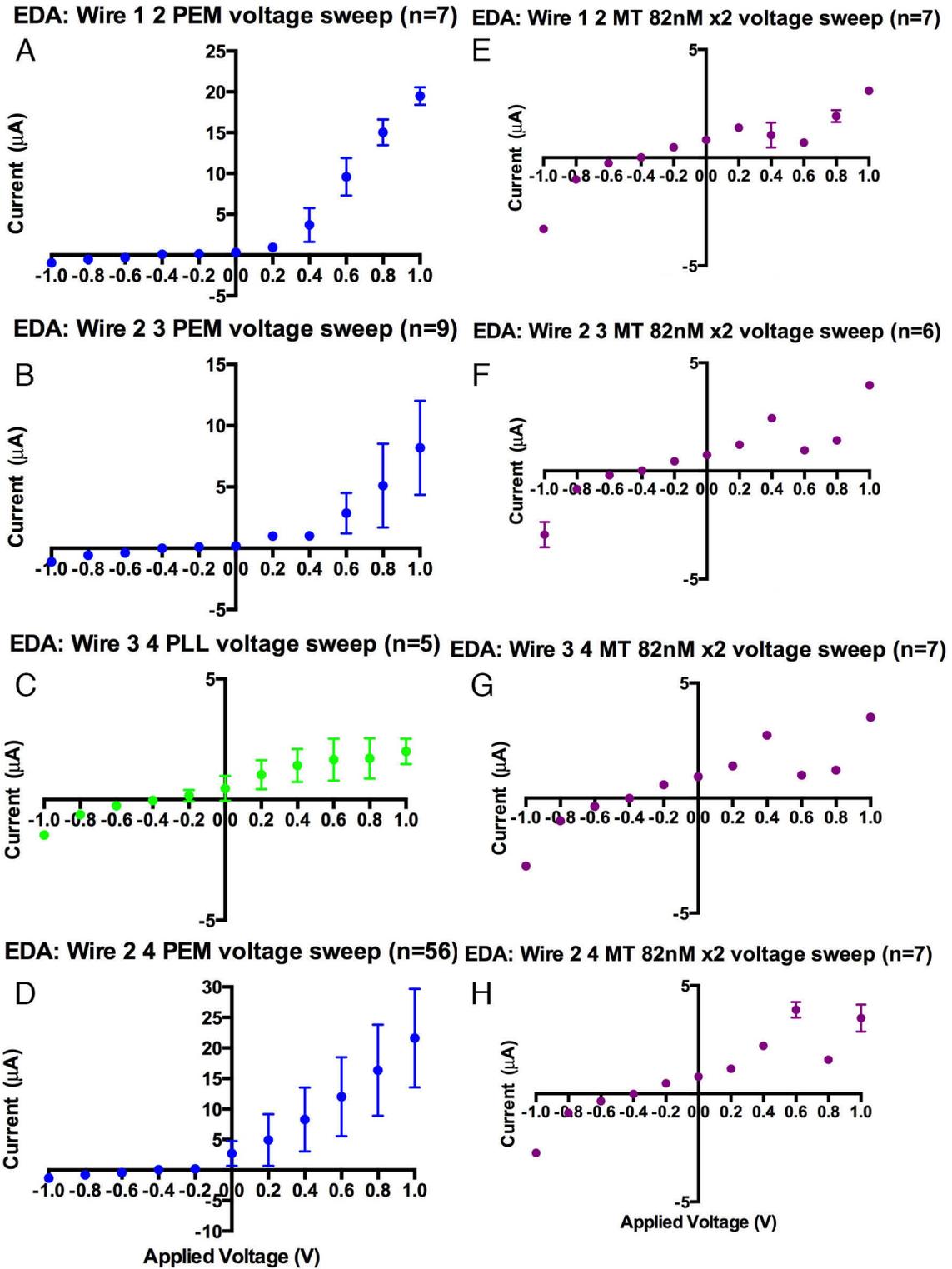
Figure 4.22. I-V voltage sweeps (±1V, 0.2 step size) of PEM (and PLL) and a second infusion of MT 82nM solution in EDA device. The I-V curves were nonlinear. All MT 82nM solutions (E)-(H) showed unexpected negative slopes in the 0.2 to 1.0 V range.

Wire 3 4 PEM voltage sweep was not taken, and so wire 3 4 PLL voltage sweep, done prior to PEM and MT solution addition, is shown in (C).
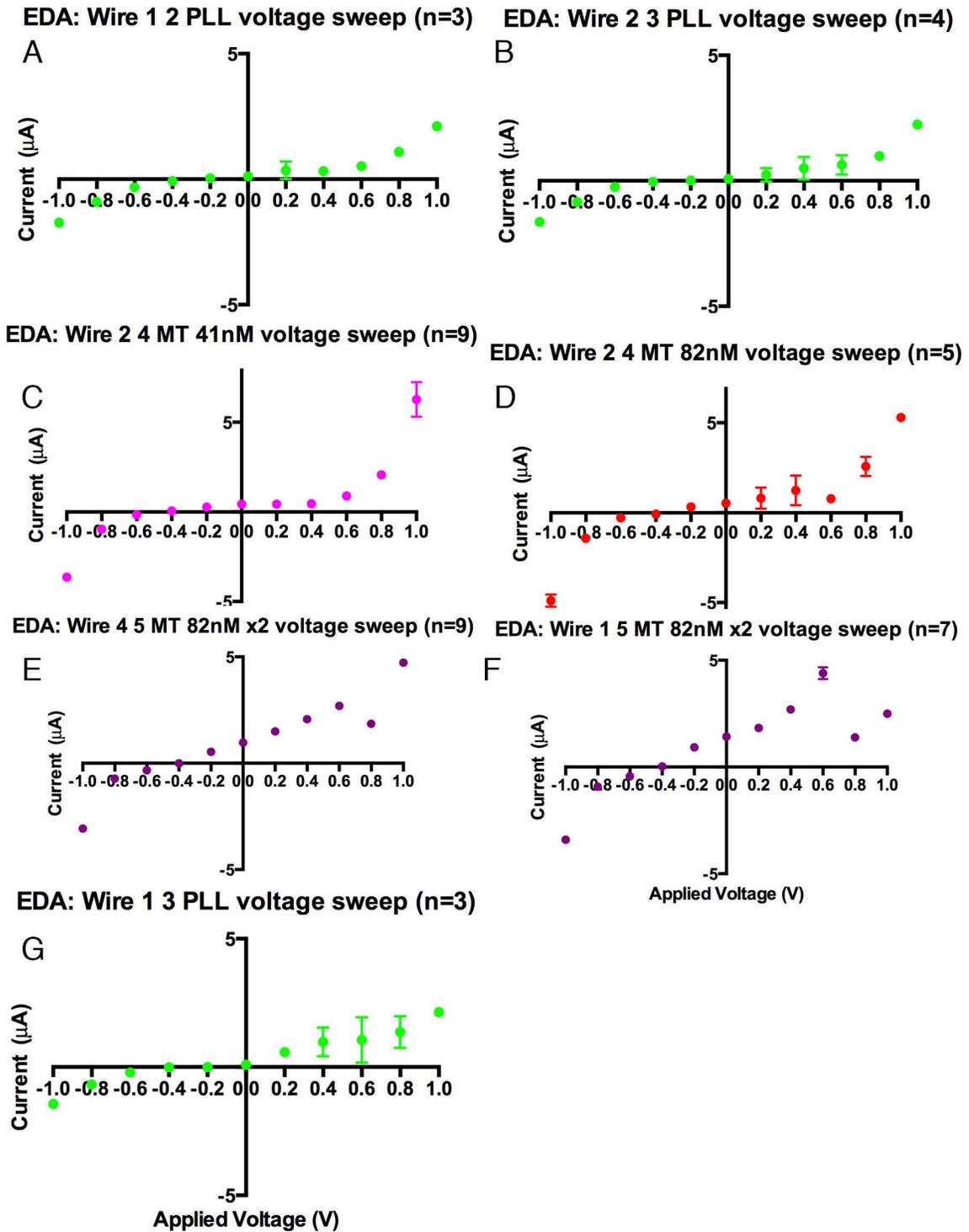
Figure 4.23. Additional I-V voltage sweeps (±1V, 0.2 step size) of PLL in adjacent wires, and between wires 1 and 3, and the initial infusion MT 41nM and MT 82nM solution in EDA device, and of a second infusion of MT 82nM solution in EDA device. The I-V

curves were nonlinear. (D), (E), and (F) showed unexpectedly negative slopes at either 0.6 V or 0.8 V.
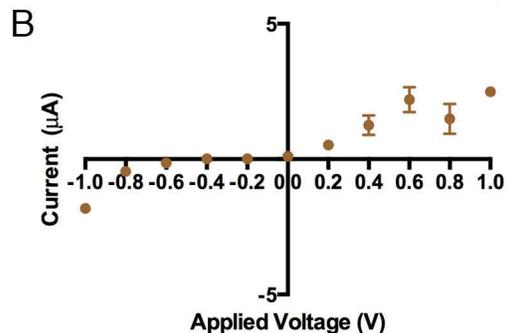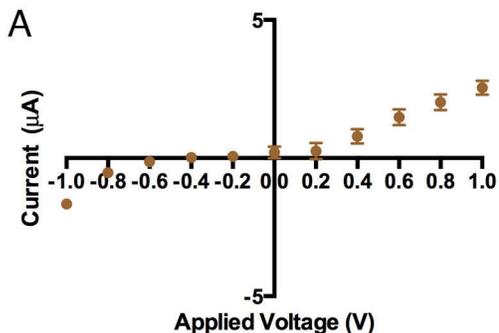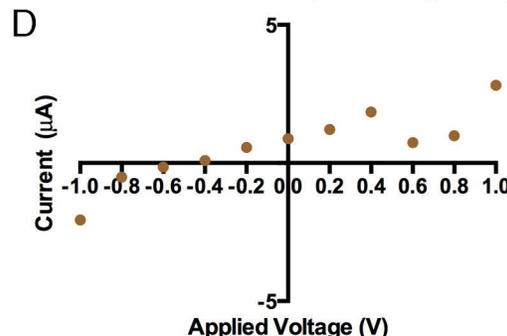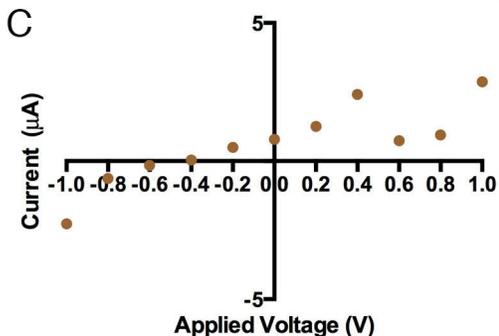
Figure 4.24. I-V voltage sweeps (±1V, 0.2 step size) of the MT (82nM) solution after imaging. It was unclear if the MT (82nM) post-image solution remained completely surrounding the electrodes in the flow cell, due to evaporation or leakage. The I-V curves were nonlinear. (B), (C), and (D) showed unexpectedly negative slopes at 0.6 V and/or 0.8 V.
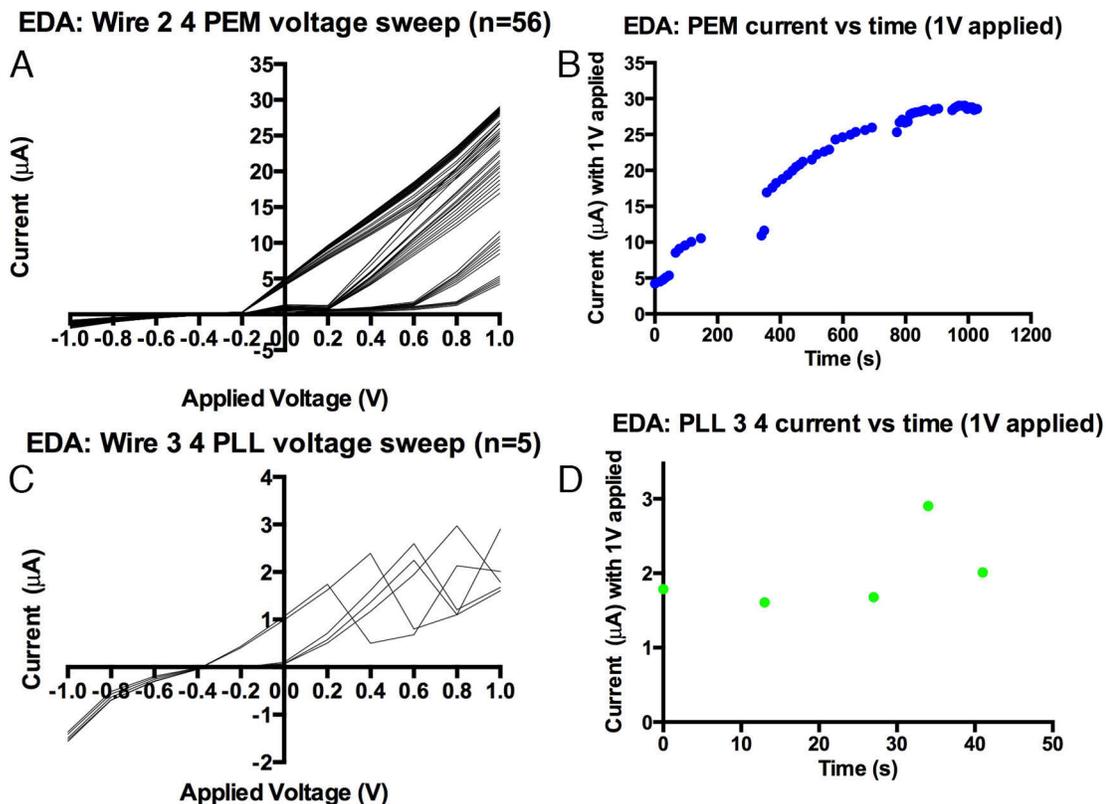
Figure 4.25. (A) Individual voltage sweeps of EDA device with PEM solution between wires 2 and 4, which is the setup design in Figure 4.5D and imaged in Figure 4.6C. (B) The current measured when 1.0 V applied is plotted over the time of the voltage sweep measurements, in order to visualize how the voltage sweeps are changing over time. As time goes on, the critical voltage applied that results is a large increase in conductance decreases from 0.8V to -0.2V. (C) Individual voltage sweeps of EDA device with PLL solution between wires 3 and 4. (B) The current measured when 1.0 V applied is plotted over the time of the voltage sweep measurements, in order to visualize how the voltage sweeps are changing over time. As time goes on, the critical voltage applied that results is a large increase in conductance decreases from 0V to -0.4V.

Summary I-V curves for PLL, PEM, and MT solutions are given (Figure 4.26). At a critical voltage above 0V, PEM conductance is highest of the three solutions, over 20 µS (Figure 4.25). The conductance of PEM between wires 2 and 4 (Figure 4.26A, red), which is the setup shown in Figure 4.6C, and similar to the EDB devices (Figure 4.12) was highest of all measurements taken in both EDA and EDB devices after a critical positive voltage applied. This would make sense if unimpeded ionic conduction was dominant between the large electrodes 30µm wide and an intermediate wire in between (Figure 4.5D). In measurements between adjacent wires, by contrast, the 30µm wide

electrodes are separated by over 150μm, and so bulk ionic conduction effects may not be as dominant, leading to less conduction between adjacent wires in PEM.
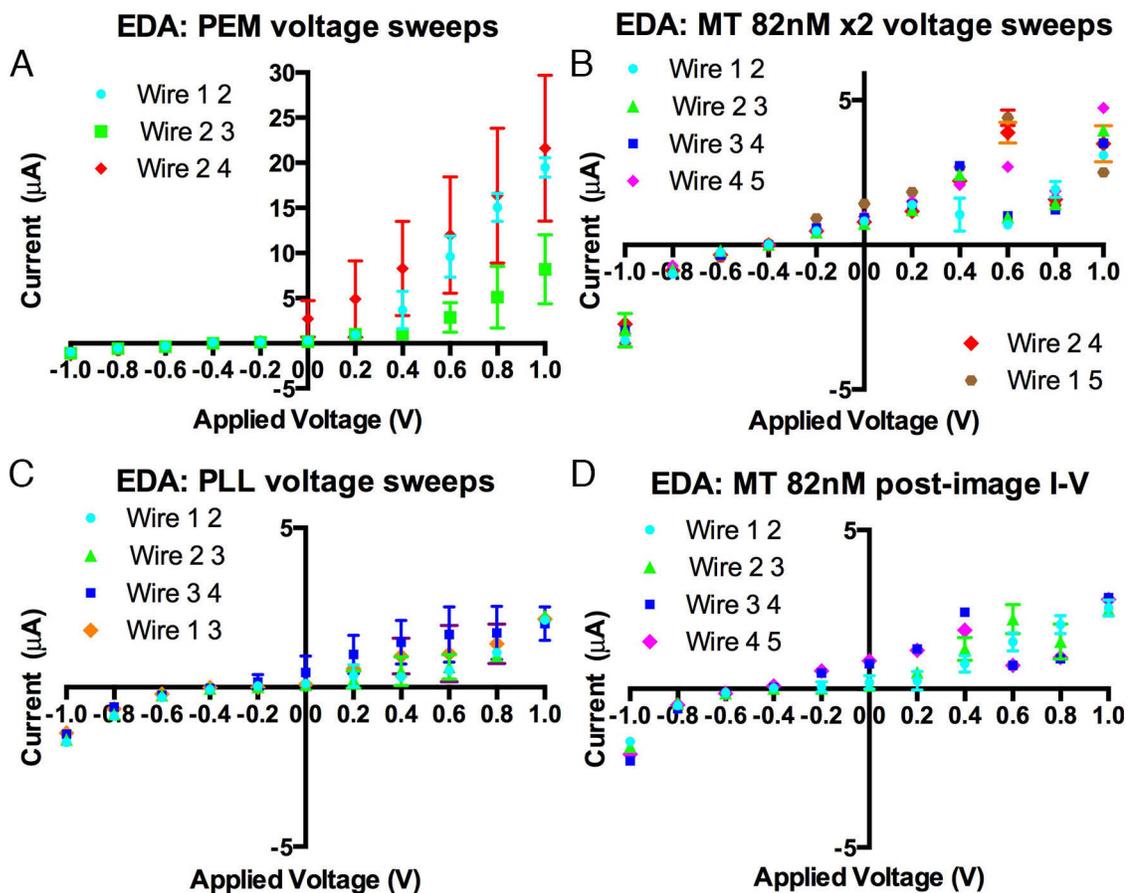
Figure 4.26. Grouped summary of voltage sweep plots of solutions for EDA devices. (A) PEM solution voltage sweeps. (A) PEM solution voltage sweeps. (B) Second MT 82nM solution added after imaging of first MT 82nM solution voltage sweeps. (C) PLL solution voltage sweeps. (D) MT 82nM solution voltage sweeps after imaging, with possible evaporation and leakage of the solution from the flow cell.

Between applied voltages of -0.6 and 0 V, I-V curves were approximately linear in this region and standard deviation of points in this region were low, with the exception of measurements with PEM between wires 2 and 4, and with PLL between wires 3 and 4 (Figure 4.26). Values for conductance in this linear region where current intersects 0A were taken as the conductance (similar to Umnov et al. [376]) (Figure 4.27).

EDA Conductance (-0.6 to 0V)
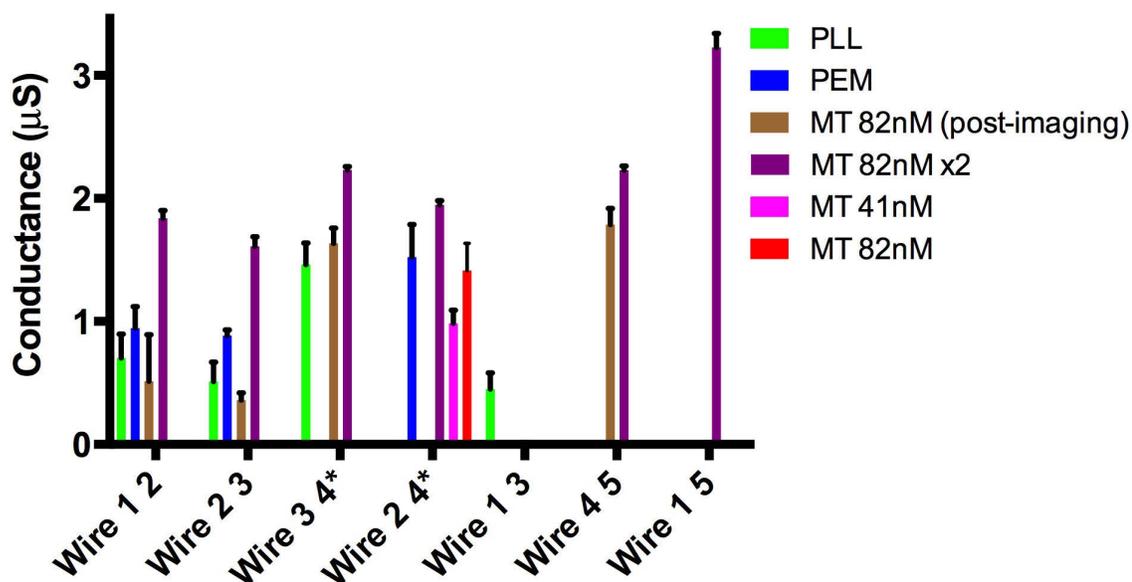
Figure 4.27. EDA conductance of all voltage sweeps of various solutions between different wires. Conductance is the mean of the slope of the linear regression of each voltage sweep. Error is standard deviation. *Conductance reported for PEM for wire 2 4 is taken from points -0.6 to 0 V, due to large variance of the 0V data point (see Figure 14.1), and that of PLL for wire 3 4 is taken from points -0.8 to -0.4, due to large variance of the -0.2 and 0 V data points (see Figure 4.25). In order of time, measurements were taken in the following order: PLL solution, PEM solution, MT 41nM solution, MT 82nM solution, then imaging was done, then MT 82nM (post-imaging), then MT 82nM x2. Replication is needed to confirm whether MTs are responsible for increased conductance between wires.

MT (82nM) x2 solution conductance was highest of all measurements in each measurement system, and notably larger than PEM and PLL conductance in this region for the EDA device (Figure 4.27). This could be because in EDA, MTs appear to be making solid electrical contacts with the electrode wires, and that with these small currents, less than 2μA in the -0.6 to 0V region, MTs may be able to increase ionic conduction. However, of note is that in the wire 1 2 system and the wire 2 3 system, the MT (82nM) post-imaging conductance was lower than that of PEM. This may be because of a lack of solution in the flow cell at the time of measurement, which led to a second addition of MT 82nM solution (MT 82nM x2) to the flow cell. Of note is that in the wire 1 2 and wire 2 3 system, a low number of MTs were observed making a direct connection between the wires (2 and 3 MTs, respectively), while in the wire 3 4 and wire 4 5

systems, there was a higher number of MTs observed making a direct connection (10 and 7, respectively). Similarly, with the MT (82nM) post-imaging results, the wire 1 2 and wire 2 3 systems showed low conductance, while the wire 3 4 and wire 4 5 systems showed higher conductance, roughly proportional to the number of MTs observed connecting the wires. This data is consistent with the simplified parallel resistor model presented in Figure 4.11. Thus, if we assume refilling the flow cell with MT (82nM) solution after imaging did not increase the number of MTs observed making direct contact between adjacent wires, and then assume the simplified parallel resistor model between wire 2 and 3 in Figure 4.11, then by taking the difference in the conductance between MT (82nM) x2 solution and PEM solution, we get the conductance of the MTs making direct contact between the adjacent wires. This analysis for the wire 2 3 system is presented in table 3. The difference in conductance is 0.73 μS, and as 3 MTs were observed making direct contact, the conductance of an MT is estimated at 0.24 μS, which corresponds to a conductivity of 4300 S/m. This is remarkably similar to the conductivity estimate of the MT in the same wire 2 3 system from the four-point probe experiment of 4400 S/m. Table 4 estimates the conductivity of a MT from the conductance data in Figure 4.27 for the wire 1 2 system, with an estimate of 8000 S/m. The estimates of MT conductivity of all experiments in this chapter are summarized in Table 5. This MT conductivity is the ionic and/or intrinsic conductivity facilitated by a MT making contact between two platinum electrode wires 8.8 μm apart in a physiological-like ionic solution. These results must be replicated to come to concrete conclusions, and it should be cautioned that the number of MTs connecting adjacent wires is based upon visual inspection of the fluorescence microscopy images of the system (see Figure 4.6), and is a large unknown.

Table 4.7. Estimate of MT conductivity from EDA wire 2 3 conductance measurements in Figure 4.27.

Wire 2 and 3	Conductance (μS)	Conductivity (S/m)
PEM	0.88 ± 0.1	
MT 82nM x2 solution	1.61 ± 0.1	
MTs wire 2 3	0.73	13000
MT	0.24	4300

The first two rows are the conductance measurements of PEM solution and MT 82nM x 2 solution. The difference in conductance of these solutions is assumed to be the conductance of MTs between wire 2 and 3, given in row three. By inspection, there appears to be 3 MTs making direct contact between wires 2 and 3, which gives an estimate of the conductance and conductivity of a single MT in row four. Error is standard deviation of linear regression of each voltage sweep from points -0.6 to 0 V.

Table 4.8. Estimate of MT conductivity from EDA wire 1 2 conductance measurements in Figure 4.27.

Wire 1 2	Conductance (µS)	Conductivity (S/m)
PEM	0.95 ± 0.2	
MT 82nM x2 solution	1.84 ± 0.1	
MTs wire 1 2	0.89	16000
MT	0.45	8000

The first two rows are the conductance measurements of PEM solution and MT 82nM x 2 solution. The difference in conductance of these solutions is assumed to be the conductance of MTs between wire 1 and 2, given in row three. By inspection, there appears to be 2 MTs making direct contact between wires 1 and 2, which gives an estimate of the conductance and conductivity of a single MT in row four. Error is standard deviation of linear regression of each voltage sweep from points -0.6 to 0 V.

Table 4.9. Estimates of MT conductivity in ionic solution from EDA device.

Method	MT conductivity, σ_{MT} (S/m)
Four-point probe wire 2 3 voltage measurements (1nA applied current)	4400
Wire 2 3 current measurement with ± 1V voltage sweep	4300
Wire 1 2 current measurement with ± 1V voltage sweep	8000

Improvements to the experiment would be to perform pulsed current experiments to test for ionic conductivity of the MTs, as well improving the design of the electrodes and/or apply MT solution while applying an external electric field to result in a larger number of MTs making direct contact between electrode wires, to potentially observe a more pronounced effect of the MTs.

4.2.2.4 EDA and EDB combined results and conclusions

Combining the results of the EDA and EDB experiments suggests the following:

- For the EDA device, with evidence of good MT contacts between wires 1.5μm wide and with 8.8μm spacing between wires, both four point probe and two electrode experiments suggested that solutions with MTs had higher conductance than both PEM and PLL solutions between wires 2 and 3. This may indicate high ionic conductivity of MTs, with estimates of 4400 and 4300 S/m for MTs connecting wires 2 and 3 of the EDA device.

- In EDB devices, when good electrical contact of MTs between electrodes does not occur, MTs may block the flow of ions between 30μm wide electrodes, 14 μm apart, especially at voltages above 200mV.

- At the voltages above 200mV for EDB devices, there was much variability of data, including regions of negative slope, potentially indicating DC experiments at this voltage range are obfuscated by charge build-up effects.

The results with the EDA device were most successful at probing MT conductivity, as fluorescence imaging appeared to show MTs making direct contact between electrode wires, while this was not shown with the EDB devices. The EDA experiment must be replicated to come to concrete conclusions; however, this experiment is the first, to my knowledge, to make electrical measurements of MTs in physiological-like solution and in direct stable contact with four electrode wires, as the MTs are adhered by PLL to the glass substrate, which opens the possibility of rapid investigation of MT electrical effects. My method described allows for reproducible experimentation, with up to 9 flow cells and 18 EDA devices able to be fabricated on one 10cm diameter glass substrate. Nanofabrication of the flow cells on glass substrates is done in less than 3 days, and involves only well documented conventional photolithography and metal evaporation methods.

The challenges in studying MT conductivity are still great due to the difficulty of decoupling the electrical effect of MTs with the ionic environment that is essential for MTs to function. It is instructive to note that Umnov et al. performed a similar experiment as the EDB experiments [376]. Umnov et al. attempted to measure the intrinsic conductivity of MTs, by immersing MTs in 5 μl of PEM into 50 ml of ultrapure water [376]. They performed a similar ±1V voltage sweep between two Au electrodes 50nm tall, 100μm wide, with a 10μm space between them. Similar to my voltage sweep

results, they found that their I-V curves were non-linear, with current as an exponential function of potential. They attributed this to the characteristic form of an electrolytic reaction. They also found that the resistance of solution with MTs and buffer is higher than that of simply buffer, similar to my EDB experiments. They speculated that this was because the MTs adsorbed the ions from the PEM (hypothesis 3.1). Their results could be explained by a combination of hypotheses 1-3. As well, when they attempt to estimate the intrinsic conductivity of MTs, they use as the basis of their calculation their measurement that (MTs+5μl PEM) in ultrapure water has a lower resistance than ultrapure water and assume the change is due to the MTs and the adsorbed charges surrounding the MTs. However, their result that 5μl PEM in ultrapure water has an even lower resistance than (MTs+5μl PEM) in ultrapure water suggests that the lower resistance of (MTs+5μl PEM) in ultrapure water compared to ultrapure water is entirely due to the ions of the 5μl PEM not adsorbed onto MTs. In their paper, the lower resistance of (MTs+5μl PEM) in ultrapure water compared to ultrapure water is instead attributed to MTs spanning the electrodes (which they did not directly image) and acting as parallel resistor to the ultrapure water resistance between the electrodes. Based on this observation, their results might be better interpreted to understand MTs ability to adsorb ions as opposed to MTs' ability to conduct electricity with or without adsorbed ions.

This analysis underscores the difficulties in testing:

- the ability of MTs to propagate ionic signals
- the ionic conductivity of MTs, and
- the intrinsic conductivity of MTs [61].

My initial results from the EDA device demonstrate that my method may provide an improvement on the previous attempts to study MT ionic conductivity by providing stable electrical contact of MTs to multiple 1.5μm wide platinum wires. This allows the possibility of studying the ability of MTs to propagate ionic signals in greater detail than the previous study of Priel et al. [356] which used micropipettes manually applied to make physical contact with MTs. Indirect methods such as using electro-orientation [368] or AC electrokinetics [369] also are not as applicable to study ionic conductivity of MTs.

4.3 Nanofluidic channel for MT isolation and electrical characterization

In addition to my flow cell experiments, I designed a nanofluidic channel for future studies to test electrical properties of a single microtubule trapped in a nanofluidic channel. This section outlines the design and initial experiments in the development of a working nanofluidic channel for future tests of MT conductivity.

4.3.1 Methods

4.3.1.1 Nanofabrication

Nanofluidic channels were created using a combination of electron-beam lithography and photolithography. A round 10cm diameter Borofloat borosilicate glass wafer (Swiftglass) was used to make devices.

A complete device consisted of following steps 1-8. The framework of the nanofabrication method was generously given to me by Dr. Walter Reisner, who has experience in nanofluidic channels to analyze DNA [481, 482]. The design was also inspired by previous publications designing fluidic channels [479, 480, 483]. The code for the design of the photolithography masks, dose tests to optimize electron beam lithography (EBL) parameters, and EBL designs is found in Appendix C.

Step 1: Initial alignment marks.

To clean, the Borofloat substrate was immersed in piranha solution (3:1 H_2SO_4 (96%) / H_2O_2 (30%)) for 15min. 50nm Cr was sputtered on substrate. Standard photolithography process was then used to pattern the alignment marks. Standardized protocol was used to spin a ~1.25µm HPR504 resist (10s @ 500rpm, 40s @ 4000rpm) onto substrate. Substrate was baked @115°C for 30min followed by rehydration for 15min, then exposed for 3s with Alignment mask. HPR 504 developed for 25s in 354 then rinsed with H_2O and inspected. Cr is then wet etched to reveal alignment marks. HPR 504 is removed with acetone and isopropyl alcohol (IPA) rinse.

Step 2: Nanochannels.

Device cleaned with 5min RIE O_2 strip (100W, 100sccm O_2, 100mTorr). 15min acetone sonication followed by IPA rinse also performed. Soap scrub followed by H_2O rinse performed to clean. Substrate prebaked for 8min @ 180°C followed by spin coat of 3ml Poly(methyl methacrylate) (PMMA) 950 A2 (Microchem) @ 2000rpm (500rpm,

100rpm/s ramp, 10s; 2000rpm, 1000rpm/s ramp, 60s), followed by 2min bake @ 180°C, leading to resist height of 70-110nm. Then, 3.1ml of Aquasave (Mutsubishi Rayon Co. Ltd.) spin coated (100rpm, 50rpm/s ramp, 4s; 2750rpm, 750rpm/s ramp, 60s) followed by 90s bake at 150°C over coverplate with pin height 115. Nanochannels with diameter 50-800nm applied using EBL with dose 150 $\mu C/cm^2$, dot dose 1.0pC, 10kV acceleration voltage, 10μm aperture, 8mm working distance. After 2-17h wait time following exposure, Aquasave removed with H_2O and then substrate heated at 70°C in convection oven followed by 5min cooling to bake off any absorbed water. Then substrate developed with MIBK/IPA 1:3 for 45s (agitated), followed by 15s IPA rinse and dry with N_2. Pattern inspected and height of PMMA measured with profilometer (Alpha-Step IQ, software 2.5.0). Pattern was etched with fluorine based RIE process: CF4 (20 sccm) + CHF3 (30 sccm) at 36mTorr, 200W for 154s. Depth measured with a profilometer (Aqua-step IQ). PMMA stripped with 10min acetone sonication. Channels inspected optically and depth of channels measured with a profilometer.

Step 3: Nanoelectrodes.

Substrate cleaned with 5min RIE O_2 strip as in step 2, followed by soap scrub and H_2O rinse. Bilayer PMMA process used for improved liftoff: PMMA 495 A2 spin coated at 4000rpm (500rpm, 100rpm/s ramp, 10s; 4000rpm, 1000rpm/s ramp, 60s) followed by 30min bake at 180°C; PMMA 950 A2 spin coated at 4000rpm (500rpm, 100rpm/s ramp, 10s; 4000rpm, 1000rpm/s ramp, 60s) followed by 30min bake at 180°C. Aquasave applied as in step 2. Nanoelectrode pattern exposed using EBL, with dose 175 $\mu C/cm^2$, dot dose 1.0pC, 10kV acceleration voltage, 10μm aperture, 8mm WD, aligned to 4 alignment marks around nanochannel etched in step 2. Aquasave removed and PMMA bilayer developed with same process as in step 2. Pattern inspected optically and depth of resist measured with profilometer. Angled evaporation at 25° of 4nmTi/14nm Pt applied, followed by 40min acetone sonication for liftoff. Additional 15min acetone sonication in new bath, followed by EPA rinse and delicate soap scrub and H_2O rinse done to clean. Substrate then inspected to confirm nanowires present and substrate clean.

Step 4: Microelectrodes and wire pads.

Photolithography, as performed in step 1, used to expose wires and contact pads on device. 20nm Ti/20nm Pt evaporated, followed by 5min acetone sonication liftoff and IPA rinse. 15min acetone sonication in fresh bath and IPA rinse then done to clean, followed by delicate soap scrub and H_2O rinse. Substrate inspected optically.

Step 5: Microchannels.

Photolithography, as performed in step 1, used to expose reservoirs and microchannels on device. Channels etched with same fluorine-based process as in step 2 (0.74nm/s etch rate), then substrate inspected and depth measured with profilometer. Then 15min acetone sonication and IPA rinse to remove HPR 504. Substrate inspected again and depth measured with profilometer. Depths used to calculate etch rate.

Step 6: Coverslip preparation

Four 2mm diameter reservoir holes on a Fisher coverslip (12-544G, #1.5, 60x22mm), sandwiched between two pieces of sacrificial glass (microscope slides) and attached with crystal bond (Aremco Products, Crystalbond 509) were drilled in a water bath using a 2mm diameter diamond tip drill bit. The crystal bond was removed upon heat and then acetone and IPA wash.

Step 7: Bonding.

Coverslips were cleaned with piranha solution (15min) and rinsed with H_2O and dried immediately. They were then soap scrubbed and rinsed with H_2O and dried immediately and covered. Substrate cleaned with acetone sonication for 15min and IPA rinsed and dried. Substrate mounted on tape in order to use high-pressure wash (HPW) and then soap scrubbed (with little to know pressure around nanochannel area). Three cycles of rinsing performed in HPW, followed by delicate soap scrub (with little to know pressure around nanochannel area) and then five cycles of HPW of rinse/dry. Soft bond then performed by aligning substrate above coverslip with spacers, then applying downward pressure. This bonding procedure sought to emulate the process in [487].

Step 8: Adding reservoirs (for syringe pump)

A ~1cm x 1cm piece of double-sided tape (3M, VHB) is punched with a 3/8" diameter hollow punch (SE, 791LP) using a hammer on wood block. The resulting outer circle is hammered using a 3/16" diameter hollow punch to make a double-sided sticky washer. Nanoports (Idex, N-124S), are cleaned with IPA on Technicloth II (Texwipe, TX1109),

then attached to washer. Washer and nanoport are then aligned manually and put in contact with substrate. Technicloth is applied over area where objective will be to protect the device from epoxy accidentally landing on unwanted area. 5min epoxy (LePage) is then applied around reservoirs and washers to ensure no leaking of solution and a secure attachment (this was initially not done and led to solution leaking through the tape). As the coverslip is soft bonded, epoxy is also applied to attach the coverslip to the substrate for protection against lateral forces. Top screws of nanoport are inserted on the nanoport, and then a clean Petri dish cover and weights are applied to provide downward force to help adhesion of the reservoir. Device was left for 24 hours to cure.

Step 8: Alternate reservoirs (no syringe pump)

1cm ends of 200µl pipette tips can be cut and applied to the access holes of the device with 5min epoxy to create reservoirs without the ability to use a syringe pump.

Step 1 can also be replaced by Step 4 to simplify the process.

4.3.1.2 Imaging

A dose test was performed to select optimal EBL dose parameters for nanochannel and nanoelectrode patterning. Doses of 150, 175, and 200 µC/cm^2 were tested for both nanochannels and nanoelectrodes in an array, following step 2 and 3. The substrate was then sputtered with 5nm of Au to prepare it for scanning electron microscope (SEM) imaging, and then the substrate was imaged to find the optimal dosing parameters. SEM imaging was performed with the Raith 150$^{\text{TWO}}$ EBL tool.

Bright field inspection of substrate after photolithography processes taken with a Zeiss Axio Lab.A1 microscope, with 5x Zeiss EC Epiplan objective (NA=0.13), 20x EC Epiplan objective (NA=0.4), 50x EC Epiplan objective (NA=0.7), and 100x EC Epiplan objective (NA=0.8). Images were acquired with a HDCE-X5 5.0MP digital camera (MicroscopeNet.com) with ScopeImage 9.0 software.

Fluorescence imaging was performed by an upright microscope (Imager.Z.1, Carl Zeiss, Inc.), using 10x, 40x Plan-Apochromat objective (NA=1.4), and 66x Plan-Apochromat objective (NA=1.4). Images were acquired by SensiCam (Cooke) charge-coupled device camera (PCO-TECH Inc.) with Metamorph software 7.8.12.0 (Universal Imaging Corp.). Images were processed using Adobe Photoshop CS6 v. 13.0.

4.3.1.3 Fluid loading

Methanol, 99.8%, ACS reagent grade (ACP Chemicals, M-3640) was used to initially wet the channel, as methanol flows easily in the microchannel and its refractive index allows for easy optical verification of its initial flow into the channel.

H_2O, for cell biology, free of endotoxins, ultrafiltered and autoclaved (Sigma, 95289) was used to bracket solvents that are not compatible. All solutions to prepare the channel, other than methanol, were filtered with 0.2 μm filters prior to introduction into the nanofluidic channel device.

0.2M NaOH (Sigma, reagent grade) was used to increase the ionization the glass channel wall, which forms a positively charged counter-ion layer along the wall, and this facilitates electro-osmotic flow (EOF), the motion of solution induced by an applied potential.

PBS, pH 7.4 (Sigma, P4417) was used as an ionic solution in initial nanofluidic channel tests.

Fluorescein isothiocyanate (FITC) (Sigma, F-7250) in methanol (790μM) solution was prepared. Prior to usage in devices it was diluted in PBS or PEM, depending on the experiment.

PEM (Cytoskeleton, BST01), is general tubulin buffer, made up of 80 mM PIPES, pH 6.9, 2mM MgCl2, and 0.5 mM EGTA. It is the buffer that MTs are stored in.

Casein (Sigma, C3400) is used to prevent MTs from sticking to the glass substrate [392]. It also prevents kinesin from denaturing in kinesin-MT bead assays, and so is commonly used in flow cell experiments involving MTs [369, 488-490].

Tubulin (Cytoskeleton, Kit #BK007R) was prepared following the protocol for the Fluorescent MTs Biochem Kit, with parameters used to obtain long MTs. Briefly, one aliquot of rhodamine tubulin was resuspended in 4.25 μl G-PEM (GTP + PEM) and 0.75 μl MT Cushion Buffer to yield 4 mg/ml fluorescent tubulin. 16 μl of unlabeled tubulin (5 mg/ml) was added to the 5 μl of fluorescent tubulin (4 mg/ml), leading to 21 μl of tubulin (1 rhodamine : 3 unlabelled; 4.76 mg/ml). Four 5 μl aliquots were made per rhodamine tubulin aliquot.

MT Solution is prepared by polymerizing 5 μl fluorescent tubulin (1 rhodamine : 3 unlabelled; 4.76 mg/ml) at 35ºC for 45min, followed by adding 100 μl PEM solution

containing Taxol (10µM or 20µM, depending on experiment), yielding a 2mM tubulin solution of fluorescent MTs. 1x Antifade (Cytoskeleton, BSM02) with beta-mercaptoethanol (Sigma, M6250) added to MT solutions to be imaged.

4.3.1.4 Resistance measurements

The Keithley 4200-SCS was used to measure resistance by attaching tungsten probe tips, with 5.0 µm tip diameter (Signatone, SE-T) in a probe station to the device contact pads. A voltage sweep from -1V to 1V was performed, step size 0.5V. Error reported is standard deviation of linear regression of ±1V voltage sweep.

4.3.1.5 Electrophoresis

Electrophoresis experiments on device v1.0 were performed using an in-house built power supply controlled with Labview software, as described in [491].

Electrophoresis experiments on device v2.0 were performed with a Micralyne Microfluidic Tool Kit (Micralyne Inc.) with software v. 3.40.01.

4.3.2   Results

With the goal to obtain precise electrical effects of a single microtubule, I designed a nanofluidic channel to isolate a single MT and be able to perform electrical recordings on the MT (see Figure 4.28 and Appendix C).
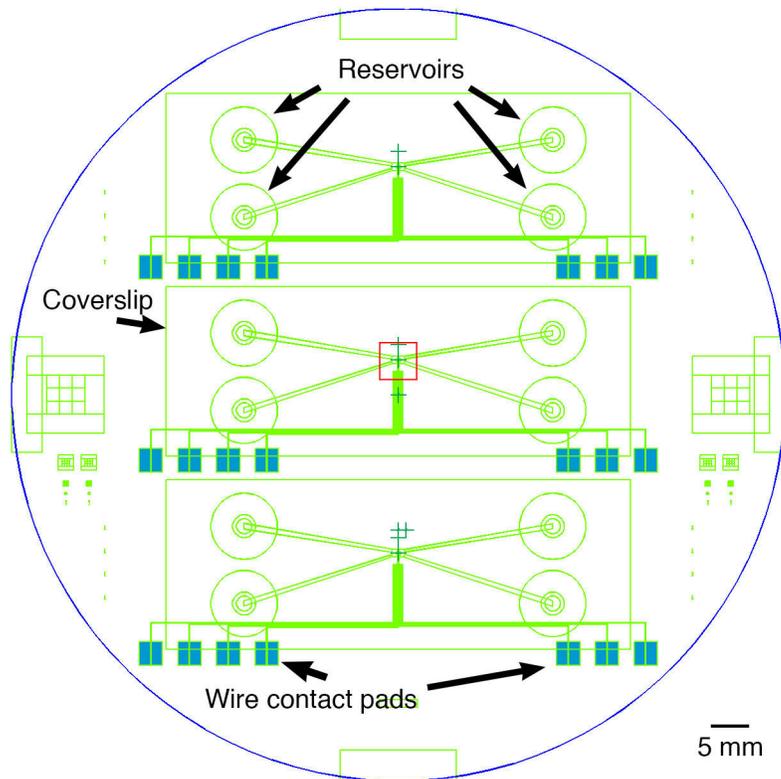
Figure 4.28. Matlab design of three nanofluidic devices. Each device contains four reservoirs that converge into the central area which contains the nanofluidic channel. The nanofluidic channel is in the central area of each device, indicated by the red square. The top, middle, and bottom devices are designed to have nanochannels 400nm, 600, and 800nm wide, respectively. Seven wires beginning at the seven wire contact pads (in blue) extend to the central region and interface with the nanochannel. The location of where a glass coverslip will cover the underlying device substrate to make the channel is also shown. The coverslip has four holes at the location of the reservoirs in order to introduce solution into the channel.

The process developed allowed me to make a device (v. 1.0), referred to as D1, complete with a nanofluidic channel (189nm deep, 400, 600, and 800nm wide), and nanoelectrodes (see Figure 4.29).
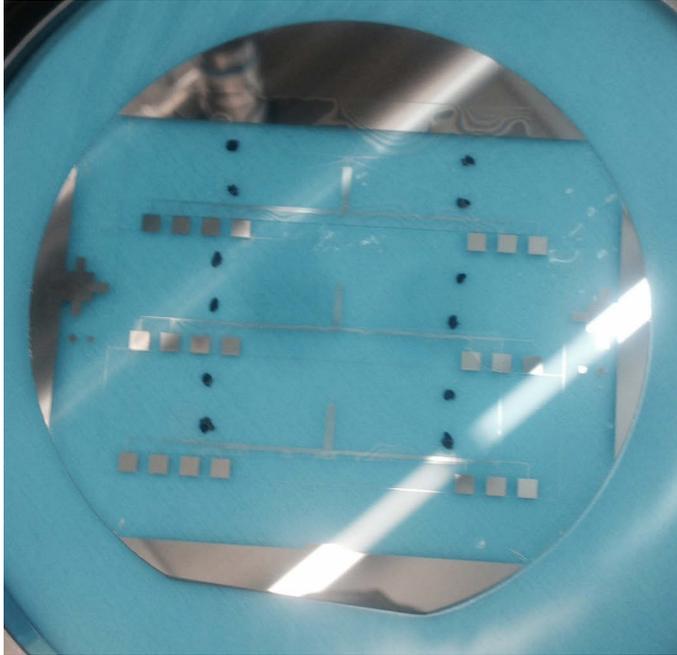
Figure 4.29. The completed device, prior to the coverslips being bonded. Where the coverslip holes will be is marked as black circles by black marker on a surface below the actual substrate. The platinum contact pads and wires leading to the central region where the nanofluidic channel is can be clearly seen.

The device has four access holes, two on each side of the nanochannel, where microchannels (575nm deep and ~30µm wide) connect the access holes with the central region. There are two access holes on each side of the device to guard access air bubbles forming when introducing solution into the device [481]. The design of the region of interest, where the nanochannel and nanoelectrodes are, is shown in Figure 4.30.
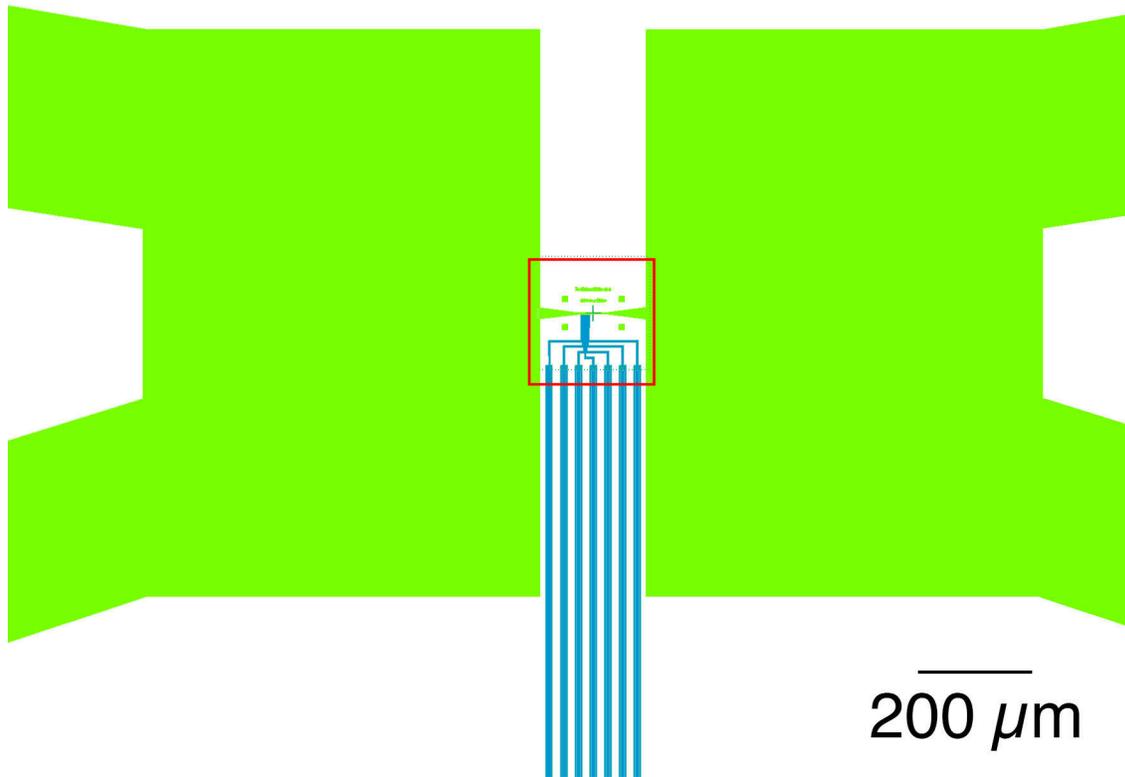
Figure 4.30. Matlab design of central area where two microchannels (green) on each side connect with a nanochannel in the middle (green). Seven electrode wires (blue) interface with the channel.

A nanochannel (189nm deep) connects two larger areas that the microchannels flow into (575nm deep). This region of interest of D1 is correspondingly shown after bonding the coverslip (step 7) in Figure 4.31.
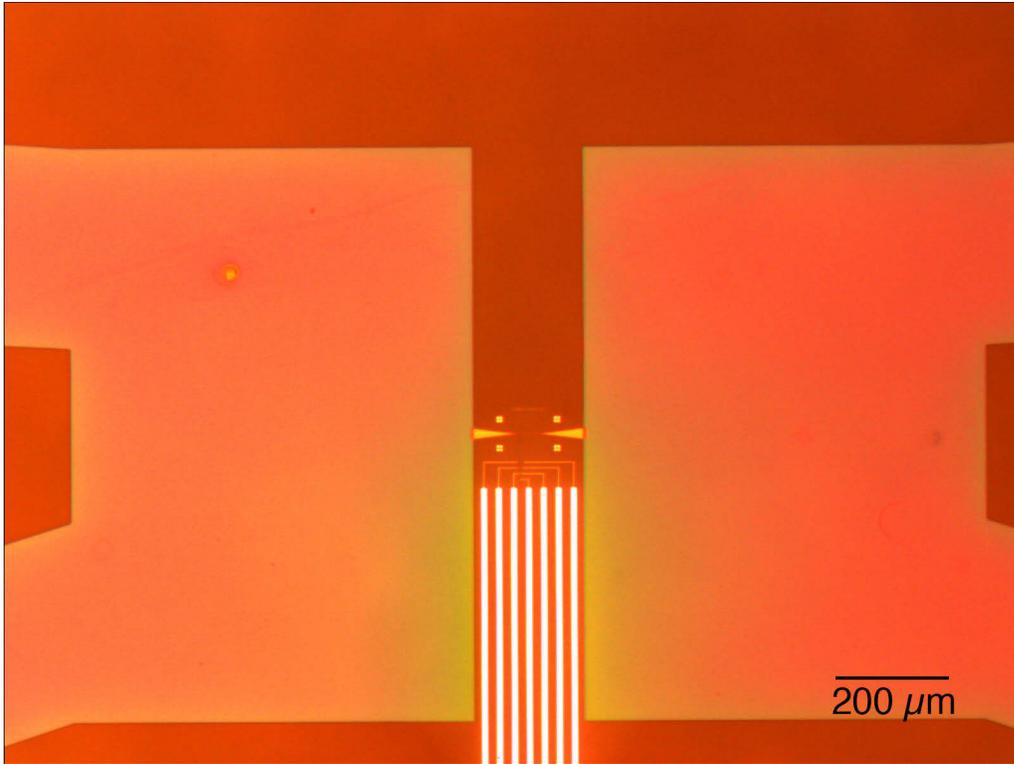
Figure 4.31. D1 after final bond. This is an optical 5x image of the bottom 800nm device, after the 0.17 μm coverslip has been bonded. The etched channels are clearly visible. The seven electrode wires (Pt) are bright, and higher magnification images show they are continuous to the nanochannel.

While previous designs of nanoelectrodes interfaced with nanochannels creates transverse electrodes to measure resistance across a nanochannel [479, 483], I sought to make electrodes on one side of the nanochannel only, and for the electrodes to be embedded in the channel regularly in order that a MT would be able to make solid contact with multiple electrodes (4 for a 4 point probe measurement, and more than 4 for length dependent measurements). I developed a process that makes seven regular electrodes embedded 200 nm into a 400-800 nm channel, which I refer to as wires 1 to 7, from the left. The design of this is shown in Figure 4.32.

156
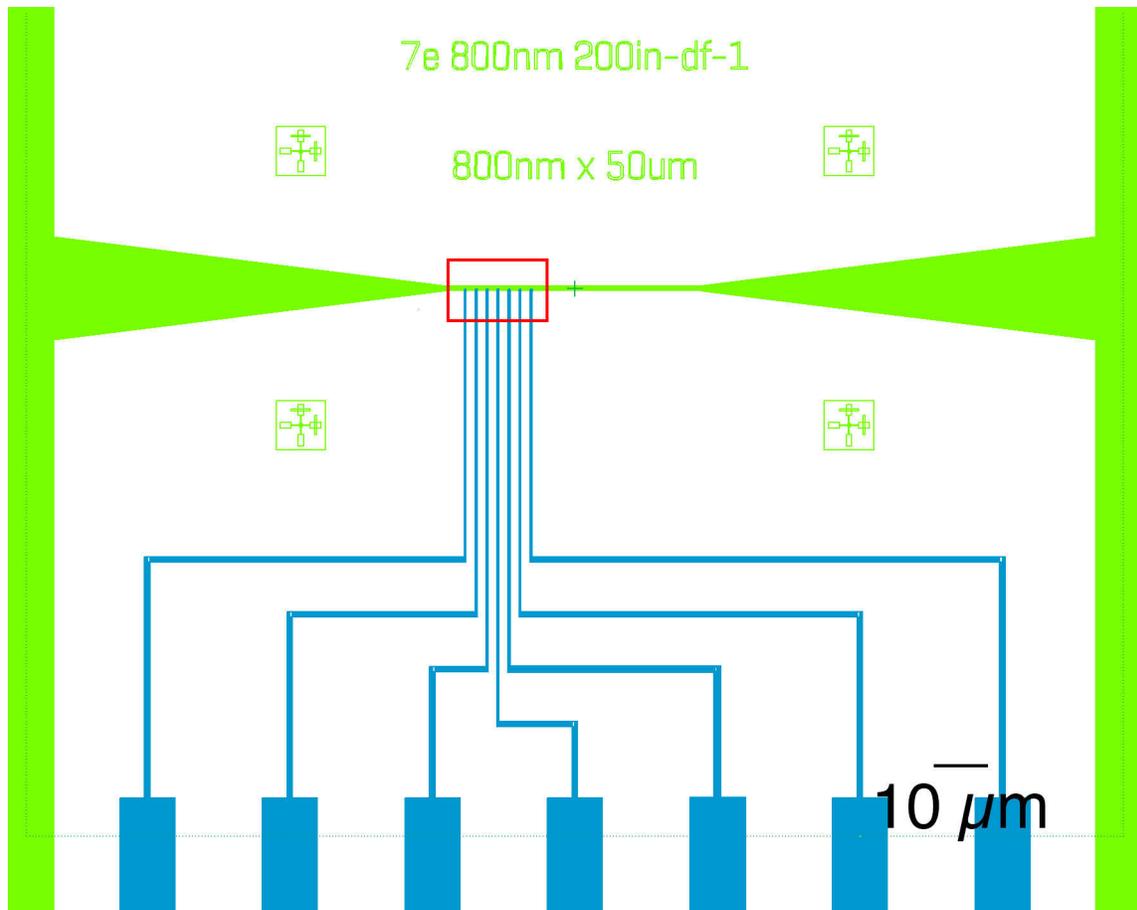
Figure 4.32. Matlab design of region of interest, which is 200µm long, and was patterned with EBL. This is the region where it is targeted that a MT would be trapped. Etched regions for liquid solutions in green, and platinum electrodes are in blue.

The corresponding image of this on D1 is shown in Figure 4.33, showing I have continuous platinum (Pt) wires less than 1µm wide interfacing with the nanochannel.
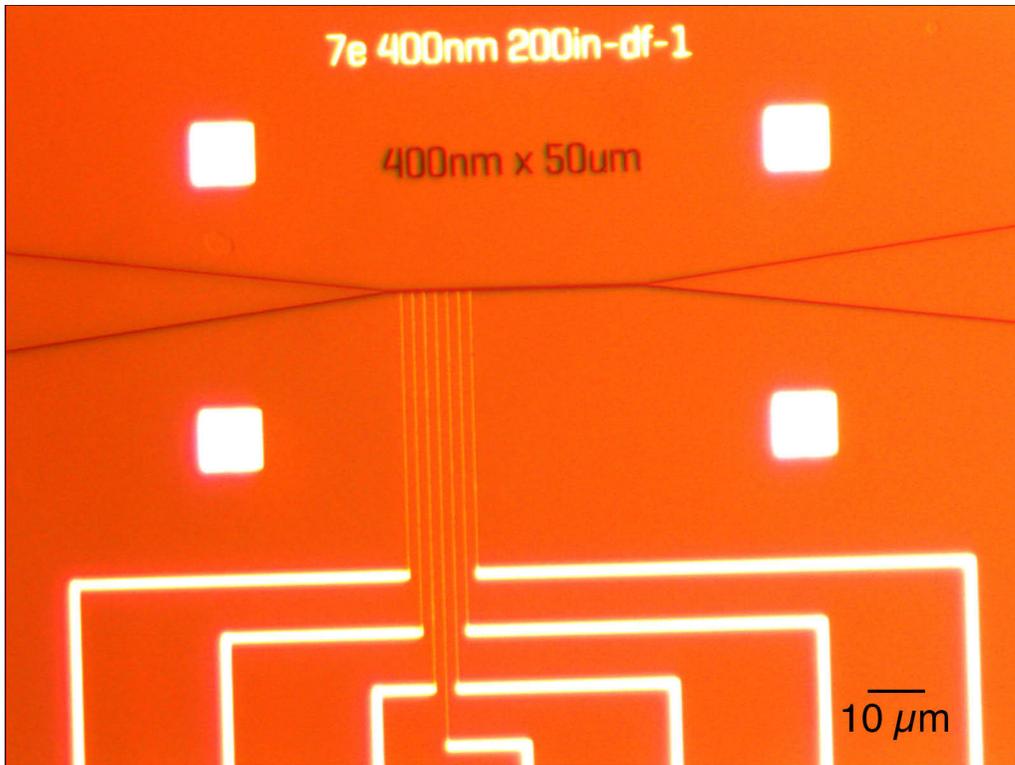
Figure 4.33. D1 top device prior to the coverslip bonded. Optical image (50x) showing seven platinum nanoelectrodes (bright) continuous to nanochannel (400nm wide) interface.

It was confirmed that these nanoelectrodes persisted after the bonding process with the coverslip (Figure 4.34).
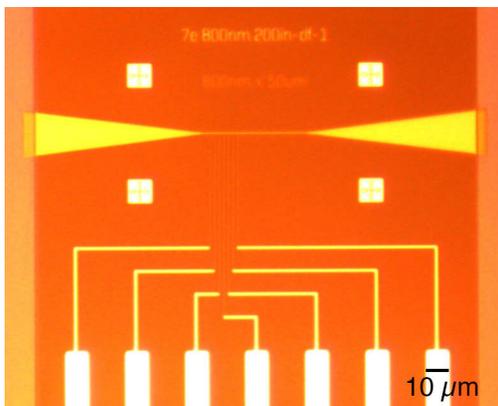
Figure 4.34. D1 bottom device with the coverslip bonded. Optical image (20x) showing seven platinum nanoelectrodes (bright) continuous to nanochannel interface.

The design of nanoelectrodes embedded 200nm into a 800nm wide nanochannel is shown in Figure 4.35.
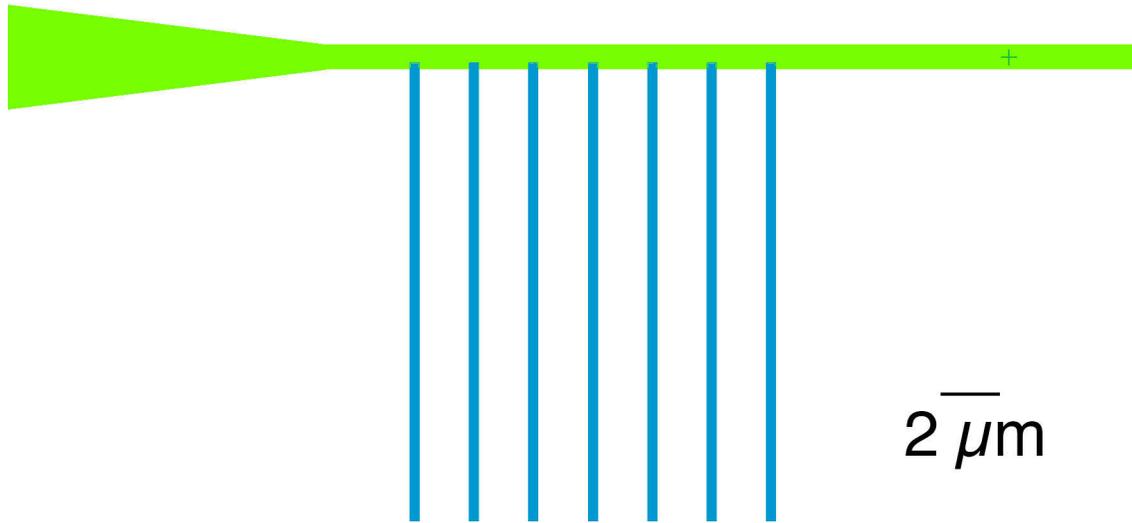
Figure 4.35. Matlab design of 800nm wide nanochannel (green) and seven interfacing nanoelectrodes (blue), embedded 200nm into the nanochannel. This is the region where the goal is for a MT to be trapped and make solid electrical contact with the seven interfacing nanoelectrodes.

The interface between the nanochannel and nanoelectrodes on the order of 200nm, and is difficult to verify with an optical microscope (see Figure 4.36).
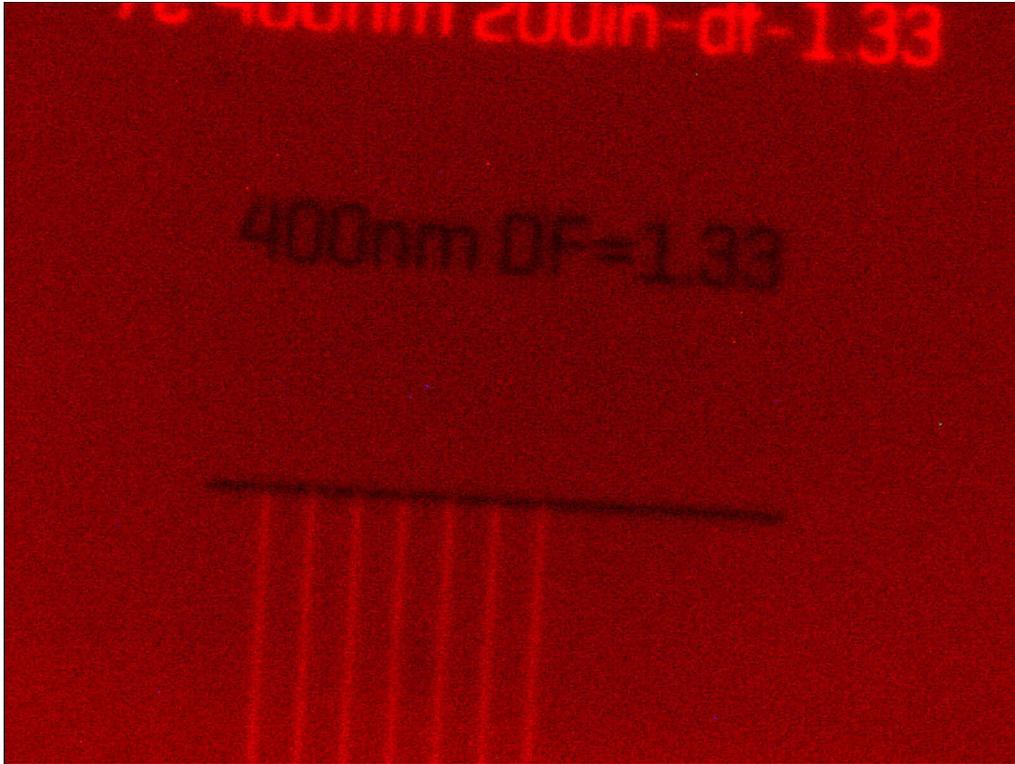
Figure 4.36. Image of a dose test to optimize EBL parameters for nanochannel and nanoelectrode design. At 100x magnification, an optical microscope cannot effectively confirm the nanoelectrodes are embedded regularly in the nanochannel.

SEM imaging of nanochannels and nanoelectrodes created by our process allowed us to select proper EBL doses to pattern nanoelectrodes correctly uniformly embedded 200nm into the nanochannel (see Figure 4.37).
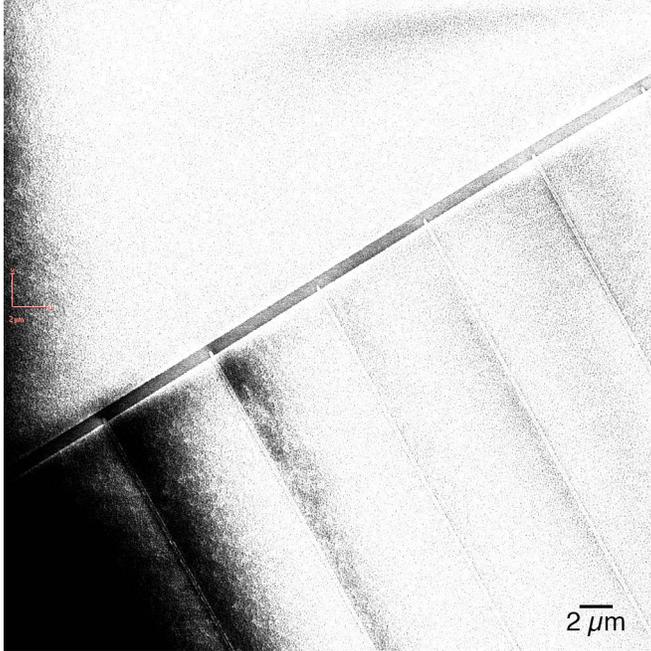
Figure 4.37. SEM image of nanoelectrodes. This figure is of a nanochannel designed 400nm wide, with nanoelectrodes designed to be embedded 200nm into the nanochannel ie. half-way into the nanochannel. The doses used to create this system was 150 μC/cm^2 for nanochannels and 175 μC/cm^2 for nanoelectrodes, and these doses and process were used in subsequent devices. This image confirms I have regularly embedded nanoelectrodes in the nanochannel.

150 μC/cm^2 for nanochannels and 175 μC/cm^2 for nanoelectrodes was selected based on the SEM images. Once D1 was complete, it was tested to confirm the nanochannels and nanoelectrodes were functional. I loaded the channel with doubly distilled methanol, followed by H$_2$O, then 0.2M NaOH, then PBS, pH 7.4. I loaded one side of the device with FITC (a fluorescent marker), and applied electrodes inside reservoirs on both sides of the device (see Figure 4.38).
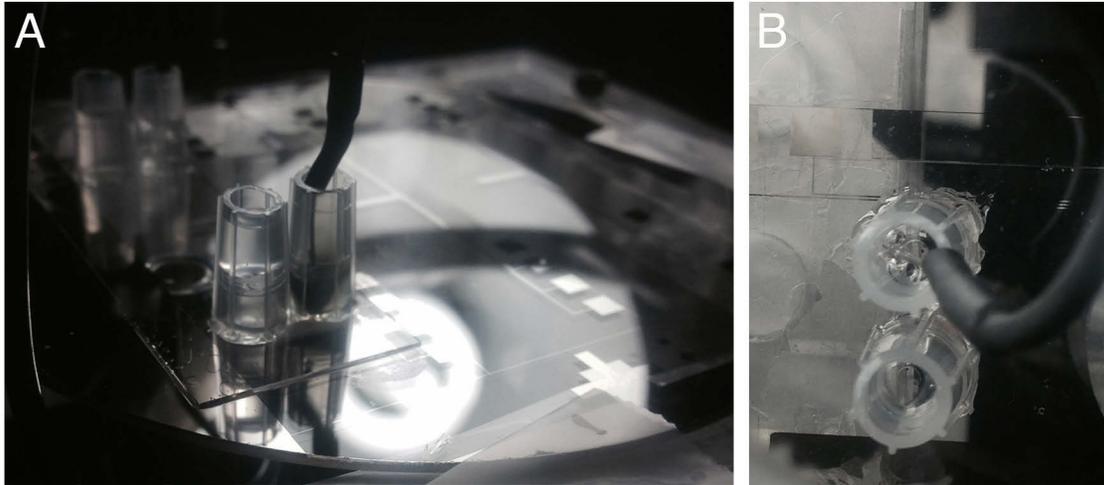
Figure 4.38. (A) D1 with FITC loaded into the near reservoir with electrode wire entering the solution, and electrode on opposite sides of the device to test electrolysis driving the FITC through the nanofluidic channel. (B) Wire on opposite side of D1 used to drive electrolysis.

I applied a potential of 1-4 kV across the device to experiment with driving FITC through the nanochannel, with the goal of using a photomultiplier tube (PMT) to measure increased FITC concentration over time. 4kV was too large a potential and created air bubbles in the microchannels due to heating from a large resistance. PMT recordings were inconclusive (data not shown). This device revealed challenges with the coverslips with soft-bonding easily coming off when suction with a vacuum hose was applied on the reservoirs, or if lateral force was applied on the reservoirs. The resistance between nanoelectrodes was also tested to verify nanoelectrode wires were able to detect signals (see Table 4.10 and setup in Figure 4.39).

Figure 4.39. Probe tips making resistance measurement on a metal contact pad.

Table 4.10. D1 Chromium short circuited wires

Contact	Resistance (Ω)	Resistance after diamond cut (Ω)
Metal/metal	52 ± 4 Ω	
Metal/glass	4.7 ± 2.7 $x10^{14}\Omega$	
Electrode 6/7	6.4 ± 0.003 kΩ	9.7 ± 1.9 $x10^{10}\Omega$
Electrode 5/7	68 ± 9.6 kΩ	5 ± 20 $x10^{11}\Omega$

Error is standard deviation of linear regression of ±1V voltage sweep. Metal/metal is the resistance measured between two probes on the same contact pad as seen in Figure 4.39. Metal/glass is with one probe on the contact pad, and the other on the bare glass substrate. Electrode 6/7 and 5/7 is with probes on the contact pads of the respective wires, numerating the wires from the left.

Resistance between two probes on the same Pt wire contact pad gave resistance in the order of 10^2 Ω, while resistance between a probe on the Pt contact pad and the glass without Pt was on the order of 10^{14} Ω. Resistance measurements of D1 between wires gave abnormally low resistance ($\sim 10^3 - 10^4$ Ω), which revealed that the Cr alignment marks short-circuited electric measurements as they electrically connected the contact pads. This was confirmed by using a diamond scribe to remove the Cr alignment marks between contact pads, which resulted in the resistance becoming on the order of 10^{11} Ω (see Figure 4.40).
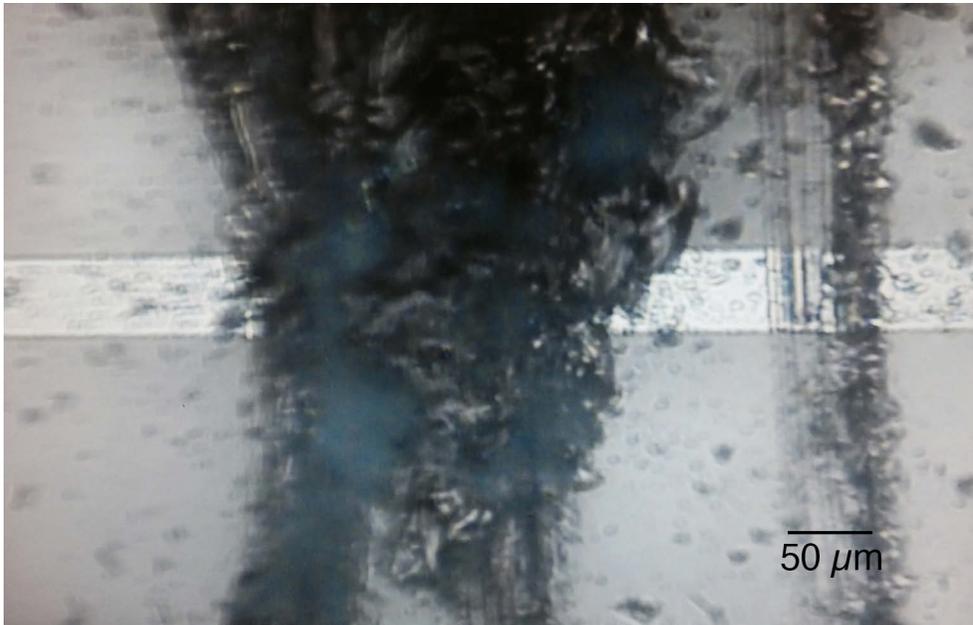
Figure 4.40. Diamond scribe scratches used to remove Cr alignment line (white) that was short-circuiting electrical measurements on D1.

After this was done, resistance measurements were taken to measure the effects of H_2O and PBS, pH 7.4. The results are in Table 4.11. The resistance between wire 1 and 7 of D1, bottom device, was $\sim 10^{12}$ Ω. Adding H_2O across the wires reduced the resistance by ~ 1 order of magnitude, to $\sim 10^{11}$ Ω, and PBS reduced the resistance between wires by another ~ 5 orders of magnitude, to $\sim 10^6$ Ω.

Table 4.11. Measured resistance between wire 1 and 7 of D1 bottom device.

	Resistance (Ω)
No solution	$4.3 \pm 0.9 \times 10^{12}$
H_2O	$1.4 \pm 0.1 \times 10^{11}$
H_2O removed	$1.6 \pm 0.1 \times 10^{13}$
PBS	$9.0 \pm 1.1 \times 10^5$

Error is standard deviation of linear regression of $\pm 1V$ voltage sweep.

I then prepared v. 2.0 of the device, referred to as D2, without nanoelectrodes (steps 1, 3 and 4 omitted) to test the ability of the nanochannel to isolate MTs using improved reservoirs that could be interfaced with a syringe pump (see Figure 4.41).
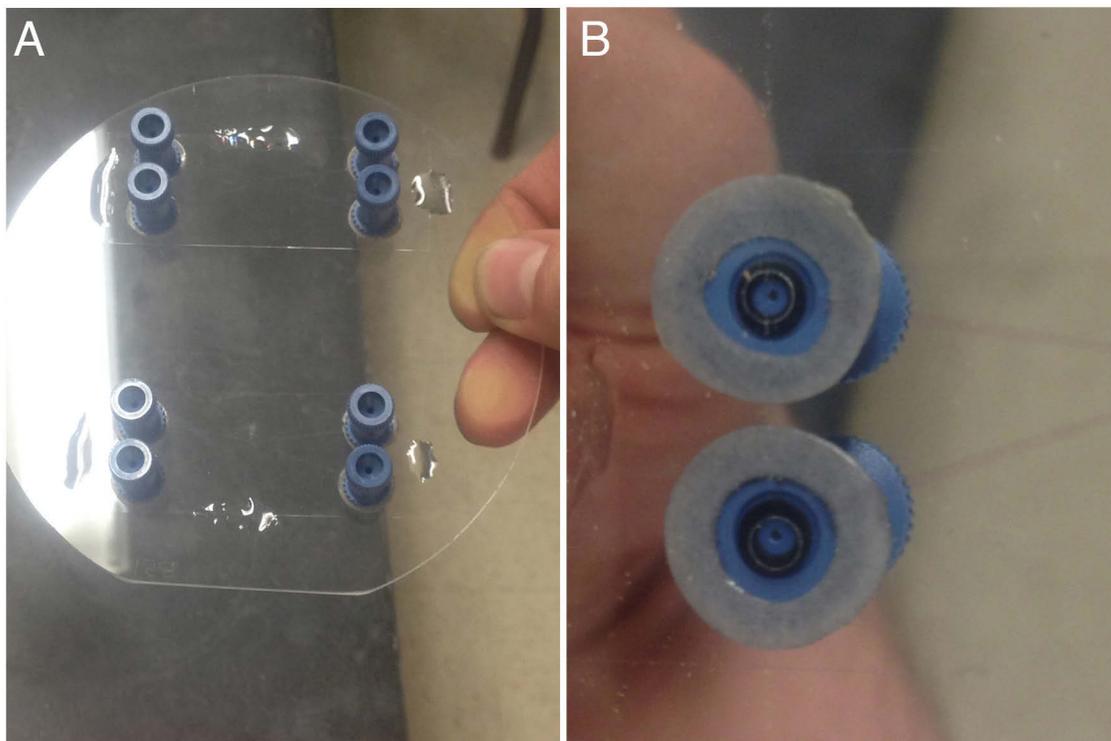
Figure 4.41. (A) D2 (steps 1, 3, and 4 omitted) made of microchannels and nanochannels. Metal electrodes are omitted. (B) Back side of D2, showing attachment of nanoport reservoirs to coverslip hole. Reservoir is attached to coverslip with grey double-sided tape.

I experimented with the bottom device to detect whether the nanofluidic channel was open. I wetted one side of the channel with methanol, which freely entered the microchannel, but did not pass through the nanochannel; thus in all steps I introduced solutions from both sides. I introduced methanol, followed by H_2O, followed by 0.2M

NaOH, followed by PBS. Then I applied FITC to one side and applied a 100V potential, by applying electrodes into reservoirs on opposite sides of the channel for less than 3 hours. After 20 hours, I imaged the nanochannel, showing FITC entering the nanochannel funnel, and little, if any, of the FITC travelling through the 800nm nanochannel (Figure 4.42). I also discovered leaking eventually out of the reservoirs, through the double-sided tape.
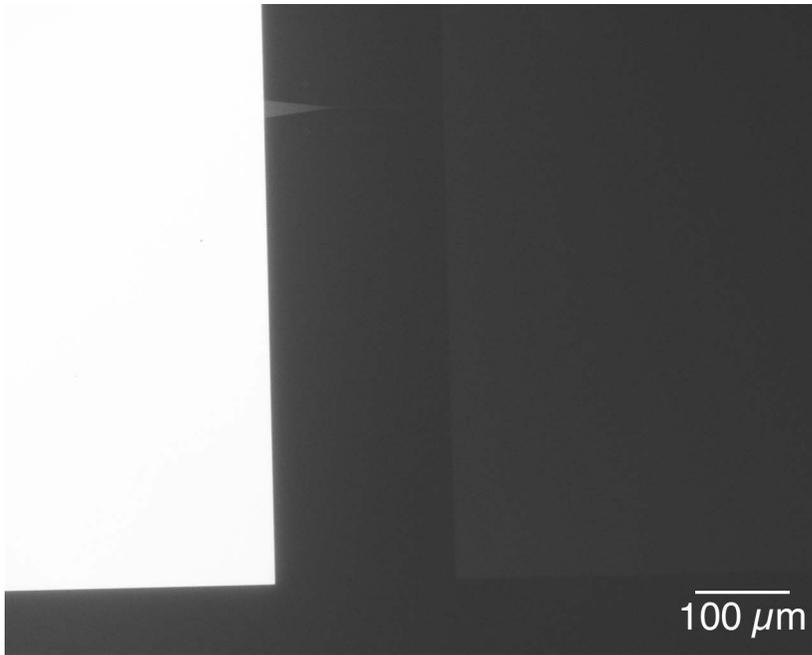
Figure 4.42. Fluorescence green (FITC channel) image (10x) of D2, 800nm wide nanochannel, after 20 hours of FITC introduction. FITC clearly enters nanochannel funnel. FITC signal is very weak (if present) on opposite side of nanochannel. Image is flipped on vertical axis from original.

I also experimented with the 400nm wide nanochannel on D2. I wetted the device by initially introducing methanol, which again did not travel through the nanochannel on inspection within 5min; thus in all steps, I loaded solution in both sides of the nanochannel. I wetted the device with methanol, then water, then 0.2M NaOH, then PBS. I performed a conductance test to confirm the nanochannel was filled with solution. Figure 4.43 displays the test using the Keithley 4200-SCS analyzer.
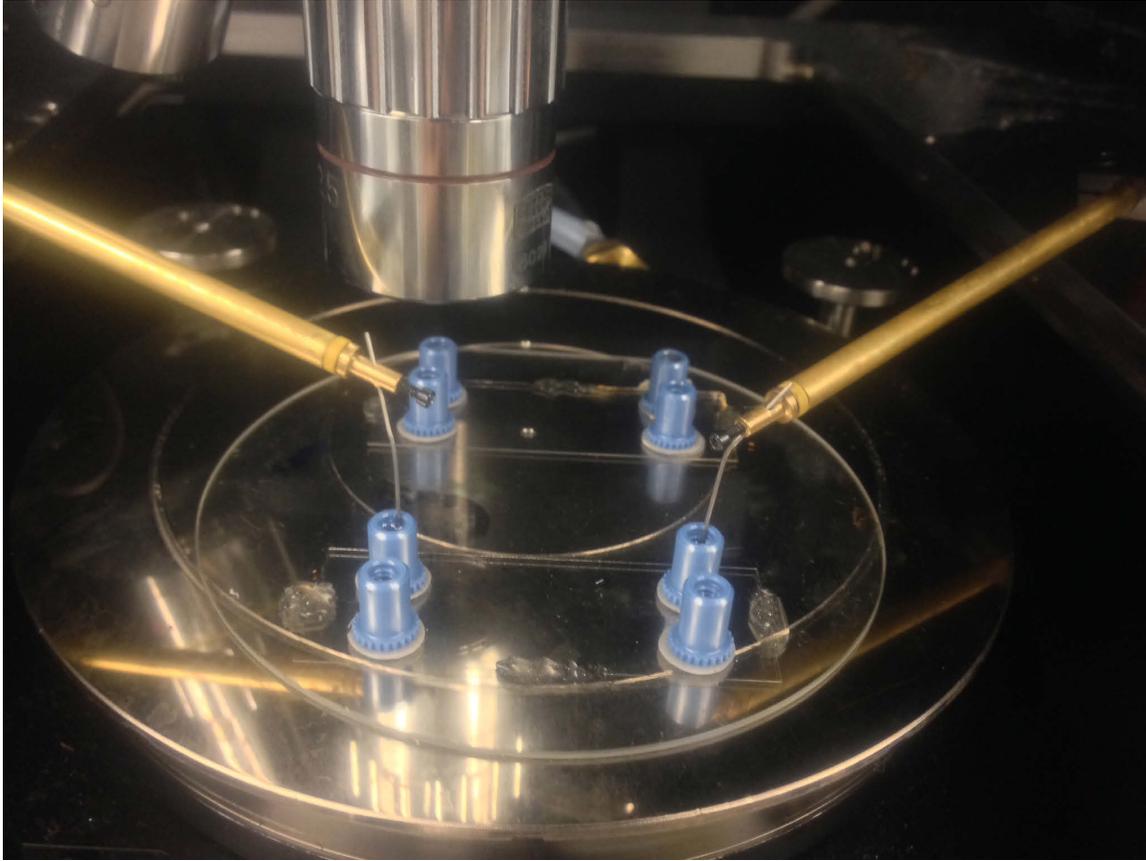
Figure 4.43. D2, 400nm wide nanochannel device being tested for resistance through the device. Tungsten wires from the probe station are immersed in the solution.

A ±1V voltage sweep was performed in air, yielding current in the fA range (ie. no conductance). The resistance of the glass substrate is on the order of $10^{14}\Omega$. When the probes were inserted into reservoirs on opposite sides of the nanochannel, the I-V curve was linear (ohmic), with a resistance of 77 ± 0.06 MΩ (see Figure 4.44). This indicates there is conductive solution across the 400nm nanochannel.
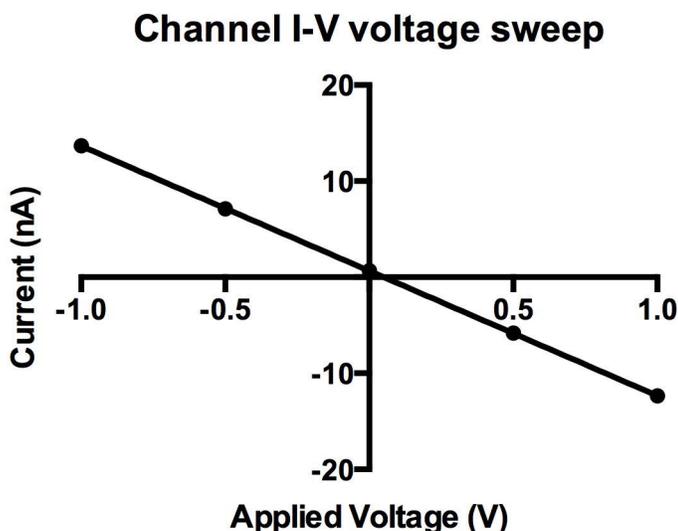
Figure 4.44. Voltage sweeps of D2 top device loaded with PBS (n=4). Error is standard deviation (too small for error bars). Linear regression is y=-13.00*x + 0.66. Slope is -13.00 ± 0.01.

I then proceeded to test whether MTs could be introduced into the nanochannel. I replaced PBS with PEM. I prepared a 0.9 mg/ml casein solution in PEM, which was introduced in the channel for 3.5 hours. I then replaced the casein with PEM/Taxol, and let this stand for 10min. I then added MT solution (2mM tubulin). Imaging did not show MTs entering the microchannels. Tests of applying 100–400V through inserted electrode wires in the solution in the two reservoirs on the side the MTs were introduced did not result in subsequent detection of MTs in the microchannels upon fluorescence imaging. I experienced difficulties with flow through the channels. I introduced FITC (790µM) to the channel on the opposite side that MTs were introduced. After experimentation on subsequent devices made up of only microchannels (steps 5-8), I found that the microchannels were too shallow to support flow of solutions without high pressure, and that such high pressure was likely to break the soft bond of the coverslip with the substrate. Additionally, higher pressures led to solutions leaking out through the reservoir tape unless the reservoirs were attached with epoxy as well. Subsequent imaging of D2 top device with the 400nm nanochannel, 10 days after FITC introduction in the channel and 16 days after MT introduction, showed short MTs in the microchannel, that became less pronounced closer to the nanochannel (see Figure 4.45).
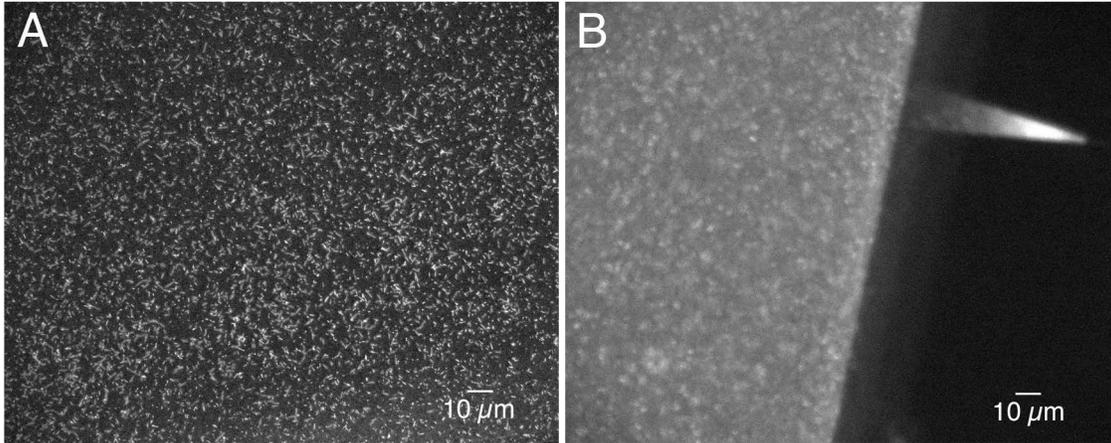
Figure 4.45. (A) 40x red (Cy3) image of MTs in D2, close to reservoir. (B) 40x red (Cy3) image of MTs in D2, close to reservoir. This image is taken 16 days after MTs being introduced into the device, and it appears the MTs have mostly depolymerised during this time.

Fluorescent tubulin entering the nanochannel is visible, but no tubulin is visible through the nanochannel (see Figure 4.46). FITC is clearly entering the nanochannel funnel from the opposite side, and likewise, no FITC appears to have traversed the nanochannel (see Figure 4.47). No confirmed flow appears to exist through the nanochannel based on FITC and fluorescent tubulin intensity.
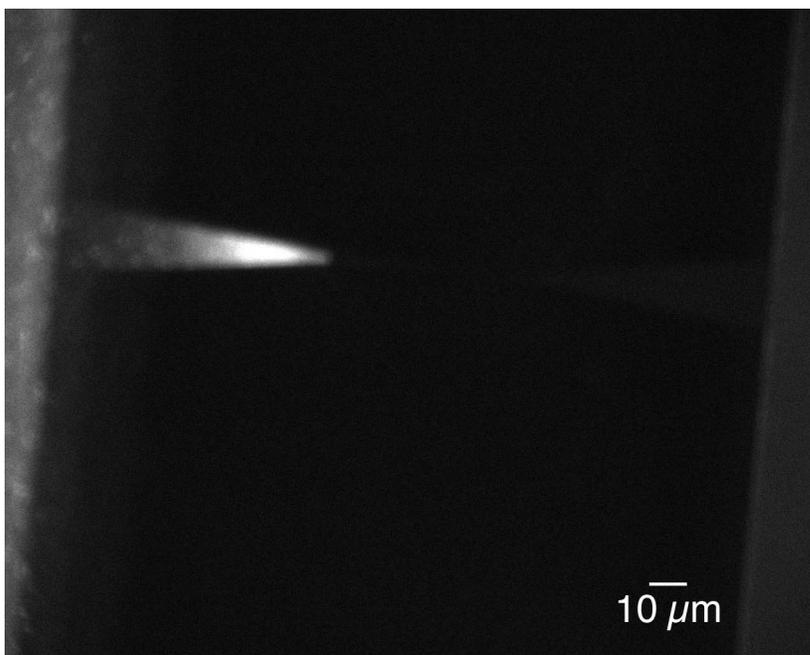
Figure 4.46. 40x red (Cy3) image of tubulin in D2 in 400nm nanochannel funnel. No tubulin seems to have entered the nanochannel, although it has entered the funnel leading to the nanochannel.
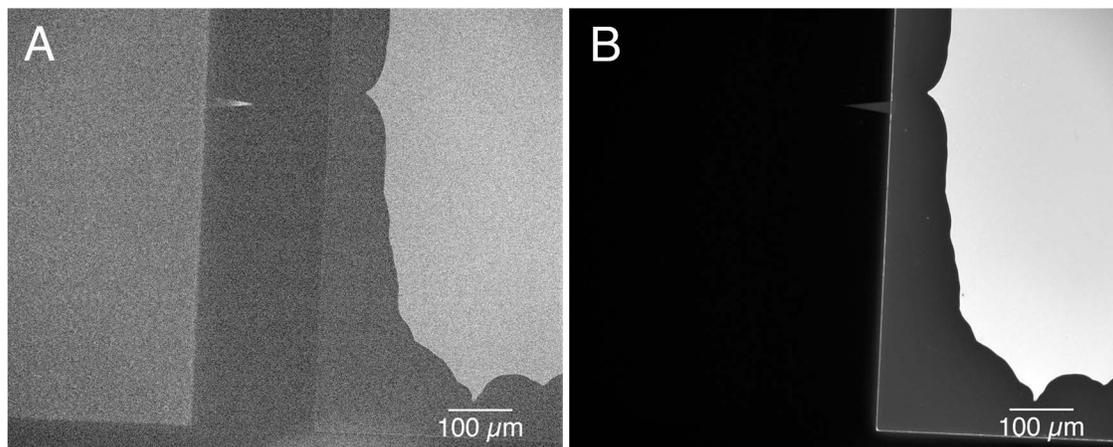
Figure 4.47. (A) 10x red (Cy3 channel) image of tubulin in D2 in 400nm nanochannel funnel. The bright fluorescence on the right side of the nanochannel, as shown in (B), appears to come from the FITC, while the fluorescent tubulin enters the 400nm nanochannel funnel, but little if any tubulin seems to make it through the nanochannel. (B) 10x green (FITC channel) image of tubulin in D2 in 400nm nanochannel funnel. This shows the FITC entering the nanochannel funnel but none if any FITC making it through the nanochannel. (A) and (B) images are taken subsequently at the exact same location and focus.

MTs are able to remain intact 10 days after creation at room temperature. Figure 4.48 shows MTs of length greater than 30 μm persisting after 10 days on a microscope slide at room temperature.
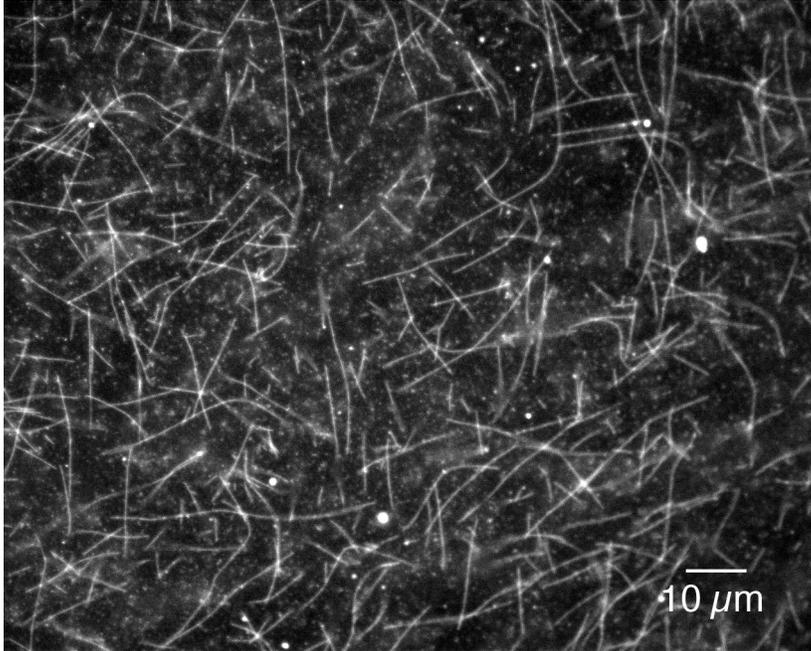
Figure 4.48. MTs (10nM tubulin) 63x red (Cy3) fluorescence image after 10 days at room temperature. MTs longer than 30 µm can be seen.

A new device v. 3.0 (D3) was created, similar to D2 with only microchannels (steps 1, 3 and 4 omitted), to test the width of a nanochannel needed for a MT to enter it. D3 has nanochannels: 200, 300, 400, 600, 800, and 1000 nm wide, as well as a 500nm wide channel with funnels (see Figure 4.49).

Figure 4.49. 20x optical image of D3 after creation of nanochannels. The bottom and top channels are 500nm wide, and the middle nanochannels are designed to be 200, 300, 400, 600, 800, and 1000 nm, starting from the bottom (the 200nm channel is barely visible).

The nanochannels were variable between 87-117nm deep. The microchannels were 1050nm deep. D3 was wetted with methanol, followed by H_2O, casein (0.9 mg/ml) in PEM (for 2 hours). Then MTs (21nM tubulin) were added. No tubulin fluorescence was detected in microchannels or nanochannels, I suspect due to the microchannels being too shallow (~1 μm deep). FITC was added to one side of the device, and was observed to enter and pass through the majority of channels 400nm in width and wider (see Figure 4.50).
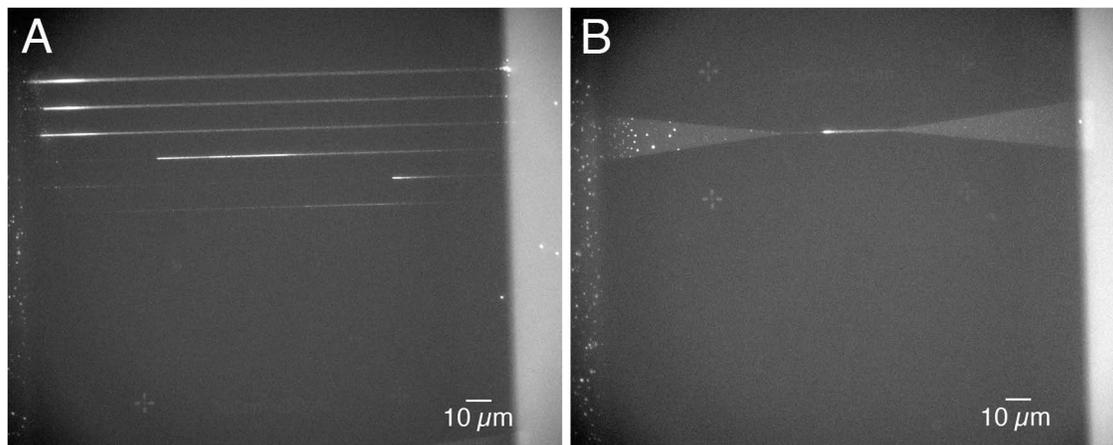
Figure 4.50. (A) 40x green (FITC channel) image of D3. FITC can be seen traversing the nanochannels of width 600, 800, and 1000 nm. FITC is not as visible in the 200, 300, and 400 nm channels. Channels are narrowest at the bottom and widest at the top. (B) 40x green (FITC channel) image of D3. FITC can be seen entering the nanochannel 500nm wide.

4.3.3 Discussion

The device presented represents an important foundation for the design of nanofluidic devices able to isolate a single macromolecule and measure electrical properties of the macromolecule. I demonstrated the ability to manufacture nanoelectrodes embedded in a nanochannel a uniform distance into the channel (Figure 4.37), and data confirming solution traversing channels 400nm and wider (Figure 4.50).

Experimentation with the process used led to a problem where, since the coverslip was soft-bonded to the substrate, exerting too much pressure to push solutions into the reservoir with the syringe pump led to the bond failing. This was caused due to the microchannels at 1μm depth being too shallow and causing too much pressure needed for flow through the ~40mm microchannels. The following recommendations are suggested to refine the device:

- Use a deep reactive ion etching process to make deeper microchannels on the order of 20μm. This process can be done with KMPR negative resist and standard photolithography.

- Use an adhesive bonding procedure with PMMA, as done in [490], so that the coverslip can withstand additional pressure.

Additionally, some improvements to the process may be further optimized. A dose test for optimal exposure parameters was performed, giving 150μC/cm^2 for nanochannels and 175μC/cm^2 for nanowires. Lower dose rates, in the range of 125 μC/cm^2 could be explored further as SEM revealed possible slight overexposure using this process.

Obtaining mass fabricated substrates with prefabricated holes (as was done in [392]) would lead to a large simplification of step 6, as drilling holes in thin coverslips is time consuming and leads to low yield. As well, this setup would lead to attaching the reservoirs to the substrate, and during experiments having the coverslip on the bottom, which would allow an inverted confocal microscope to be used, which in turn would allow for shorter microchannels needed, leading to more devices to be fabricated on a single substrate.

4.4   Discussion and future work

As technology improves to be able to probe smaller features relevant to biology, we will be able to measure with increasing accuracy bioelectric phenomena that have hitherto been inaccessible. It has been hypothesized that MTs, actin, and collagen may form, in addition to a mechanical tensegrity system, a bioelectrical communication system integral to a multicellular organism's organization [61]. Bioelectromagnetics is already having a large impact in cancer treatment [492] and has the potential to be transformative to applications in the field of regeneration and cancer suppression [477, 493]. Exploring such a system is at the edge of our scientific capability, with super-resolution microscopy making advances to image *in vivo* MT dynamics, and nanotechnology able to create systems to probe electrical effects occurring at the nanoscale. As a first step to understanding MT electrical properties *in vivo*, I performed experiments to characterize MT electrical properties in physiological-like solution with micro- and nano-electrodes. I designed and created a microfabricated device with microelectrodes in a flow cell that appeared to have MTs spanning the electrode wires, with initial data supporting the hypothesis that MTs have higher ionic conductivity than physiological-like solutions. I also performed experiments that show that MTs that do not directly connect to electrodes seem to interfere with ionic mobility, which may explain some previous conflicting results on MT conductivity [356, 376]. My design of my flow cells allows for multiple experiments to be performed in a range of ionic environments

174

and conditions, allowing for more high-throughput experimentation than previous work [356]. I also designed and fabricated a nanofluidic channel 400nm wide, interfaced with nanoelectrodes that were regularly embedded 200nm into the nanochannel. I combined these small features made with electron beam lithography to larger microchannels and microelectrode wires and contact pads, forming a device that could in theory trap individual MTs and perform electrical recordings on individual MTs. I confirmed the ability to create nanofluidic channels 400nm and wider; however, further work is needed to perfect the device so that MTs can successfully be trapped in the nanochannel and electrical recordings taken.

My experiments with my flow cell system showed indications that MTs made electrical contact with my microelectrodes, and facilitated electrical signaling across them. Further experimentation is needed to confirm this effect. My experiments show the framework for performing extensive electrical characterization of MTs in a physiological-like environment. Outstanding questions in studying MT electrical effects include:

1. Do MTs have a relevant effect on ionic signals in the salty environment of the cytoplasm?

2. What is the relative electrical effect of possible ionic waves and protonic jump conduction along the outside of the MTs, where MT C-termini may act as a binary signal modulator, versus the lumen of the MT, where a possible highly ordered environment exists, versus intrinsic conductivity of the MT proteins?

3. Is there a length dependence on MT-facilitated conductance?

My experiments show indications that *in vitro*, MTs have higher ionic conductivity than the surrounding physiological-like ionic solution, which is a first step to answering (1). My flow cell experimental setup can be used to rapidly quantify the effects MTs have in physiological-like solutions, which can be used to answer (1) *in vitro*. My system can rapidly study the effects of solutions of various ionic concentrations, especially as MTs appear stuck to the microelectrodes and so different ionic solutions could be introduced over time into the flow cell, and the electrical effect monitored. Once the dependence of MT conductivity on ionic concentration was measured, it might be possible to infer a base conductivity supplied intrinsically by the MT, especially in collaboration with the

group of Bandyopadhyay who is investigating intrinsic MT conductivity using STM and AFM [347, 375], which could answer aspects of (2). Creation of a nanofluidic channel isolating an MT might be adapted to block ionic transport along the outside of the MT but not through the lumen of the MT which could be used as well to answer (2). My flow cell design can be used to answer (3) by modifying the lengths between electrode wires.

Additionally, my flow cell design can be used to perform many more electrical experiments: ultra-fast pulsed I-V experiments can be performed to measure possible increased ionic conductivity along MTs, and AC impedance experiments can be performed to find possible frequencies that facilitate electrical conductivity along MTs. My system could also be used to characterize electrical properties of actin in a similar manner as MTs.

The goal of this research program is to electrically characterize the building blocks of the hypothesized electrical communication system, namely MTs, actin, and collagen, that interconnects the non-excitable cells of the organism. This communication may be instrumental to organism-wide organization and shape maintenance, which when understood could lead to breakthroughs in detection and treatment of cancer and chronic disease that arises from breakdowns in the organization and communication between various systems of the body [61]. The insights into electrical properties of MTs may also lead to breakthroughs in understanding memory, consciousness, and neurodegenerative disease [61, 361, 365].

Future advances relevant to this research program involve not just measuring electrical signals, but imaging them as well.

4.4.1   Imaging electrical signals

Ideally, imaging electrical signal propagation in biological systems would be ideal to study bioelectrical effects. This area has been most active in attempting to image voltage in neurons [494], as electrical signal propagation in neurons is a well-known phenomenon leading to the nervous system. The current challenges of voltage imaging include [494]:

- Having a voltage sensor fast and sensitive enough to show something when the signal may be sub-millisecond
- Localizing the sensor to the domain where the signal is (potentially a few nm in size) without interfering with the system

176

- Having real-time imaging fast enough to image every few ms or less

- Having real-time imaging at enough resolution for the system being studied

Advances to measure voltage changes real-time in live cell is ongoing. A bright voltage sensor that can detect changes in voltage with on and off kinetics in the 2ms range, allowing for reliable detection of action potentials and sub-threshold action potentials in the neuron membrane has recently been reported [495].

Imaging ionic waves along MTs would first involve imaging MTs live. This is now possible with super-resolution STED imaging [496]. Imaging ionic waves instead of just MTs themselves would involve having a voltage sensitive biosensor attached to MTs instead of just having a fluorescent marker for MTs. As a first step towards this, a H_2O_2 sensor has been bound to EB3 (a MT end-binding protein) to show real-time super-resolution STED imaging of H_2O_2 processes in live NIH 3T3 cells [497]. The following limitations were reported [497]:

- Needing brighter biosensors

- Biosensors with higher photostability (to guard against photobleaching)

- Need for faster STED (super-resolution) imaging to see faster processes (especially when proteins and structures are moving in the cell)

As advances in these areas occur, the goal of imaging electrical signals in cells may be reached. Already, advances have been made that allow for long term *in vivo* subcellular monitoring of transmembrane potential of non-excitable cells [498]. This has led to understanding on the membrane potentials role in regulating cell proliferation, migration, shape, and apoptosis [28, 493, 499]. Further studies tracking bioelectric potentials promise great advancements in organ regeneration and cancer suppression [477, 499].

Chapter 5

Conclusions

5.1 Biophysical insights into cancer

The goal of this thesis is that the results and insights obtained by focusing on the biophysical aspects of cancer involving microtubules (MTs) and energy metabolism will lead to improved treatment and prevention of cancer.

Chapter 2 presented the discovery of the first known drug-like interaction with γ-tubulin to our knowledge [137]. This has significance in the development of a novel chemotherapeutic agent for glioblastoma multiforme (GBM), as γ-tubulin, which is instrumental in nucleating microtubules, is overexpressed in GBM [22-26]. My results, which include computational prediction of colchicine's binding site and pose on γ-tubulin, were a significant first step in the rational drug design of an effective small-molecular inhibitor of γ-tubulin. This achievement of discovering the first drug-like ligand interacting with γ-tubulin paved the way forward to investigate γ-tubulin's biological roles in maintaining shape in the cell and its suitability as a cancer target, which has been further explored in [138].

In Chapter 3, I performed two main studies related to altered metabolism found in cancer. First, I quantitatively described how changes in energy metabolism, which are characteristic of cancer cells, lead to a high energetic cost of cancer to the body, especially in late stage cachexic cancer patients. I modeled how a tumor's high demand for glucose and glutamine combined with its high energetic cost contributes to muscle wasting seen in cachexic patients. I used our model to provide an updated estimate of the energetic cost of cancer based on data from previous metabolic studies, for cancer of various mass and levels of anaerobic energy production. This model provides a quantitative understanding of a cause of cachexia in cancer patients from a bioenergetics framework that incorporates the state of altered energy metabolism found in cancer cells [52]. These results lay the foundation for developing additional biomarkers of cancer

progression by monitoring metabolic biomarkers, and my findings suggest therapeutic strategies targeting a tumor's altered energy metabolism could be of benefit in reducing muscle wasting in cancer patients. Second, I investigated targeting energy metabolism using the small molecular compound 3-bromopyruvate (3BP) to develop a combination chemotherapeutic strategy for recurrent epithelial ovarian cancer. This was done using a cell line model of epithelial ovarian cancer at different stages of progression of the disease, which showed changes in cytoskeletal structure and metabolism [40, 58-60]. This study found 3BP to target late-stage ovarian cancer cells preferentially to early-stage cancer cells and gives proof-of-concept of using energy metabolism to target the most tumorigenic and drug resistant ovarian cancer cells, which might be prevalent in recurrent ovarian cancer.

Finally, in Chapter 4, I reviewed direct and indirect evidence indicating conductive properties of microtubules, actin, and collagen, which I refer to as bionanowires [61]. I integrated this knowledge with the understanding that through connections made by integrins and connective proteins, these bionanowires form an organism-wide matrix, which has been hypothesized to function as a communication system regulating the coordination of the organism [63]. I then reported my preliminary findings on measuring MT electrical properties in a physiological-like ionic solution, which support MTs being able to propagate ionic signals, with conductivity in the range of $10^3 - 10^4$ S/m. I also reported my process of microfabricating flow cells to make these electrical measurements, and a process to create nanofluidic channels that upon further refinement could make electrical recordings of individual MTs trapped in the nanofluidic channel.

5.2 Future work

The study to search for γ-tubulin inhibitors in Chapter 2 predicted the binding location of drug-like ligand interactions with γ-tubulin. Experimental verification of these binding locations is the next step for the rational drug design of an effective small-molecular inhibitor of γ-tubulin, and still needs to be done, and could be done in collaboration with recent new findings on specific inhibitors of γ-tubulin [138].

In Chapter 3, my model estimating the energetic cost of cancer based on data from previous metabolic studies, for cancer of various mass and levels of anaerobic energy production, needs to be validated. This will ideally involve a study with estimates of

tumor burden, tumor energy consumption through indirect calorimetry, tumor substrate utilization, and ideally liver glycogen reserves at different stages of cancer disease progression in order to better understand the tumor's energy consumption as a cause of hypermetabolism and weight loss. The key development in technology to aid in our model's validation will be accurate measurement of an *in vivo* tumor's energy substrate usage and energy metabolism profile [190].

Additionally in Chapter 3, we obtained promising *in vitro* data that 3BP targets the most tumorigenic and drug-resistant cells in an epithelial ovarian cancer progression model. A study in immunocompetent mice evaluating 3BP treatment, similar to that done by Ko et al. [173], is indicated. As 3BP is more challenging to work with than most drugs due to its instability in solution, it is recommended that this study be done by those experienced in the delivery of 3BP to animals as done in previous studies [173, 243].

Further replication of results of electrical conductivity from MTs using the methods in Chapter 4 is recommended and planned. As well, further refinement in the microfabrication and nanofabrication methods, and electrical experiments done, as detailed in Chapter 4, is also recommended and planned. Characterizing electrical properties of MTs is the first step toward the larger goal of characterizing electrical properties of actin and collagen to evaluate the possibility of organism-wide electrical signalling, which may be key to the organization and order of an organism, and which may be one factor perturbed in cancer. If this is the case, development of a non-invasive device to detect electrical signaling might be used to monitor and prevent cancer.

References

1. Ingber DE: **Can cancer be reversed by engineering the tumor microenvironment?** *Semin Cancer Biol* 2008, **18:**356-364.
2. Soto AM, Sonnenschein C: **The tissue organization field theory of cancer: a testable replacement for the somatic mutation theory.** *Bioessays* 2011, **33:**332-340.
3. Szent-Györgyi A: **Bioelectronics and cancer.** *J Bioenerg Biomembr* 1973, **4:**533-562.
4. Szent-Györgyi A: **Electronic biology and its relation to cancer.** *Life Sci* 1974, **15:**863-875.
5. Davies PCW, Lineweaver CH: **Cancer tumors as Metazoa 1.0: tapping genes of ancient ancestors.** *Phys Biol* 2011, **8:**015001.
6. Szent-Györgyi A: *Bioelectronics: A Study in Cellular Regulations, Defense, and Cancer.* New York: Academic Press; 1968.
7. Ingber DE: **Cancer as a disease of epithelial–mesenchymal interactions and extracellular matrix regulation.** *Differentiation* 2002, **70:**547-560.
8. Levin M: **Morphogenetic fields in embryogenesis, regeneration, and cancer: Non-local control of complex patterning.** *BioSystems* 2012, **109:**243-261.
9. Levin M: **Bioelectric mechanisms in regeneration: Unique aspects and future perspectives.** *Semin Cell Dev Biol* 2009, **20:**543-556.
10. Cone CD, Jr.: **The role of the surface electrical transmembrane potential in normal and malignant mitogenesis.** *Ann N Y Acad Sci* 1974, **238:**420-435.
11. Levin M, Stevenson CG: **Regulation of Cell Behavior and Tissue Patterning by Bioelectrical Signals: Challenges and Opportunities for Biomedical Engineering.** *Annu Rev Biomed Eng* 2012, **14:**295-323.
12. Shacter E, Weitzman SA: **Chronic Inflammation and Cancer.** *Oncology* 2002, **16:**217-226.
13. Pokorný J, Foletti A, Kobilková J, Jandová A, Vrba J, Vrba JJ, Nedbalová M, Čoček A, Danani A, Tuszynski JA: **Biophysical insights into cancer transformation and treatment.** *The Scientific World Journal* 2013, **2013:**195028.
14. Pokorny J: **Biophysical cancer transformation pathway.** *Electromagn Biol Med* 2009, **28:**105-123.
15. Pokorny J, Vedruccio C, Cifra M, Kucera O: **Cancer physics: diagnostics based on damped cellular elastoelectrical vibrations in microtubules.** *Eur Biophys J* 2011, **40:**747-759.
16. Damadian R: **Tumor Detection by Nuclear Magnetic Resonance.** *Science* 1971, **171:**1151-1153.
17. Kenny PA, Bissell MJ: **Tumor reversion: correction of malignant behavior by microenvironmental cues.** *Int J Cancer* 2003, **107:**688-695.
18. Hendrix MJC, Seftor EA, Seftor REB, Kasemeier-Kulesa J, Kulesa PM, Postovit L-M: **Reprogramming metastatic tumour cells with embryonic microenvironments.** *Nat Rev Cancer* 2007, **7:**246-255.

19. Chernet BT, Levin M: **Transmembrane voltage potential is an essential cellular parameter for the detection and control of tumor development in a Xenopus model.** *Dis Model Mech* 2013, **6:**595-607.

20. Israel BA, Schaeffer WI: **Cytoplasmic suppression of malignancy.** *In Vitro Cell Dev Biol* 1987, **23:**627-632.

21. Davies PCW, Demetrius L, Tuszynski JA: **Cancer as a dynamical phase transition.** *Theor Biol Med Model* 2011, **8:**30.

22. Katsetos CD, Draberova E, Legido A, Draber P: **Tubulin targets in the pathobiology and therapy of glioblastoma multiforme. II. gamma-Tubulin.** *J Cell Physiol* 2009, **221:**514-520.

23. Caracciolo V, D'Agostino L, Draberova E, Sladkova V, Crozier-Fitzgerald C, Agamanolis DP, de Chadarevian JP, Legido A, Giordano A, Draber P, Katsetos CD: **Differential expression and cellular distribution of gamma-tubulin and betaIII-tubulin in medulloblastomas and human medulloblastoma cell lines.** *J Cell Physiol* 2010, **223:**519-529.

24. Katsetos CD, Reddy G, Draberova E, Smejkalova B, Del Valle L, Ashraf Q, Tadevosyan A, Yelin K, Maraziotis T, Mishra OP, et al: **Altered cellular distribution and subcellular sorting of gamma-tubulin in diffuse astrocytic gliomas and human glioblastoma cell lines.** *J Neuropathol Exp Neurol* 2006, **65:**465-477.

25. Katsetos CD, Draberova E, Legido A, Dumontet C, Draber P: **Tubulin targets in the pathobiology and therapy of glioblastoma multiforme. I. Class III beta-tubulin.** *J Cell Physiol* 2009, **221:**505-513.

26. Katsetos CD, Draberova E, Smejkalova B, Reddy G, Bertrand L, de Chadarevian JP, Legido A, Nissanov J, Baas PW, Draber P: **Class III beta-tubulin and gamma-tubulin are co-expressed and form complexes in human glioblastoma cells.** *Neurochem Res* 2007, **32:**1387-1398.

27. Cone CD, Jr.: **Unified theory on the basic mechanism of normal mitotic control and oncogenesis.** *J Theor Biol* 1971, **30:**151-181.

28. Levin M: **Molecular bioelectricity in developmental biology: New tools and recent discoveries.** *Bioessays* 2012, **34:**205-217.

29. Bonnet S, Archer SL, Allalunis-Turner J, Haromy A, Beaulieu C, Thompson R, Lee CT, Lopaschuk GD, Puttagunta L, Harry G, et al: **A mitochondria-K+ channel axis is suppressed in cancer and its normalization promotes apoptosis and inhibits cancer growth.** *Cancer Cell* 2007, **11:**37-51.

30. Chen LB: **Mitochondrial membrane potential in living cells.** *Annu Rev Cell Biol* 1988, **4:**155-181.

31. Modica-Napolitano JS, Singh KK: **Mitochondria as targets for detection and treatment of cancer.** *Expert Reviews in Molecular Medicine* 2002, **4:**1-19.

32. Gillies RJ, Raghunand N, Karczmar GS, Bhujwalla ZM: **MRI of the tumor microenvironment.** *J Magn Reson Imaging* 2002, **16:**430-450.

33. Reshkin SJ, Bellizzi A, Caldeira S, Albarani V, Malanchi I, Poignee M, Alunni-Fabbroni M, Casavola V, Tommasino M: **Na+/H+ exchanger-dependent intracellular alkalinization is an early event in malignant transformation and plays an essential role in the development of subsequent transformation-associated phenotypes.** *FASEB J* 2000, **14:**2185-2197.

34.   Stock C, Schwab A: **Protons make tumor cells move like clockwork.** *Pflugers Archiv - European Journal of Physiology* 2009, **458:**981-992.

35.   Harguindey S, Arranz JL, Wahl ML, Orive G, Reshkin SJ: **Proton transport inhibitors as potentially selective anticancer drugs.** *Anticancer Res* 2009, **29:**2127-2136.

36.   Suresh S: **Biomechanics and biophysics of cancer cells.** *Acta Biomater* 2007, **3:**413-438.

37.   Lekka M, Laidler P, Gil D, Lekki J, Stachura Z, Hrynkiewicz AZ: **Elasticity of normal and cancerous human bladder cells studied by scanning force microscopy.** *Eur Biophys J* 1999, **28:**312-316.

38.   Li QS, Lee GYH, Ong CN, Lim CT: **Probing the Elasticity of Breast Cancer Cells Using AFM.** In *13th International Conference on Biomedical Engineering. Volume* 23. Edited by Lim CT, Goh JCH. Singapore: Springer Berlin Heidelberg; 2009: 2122-2125.

39.   Guck J, Schinkinger S, Lincoln B, Wottawah F, Ebert S, Romeyke M, Lenz D, Erickson HM, Ananthakrishnan R, Mitchell D, et al: **Optical deformability as an inherent cell marker for testing malignant transformation and metastatic competence.** *Biophys J* 2005, **88:**3689-3698.

40.   Creekmore AL, Silkworth WT, Cimini D, Jensen RV, Roberts PC, Schmelz EM: **Changes in gene expression and cellular architecture in an ovarian cancer progression model.** *PLoS ONE* 2011, **6:**e17676.

41.   Ketene AN: **The AFM Study of Ovarian Cell Structural Mechanics in the Progression of Cancer.** *Master's thesis.* Virginia Tech, Mechanical Engineering; 2011.

42.   Rao J, Li N: **Microfilament actin remodeling as a potential target for cancer drug development.** *Curr Cancer Drug Targets* 2004, **4:**345-354.

43.   Summerhayes IC, Wong D, Chen LB: **Effect of microtubules and intermediate filaments on mitochondrial distribution.** *J Cell Sci* 1983, **61:**87-105.

44.   Aufderheide KJ: **Mitochondrial associations with specific microtubular components of the cortex of Tetrahymena thermophila. II. Response of the mitochondrial pattern to changes in the microtubule pattern.** *J Cell Sci* 1980, **42:**247-260.

45.   Anesti V, Scorrano L: **The relationship between mitochondrial shape and function and the cytoskeleton.** *Biochim Biophys Acta* 2006, **1757:**692-699.

46.   Frederick RL, Shaw JM: **Moving mitochondria: establishing distribution of an essential organelle.** *Traffic* 2007, **8:**1668-1675.

47.   Yaffe MP, Stuurman N, Vale RD: **Mitochondrial positioning in fission yeast is driven by association with dynamic microtubules and mitotic spindle poles.** *Proc Natl Acad Sci USA* 2003, **100:**11424-11428.

48.   Levi V, Serpinskaya AS, Gratton E, Gelfand V: **Organelle transport along microtubules in Xenopus melanophores: evidence for cooperation between multiple motors.** *Biophys J* 2006, **90:**318-327.

49.   Watanabe T, Noritake J, Kaibuchi K: **Regulation of microtubules in cell migration.** *Trends Cell Biol* 2005, **15:**76-83.

50.   Pokorny J: **Excitation of vibrations in microtubules in living cells.** *Bioelectrochemistry* 2004, **63:**321-326.

51. Pokorny J: **Electrodynamic activity of healthy and cancer cells.** *J Phys: Conf Ser* 2011, **329:**012007.

52. Friesen DE, Baracos VE, Tuszynski JA: **Modeling the energetic cost of cancer as a result of altered energy metabolism: implications for cachexia.** *Theor Biol Med Model* 2015, **12:**17.

53. Ko YH, Verhoeven HA, Lee MJ, Corbin DJ, Vogl TJ, Pedersen PL: **A translational study "case report" on the small molecule "energy blocker" 3-bromopyruvate (3BP) as a potent anticancer agent: from bench side to bedside.** *J Bioenerg Biomembr* 2012, **44:**163-170.

54. Wintzell M, Lofsted L, Johansson J, Pedersen AB, Fuxe J, Shoshan M: **Repeated cisplatin treatment can lead to a multiresistant tumor cell population with stem cell features and sensitivity to 3-bromopyruvate.** *Cancer Biol Ther* 2012, **13:**1454-1462.

55. Bapat SA, Mali AM, Koppikar CB, Kurrey NK: **Stem and progenitor-like cells contribute to the aggressive behavior of human epithelial ovarian cancer.** *Cancer Res* 2005, **65:**3025-3029.

56. Zhang S, Balch C, Chan MW, Lai H-C, Matei D, Schilder JM, Yan PS, Huang TH-M, Nephew KP: **Identification and characterization of ovarian cancer-initiating cells from primary human tumors.** *Cancer Res* 2008, **68:**4311-4320.

57. Shoshan MC: **3-Bromopyruvate: targets and outcomes.** *J Bioenerg Biomembr* 2012, **44:**7-15.

58. Roberts PC, Mottillo EP, Baxa AC, Heng HHQ, Doyon-Reale N, Gregoire L, Lancaster WD, Rabah R, Schmelz EM: **Sequential molecular and cellular events during neoplastic progression: a mouse syngeneic ovarian cancer model.** *Neoplasia* 2005, **7:**944-956.

59. Anderson AS, Roberts PC, Frisard MI, Brown T, Hulver MW, Schmelz EM: **Metabolic Changes in Ovarian Cancer Progression and Mediation by Sphingosine: The MOSE Model.** In *Virginia Tech Cancer Research Symposium.* 2011

60. Anderson AS, Roberts PC, Frisard MI, McMillan RP, Brown TJ, Lawless MH, Hulver MW, Schmelz EM: **Metabolic Changes During Ovarian Cancer Progression as Targets for Sphingosine Treatment.** *Exp Cell Res* 2013, **319:**1431-1442.

61. Friesen DE, Craddock TJA, Kalra AP, Tuszynski JA: **Biological wires, communication systems, and implications for disease.** *BioSystems* 2015, **127:**14-27.

62. Ingber DE, Wang N, Stamenovic D: **Tensegrity, cellular biophysics, and the mechanics of living systems.** *Rep Prog Phys* 2014, **77:**046603.

63. Oschman JL: *Energy medicine in therapeutics and human performance.* Amsterdam: Butterworth Heinemann; 2003.

64. Stupp R, Hegi ME, Mason WP, van den Bent MJ, Taphoorn MJ, Janzer RC, Ludwin SK, Allgeier A, Fisher B, Belanger K, et al: **Effects of radiotherapy with concomitant and adjuvant temozolomide versus radiotherapy alone on survival in glioblastoma in a randomised phase III study: 5-year analysis of the EORTC-NCIC trial.** *Lancet Oncol* 2009, **10:**459-466.

65. Raynaud-Messina B, Merdes A: **Gamma-tubulin complexes and microtubule organization.** *Curr Opin Cell Biol* 2007, **19:**24-30.

66. Joshi HC, Palacios MJ, McNamara L, Cleveland DW: **Gamma-tubulin is a centrosomal protein required for cell cycle-dependent microtubule nucleation.** *Nature* 1992, **356:**80-83.

67. Zheng Y, Jung MK, Oakley BR: **Gamma-tubulin is present in Drosophila melanogaster and Homo sapiens and is associated with the centrosome.** *Cell* 1991, **65:**817-823.

68. Stearns T, Evans L, Kirschner M: **Gamma-tubulin is a highly conserved component of the centrosome.** *Cell* 1991, **65:**825-836.

69. Keating TJ, Borisy GG: **Immunostructural evidence for the template mechanism of microtubule nucleation.** *Nat Cell Biol* 2000, **2:**352-357.

70. Wiese C, Zheng Y: **A new function for the gamma-tubulin ring complex as a microtubule minus-end cap.** *Nat Cell Biol* 2000, **2:**358-364.

71. Moritz M, Braunfeld MB, Guenebaut V, Heuser J, Agard DA: **Structure of the gamma-tubulin ring complex: a template for microtubule nucleation.** *Nat Cell Biol* 2000, **2:**365-370.

72. Moritz M, Agard DA: **Gamma-tubulin complexes and microtubule nucleation.** *Curr Opin Struct Biol* 2001, **11:**174-181.

73. Wise DO, Krahe R, Oakley BR: **The gamma-tubulin gene family in humans.** *Genomics* 2000, **67:**164-170.

74. Yuba-Kubo A, Kubo A, Hata M, Tsukita S: **Gene knockout analysis of two gamma-tubulin isoforms in mice.** *Dev Biol* 2005, **282:**361-373.

75. Marziale F, Pucciarelli S, Ballarini P, Melki R, Uzun A, Ilyin VA, Detrich HW, 3rd, Miceli C: **Different roles of two gamma-tubulin isotypes in the cytoskeleton of the Antarctic ciliate Euplotes focardii: remodelling of interaction surfaces may enhance microtubule nucleation at low temperature.** *FEBS J* 2008, **275:**5367-5382.

76. Zhou J, Giannakakou P: **Targeting microtubules for cancer chemotherapy.** *Current Medicinal Chemistry - Anti-Cancer Agents* 2005, **5:**65-71.

77. Dumontet C, Jordan MA: **Microtubule-binding agents: a dynamic field of cancer therapeutics.** *Nat Rev Drug Discov* 2010, **9:**790-803.

78. Pettit GR, Singh SB, Hamel E, Lin CM, Alberts DS, Garcia-Kendall D: **Isolation and structure of the strong cell growth and tubulin inhibitor combretastatin A-4.** *Experientia* 1989, **45:**209-211.

79. Bennett MJ, Barakat K, Huzil JT, Tuszynski J, Schriemer DC: **Discovery and characterization of the laulimalide-microtubule binding mode by mass shift perturbation mapping.** *Chem Biol* 2010, **17:**725-734.

80. Huzil JT, Chik JK, Slysz GW, Freedman H, Tuszynski J, Taylor RE, Sackett DL, Schriemer DC: **A unique mode of microtubule stabilization induced by peloruside A.** *J Mol Biol* 2008, **378:**1016-1030.

81. Ye K, Ke Y, Keshava N, Shanks J, Kapp JA, Tekmal RR, Petros J, Joshi HC: **Opium alkaloid noscapine is an antitumor agent that arrests metaphase and induces apoptosis in dividing cells.** *Proc Natl Acad Sci USA* 1998, **95:**1601-1606.

82.   Martin MA, Osmani SA, Oakley BR: **The role of gamma-tubulin in mitotic spindle formation and cell cycle progression in Aspergillus nidulans.** *J Cell Sci* 1997, **110:**623-633.

83.   Oakley BR, Oakley CE, Yoon Y, Jung MK: **Gamma-tubulin is a component of the spindle pole body that is essential for microtubule function in Aspergillus nidulans.** *Cell* 1990, **61:**1289-1301.

84.   Nayak T: **Investigations of the functions of gamma-tubulin in cell cycle regulation in Aspergillus Nidulans.** *PhD dissertation.* Ohio State University, Molecular Genetics; 2008.

85.   Jemal A, Siegel R, Xu J, Ward E: **Cancer statistics, 2010.** *CA Cancer J Clin* 2010, **60:**277-300.

86.   Clarke J, Butowski N, Chang S: **Recent advances in therapy for glioblastoma.** *Arch Neurol* 2010, **67:**279-283.

87.   Johnson DR, O'Neill BP: **Glioblastoma survival in the United States before and during the temozolomide era.** *J Neurooncol* 2012, **107:**359-364.

88.   Stupp R, Taillibert S, Kanner AA, Kesari S, Steinberg DM, Toms SA, Taylor LP, Lieberman F, Silvani A, Fink KL, et al: **Maintenance Therapy With Tumor-Treating Fields Plus Temozolomide vs Temozolomide Alone for Glioblastoma: A Randomized Clinical Trial.** *JAMA* 2015, **314:**2535-2543.

89.   Orsetti B, Nugoli M, Cervera N, Lasorsa L, Chuchana P, Ursule L, Nguyen C, Redon R, du Manoir S, Rodriguez C, Theillet C: **Genomic and expression profiling of chromosome 17 in breast cancer reveals complex patterns of alterations and novel candidate genes.** *Cancer Res* 2004, **64:**6453-6460.

90.   Liu T, Niu Y, Yu Y, Liu Y, Zhang F: **Increased gamma-tubulin expression and P16INK4A promoter methylation occur together in preinvasive lesions and carcinomas of the breast.** *Ann Oncol* 2009, **20:**441-448.

91.   Niu Y, Liu T, Tse GM, Sun B, Niu R, Li HM, Wang H, Yang Y, Ye X, Wang Y, et al: **Increased expression of centrosomal alpha, gamma-tubulin in atypical ductal hyperplasia and carcinoma of the breast.** *Cancer Sci* 2009, **100:**580-587.

92.   Aldaz H, Rice LM, Stearns T, Agard DA: **Insights into microtubule nucleation from the crystal structure of human gamma-tubulin.** *Nature* 2005, **435:**523-527.

93.   Rice LM, Montabana EA, Agard DA: **The lattice as allosteric effector: structural studies of alphabeta- and gamma-tubulin clarify the role of GTP in microtubule assembly.** *Proc Natl Acad Sci USA* 2008, **105:**5378-5383.

94.   Gasteiger E, Hoogland C, Gattiker A, Duvaud S, Wilkins MR, Appel RD, Bairoch A: **Protein Identification and Analysis Tools on the ExPASy Server.** In *The Proteomics Protocols Handbook.* Edited by Walker JM. Totowa, NJ: Humana Press; 2005: 571-607.

95.   Yang M, Xi X, Yang P: **Thermodynamic analysis of fluorescence enhancement and Quenching theory equations.** *Front Chem China* 2008, **3:**254-261.

96.   Lee JC, Harrison D, Timasheff SN: **Interaction of Vinblastine with Calf Brain Microtubule Protein.** *J Biol Chem* 1975, **250:**9276-9282.

97. Barakat K, Mane J, Friesen D, Tuszynski J: **Ensemble-based virtual screening reveals dual-inhibitors for the p53-MDM2/MDMX interactions.** *J Mol Graph Model* 2010, **28:**555-568.

98. Phillips JC, Braun R, Wang W, Gumbart J, Tajkhorshid E, Villa E, Chipot C, Skeel RD, Kale L, Schulten K: **Scalable molecular dynamics with NAMD.** *Journal of Computational Chemistry* 2005, **26:**1781-1802.

99. Dolinsky TJ, Nielsen JE, McCammon JA, Baker NA: **PDB2PQR: an automated pipeline for the setup of Poisson-Boltzmann electrostatics calculations.** *Nucleic Acids Res* 2004, **32:**W665-667.

100. Hornak V, Abel R, Okur A, Strockbine B, Roitberg A, Simmerling C: **Comparison of multiple Amber force fields and development of improved protein backbone parameters.** *Proteins* 2006, **65:**712-725.

101. Case DA, Darden TA, Cheatham TE, Simmerling CL, Wang J, Duke RE, Luo R, Crowley M, Walker RC, Zhang W, et al: *Amber 10.* University of California; 2008.

102. Guex N, Peitsch MC: **SWISS-MODEL and the Swiss-PdbViewer: an environment for comparative protein modeling.** *Electrophoresis* 1997, **18:**2714-2723.

103. Meagher KL, Redman LT, Carlson HA: **Development of polyphosphate parameters for use with the AMBER force field.** *Journal of Computational Chemistry* 2003, **24:**1016-1025.

104. Barakat K, Tuszynski J: **Relaxed complex scheme suggests novel inhibitors for the lyase activity of DNA polymerase beta.** *J Mol Graph Model* 2011, **29:**702-716.

105. Case DA, Darden TA, Cheatham TE, Simmerling CL, Wang J, Duke RE, Luo R, Walker RC, Zhang W, Merz KM, et al: *Amber 11.* University of California; 2010.

106. Ravelli RB, Gigant B, Curmi PA, Jourdain I, Lachkar S, Sobel A, Knossow M: **Insight into tubulin regulation from a complex with colchicine and a stathmin-like domain.** *Nature* 2004, **428:**198-202.

107. Morris GM, Goodsell DS, Halliday RS, Huey R, Hart WE, Belew RK, Olson AJ: *Automated docking using a Lamarckian genetic algorithm and an empirical binding free energy function.* New York, USA: Wiley; 1998.

108. Gasteiger J, Marsili M: **Iterative partial equalization of orbital electronegativity - a rapid access to atomic charges.** *Tetrahedron* 1980, **36:**3219-3228.

109. Mane JY, Klobukowski M, Huzil JT, Tuszynski J: **Free energy calculations on the binding of colchicine and its derivatives with the alpha/beta-tubulin isoforms.** *J Chem Inf Model* 2008, **48:**1824-1832.

110. Dumont R, Brossi A, Chignell CF, Quinn FR, Suffness M: **A novel synthesis of colchicide and analogues from thiocolchicine and congeners: reevaluation of colchicide as a potential antitumor agent.** *J Med Chem* 1987, **30:**732-735.

111. Schaftenaar G, Noordik JH: **Molden: a pre- and post-processing program for molecular and electronic structures.** *J Comput Aided Mol Des* 2000, **14:**123-134.

112. Humphrey W, Dalke A, Schulten K: **VMD: visual molecular dynamics.** *J Mol Graph* 1996, **14:**33-38, 27-38.

187

113. Baker NA, Sept D, Joseph S, Holst MJ, McCammon JA: **Electrostatics of nanosystems: application to microtubules and the ribosome.** *Proc Natl Acad Sci USA* 2001, **98:**10037-10041.

114. Thompson JD, Higgins DG, Gibson TJ: **CLUSTAL W: improving the sensitivity of progressive multiple sequence alignment through sequence weighting, position-specific gap penalties and weight matrix choice.** *Nucleic Acids Res* 1994, **22:**4673-4680.

115. Tahir SK, Kovar P, Rosenberg SH, Ng SC: **Rapid colchicine competition-binding scintillation proximity assay using biotin-labeled tubulin.** *Biotechniques* 2000, **29:**156-160.

116. Lakowicz JR: *Principles of Fluorescence Spectroscopy.* New York, USA: Plenum Press; 1983.

117. Banerjee M, Poddar A, Mitra G, Surolia A, Owa T, Bhattacharyya B: **Sulfonamide drugs binding to the colchicine site of tubulin: thermodynamic analysis of the drug-tubulin interactions by isothermal titration calorimetry.** *J Med Chem* 2005, **48:**547-555.

118. Sardar PS, Maity SS, Das L, Ghosh S: **Luminescence studies of perturbation of tryptophan residues of tubulin in the complexes of tubulin with colchicine and colchicine analogues.** *Biochemistry* 2007, **46:**14544-14556.

119. Banerjee A: **Differential effects of colchicine and its B-ring modified analog MTPT on the assembly-independent GTPase activity of purified beta-tubulin isoforms from bovine brain.** *Biochem Biophys Res Commun* 1997, **231:**698-700.

120. Mane JY, Semenchenko V, Perez-Pineiro R, Winter P, Wishart D, Tuszynski JA: **Experimental and computational study of the interaction of novel colchicinoids with a recombinant human αI/βI-tubulin heterodimer.** *Chem Biol Drug Des* 2013, **82:**60-70.

121. Burns RG: **Analysis of the colchicine-binding site of beta-tubulin.** *FEBS Lett* 1992, **297:**205-208.

122. Detrich HW, 3rd, Williams RC, Jr., Macdonald TL, Wilson L, Puett D: **Changes in the circular dichroic spectrum of colchicine associated with its binding to tubulin.** *Biochemistry* 1981, **20:**5999-6005.

123. Kelleher JK: **Tubulin binding affinities of podophyllotoxin and colchicine analogues.** *Mol Pharmacol* 1977, **13:**232-241.

124. Siemann DW, Chaplin DJ, Walicke PA: **A review and update of the current status of the vasculature-disabling agent combretastatin-A4 phosphate (CA4P).** *Expert Opin Investig Drugs* 2009, **18:**189-197.

125. Lin JH, Perryman AL, Schames JR, McCammon JA: **Computational drug design accommodating receptor flexibility: the relaxed complex scheme.** *J Am Chem Soc* 2002, **124:**5632-5633.

126. Amaro RE, Baron R, McCammon JA: **An improved relaxed complex scheme for receptor flexibility in computer-aided drug design.** *J Comput Aided Mol Des* 2008, **22:**693-705.

127. Lin JH, Perryman AL, Schames JR, McCammon JA: **The relaxed complex method: Accommodating receptor flexibility for drug design with an improved scoring scheme.** *Biopolymers* 2003, **68:**47-62.

128. Mohan V, Gibbs AC, Cummings MD, Jaeger EP, DesJarlais RL: **Docking: successes and challenges.** *Curr Pharm Des* 2005, **11:**323-333.
129. Shao J, Tanner SW, Thompson N, Cheatham TE: **Clustering Molecular Dynamics Trajectories: 1. Characterizing the Performance of Different Clustering Algorithms.** *Journal of Chemical Theory and Computation* 2007, **3:**2312-2334.
130. Davies DL, Bouldin DW: **A cluster separation measure.** *IEEE Transactions on Pattern Analysis and Machine Intelligence* 1979, **1:**224-227.
131. Dyer N: **Tubulin and its prokaryotic homologue FtsZ: a structural and functional comparison.** *Sci Prog* 2009, **92:**113-137.
132. Torin Huzil J, Winter P, Johnson L, Weis AL, Bakos T, Banerjee A, Luduena RF, Damaraju S, Tuszynski JA: **Computational design and biological testing of highly cytotoxic colchicine ring A modifications.** *Chem Biol Drug Des* 2010, **75:**541-550.
133. Alisaraie L, Tuszynski JA: **Determination of noscapine's localization and interaction with the tubulin-alpha/beta heterodimer.** *Chem Biol Drug Des* 2011, **78:**535-546.
134. Semenchenko V, Perez-Pineiro R, Wishart DS: **Unpublished results.** n.d.
135. Guillet V, Knibiehler M, Gregory-Pauron L, Remy MH, Chemin C, Raynaud-Messina B, Bon C, Kollman JM, Agard DA, Merdes A, Mourey L: **Crystal structure of gamma-tubulin complex protein GCP4 provides insight into microtubule nucleation.** *Nat Struct Mol Biol* 2011, **18:**915-919.
136. Inclan YF, Nogales E: **Structural models for the self-assembly and microtubule interactions of gamma-, delta- and epsilon-tubulin.** *J Cell Sci* 2001, **114:**413-422.
137. Friesen DE, Barakat KH, Semenchenko V, Perez-Pineiro R, Fenske BW, Mane J, Wishart DS, Tuszynski JA: **Discovery of small molecule inhibitors that interact with gamma-tubulin.** *Chem Biol Drug Des* 2012, **79:**639-652.
138. Chinen T, Liu P, Shioda S, Pagel J, Cerikan B, Lin T-c, Gruss O, Hayashi Y, Takeno H, Shima T, et al: **The γ-tubulin-specific inhibitor gatastatin reveals temporal requirements of microtubule nucleation during the cell cycle.** *Nat Commun* 2015, **6:**8722.
139. Canadian Cancer Society's Advisory Committee on Cancer Statistics: *Canadian Cancer Statistics 2015.* Toronto, ON: Canadian Cancer Society; 2015.
140. Semenza GL, Artemov D, Bedi A, Bhujwalla Z, Chiles K, Feldser D, Laughner E, Ravi R, Simons J, Taghavi P, Zhong H: **'The metabolism of tumours': 70 years later.** *Novartis Found Symp* 2001, **240:**251-260; discussion 260-254.
141. Altenberg B, Greulich KO: **Genes of glycolysis are ubiquitously overexpressed in 24 cancer classes.** *Genomics* 2004, **84:**1014-1020.
142. Moreno-Sanchez R, Rodriguez-Enriquez S, Marin-Hernandez A, Saavedra E: **Energy metabolism in tumor cells.** *FEBS J* 2007, **274:**1393-1418.
143. Gatenby RA, Gillies RJ: **Why do cancers have high aerobic glycolysis?** *Nat Rev Cancer* 2004, **4:**891-899.
144. Vazquez A, Liu J, Zhou Y, Oltvai ZN: **Catabolic efficiency of aerobic glycolysis: the Warburg effect revisited.** *BMC Syst Biol* 2010, **4:**58.

145. King A, Selak MA, Gottlieb E: **Succinate dehydrogenase and fumarate hydratase: linking mitochondrial dysfunction and cancer.** *Oncogene* 2006, **25:**4675-4682.
146. Warburg O: **On the origin of cancer cells.** *Science* 1956, **123:**309-314.
147. Brand KA, Hermfísse U: **Aerobic glycolysis by proliferating cells: a protective strategy against reactive oxygen species.** *FASEB J* 1997, **11:**388-395.
148. Hanahan D, Weinberg RA: **The hallmarks of cancer.** *Cell* 2000, **100:**57-70.
149. Hanahan D, Weinberg RA: **Hallmarks of cancer: the next generation.** *Cell* 2011, **144:**646-674.
150. Warburg O: **On respiratory impairment in cancer cells.** *Science* 1956, **124:**269-270.
151. Weinhouse S: **On respiratory impairment in cancer cells.** *Science* 1956, **124:**267-272.
152. Weinhouse S: **The Warburg hypothesis fifty years later.** *Zeitschrift für Krebsforschung und Klinische Onkologie* 1976, **87:**115-126.
153. Seyfried T: *Cancer as a Metabolic Disease: On the Origin, Management, and Prevention of Cancer.* Hoboken, NJ: Wiley; 2012.
154. Koppenol WH, Bounds PL, Dang CV: **Otto Warburg's contributions to current concepts of cancer metabolism.** *Nat Rev Cancer* 2011, **11:**325-337.
155. Gambhir SS: **Molecular imaging of cancer with positron emission tomography.** *Nat Rev Cancer* 2002, **2:**683-693.
156. Belhocine T, Spaepen K, Dusart M, Castaigne C, Muylle K, Bourgeois P, Bourgeois D, Dierickx L, Flamen P: **18FDG PET in oncology: the best and the worst (Review).** *Int J Oncol* 2006, **28:**1249-1261.
157. Czernin J, Phelps ME: **Positron emission tomography scanning: current and future applications.** *Annu Rev Med* 2002, **53:**89-112.
158. Garber K: **Energy deregulation: licensing tumors to grow.** *Science* 2006, **312:**1158-1159.
159. Bensinger SJ, Christofk HR: **New aspects of the Warburg effect in cancer cell biology.** *Semin Cell Dev Biol* 2012, **23:**352-361.
160. Pelicano H, Martin DS, Xu RH, Huang P: **Glycolysis inhibition for anticancer treatment.** *Oncogene* 2006, **25:**4633-4646.
161. Vander Heiden MG, Cantley LC, Thompson CB: **Understanding the Warburg effect: the metabolic requirements of cell proliferation.** *Science* 2009, **324:**1029-1033.
162. Tennant DA, Durán RV, Gottlieb E: **Targeting metabolic transformation for cancer therapy.** *Nat Rev Cancer* 2010, **10:**267-277.
163. Galluzzi L, Kepp O, Heiden MGV, Kroemer G: **Metabolic targets for cancer therapy.** *Nature Reviews Drug Discovery* 2013, **12:**829-846.
164. Schulze A, Harris AL: **How cancer metabolism is tuned for proliferation and vulnerable to disruption.** *Nature* 2012, **491:**364-373.
165. Frieden BR, Gatenby RA: **Information dynamics in living systems: prokaryotes, eukaryotes, and cancer.** *PLoS ONE* 2011, **6:**e22085.
166. Gatenby RA, Frieden BR: **Information dynamics in carcinogenesis and tumor growth.** *Mutat Res* 2004, **568:**259-273.

167. Gatenby RA, Gillies RJ: **A microenvironmental model of carcinogenesis.** *Nat Rev Cancer* 2008, **8:**56-61.

168. Gatenby RA, Gillies RJ, Brown JS: **Evolutionary dynamics of cancer prevention.** *Nat Rev Cancer* 2010, **10:**526-527.

169. Rasmussen AK, Chatterjee A, Rasmussen LJ, Singh KK: **Mitochondria-mediated nuclear mutator phenotype in Saccharomyces cerevisiae.** *Nucleic Acids Res* 2003, **31:**3909-3917.

170. Hirschey MD, DeBerardinis RJ, Diehl AME, Drew JE, Frezza C, Green MF, Jones LW, Ko YH, Le A, Lea MA, et al: **Dysregulated metabolism contributes to oncogenesis.** *Semin Cancer Biol* 2015, **35 Suppl:**S129-150.

171. Seyfried TN, Shelton LM: **Cancer as a metabolic disease.** *Nutr Metab* 2010, **7:**7.

172. Boroughs LK, DeBerardinis RJ: **Metabolic pathways promoting cancer cell survival and growth.** *Nat Cell Biol* 2015, **17:**351-359.

173. Ko YH, Smith BL, Wang Y, Pomper MG, Rini DA, Torbenson MS, Hullihen J, Pedersen PL: **Advanced cancers: eradication in all cases using 3-bromopyruvate therapy to deplete ATP.** *Biochem Biophys Res Commun* 2004, **324:**269-275.

174. Karst AM, Drapkin R: **Ovarian cancer pathogenesis: a model in evolution.** *Journal of Oncology* 2010, **2010:**932371.

175. Jemal A, Siegel R, Ward E, Hao Y, Xu J, Murray T, Thun MJ: **Cancer statistics, 2008.** *CA Cancer J Clin* 2008, **58:**71-96.

176. Sharma R, Anker S: **First Cachexia Symposium, Berlin, Germany, 1st–2nd December, 2000.** *Eur J Heart Fail* 2001, **3:**751-754.

177. Fearon K, Strasser F, Anker SD, Bosaeus I, Bruera E, Fainsinger RL, Jatoi A, Loprinzi C, Macdonald N, Mantovani G, et al: **Definition and classification of cancer cachexia: an international consensus.** *Lancet Oncol* 2011, **12:**489-495.

178. Evans WJ, Morley JE, Argilés J, Bales C, Baracos V, Guttridge D, Jatoi A, Kalantar-Zadeh K, Lochs H, Mantovani G, et al: **Cachexia: A new definition.** *Clin Nutr* 2008, **27:**793-799.

179. Dodson S, Baracos VE, Jatoi A, Evans WJ, Cella D, Dalton JT, Steiner MS: **Muscle wasting in cancer cachexia: clinical implications, diagnosis, and emerging treatment strategies.** *Annu Rev Med* 2011, **62:**265-279.

180. Johns N, Stephens NA, Fearon KCH: **Muscle wasting in cancer.** *Int J Biochem Cell Biol* 2013, **45:**2215-2229.

181. Fearon KCH, Moses AGW: **Cancer cachexia.** *Int J Cardiol* 2002, **85:**73-81.

182. Bosaeus I, Daneryd P, Svanberg E, Lundholm K: **Dietary intake and resting energy expenditure in relation to weight loss in unselected cancer patients.** *Int J Cancer* 2001, **93:**380-383.

183. Cao D-x, Wu G-h, Zhang B, Quan Y-j, Wei J, Jin H, Jiang Y, Yang Z-a: **Resting energy expenditure and body composition in patients with newly detected cancer.** *Clin Nutr* 2010, **29:**72-77.

184. Del Fabbro E, Hui D, Dalal S, Dev R, Nooruddin ZI, Noorhuddin Z, Bruera E: **Clinical outcomes and contributors to weight loss in a cancer cachexia clinic.** *J Palliat Med* 2011, **14:**1004-1008.

185. Xu WP, Cao DX, Lin ZM, Wu GH, Chen L, Zhang JP, Zhang B, Yang ZA, Jiang Y, Han YS, et al: **Analysis of energy utilization and body composition in**

kidney, bladder, and adrenal cancer patients. *Urologic Oncology* 2012, **30:**711-718.

186. Moreno-Sanchez R, Rodriguez-Enriquez S, Saavedra E, Marin-Hernandez A, Gallardo-Perez JC: **The bioenergetics of cancer: is glycolysis the main ATP supplier in all tumor cells?** *Biofactors* 2009, **35:**209-225.

187. Zu XL, Guppy M: **Cancer metabolism: facts, fantasy, and fiction.** *Biochem Biophys Res Commun* 2004, **313:**459-465.

188. Rodríguez-Enríquez S, Gallardo-Pérez JC, Avilés-Salas A, Marín-Hernández A, Carreño-Fuentes L, Maldonado-Lagunas V, Moreno-Sánchez R: **Energy metabolism transition in multi-cellular human tumor spheroids.** *J Cell Physiol* 2008, **216:**189-197.

189. Kiebish MA, Han X, Cheng H, Seyfried TN: **In vitro growth environment produces lipidomic and electron transport chain abnormalities in mitochondria from non-tumorigenic astrocytes and brain tumours.** *ASN Neuro* 2009, **1:**art:e00011.

190. Maher EA, Marin-Valencia I, Bachoo RM, Mashimo T, Raisanen J, Hatanpaa KJ, Jindal A, Jeffrey FM, Choi C, Madden C, et al: **Metabolism of [U-13 C]glucose in human brain tumors in vivo.** *NMR Biomed* 2012, **25:**1234-1244.

191. Fan TWM, Lane AN, Higashi RM, Farag MA, Gao H, Bousamra M, Miller DM: **Altered regulation of metabolic pathways in human lung cancer discerned by (13)C stable isotope-resolved metabolomics (SIRM).** *Mol Cancer* 2009, **8:**41.

192. Edén E, Edström S, Bennegård K, Scherstén T, Lundholm K: **Glucose flux in relation to energy expenditure in malnourished patients with and without cancer during periods of fasting and feeding.** *Cancer Res* 1984, **44:**1718-1724.

193. Holroyde CP, Skutches CL, Boden G, Reichard GA: **Glucose Metabolism in Cachectic Patients with Colorectal Cancer.** *Cancer Res* 1984, **44:**5910-5913.

194. Holroyde CP, Gabuzda TG, Putnam RC, Paul P, Reichard GA: **Altered glucose metabolism in metastatic carcinoma.** *Cancer Res* 1975, **35:**3710-3714.

195. Lundholm K, Edström S, Karlberg I, Ekman L, Scherstén T: **Glucose turnover, gluconeogenesis from glycerol, and estimation of net glucose cycling in cancer patients.** *Cancer* 1982, **50:**1142-1150.

196. Tayek JA, Katz J: **Glucose production, recycling, Cori cycle, and gluconeogenesis in humans: relationship to serum cortisol.** *Am J Physiol Endocrinol Metab* 1997, **272:**E476-E484.

197. Kallerhoff M, Karnebogen M, Singer D, Dettenbach A, Gralher U, Ringert RH: **Microcalorimetric measurements carried out on isolated tumorous and nontumorous tissue samples from organs in the urogenital tract in comparison to histological and impulse-cytophotometric investigations.** *Urol Res* 1996, **24:**83-91.

198. DeBerardinis RJ, Mancuso A, Daikhin E, Nissim I, Yudkoff M, Wehrli S, Thompson CB: **Beyond aerobic glycolysis: transformed cells can engage in glutamine metabolism that exceeds the requirement for protein and nucleotide synthesis.** *Proc Natl Acad Sci USA* 2007, **104:**19345-19350.

199. Ferrannini E: **The theoretical bases of indirect calorimetry: a review.** *Metabolism* 1988, **37:**287-301.

200. Douglas RG, Shaw JHF: **Metabolic effects of cancer.** *Br J Surg* 1990, **77:**246-254.
201. Gold J: **Cancer cachexia and gluconeogenesis.** *Ann N Y Acad Sci* 1974, **230:**103-110.
202. Hall KD, Baracos VE: **Computational modeling of cancer cachexia.** *Curr Opin Clin Nutr Metab Care* 2008, **11:**214-221.
203. Koea JB, Shaw JH: **The effect of tumor bulk on the metabolic response to cancer.** *Ann Surg* 1992, **215:**282-288.
204. Straub RH, Cutolo M, Buttgereit F, Pongratz G: **Energy regulation and neuroendocrine-immune control in chronic inflammatory diseases.** *J Intern Med* 2010, **267:**543-560.
205. Rich PR: **The molecular machinery of Keilin's respiratory chain.** *Biochem Soc Trans* 2003, **31:**1095-1105.
206. Lieffers JR, Mourtzakis M, Hall KD, McCargar LJ, Prado CM, Baracos VE: **A viscerally driven cachexia syndrome in patients with advanced colorectal cancer: contributions of organ and tumor mass to whole-body energy demands.** *Am J Clin Nutr* 2009, **89:**1173-1179.
207. Dempsey DT, Feurer ID, Knox LS, Crosby LO, Buzby GP, Mullen JL: **Energy expenditure in malnourished gastrointestinal cancer patients.** *Cancer* 1984, **53:**1265-1273.
208. Cunningham JJ: **Body composition as a determinant of energy expenditure: a synthetic review and a proposed general prediction equation.** *Am J Clin Nutr* 1991, **54:**963-969.
209. Heymsfield SB, Müller MJ, Bosy-Westphal A, Thomas D, Shen W: **Human brain mass: similar body composition associations as observed across mammals.** *American Journal of Human Biology* 2012, **24:**479-485.
210. Elia M: **Organ and tissue contribution to metabolic rate.** In *Energy metabolism: tissue determinants and cellular corollaries.* Edited by Kinney J, Tucker HN. New York: Raven Press; 1992: 61-79.
211. Fanciulli M, Bruno T, Castiglione S, Del Carlo C, Paggi MG, Floridi A: **Glucose metabolism in adriamycin-sensitive and -resistant LoVo human colon carcinoma cells.** *Oncol Res* 1993, **5:**357-362.
212. Busk M, Horsman MR, Kristjansen PEG, van der Kogel AJ, Bussink J, Overgaard J: **Aerobic glycolysis in cancers: implications for the usability of oxygen-responsive genes and fluorodeoxyglucose-PET as markers of tissue hypoxia.** *Int J Cancer* 2008, **122:**2726-2734.
213. Guppy M, Leedman P, Zu X, Russell V: **Contribution by different fuels and metabolic pathways to the total ATP turnover of proliferating MCF-7 breast cancer cells.** *Biochem J* 2002, **364:**309-315.
214. Scott CB: **Contribution of anaerobic energy expenditure to whole body thermogenesis.** *Nutr Metab* 2005, **2:**14.
215. Jebb SA, Osborne RJ, Dixon AK, Bleehen NM, Elia M: **Measurements of resting energy expenditure and body composition before and after treatment of small cell lung cancer.** *Ann Oncol* 1994, **5:**915-919.

216. Reichard GA, Moury NF, Hochella NJ, Patterson AL, Weinhouse S: **Quantitative Estimation of the Cori Cycle in the Human.** *J Biol Chem* 1963, **238:**495-501.

217. Hirai K, Ishiko O, Tisdale M: **Mechanism of Depletion of Liver Glycogen in Cancer Cachexia.** *Biochem Biophys Res Commun* 1997, **241:**49-52.

218. Kleiber M: **Body size and metabolism.** *Hilgardia* 1932, **6:**315-353.

219. Ptitsyn AA, Weil MM, Thamm DH: **Systems biology approach to identification of biomarkers for metastatic progression in cancer.** *BMC Bioinformatics* 2008, **9:**S8.

220. Mandrekar SJ, An M-W, Meyers J, Grothey A, Bogaerts J, Sargent DJ: **Evaluation of Alternate Categorical Tumor Metrics and Cut Points for Response Categorization Using the RECIST 1.1 Data Warehouse.** *J Clin Oncol* 2014, **32:**841-850.

221. Tateishi U, Tatsumi M, Terauchi T, Ando K, Niitsu N, Kim WS, Suh C, Ogura M, Tobinai K: **Prognostic significance of metabolic tumor burden by positron emission tomography/computed tomography in patients with relapsed/refractory diffuse large B-cell lymphoma.** *Cancer Sci* 2015, **106:**186-193.

222. Zhao Y, Butler EB, Tan M: **Targeting cellular metabolism to improve cancer therapeutics.** *Cell Death Dis* 2013, **4:**e532.

223. Brand K: **Aerobic glycolysis by proliferating cells: protection against oxidative stress at the expense of energy yield.** *J Bioenerg Biomembr* 1997, **29:**355-364.

224. Vaupel P, Kallinowski F, Okunieff P: **Blood flow, oxygen and nutrient supply, and metabolic microenvironment of human tumors: a review.** *Cancer Res* 1989, **49:**6449-6465.

225. Medina MÁ: **Glutamine and Cancer.** *J Nutr* 2001, **131:**25395-25425.

226. Vasseur S, Tomasini R, Tournaire R, Iovanna JL: **Hypoxia induced tumor metabolic switch contributes to pancreatic cancer aggressiveness.** *Cancers* 2010, **2:**2138-2152.

227. Brennan MF: **Uncomplicated starvation versus cancer cachexia.** *Cancer Res* 1977, **37:**2359-2364.

228. Barber MD, Ross JA, Fearon KCH: **Cancer cachexia.** *Surg Oncol* 1999, **8:**133-141.

229. Fearon KCH, von Meyenfeldt MF, Moses AGW, Van Geenen R, Roy A, Gouma DJ, Giacosa A, Van Gossum A, Bauer J, Barber MD, et al: **Effect of a protein and energy dense N-3 fatty acid enriched oral supplement on loss of weight and lean tissue in cancer cachexia: a randomised double blind trial.** *Gut* 2003, **52:**1479-1486.

230. Ravasco P: **Dietary Counseling Improves Patient Outcomes: A Prospective, Randomized, Controlled Trial in Colorectal Cancer Patients Undergoing Radiotherapy.** *J Clin Oncol* 2005, **23:**1431-1438.

231. Bozzetti F, Arends J, Lundholm K, Micklewright A, Zurcher G, Muscaritoli M, ESPEN: **ESPEN Guidelines on Parenteral Nutrition: non-surgical oncology.** *Clin Nutr* 2009, **28:**445-454.

232. Arends J, Bodoky G, Bozzetti F, Fearon K, Muscaritoli M, Selga G, van Bokhorst-de van der Schueren MAE, von Meyenfeldt M, Zurcher G, Fietkau R, et al: **ESPEN Guidelines on Enteral Nutrition: Non-surgical oncology.** *Clin Nutr* 2006, **25:**245-259.

233. Dev R, Hui D, Chisholm G, Delgado-Guay M, Dalal S, Del Fabbro E, Bruera E: **Hypermetabolism and symptom burden in advanced cancer patients evaluated in a cachexia clinic.** *Journal of Cachexia, Sarcopenia and Muscle* 2015, **6:**95-98.

234. Ferlay J, Shin HR, Bray F, Forman D, C. M, Parkin DM: **GLOBOCAN 2008 v2.0, Cancer Incidence and Mortality Worldwide: IARC CancerBase No. 10.** 2010 [http://globocan.iarc.fr]

235. Jemal A, Siegel R, Ward E, Hao Y, Xu J, Thun MJ: **Cancer Statistics, 2009.** *CA Cancer J Clin* 2009, **59:**225-249.

236. Pecorelli S, Favalli G, Zigliani L, Odicino F: **Cancer in women.** *International Journal of Gynecology and Obstetrics* 2003, **82:**369-379.

237. Luo L, Zeng J, Liang B, Zhao Z, Sun L, Cao D, Yang J, Shen K: **Ovarian cancer cells with the CD117 phenotype are highly tumorigenic and are related to chemotherapy outcome.** *Exp Mol Pathol* 2011, **91:**596-602.

238. Vanderhyden BC, Shaw TJ, Ethier JF: **Animal models of ovarian cancer.** *Reprod Biol Endocrinol* 2003, **1:**67.

239. Boger-Megiddo I, Weiss NS: **Histologic subtypes and laterality of primary epithelial ovarian tumors.** *Gynecol Oncol* 2005, **97:**80-83.

240. Berry NB, Bapat SA: **Ovarian cancer plasticity and epigenomics in the acquisition of a stem-like phenotype.** *J Ovarian Res* 2008, **1:**8.

241. Szotek PP, Pieretti-Vanmarcke R, Masiakos PT, Dinulescu DM, Connolly D, Foster R, Dombkowski D, Preffer F, MacLaughlin DT, Donahoe PK: **Ovarian cancer side population defines cells with stem cell-like characteristics and Mullerian Inhibiting Substance responsiveness.** *Proc Natl Acad Sci USA* 2006.

242. Kroemer G, Pouyssegur J: **Tumor Cell Metabolism: Cancer's Achilles' Heel.** *Cancer Cell* 2008, **13:**472-482.

243. Vali M, Vossen JA, Buijs M, Engles JM, Liapi E, Ventura VP, Khwaja A, Acha-Ngwodo O, Shanmugasundaram G, Syed L, et al: **Targeting of VX2 Rabbit Liver Tumor by Selective Delivery of 3-Bromopyruvate: A Biodistribution and Survival Study.** *J Pharmacol Exp Ther* 2008, **327:**32-37.

244. Birsoy K, Wang T, Possemato R, Yilmaz OH, Koch CE, Chen WW, Hutchins AW, Gultekin Y, Peterson TR, Carette JE, et al: **MCT1-mediated transport of a toxic molecule is an effective strategy for targeting glycolytic tumors.** *Nat Genet* 2013, **45:**104-108.

245. Latifi A, Abubaker K, Castrechini N, Ward AC, Liongue C, Dobill F, Kumar J, Thompson EW, Quinn MA, Findlay JK, Ahmed N: **Cisplatin treatment of primary and metastatic epithelial ovarian carcinomas generates residual cells with mesenchymal stem cell-like profile.** *J Cell Biochem* 2011, **112:**2850-2864.

246. Limei Z, Yong C, Yan X, Shuai T, Jiangyan X, Zhiqing L: **Accuracy of Positron Emission Tomography/Computed Tomography in the Diagnosis and Restaging for Recurrent Ovarian Cancer: A Meta-Analysis.** *Int J Gynecol Cancer* 2013, **23:**1-10.

247. Yuan S, Wang F, Chen G, Zhang H, Feng L, Wang L, Colman H, Keating MJ, Li X, Xu RH, et al: **Effective elimination of cancer stem cells by a novel drug combination strategy.** *Stem Cells* 2013, **31:**23-34.

248. Pedersen PL: **3-bromopyruvate (3BP) a fast acting, promising, powerful, specific, and effective "small molecule" anti-cancer agent taken from labside to bedside: introduction to a special issue.** *J Bioenerg Biomembr* 2012, **44:**1-6.

249. Auersperg N, Wong AST, Choi K-C, Kang SK, Leung PCK: **Ovarian Surface Epithelium: Biology, Endocrinology, and Pathology.** *Endocr Rev* 2001, **22:**255-288.

250. Goff BA: **Ovarian cancer: screening and early detection.** *Obstet Gynecol Clin North Am* 2012, **39:**183-194.

251. Buys SS, Partridge E, Black A, Johnson CC, Lamerato L, Isaacs C, Reding DJ, Greenlee RT, Yokochi LA, Kessel B, et al: **Effect of screening on ovarian cancer mortality: the Prostate, Lung, Colorectal and Ovarian (PLCO) Cancer Screening Randomized Controlled Trial.** *JAMA* 2011, **305:**2295-2303.

252. Vaughan S, Coward JI, Bast RC, Berchuck A, Berek JS, Brenton JD, Coukos G, Crum CC, Drapkin R, Etemadmoghadam D, et al: **Rethinking ovarian cancer: recommendations for improving outcomes.** *Nat Rev Cancer* 2011, **11:**719-725.

253. Pinato DJ, Graham J, Gabra H, Sharma R: **Evolving concepts in the management of drug resistant ovarian cancer: dose dense chemotherapy and the reversal of clinical platinum resistance.** *Cancer Treat Rev* 2013, **39:**153-160.

254. Matei D, Fang F, Shen C, Schilder J, Arnold A, Zeng Y, Berry WA, Huang T, Nephew KP: **Epigenetic resensitization to platinum in ovarian cancer.** *Cancer Res* 2012, **72:**2197-2205.

255. Khalique L, Ayhan A, Weale ME, Jacobs IJ, Ramus SJ, Gayther SA: **Genetic intra-tumour heterogeneity in epithelial ovarian cancer and its implications for molecular diagnosis of tumours.** *J Pathol* 2007, **211:**286-295.

256. Kurman RJ, Shih I-M: **The origin and pathogenesis of epithelial ovarian cancer: a proposed unifying theory.** *Am J Surg Pathol* 2010, **34:**433-443.

257. Bowtell DDL: **The genesis and evolution of high-grade serous ovarian cancer.** *Nat Rev Cancer* 2010, **10:**803-808.

258. Matei DE, Nephew KP: **Epigenetic therapies for chemoresensitization of epithelial ovarian cancer.** *Gynecol Oncol* 2010, **116:**195-201.

259. Dang CV, Hamaker M, Sun P, Le A, Gao P: **Therapeutic targeting of cancer cell metabolism.** *J Mol Med* 2011, **89:**205-212.

260. Kim HW, Won KS, Zeon SK, Ahn B-C, Gayed IW: **Peritoneal carcinomatosis in patients with ovarian cancer: enhanced CT versus 18F-FDG PET/CT.** *Clin Nucl Med* 2013, **38:**93-97.

261. Qin JZ, Xin H, Nickoloff BJ: **3-Bromopyruvate induces necrotic cell death in sensitive melanoma cell lines.** *Biochem Biophys Res Commun* 2010, **396:**495-500.

262. Sheng H, Niu B, Sun H: **Metabolic targeting of cancers: from molecular mechanisms to therapeutic strategies.** *Curr Med Chem* 2009, **16:**1561-1587.

263. Michelakis ED, Sutendra G, Dromparis P, Webster L, Haromy A, Niven E, Maguire C, Gammer TL, Mackey JR, Fulton D, et al: **Metabolic modulation of glioblastoma with dichloroacetate.** *Sci Transl Med* 2010, **2:**31ra34.

264. Mathupala SP, Ko YH, Pedersen PL: **The pivotal roles of mitochondria in cancer: Warburg and beyond and encouraging prospects for effective therapies.** *Biochim Biophys Acta* 2010, **1797:**1225-1230.

265. Pedersen PL, Mathupala S, Rempel A, Geschwind JF, Ko YH: **Mitochondrial bound type II hexokinase: a key player in the growth and survival of many cancers and an ideal prospect for therapeutic intervention.** *Biochim Biophys Acta* 2002, **1555:**14-20.

266. Xu RH, Pelicano H, Zhou Y, Carew JS, Feng L, Bhalla KN, Keating MJ, Huang P: **Inhibition of glycolysis in cancer cells: a novel strategy to overcome drug resistance associated with mitochondrial respiratory defect and hypoxia.** *Cancer Res* 2005, **65:**613-621.

267. Lunt SY, Vander Heiden MG: **Aerobic glycolysis: meeting the metabolic requirements of cell proliferation.** *Annu Rev Cell Dev Biol* 2011, **27:**441-464.

268. Wallace DC: **Mitochondria and cancer.** *Nat Rev Cancer* 2012, **12:**685-698.

269. Rodríguez-Enríquez S, Marín-Hernández A, Gallardo-Pérez JC, Carreño-Fuentes L, Moreno-Sánchez R: **Targeting of cancer energy metabolism.** *Mol Nutr Food Res* 2009, **53:**29-48.

270. Madhok BM, Yeluri S, Perry SL, Hughes TA, Jayne DG: **Targeting Glucose Metabolism.** *Am J Clin Oncol* 2011, **34:**628-635.

271. Yeluri S, Madhok B, Prasad KR, Quirke P, Jayne DG: **Cancer's craving for sugar: an opportunity for clinical exploitation.** *J Cancer Res Clin Oncol* 2009, **135:**867-877.

272. Yeluri S, Madhok BM, Jayne DG: **New Horizons in Cancer Therapy: Manipulating Tumour Metabolism.** *Biomedical Research*, **23:**17-23.

273. Hockenbery DM: **Targeting mitochondria for cancer therapy.** *Environ Mol Mutagen* 2010, **51:**476-489.

274. Pedersen PL: **The cancer cell's "power plants" as promising therapeutic targets: An overview.** *J Bioenerg Biomembr* 2007, **39:**1-12.

275. DeBerardinis RJ, Lum JJ, Hatzivassiliou G, Thompson CB: **The biology of cancer: metabolic reprogramming fuels cell growth and proliferation.** *Cell Metab* 2008, **7:**11-20.

276. Vander Heiden MG, Locasale JW, Swanson KD, Sharfi H: **Evidence for an Alternative Glycolytic Pathway in Rapidly Proliferating Cells.** *Science* 2010, **329:**1492-1499.

277. El Mjiyad N, Caro-Maldonado A, Ramírez-Peinado S, Muñoz-Pinedo C: **Sugar-free approaches to cancer cell killing.** *Oncogene* 2010, **30:**253-264.

278. Wallace DC: **A Mitochondrial Paradigm of Metabolic and Degenerative Diseases, Aging, and Cancer: A Dawn for Evolutionary Medicine.** *Annu Rev Genet* 2005, **39:**359-407.

279. Hsu PP, Sabatini DM: **Cancer cell metabolism: Warburg and beyond.** *Cell* 2008, **134:**703-707.

280. Sheng H, Niu B, Sun H: **Metabolic Targeting of Cancers: From Molecular Mechanisms to Therapeutic Strategies.** *Curr Med Chem* 2009, **16:**1561-1587.

281. Vander Heiden MG: **Targeting cancer metabolism: a therapeutic window opens.** *Nature Reviews Drug Discovery* 2011, **10:**671-684.

282. Folmes CDL, Nelson TJ, Dzeja PP, Terzic A: **Energy metabolism plasticity enables stemness programs.** *Ann N Y Acad Sci* 2012, **1254:**82-89.

283. Folmes CDL, Dzeja PP, Nelson TJ, Terzic A: **Metabolic plasticity in stem cell homeostasis and differentiation.** *Cell Stem Cell* 2012, **11:**596-606.

284. Fonda ML: **Bromopyruvate inactivation of glutamate apodecarboxylase. Kinetics and specificity.** *J Biol Chem* 1976, **251:**229-235.

285. Cardaci S, Desideri E, Ciriolo MR: **Targeting aerobic glycolysis: 3-bromopyruvate as a promising anticancer drug.** *J Bioenerg Biomembr* 2012, **44:**17-29.

286. PreScience Labs Inc.: **IND Application.** 2015 [http://presciencelabs.com/cancer-treatment-progress/ind-application.php]

287. Rempel A, Mathupala SP, Griffin CA, Hawkins AL, Pedersen PL: **Glucose catabolism in cancer cells: amplification of the gene encoding type II hexokinase.** *Cancer Res* 1996, **56:**2468-2471.

288. Chen Z, Zhang H, Lu W, Huang P: **Role of mitochondria-associated hexokinase II in cancer cell death induced by 3-bromopyruvate.** *Biochim Biophys Acta* 2009, **1787:**553-560.

289. Pastorino JG: **Mitochondrial Binding of Hexokinase II Inhibits Bax-induced Cytochrome c Release and Apoptosis.** *J Biol Chem* 2001, **277:**7610-7618.

290. Pedersen PL: **Voltage dependent anion channels (VDACs): a brief introduction with a focus on the outer mitochondrial compartment's roles together with hexokinase-2 in the "Warburg effect" in cancer.** *J Bioenerg Biomembr* 2008, **40:**123-126.

291. Mathupala SP, Ko YH, Pedersen PL: **Hexokinase-2 bound to mitochondria: cancer's stygian link to the "Warburg Effect" and a pivotal target for effective therapy.** *Semin Cancer Biol* 2009, **19:**17-24.

292. Xu R-H, Pelicano H, Zhou Y, Carew JS, Feng L, Bhalla KN, Keating MJ, Huang P: **Inhibition of glycolysis in cancer cells: a novel strategy to overcome drug resistance associated with mitochondrial respiratory defect and hypoxia.** *Cancer Res* 2005, **65:**613-621.

293. Ganapathy-Kanniappan S, Vali M, Kunjithapatham R, Buijs M, Syed LH, Rao PP, Ota S, Kwak BK, Loffroy R, Geschwind JF: **3-Bromopyruvate: A New Targeted Antiglycolytic Agent and a Promise for Cancer Therapy.** *Curr Pharm Biotechnol* 2010, **11:**510-517.

294. Ganapathy-Kanniappan S, Geschwind J-FH, Kunjithapatham R, Buijs M, Vossen JA, Tchernyshyov I, Cole RN, Syed LH, Rao PP, Ota S, Vali M: **Glyceraldehyde-3-phosphate Dehydrogenase (GAPDH) Is Pyruvylated during 3-Bromopyruvate Mediated Cancer Cell Death.** *Anticancer Res* 2009, **29:**4909-4918.

295. Ganapathy-Kanniappan S, Kunjithapatham R, Geschwind DH: **Anticancer Efficacy of the Metabolic Blocker 3-Bromopyruvate: Specific Molecular Targeting.** *Anticancer Res* 2013, **33:**13-20.

296. Dell'Antone P: **Targets of 3-bromopyruvate, a new, energy depleting, anticancer agent.** *Med Chem* 2009, **5:**491-496.

297. Ganapathy-Kanniappan S, Kunjithapatham R, Geschwind J-F: **Glyceraldehyde-3-phosphate dehydrogenase: a promising target for molecular therapy in hepatocellular carcinoma.** *Oncotarget* 2012, **3:**940-953.

298. Colell A, Ricci J-E, Tait S, Milasta S, Maurer U, Bouchier-Hayes L, Fitzgerald P, Guio-Carrion A, Waterhouse NJ, Li CW, et al: **GAPDH and autophagy preserve survival after apoptotic cytochrome c release in the absence of caspase activation.** *Cell* 2007, **129:**983-997.

299. Du Z-X, Wang H-Q, Zhang H-Y, Gao D-X: **Involvement of glyceraldehyde-3-phosphate dehydrogenase in tumor necrosis factor-related apoptosis-inducing ligand-mediated death of thyroid cancer cells.** *Endocrinology* 2007, **148:**4352-4361.

300. Sukhanov S, Higashi Y, Shai S-Y, Itabe H, Ono K, Parthasarathy S, Delafontaine P: **Novel effect of oxidized low-density lipoprotein: cellular ATP depletion via downregulation of glyceraldehyde-3-phosphate dehydrogenase.** *Circ Res* 2006, **99:**191-200.

301. Tarze A, Deniaud A, Le Bras M, Maillier E, Molle D, Larochette N, Zamzami N, Jan G, Kroemer G, Brenner C: **GAPDH, a novel regulator of the pro-apoptotic mitochondrial membrane permeabilization.** *Oncogene* 2007, **26:**2606-2620.

302. Ganapathy-Kanniappan S, Geschwind J-FH, Kunjithapatham R, Buijs M, Syed LH, Rao PP, Ota S, Kwak BK, Loffroy R, Vali M: **3-Bromopyruvate Induces Endoplasmic Reticulum Stress, Overcomes Autophagy and Causes Apoptosis in Human HCC Cell Lines.** *Anticancer Res* 2010, **30:**923-936.

303. Ihrlund LS, Hernlund E, Khan O, Shoshan MC: **3-Bromopyruvate as inhibitor of tumour cell energy metabolism and chemopotentiator of platinum drugs.** *Mol Oncol* 2008, **2:**94-101.

304. Schaefer NG, Geschwind JF, Engles J, Buchanan JW, Wahl RL: **Systemic administration of 3-bromopyruvate in treating disseminated aggressive lymphoma.** *Transl Res* 2012, **159:**51-57.

305. Fang J, Quinones QJ, Holman TL, Morowitz MJ, Wang Q, Zhao H, Sivo F, Maris JM, Wahl ML: **The H+-linked monocarboxylate transporter (MCT1/SLC16A1): a potential therapeutic target for high-risk neuroblastoma.** *Mol Pharmacol* 2006, **70:**2108-2115.

306. Queirós O, Preto A, Pacheco A, Pinheiro C, Azevedo-Silva J, Moreira R, Pedro M, Ko YH, Pedersen PL, Baltazar F, Casal M: **Butyrate activates the monocarboxylate transporter MCT4 expression in breast cancer cells and enhances the antitumor activity of 3-bromopyruvate.** *J Bioenerg Biomembr* 2012, **44:**141-153.

307. Keith B, Simon MC: **Hypoxia-Inducible Factors, Stem Cells, and Cancer.** *Cell* 2007, **129:**465-472.

308. Shackleton M: **Normal stem cells and cancer stem cells: similar and different.** *Semin Cancer Biol* 2010, **20:**85-92.

309. Kusumbe AP, Bapat SA: **Cancer Stem Cells and Aneuploid Populations within Developing Tumors Are the Major Determinants of Tumor Dormancy.** *Cancer Res* 2009, **69:**9245-9253.

310. Scatena R, Bottoni P, Pontoglio A, Giardina B: **Cancer stem cells: the development of new cancer therapeutics.** *Expert Opin Biol Ther* 2011, **11:**875-892.

311. Frank NY, Schatton T, Frank MH: **The therapeutic promise of the cancer stem cell concept.** *J Clin Invest* 2010, **120:**41-50.

312. Sachlos E, Risueño RM, Laronde S, Shapovalova Z, Lee J-H, Russell J, Malig M, McNicol JD, Fiebig-Comyn A, Graham M, et al: **Identification of drugs including a dopamine receptor antagonist that selectively target cancer stem cells.** *Cell* 2012, **149:**1284-1297.

313. Vacanti NM, Metallo CM: **Exploring metabolic pathways that contribute to the stem cell phenotype.** *Biochim Biophys Acta* 2013, **1830:**2361-2369.

314. Varum S, Rodrigues AS, Moura MB, Momcilovic O, Easley CA, Ramalho-Santos J, Van Houten B, Schatten G: **Energy metabolism in human pluripotent stem cells and their differentiated counterparts.** *PLoS ONE* 2011, **6:**e20914.

315. Zhou Y, Zhou Y, Shingu T, Feng L, Chen Z, Ogasawara M, Keating MJ, Kondo S, Huang P: **Metabolic Alterations in Highly Tumorigenic Glioblastoma Cells: Preference For Hypoxia and High Dependency on Glycolysis.** *J Biol Chem* 2011, **286:**32843-32853.

316. Vaupel P, Mayer A: **Hypoxia in cancer: significance and impact on clinical outcome.** *Cancer Metastasis Rev* 2007, **26:**225-239.

317. Brahimi-Horn MC, Chiche J, Pouyssegur J: **Hypoxia and cancer.** *J Mol Med* 2007, **85:**1301-1307.

318. Semenza GL: **Targeting HIF-1 for Cancer Therapy.** *Nat Rev Cancer* 2003, **3:**721-732.

319. Cheng J-C, Klausen C, Leung PCK: **Hypoxia-inducible factor 1 alpha mediates epidermal growth factor-induced down-regulation of E-cadherin expression and cell invasion in human ovarian cancer cells.** *Cancer Lett* 2013, **329:**197-206.

320. Osada R, Horiuchi A, Kikuchi N, Yoshida J, Hayashi A, Ota M, Katsuyama Y, Melillo G, Mellilo G, Konishi I: **Expression of hypoxia-inducible factor 1alpha, hypoxia-inducible factor 2alpha, and von Hippel-Lindau protein in epithelial ovarian neoplasms and allelic loss of von Hippel-Lindau gene: nuclear expression of hypoxia-inducible factor 1alpha is an independent prognostic factor in ovarian carcinoma.** *Hum Pathol* 2007, **38:**1310-1320.

321. Horiuchi A, Hayashi T, Kikuchi N, Hayashi A, Fuseya C, Shiozawa T, Konishi I: **Hypoxia upregulates ovarian cancer invasiveness via the binding of HIF-1α to a hypoxia-induced, methylation-free hypoxia response element of S100A4 gene.** *Int J Cancer* 2012, **131:**1755-1767.

322. Liang D, Ma Y, Liu J, Trope CG, Holm R, Nesland JM, Suo Z: **The hypoxic microenvironment upgrades stem-like properties of ovarian cancer cells.** *BMC Cancer* 2012, **12:**201.

323. Chapiro J, Sur S, Savic LJ, Ganapathy-Kanniappan S, Reyes J, Duran R, Thiruganasambandam SC, Moats CR, Lin M, Luo W, et al: **Systemic delivery of microencapsulated 3-bromopyruvate for the therapy of pancreatic cancer.** *Clin Cancer Res* 2014, **20:**6406-6417.

324. Marín-Hernández A, Rodríguez-Enríquez S, Vital-González PA, Flores-Rodríguez FL, Macías-Silva M, Sosa-Garrocho M, Moreno-Sánchez R: **Determining and understanding the control of glycolysis in fast-growth tumor cells. Flux control by an over-expressed but strongly product-inhibited hexokinase.** *FEBS J* 2006, **273:**1975-1988.

325. Icard P, Zhang XD, Varin E, Allouche S, Coquerel A: **Why Anti-Energetic Agents Such as Citrate or 3-Bromopyruvate Should be Tested as Anti-Cancer Agents: Experimental In Vitro and In Vivo Studies.** In *Mesotheliomas - Synonyms and Definition, Epidemiology, Etiology, Pathogenesis, Cyto-Histopathological Features, Clinic, Diagnosis, Treatment, Prognosis.* Edited by Zubritsky A: InTech; 2012: 225-244.

326. El Sayed SM, El-Magd RMA, Shishido Y, Chung SP, Diem TH, Sakai T, Watanabe H, Kagami S, Fukui K: **3-Bromopyruvate antagonizes effects of lactate and pyruvate, synergizes with citrate and exerts novel anti-glioma effects.** *J Bioenerg Biomembr* 2012, **44:**61-79.

327. Zhang X-D, Varin E, Allouche S, Lu Y, Poulain L, Icard P: **Effect of citrate on malignant pleural mesothelioma cells: a synergistic effect with cisplatin.** *Anticancer Res* 2009, **29:**1249-1254.

328. Ganapathy-Kanniappan S, Geschwind J-FH, Kunjithapatham R, Buijs M, Syed LH, Rao PP, Ota S, Vali M: **The pyruvic acid analog 3-bromopyruvate interferes with the tetrazolium reagent MTS in the evaluation of cytotoxicity.** *Assay Drug Dev Technol* 2010, **8:**258-262.

329. Abraham VC, Towne DL, Waring JF, Warrior U, Burns DJ: **Application of a high-content multiparameter cytotoxicity assay to prioritize compounds based on toxicity potential in humans.** *J Biomol Screen* 2008, **13:**527-537.

330. PreScience Labs Inc.: **Clinical Development.** 2015 [http://presciencelabs.com/cancer-treatment-progress/clinical-development.php]

331. Bouchard-Fortier G, Rosen B, Vyarvelska I, Pasetka M, Covens A, Gien LT, Kupets R, Pulman K, Ferguson SE, Vicus D: **A comparison of the toxicity and tolerability of two intraperitoneal chemotherapy regimens for advanced-stage epithelial ovarian cancer.** *Gynecol Oncol* 2015, **140:**36-41.

332. Glick M, Biddle P, Jantzi J, Weaver S, Schirch D: **The antitumor agent 3-bromopyruvate has a short half-life at physiological conditions.** *Biochem Biophys Res Commun* 2014, **452:**170-173.

333. Wang N, Tytell JD, Ingber DE: **Mechanotransduction at a distance: mechanically coupling the extracellular matrix with the nucleus.** *Nat Rev Mol Cell Biol* 2009, **10:**75-82.

334. Levin M: **Bioelectromagnetics in morphogenesis.** *Bioelectromagnetics* 2003, **24:**295-315.

335. Oschman JL: **Structure and properties of ground substances.** *Am Zool* 1984, **24:**199-215.

336. Oschman JL: **Charge transfer in the living matrix.** *Journal of Bodywork and Movement Therapy* 2009, **13:**215-228.

337. Ho MW: *The Rainbow and the Worm: The Physics of Organisms.* Singapore: World Scientific; 1998.

338. Szent-Györgyi A: **The Study of Energy-Levels in Biochemistry.** *Nature* 1941, **148:**157-159.

339. Szent-Györgyi A: *Bioenergetics.* New York: Academic Press; 1957.

340. Priel A, Tuszynski JA, Cantiello HF: **Electrodynamic Signaling by the Dendritic Cytoskeleton: Toward an Intracellular Information Processing Model.** *Electromagn Biol Med* 2005, **24:**221-231.

341. Tuszynski JA, Priel A, Brown JA, Cantiello HF, Dixon JM: **Electronic and Ionic Conductivities of Microtubules and Actin Filaments, Their Consequences for Cell Signaling and Applications to Bioelectronics.** In *CRC Nano and Molecular Electronics Handbook.* Edited by Lyshevski SE. London: Taylor and Francis; 2007: 1-46.

342. Woolf NJ, Priel A, Tuszynski JA: *Nanoneuroscience: Structural and Functional Roles of the Neuronal Cytoskeleton in Health and Disease.* New York: Springer; 2009.

343. Na S, Collin O, Chowdhury F, Tay B, Ouyang M, Wang Y, Wang N: **Rapid signal transduction in living cells is a unique feature of mechanotransduction.** *Proc Natl Acad Sci USA* 2008, **105:**6626-6631.

344. Cope FW: **A review of the applications of solid state physics concepts to biological systems.** *J Biol Phys* 1975, **3:**1-41.

345. Fels D: **Cellular Communication through Light.** *PLoS ONE* 2009, **4:**e5086.

346. Craddock TJA, Tuszynski JA, Priel A, Freedman H: **Microtubule ionic conduction and its implications for higher cognitive functions.** *J Integr Neurosci* 2010, **9:**103-122.

347. Sahu S, Ghosh S, Ghosh B, Aswani K, Hirata K, Fujita D, Bandyopadhyay A: **Atomic water channel controlling remarkable properties of a single brain microtubule: Correlating single protein to its supramolecular assembly.** *Biosens Bioelectron* 2013, **47:**141-148.

348. Cifra M, Fields JZ, Farhadi A: **Electromagnetic cellular interactions.** *Prog Biophys Mol Biol* 2011, **105:**223-246.

349. McCaig CD, Rajnicek AM, Song B, Zhao M: **Controlling cell behavior electrically: current views and future potential.** *Physiol Rev* 2005, **85:**943-978.

350. Scholkmann F, Fels D, Cifra M: **Non-chemical and non-contact cell-to-cell communication: a short review.** *Am J Transl Res* 2013, **5:**586-593.

351. Zheng JM, Chin WC, Khijniak E, Khijniak E, Jr., Pollack GH: **Surfaces and interfacial water: evidence that hydrophilic surfaces have long-range impact.** *Adv Colloid Interface Sci* 2006, **127:**19-27.

352. Rosenberg B, Postow E: **Semiconduction in proteins and lipids - Its possible biological import.** *Ann N Y Acad Sci* 1969, **158:**161-190.

353. Blumenfeld LA, Chernavskii DS: **Tunnelling of electrons in biological processes.** *J Theor Biol* 1973, **39:**1-7.

354. Reece SY, Hodgkiss JM, Stubbe J, Nocera DG: **Proton-coupled electron transfer: the mechanistic underpinning for radical transport and catalysis in biology.** *Philos Trans R Soc Lond, B* 2006, **361:**1351-1364.

355. Gascoyne PR, Pethig R, Szent-Gyorgyi A: **Water structure-dependent charge transport in proteins.** *Proc Natl Acad Sci USA* 1981, **78:**261-265.

356. Priel A, Ramos AJ, Tuszynski JA, Cantiello HF: **A biopolymer transistor: electrical amplification by microtubules.** *Biophys J* 2006, **90:**4639-4643.

357. Sekulić DL, Satarić BM, Tuszyński JA, Satarić MV: **Nonlinear ionic pulses along microtubules.** *Eur Phys J E* 2011, **34:**49.

358. Wang N, Butler JP, Ingber DE: **Mechanotransduction across the cell surface and through the cytoskeleton.** *Science* 1993, **260:**1124-1127.

359. Jibu M, Hagan S, Hameroff SR, Pribram KH, Yasue K: **Quantum optical coherence in cytoskeletal microtubules: implications for brain function.** *BioSystems* 1994, **32:**195-209.

360. Hameroff SR, Nip A, Porter M, Tuszynski J: **Conduction pathways in microtubules, biological quantum computation, and consciousness.** *BioSystems* 2002, **64:**149-168.

361. Hameroff SR, Penrose R: **Consciousness in the universe.** *Phys Life Rev* 2014, **11:**39-78.

362. Tuszynski JA, Hameroff SR, Satarić MV, Trpisová B, Nip MLA: **Ferroelectric behavior in microtubule dipole lattices: Implications for information processing, signaling and assembly/disassembly.** *J Theor Biol* 1995, **174:**371-380.

363. Chou KC, Zhang CT, Maggiora GM: **Solitary wave dynamics as a mechanism for explaining the internal motion during microtubule growth.** *Biopolymers* 1994, **34:**143-153.

364. Kucera O, Havelka D: **Mechano-electrical vibrations of microtubules—Link to subcellular morphology.** *BioSystems* 2012, **109:**346-355.

365. Craddock TJA, Tuszynski JA, Hameroff SR: **Cytoskeletal signaling: is memory encoded in microtubule lattices by CaMKII phosphorylation?** *PLoS Comput Biol* 2012, **8:**e1002421.

366. Craddock TJA, Tuszynski JA: **A critical assessment of the information processing capabilities of neuronal microtubules using coherent excitations.** *J Biol Phys* 2009, **36:**53-70.

367. Priel A, Tuszynski JA: **A nonlinear cable-like model of amplified ionic wave propagation along microtubules.** *Europhysics Letters* 2008, **83:**68004.

368. Minoura I, Muto E: **Dielectric measurement of individual microtubules using the electroorientation method.** *Biophys J* 2006, **90:**3739-3748.

369. Uppalapati M, Huang Y-M, Jackson TN, Hancock WO: **Microtubule alignment and manipulation using AC electrokinetics.** *Small* 2008, **4:**1371-1381.

370. Foster KR, Bidinger JM, Carpenter DO: **The electrical resistivity of cytoplasm.** *Biophys J* 1976, **16:**991-1001.

371. Fritzsche W, Böhm KJ, Unger E, Köhler JM: **Metallic nanowires created by biopolymer masking.** *Appl Phys Lett* 1999, **75:**2854-2856.

372. Cole KS: **Resistivity of axoplasm. I. Resistivity of extruded squid axoplasm.** *J Gen Physiol* 1975, **66:**133-138.

373. Shang JQ, Mohamedelhassan E, Ismail M: **Electrochemical cementation of offshore calcareous soil.** *Canadian Geotechnical Journal* 2004, **41:**877-893.

374. Wada K, Tarhan MC, Bottier C, Collard D, Fujita H, Yokokawa R: **Fabrication and characterization of multiple nanowires using microtubule structures.** In

Transducers 2009 - 2009 International Solid-State Sensors, Actuators and Microsystems Conference. pp. 1337-1340: IEEE; 2009:1337-1340.

375. Sahu S, Ghosh S, Hirata K, Fujita D, Bandyopadhyay A: **Multi-level memory-switching properties of a single brain microtubule.** *Appl Phys Lett* 2013, **102:**123701.

376. Umnov M, Palusinski OA, Deymier PA, Guzman R, Hoying J, Barnaby H, Yang Y, Raghavan S: **Experimental evaluation of electrical conductivity of microtubules.** *J Mater Sci* 2006, **42:**373-378.

377. Goddard G, Whittier JE: **Bio-molecules as nanomaterials: interface characterization for sensor development.** *Proc of SPIE–Smart Structures and Materials 2006: Smart Electronics, MEMS, BioMEMS, and Nanotechnology* 2006, **6172:**43-54.

378. Dellago C, Naor M, Hummer G: **Proton Transport through Water-Filled Carbon Nanotubes.** *Phys Rev Lett* 2003, **90:**105902.

379. Guckenberger R, Heim M, Cevc G, Knapp H, Wiegrabe W, Hillebrand A: **Scanning tunneling microscopy of insulators and biological specimens based on lateral conductivity of ultrathin water films.** *Science* 1994, **266:**1538-1540.

380. Priel A, Tuszynski JA, Woolf NJ: **Transitions in microtubule C-termini conformations as a possible dendritic signaling phenomenon.** *Eur Biophys J* 2005, **35:**40-52.

381. Tuszynski JA, Brown JA, Hawrylak P: **Dielectric polarization, electrical conduction, information processing and quantum computation in microtubules. Are they plausible?** *Phil Trans R Soc Lond A* 1998, **356:**1897-1926.

382. Havelka D, Cifra M, Kucera O: **Multi-mode electro-mechanical vibrations of a microtubule: In silico demonstration of electric pulse moving along a microtubule.** *Appl Phys Lett* 2014, **104:**243702.

383. Mavromatos NE: **Quantum Coherence in (Brain) Microtubules and Efficient Energy and Information Transport.** *J Phys: Conf Ser* 2011, **329:**012026.

384. Engel GS, Calhoun TR, Read EL, Ahn TK, Mančal T, Cheng YC, Blankenship RE, Fleming GR: **Evidence for wavelike energy transfer through quantum coherence in photosynthetic systems.** *Nature* 2007, **446:**782-786.

385. Panitchayangkoon G, Hayes D, Fransted KA, Caram JR, Harel E, Wen J, Blankenship RE, Engel GS: **Long-lived quantum coherence in photosynthetic complexes at physiological temperature.** *Proc Natl Acad Sci USA* 2010, **107:**12766-12770.

386. Lin EC, Cantiello HF: **A novel method to study the electrodynamic behavior of actin filaments. Evidence for cable-like properties of actin.** *Biophys J* 1993, **65:**1371-1378.

387. Cantiello HF, Patenaude C, Zaner K: **Osmotically induced electrical signals from actin filaments.** *Biophys J* 1991, **59:**1284-1289.

388. Lodish H, Berk A, Matsudaira P, Kaiser C, Krieger M, Scott M, Zipursky S, Darnell J: *Molecular Cell Biology.* W. H. Freeman; 2004.

389. Tuszynski JA, Portet S, Dixon JM, Luxford C, Cantiello HF: **Ionic wave propagation along actin filaments.** *Biophys J* 2004, **86:**1890-1903.

390. Satarić MV, Bednar N, Satarić BM, Stojanovic G: **Actin filaments as nonlinear RLC transmission lines.** *Int J Mod Phys B* 2009, **23:**4697-4711.

391. Ripoll C, Norris V, Thellier M: **Ion condensation and signal transduction.** *Bioessays* 2004, **26:**549-557.

392. van den Heuvel MGL, De Graaff MP, Lemay SG, Dekker C: **Electrophoresis of individual microtubules in microchannels.** *Proc Natl Acad Sci USA* 2007, **104:**7770-7775.

393. Arsenault ME, Zhao H, Purohit PK, Goldman YE, Bau HH: **Confinement and manipulation of actin filaments by electric fields.** *Biophys J* 2007, **93:**L42-44.

394. Di Lullo GA, Sweeney SM, Korkko J, Ala-Kokko L, San Antonio JD: **Mapping the ligand-binding sites and disease-associated mutations on the most abundant protein in the human, type I collagen.** *J Biol Chem* 2002, **277:**4223-4231.

395. Bardelmeyer GH: **Electrical conduction in hydrated collagen. I. Conductivity mechanisms.** *Biopolymers* 1973, **12:**2289-2302.

396. Bardelmeyer GH: **Electrical conduction in collagen. II. Some aspects of hydration.** *Biopolymers* 1973, **12:**2303-2307.

397. Sasaki N: **Dielectric properties of slightly hydrated collagen- Time–water content superposition analysis.** *Biopolymers* 1984, **23:**1725-1734.

398. Fullerton G, Amurao M: **Evidence that collagen and tendon have monolayer water coverage in the native state.** *Cell Biol Int* 2006, **30:**56-65.

399. Jaroszyk F, Marzec E: **Dielectric Properties of BAT Collagen in the Temperature Range of Thermal Denaturation.** *Berichte der Bunsengesellschaft für physikalische Chemie* 2010, **97:**868-871.

400. Ho MW, Musumeci F, Scordino A, Triglia A, Privitera G: **Delayed luminescence from bovine Achilles' tendon and its dependence on collagen structure.** *Journal of Photochemistry and Photobiology B: Biology* 2002, **66:**165-170.

401. Scordino A, Grasso R, Gulino M, Lanzanò L, Musumeci F, Privitera G, Tedesco M, Triglia A, Brizhik L: **Delayed luminescence from collagen as arising from soliton and small polaron states.** *Int J Quantum Chem* 2010, **110:**221-229.

402. Ahn AC, Park M, Shaw JR, McManus CA, Kaptchuk TJ, Langevin HM: **Electrical Impedance of Acupuncture Meridians: The Relevance of Subcutaneous Collagenous Bands.** *PLoS ONE* 2010, **5:**e11907.

403. Maniotis AJ, Chen CS, Ingber DE: **Demonstration of mechanical connections between integrins, cytoskeletal filaments, and nucleoplasm that stabilize nuclear structure.** *Proc Natl Acad Sci USA* 1997, **94:**849-854.

404. Harburger DS, Calderwood DA: **Integrin signalling at a glance.** *J Cell Sci* 2009, **122:**159-163.

405. Hynes RO: **Integrins: bidirectional, allosteric signaling machines.** *Cell* 2002, **110:**673-687.

406. Fuchs E, Karakesisoglou I: **Bridging cytoskeletal intersections.** *Genes Dev* 2001, **15:**1-14.

407. Jiang G, Giannone G, Critchley DR, Fukumoto E, Sheetz MP: **Two-piconewton slip bond between fibronectin and the cytoskeleton depends on talin.** *Nature* 2003, **424:**334-337.

408. Pankov R, Yamada KM: **Fibronectin at a glance.** *J Cell Sci* 2002, **115:**3861-3863.

409. Geiger B, Bershadsky A, Pankov R, Yamada KM: **Transmembrane crosstalk between the extracellular matrix and the cytoskeleton.** *Nat Rev Mol Cell Biol* 2001, **2:**793-805.

410. Dehmelt L, Halpain S: **The MAP2/Tau family of microtubule-associated proteins.** *Genome Biol* 2005, **6:**204.

411. Rodriguez OC, Schaefer AW, Mandato CA, Forscher P, Bement WM, Waterman-Storer CM: **Conserved microtubule-actin interactions in cell movement and morphogenesis.** *Nat Cell Biol* 2003, **5:**599-609.

412. Selden SC, Pollard TD: **Interaction of Actin Filaments with Microtubules Is Mediated by Microtubule-Associated Proteins and Regulated by Phosphorylation.** *Ann N Y Acad Sci* 1986, **466:**803-812.

413. Levin M: **Large-scale biophysics: ion flows and regeneration.** *Trends Cell Biol* 2007, **17:**261-270.

414. Pilla AA, Nasser PR, Kaufman JJ: **Cell-Cell Communication Significantly Decreases Thermal Noise Limits for Electromagnetic Bioeffects.** *Engineering in Medicine and Biology Society, 1992 14th Annual International Conference fo the IEEE* 1992, **1:**300-301.

415. Kimura H, Oyamada Y, Ohshika H, Mori M, Oyamada M: **Reversible inhibition of gap junctional intercellular communication, synchronous contraction, and synchronism of intracellular Ca2+ fluctuation in cultured neonatal rat cardiac myocytes by heptanol.** *Exp Cell Res* 1995, **220:**348-356.

416. Hameroff SR: **The "conscious pilot"—dendritic synchrony moves through the brain to mediate consciousness.** *J Biol Phys* 2009, **36:**71-93.

417. Wang X, Gerdes H-H: **Long-distance electrical coupling via tunneling nanotubes.** *Biochim Biophys Acta* 2012, **1818:**2082-2086.

418. Wang X, Veruki ML, Bukoreshtliev NV, Hartveit E, Gerdes H-H: **Animal cells connected by nanotubes can be electrically coupled through interposed gap-junction channels.** *Proc Natl Acad Sci USA* 2010, **107:**17194-17199.

419. Gerdes H-H, Rustom A, Wang X: **Tunneling nanotubes, an emerging intercellular communication route in development.** *Mech Dev* 2013, **130:**381-387.

420. Ho MW: **Towards a theory of the organism.** *Integr Physiol Behav Sci* 1997, **32:**343-363.

421. Phillips R, Kondev J, Theriot J: *Physical biology of the cell.* New York: Garland Science; 2009.

422. Cussler EL: *Diffusion: Mass Transfer in Fluid Systems.* New York: Cambridge University Press; 1997.

423. Schipke CG, Boucsein C, Ohlemeyer C, Kirchhoff F, Kettenmann H: **Astrocyte Ca2+ waves trigger responses in microglial cells in brain slices.** *The FASEB Journal* 2002, **16:**255-257.

424. Gatenby RA, Frieden BR: **Coulomb interactions between cytoplasmic electric fields and phosphorylated messenger proteins optimize information flow in cells.** *PLoS ONE* 2010, **5:**e12084.

425. Xu T, Bashford GR: **Resolving the lateral component of blood flow velocity based on ultrasound speckle size change with scan direction and speed.** *31st Annual International Conference of the IEEE Engineering in Medicine and Biology Society* 2009, **2009:**491-494.

426. Rohr S: **Role of gap junctions in the propagation of the cardiac action potential.** *Cardiovasc Res* 2004, **62:**309-322.

427. Stoelting RK, Hillier SC: *Pharmacology and Physiology in Anesthetic Practice.* Philadelphia: Lippincott Williams & Wilkins; 2006.

428. Ho M-W: **Super-Conducting Liquid Crystalline Water Aligned with Collagen Fibres in the Fascia as Acupuncture Meridians of Traditional Chinese Medicine.** *Forum on Immunopathological Diseases and Therapeutics* 2012, **3:**221-236.

429. Colwell LJ, Brenner MP, Ribbeck K: **Charge as a selection criterion for translocation through the nuclear pore complex.** *PLoS Comput Biol* 2010, **6:**e1000747.

430. Cameron IL, Hardman WE, Fullerton GD, Miseta A, Koszegi T, Ludany A, Kellermayer M: **Maintenance of ions, proteins and water in lens fiber cells before and after treatment with non-ionic detergents.** *Cell Biol Int* 1996, **20:**127-137.

431. Pollack GH: **The role of aqueous interfaces in the cell.** *Adv Colloid Interface Sci* 2003, **103:**173-196.

432. Cameron IL, Short NJ, Fullerton GD: **Characterization of water of hydration fractions in rabbit skeletal muscle with age and time of post-mortem by centrifugal dehydration force and rehydration methods.** *Cell Biol Int* 2008, **32:**1337-1343.

433. Ross S, Newton R, Zhou YM, Haffegee J, Ho MW, Bolton JP, Knight D: **Quantitative image analysis of birefringent biological material.** *J Microsc* 1997, **187:**62-67.

434. Ho MW, Haffegee J, Newton R, Zhou Y: **Organisms as polyphasic liquid crystals.** *Bioelectrochem Bioenerg* 1996, **41:**81-91.

435. Ho M-W, Yu-Ming Z, Haffegee J, Watton A, Musumeci F, Privitera G, Scordino A, Triglia A: **The Liquid Crystalline Organism and Biological Water.** In *Water and the Cell.* Edited by Pollack GH, Cameron IL, Wheatley DN. Dordrecht: Springer Netherlands; 2006: 219-234.

436. Springer A, Hagen V, Cherepanov DA, Antonenko YN, Pohl P: **Protons migrate along interfacial water without significant contributions from jumps between ionizable groups on the membrane surface.** *Proc Natl Acad Sci USA* 2011, **108:**14461-14466.

437. Mulkidjanian AY, Heberle J, Cherepanov DA: **Protons @ interfaces: implications for biological energy conversion.** *Biochim Biophys Acta* 2006, **1757:**913-930.

438. Persson E, Halle B: **Cell water dynamics on multiple time scales.** *Proc Natl Acad Sci USA* 2008, **105:**6266-6271.

439. Jasnin M, Moulin M, Moulin M, Haertlein M, Zaccai G, Tehei M: **Down to atomic-scale intracellular water dynamics.** *EMBO Rep* 2008, **9:**543-547.

440. Qvist J, Persson E, Mattea C, Halle B: **Time scales of water dynamics at biological interfaces: peptides, proteins and cells.** *Faraday Discuss* 2008, **141:**131.

441. Cameron IL, Lanctot AC, Fullerton GD: **The molecular stoichiometric hydration model (SHM) as applied to tendon/collagen, globular proteins and cells.** *Cell Biol Int* 2011, **35:**1205-1215.

442. Rosenberg B: **Electrical conductivity of proteins.** *Nature* 1962, **193:**364-365.

443. Bone S: **Proton pathways in lysozyme.** *Biochim Biophys Acta* 1991, **1078:**336-338.

444. Pethig R: **Protein-water interactions determined by dielectric methods.** *Annu Rev Phys Chem* 1992, **43:**177-205.

445. Kornyshev AA, Kuznetsov AM, Spohr E, Ulstrup J: **Kinetics of Proton Transport in Water.** *J Phys Chem B* 2003, **107:**3351-3366.

446. Cukierman S: **Et tu, Grotthuss! and other unfinished stories.** *Biochim Biophys Acta* 2006, **1757:**876-885.

447. Agmon N: **The Grotthuss mechanism.** *Chemical Physics Letters* 1995, **244:**456-462.

448. Becker RO: **Search for Evidence of Axial Current Flow in Peripheral Nerves of Salamander.** *Science* 1961, **134:**101-102.

449. Becker RO: **The basic biological data transmission and control system influenced by electrical forces.** *Ann N Y Acad Sci* 1974, **238:**236-241.

450. Borgens RB: **Natural and applied currents in limb regeneration and development.** In *Electric Fields in Vertebrate Repair.* Edited by Borgens RB, Robinson KR, Vanable J, Joseph W, McGinnis ME. New York: Alan R. Liss, Inc.; 1989.

451. Borgens RB, Vanable J, Joseph W, Jaffe LF: **Bioelectricity and Regeneration.** *Bioscience* 1979, **29:**468-474.

452. Smith SD: **Limb regeneration.** In *Modern Bioelectricity.* Edited by Marino AA. New York: Marcel Dekker, Inc.; 1988.

453. Berridge MJ, Lipp P, Bootman MD: **The versatility and universality of calcium signalling.** *Nat Rev Mol Cell Biol* 2000, **1:**11-21.

454. Borgens RB, Vanable JW, Jaffe LF: **Bioelectricity and regeneration: large currents leave the stumps of regenerating newt limbs.** *Proc Natl Acad Sci USA* 1977, **74:**4528-4532.

455. Adams DS, Levin M: **Endogenous voltage gradients as mediators of cell-cell communication: strategies for investigating bioelectrical signals during pattern formation.** *Cell Tissue Res* 2012, **352:**95-122.

456. Albrecht-Buehler G: **Cellular infrared detector appears to be contained in the centrosome.** *Cell Motil Cytoskeleton* 1994, **27:**262-271.

457. Cifra M, Pospíšil P: **Ultra-weak photon emission from biological samples: Definition, mechanisms, properties, detection and applications.** *Journal of Photochemistry and Photobiology B: Biology* 2014, **139:**2-10.

458. Popp F-A: **Cancer Growth and Its Inhibition in Terms of Coherence.** *Electromagn Biol Med* 2009, **28:**53-60.

459. Kreslavski VD, Fomina IR, Los DA, Carpentier R, Kuznetsov VV, Allakhverdiev SI: **Red and near infra-red signaling: Hypothesis and perspectives.** *Journal of Photochemistry and Photobiology C: Photochemistry Reviews* 2012, **13:**190-203.

460. Kucera O, Cifra M: **Cell-to-Cell Signaling Through Light: Just a Ghost of Chance?** *Cell Communication and Signaling* 2013, **11:**87.

461. Hobbie RK, Roth BJ: *Intermediate Physics for Medicine and Biology.* New York: Springer; 2007.

462. Bischof M, Del Giudice E: **Communication and the emergence of collective behavior in living organisms: a quantum approach.** *Mol Biol Int* 2013, **2013:**987549.

463. Reiter GF, Kolesnikov AI, Paddison SJ, Platzman PM, Moravsky AP, Adams MA, Mayers J: **Evidence for an anomalous quantum state of protons in nanoconfined water.** *Phys Rev B* 2012, **85:**045403.

464. Berg H, Gunther B, Hilger I, Radeva M, Traitcheva N, Wollweber L: **Bioelectromagnetic Field Effects on Cancer Cells and Mice Tumors.** *Electromagn Biol Med* 2010, **29:**132-143.

465. Funk RH, Monsees T, Ozkucur N: **Electromagnetic effects - From cell biology to medicine.** *Prog Histochem Cytochem* 2009, **43:**177-264.

466. Tuszynski JA, Kurzyński M: *Introduction to Molecular Biophysics.* CRC Press; 2003.

467. Gagliardi LJ: **Electrostatic force in prometaphase, metaphase, and anaphase-A chromosome motions.** *Phys Rev E* 2002, **66:**011901.

468. King RW, Wu TT: **Electric field induced in cells in the human body when this is exposed to low-frequency electric fields.** *Phys Rev E* 1998, **58:**2363-2369.

469. King RW, Wu TT: **Calculated electric field induced in bundles of long cells in the human body when it is exposed to low-frequency electric fields.** *Radiat Res* 2000, **153:**715-721.

470. Brown JA, Tuszynski JA: **The possible relationship between cell shape and electric fields.** *J Theor Biol* 1999, **200:**245-247.

471. Kirson ED, Gurvich Z, Schneiderman R, Dekel E, Itzhaki A, Wasserman Y, Schatzberger R, Palti Y: **Disruption of cancer cell replication by alternating electric fields.** *Cancer Res* 2004, **64:**3288-3295.

472. Kirson ED, Giladi M, Gurvich Z, Itzhaki A, Mordechovich D, Schneiderman RS, Wasserman Y, Ryffel B, Goldsher D, Palti Y: **Alternating electric fields (TTFields) inhibit metastatic spread of solid tumors to the lungs.** *Clin Exp Metastasis* 2009, **26:**633-640.

473. Kirson ED, Schneiderman RS, Dbaly V, Tovarys F, Vymazal J, Itzhaki A, Mordechovich D, Gurvich Z, Shmueli E, Goldsher D, et al: **Chemotherapeutic treatment efficacy and sensitivity are increased by adjuvant alternating electric fields (TTFields).** *BMC Med Phys* 2009, **9:**1.

474. Kirson ED, Dbaly V, Tovarys F, Vymazal J, Soustiel JF, Itzhaki A, Mordechovich D, Steinberg-Shapira S, Gurvich Z, Schneiderman R, et al: **Alternating electric fields arrest cell proliferation in animal tumor models and human brain tumors.** *Proc Natl Acad Sci USA* 2007, **104:**10152-10157.

475. Zhao M, Forrester JV, McCaig CD: **A small, physiological electric field orients cell division.** *Proc Natl Acad Sci USA* 1999, **96:**4942-4946.

476. Levine M: **BioEssays 3/2012.** *Bioessays* 2012, **34:**205-217.

477. Chernet BT, Levin M: **Transmembrane voltage potential of somatic cells controls oncogene-mediated tumorigenesis at long-range.** *Oncotarget* 2014, **5:**3287-3306.

478. Van den Heuvel M, De Graaff MP, Dekker C: **Molecular Sorting by Electrical Steering of Microtubules in Kinesin-Coated Channels.** *Science* 2006, **312:**910-914.

479. Liang X, Chou SY: **Nanogap detector inside nanofluidic channel for fast real-time label-free DNA analysis.** *Nano Lett* 2008, **8:**1472-1476.

480. Liang X, Morton KJ, Austin RH, Chou SY: **Single Sub-20 nm Wide, Centimeter-Long Nanofluidic Channel Fabricated by Novel Nanoimprint Mold Fabrication and Direct Imprinting.** *Nano Lett* 2007, **7:**3774-3780.

481. Reisner W, Pedersen JN, Austin RH: **DNA confinement in nanochannels: physics and biological applications.** *Rep Prog Phys* 2012, **75:**106601.

482. Reisner W, Morton KJ, Riehn R, Wang YM, Yu Z, Rosen M, Sturm JC, Chou SY, Frey E, Austin RH: **Statics and dynamics of single DNA molecules confined in nanochannels.** *Phys Rev Lett* 2005, **94:**196101.

483. Wang Z, Wang D, Jiao N, Tung S, Dong Z: **Nanochannel system fabricated by MEMS microfabrication and atomic force microscopy.** *IET Nanobiotechnol* 2011, **5:**108-113.

484. Schroder DK: *Semiconductor material and device characterization.* 3rd edn. Hoboken, N.J.: John Wiley; 2006.

485. Keithley: **Four-Probe Resistivity and Hall Voltage Measurements with the Model 4200-SCS.** 2011 [http://www.tek.com/sites/tek.com/files/media/document/resources/FourProbe%20Resistivity%20W4200AppNote.pdf]

486. Green NG, Ramos A, González A, Castellanos A, Morgan H: **Electrothermally induced fluid flow on microelectrodes.** *Journal of Electrostatics* 2001, **53:**71-87.

487. Lockyear LL: **Reversible, Room Temperature Bonding of Glass Devices for Microfluidics.** In *Microfluidic Techniques. Volume* 321. New Jersey: Humana Press; 2005: 39-44.

488. Mukhopadhyay R: **Molecular motors meet microfluidic systems.** *Anal Chem* 2005.

489. Uppalapati M, Huang Y-M, Shastry S, Jackson TN, Hancock WO: **Microtubule motors in microfluidics.** In *Methods in Bioengineering: Microfabrication and Microfluidics.* Edited by Zahn JD. Boston, MA: Artech House Publishers; 2009: 311-336.

490. Huang Y-M, Uppalapati M, Hancock WO, Jackson TN: **Microtubule transport, concentration and alignment in enclosed microfluidic channels.** *Biomedical Microdevices* 2007, **9:**175-184.

491. Wang Z, Taylor J, Jemere AB, Harrison DJ: **Microfluidic devices for electrokinetic sample fractionation.** *Electrophoresis* 2010, **31:**2575-2583.

492. Stupp R, Wong E, Scott C, Taillibert S, Kanner A, Kesari S, Ram Z, EF obot: **NT-40 * Interim Analysis of the EF-14 Trial: A Prospective, Multi-center Trial of NovoTTF-100A Together With Temozolomide Compared to**

Temozolomide Alone in Patients with Newly Diagnosed GBM. *Neuro-oncol* 2014, **16:**v167-v167.

493. Tseng A, Levin M: **Cracking the bioelectric code: Probing endogenous ionic controls of pattern formation.** *Commun Integr Biol* 2013, **6:**e22595.

494. Peterka DS, Takahashi H, Yuste R: **Imaging voltage in neurons.** *Neuron* 2011, **69:**9-21.

495. St-Pierre F, Marshall JD, Yang Y, Gong Y, Schnitzer MJ, Lin MZ: **High-fidelity optical reporting of neuronal electrical activity with an ultrafast fluorescent voltage sensor.** *Nat Neurosci* 2014, **17:**884-889.

496. Lukinavičius G, Reymond L, D'Este E, Masharina A, Göttfert F, Ta H, Güther A, Fournier M, Rizzo S, Waldmann H, et al: **Fluorogenic probes for live-cell imaging of the cytoskeleton.** *Nat Methods* 2014, **11:**731-733.

497. Mishina NM, Mishin AS, Belyaev Y, Bogdanova EA, Lukyanov S, Schultz C, Belousov VV: **Live-Cell STED Microscopy with Genetically Encoded Biosensor.** *Nano Lett* 2015, **15:**2928-2932.

498. Adams DS, Levin M: **Measuring Resting Membrane Potential Using the Fluorescent Voltage Reporters DiBAC4(3) and CC2-DMPE.** *Cold Spring Harb Protoc* 2012, **2012:**459-464.

499. Emmons-Bell M, Durant F, Hammelman J, Bessonov N, Volpert V, Morokuma J, Pinet K, Adams DS, Pietak A, Lobo D, Levin M: **Gap Junctional Blockade Stochastically Induces Different Species-Specific Head Anatomies in Genetically Wild-Type Girardia dorotocephala Flatworms.** *Int J Mol Sci* 2015, **16:**27865-27896.

Appendix A

Supporting information: Discovery of small molecule inhibitors that interact with gamma-tubulin.

This appendix contains material that was previously published as Friesen DE, Barakat KH, Semenchenko V, Perez-Pineiro R, Fenske BW, Mane J, Wishart DS, Tuszynski JA "Discovery of small molecule inhibitors that interact with gamma-tubulin," *Chem Biol Drug Des* 2012, 79:639-652. This was a collaborative effort. I performed molecular dynamics simulations, clustering, computer modelling, and analysis, and primarily wrote the manuscript. V. Semenchenko and R. Perez-Tineiro performed laboratory experiments. K. Barakat and B. Fenske performed docking. J. Mane, D. Wishart, and J. Tuszynski assisted with analysis.

```
10          20          30          40          50          60
MGSSHHHHHH  SSGLVPRGSH  MLEDDDDKMP  REIITLQLGQ  CGNQIGFEFW  KQLCAEHGIS

            70          80          90          100         110         120
PEGIVEEFAT  EGTDRKDVFF  YQADDEHYIP  RAVLLDLEPR  VIHSILNSPY  AKLYNPENIY

            130         140         150         160         170         180
LSEHGGGAGN  NWASGFSQGE  KIHEDIFDII  DREADGSDSL  EGFVLCHSIA  GGTGSGLGSY

            190         200         210         220         230         240
LLERLNDRYP  KKLVQTYSVF  PNQDEMSDVV  VQPYNSLLTL  KRLTQNADCV  VVLDNTALNR

            250         260         270         280         290         300
IATDRLHIQN  PSFSQINQLV  STIMSASTTT  LRYPGYMNND  LIGLIASLIP  TPRLHFLMTG

            310         320         330         340         350         360
YTPLTTDQSV  ASVRKTTVLD  VMRRLLQPKN  VMVSTGRDRQ  TNHCYIAILN  IIQGEVDPTQ

            370         380         390         400         410         420
VHKSLQRIRE  RKLANFIPWG  PASIQVALSR  KSPYLPSAHR  VSGLMMANHT  SISSLFERTC

            430         440         450         460         470
RQYDKLRKRE  AFLEQFRKED  MFKDNFDEMD  TSREIVQQLI  DEYHAATRPD  YISWGTQEQ
```

MGSSHHHHHH SSGLVPRGSH MLEDDDDK –His-tag (with Thrombin and Enterokinase recognition sites)

Figure A.1. Human g-tubulin construct sequence (TUBG1 inserted into a pET15b vector between the *XhoI* and *HindIII* restriction sites).
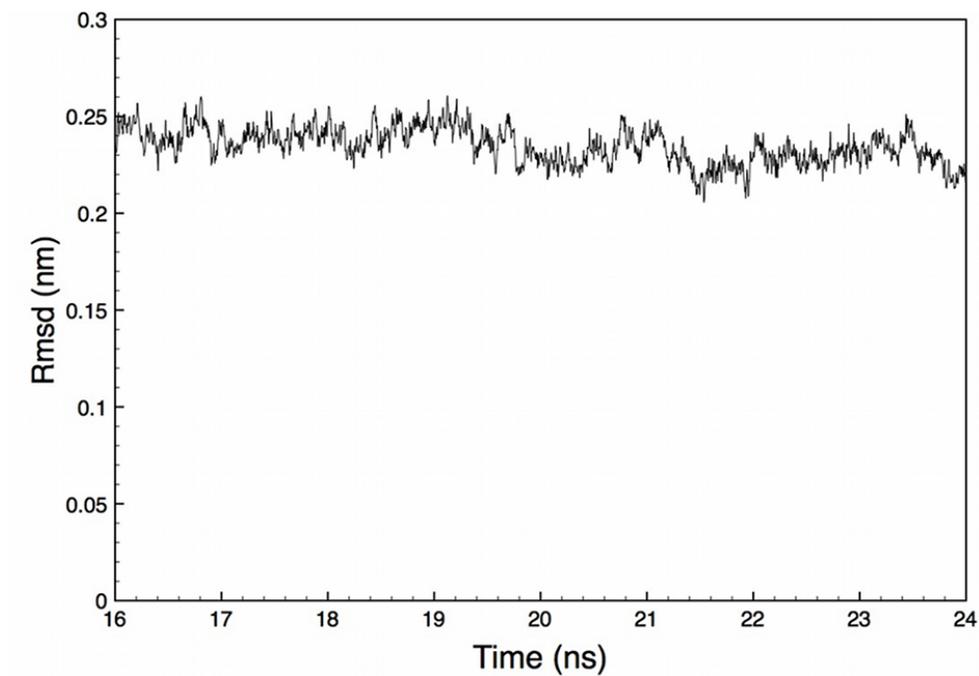
Figure A.2. RMSD of the backbone atoms from the reference structure at the beginning of the MD Simulation. The 16-24 ns period is shown which corresponded to the analyzed stable region of the RMSD during the simulation.
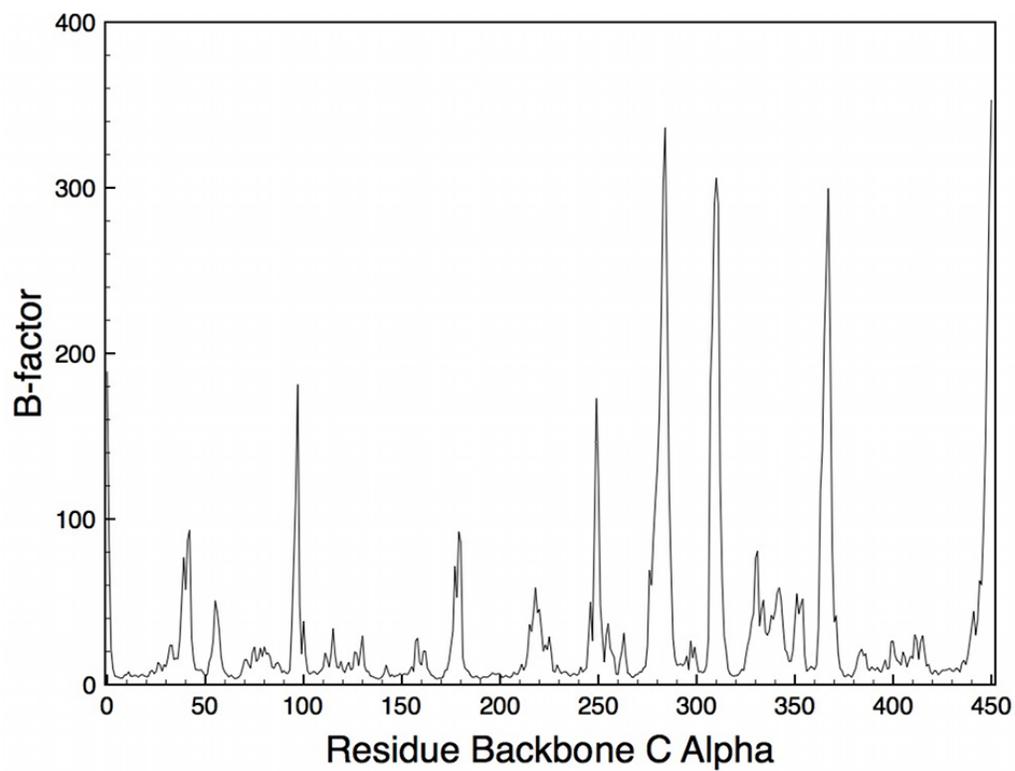
Figure A.3. B-factors of the Cα atoms of the residues of γ-tubulin during the analyzed 16-24 ns period of the MD simulation.
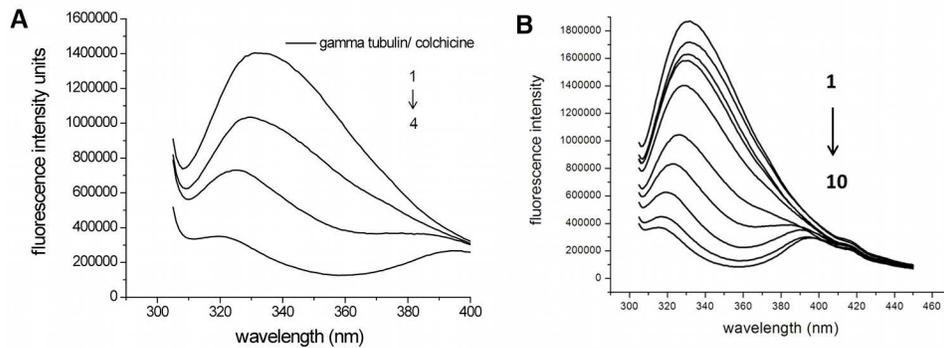
Figure A.4. Comparison of fluorescence quenching of colchicine to γ-tubulin and α_Iβ_I-tubulin. (A) Fluorescence emission spectra of γ-tubulin (2 μM) in the presence of colchicine: 0 μM (1), 10 μM (2), 40 μM (3), 80 μM (4). λexcit= 295 nm, slit width 5 nm. Tryptophan fluorescence quenching of γ-tubulin (2 μM) plotted as extinction of tubulin tryptophans (F/Fo, %) in the presence of increasing concentrations of colchicine. (B) Fluorescence emission spectra of α_Iβ_I-tubulin in the presence of colchicine at different concentrations, (A) (1) 0 M, (2) 1 μM (3) 2 μM, (4) 5 μM (5) 10 μM (6) 20 μM (7) 40 μM (8) 60 μM (9) 80 μM (10) 100 μM. λexcit= 295 nm, slit width 5 nm.

Figure A.5. Figure S5. TUBG1/TUBB-TUBA dimer amine cross-linking with DSG (disuccinimidylglutarate)

Cross-linking will produce covalent bonds and will make linked proteins stable to run on SDS-PAGE protein gel as complexes of a bigger mass (depending how many protein molecules were linked together).

In theory we have a dimer of TUBB/TUBA and TUBG1 which (if functional) should make complex TUBB/TUBA/TUBG1. Molecular mass of any of these tubulins is around 50KDa (gel is not that sensitive to show difference of 1 - 5 KDa). If we have TUBG1 bound to the dimer we will see a band of ~150KDa on a gel after cross-linking reaction. We also can see 150KDa band (theoretically) if monomer of TUBG1 will make a trimer (should not happen and checked by control) and if dimer TUBB/TUBA will be dissociated and single TUBB or TUBA will be attached to the dimer unit (because we do use dimer purified from the brain it is unlikely and is checked by control). To add to the picture we need to mention that TUBA has 19 Lysines, TUBB - 15 Lysines, TUBG1 - 17

Lysines plus N-term amines. All of them can potentially be involved in covalent bonds during cross-linking.

Line 1 (control) - in a reactive mixture only buffer, TUBG1 and DSG (cross-linking reagent). Result: some random high molecular weight aggregates (remember 17 native Lysines) some unreacted monomers (band at 55KDa) and no 150KDa band (good, as expected).

Line 2 (control) - in a reactive mixture only buffer, TUBB/TUBA and DSG. Result: high molecular weight aggregates (some of them so big that they did not enter the gel and were stained in a loading pocket) and the band at 55KDa (unreacted dimer which runs as a monomers on SDS-PAGE). Still no 150KDa band. Knowing that dimer looked already aggregated after melting (visual turbidity in a protein solution) this result is completely expected and useful as a second control.

Line 3 - in a reactive mixture buffer, TUBB/TUBA, TUBG1, GTP and DSG.

Line 4 - same components just without GTP. Result (for the line 3 and 4): some unreacted tubulins (band at 55KDa), random high molecular weight aggregates (expected) and two recognizable bands under 130KDa (could be a tubulin dimer of TUBA/TUBG1) and band between 130-170KDa - expected trimer of TUBB/TUBA/TUBG1.
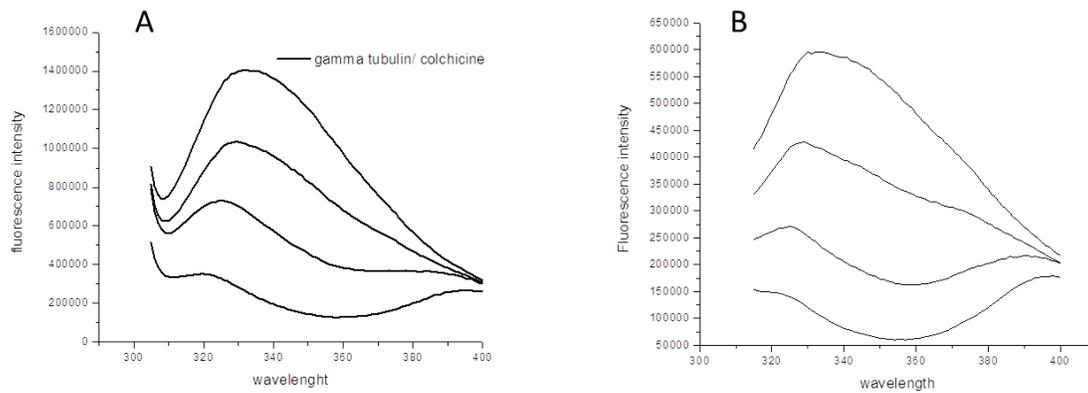
Figure A.6. Fluorescence quenching of two different batches of gamma tubulin (A) old (B) new in the presence of colchicine under the same conditions reported in the manuscript. Similar quenching occurred.
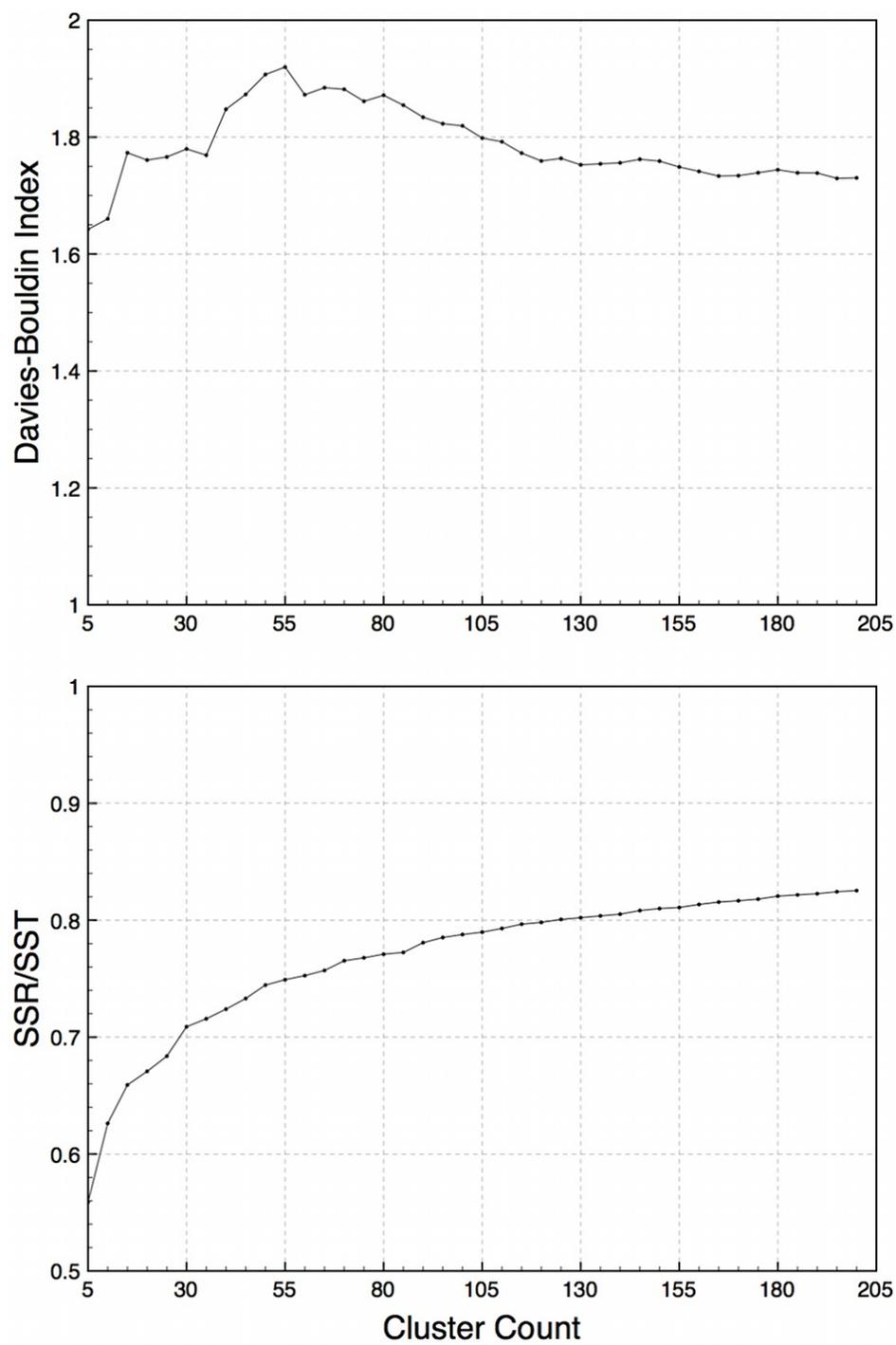
Figure A.7. Clustering analysis for the MD trajectory. Cluster size of 35 was taken due to its local minimum in DBI and the SSR/SST curve leveling substantially at this cluster size.
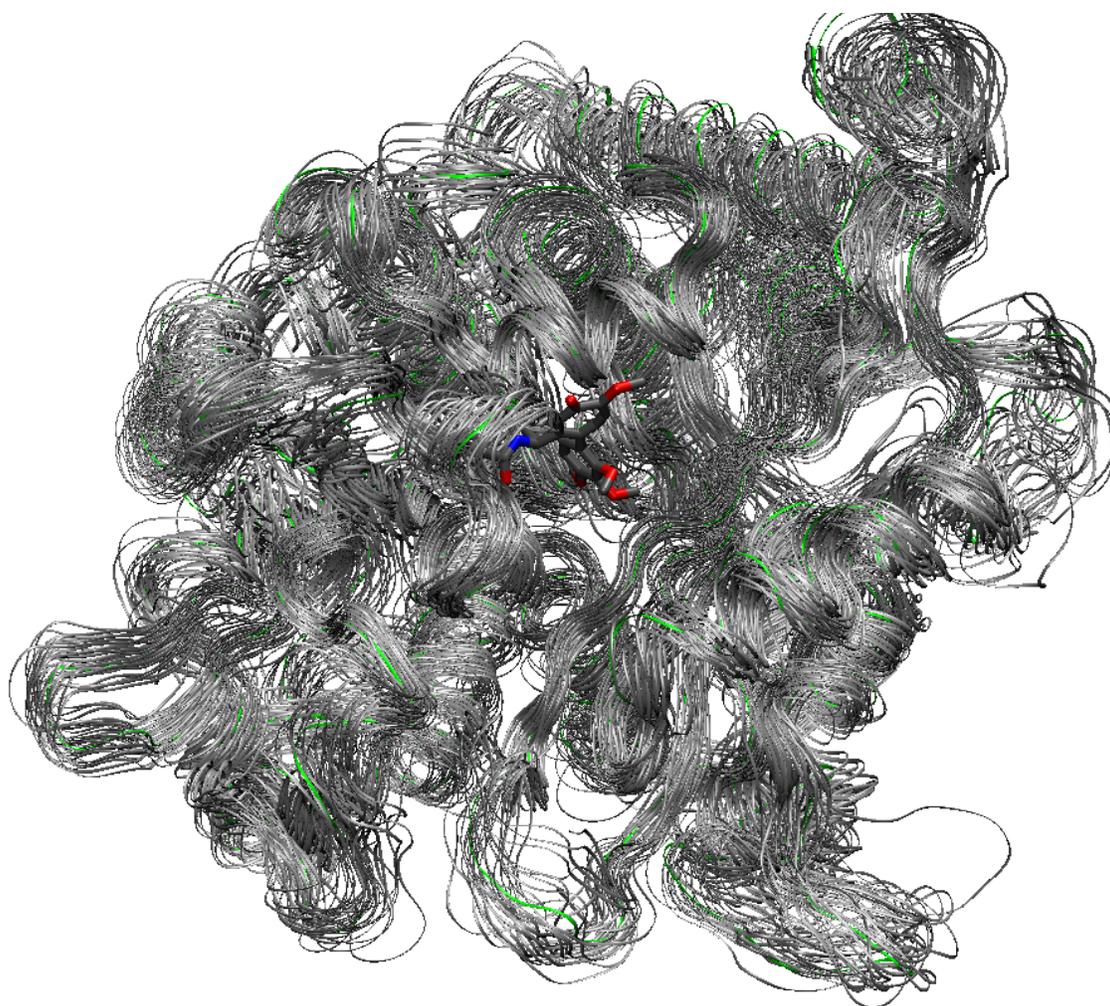
Figure A.8. Dominant conformations of γ-tubulin in our MD trajectory. The 35 representative targets are in grey. Colchicine (ligand in grey) docked to target 3 (highlighted as green) is shown.

Appendix B

Supporting information: Modeling the energetic cost of cancer as a result of altered energy metabolism: implications for cachexia.

This appendix contains material that was previously published as the supplemental material to: Friesen DE, Baracos VE, Tuszynski JA "Modeling the energetic cost of cancer as a result of altered energy metabolism: implications for cachexia," *Theor Biol Med Model* 2015, 12:17. I developed the model and drafted the manuscript. V. Baracos provided data and helped with manuscript edits. J. Tuszynski conceived of the study and helped with manuscript edits.

B.1   Tumor cost derivation

The cost to the body of the tumor in terms of glucose is:

Glucose cost = Glucose lost to aerobic portion of tumor
*   +glucose equivalents required to recycle lactate generated anaerobically by tumor* (1)

This is because the glucose consumed anaerobically by the tumor is converted to lactate and is released back into the bloodstream. The glucose consumed aerobically by the tumor is not reusable by the body.

Consider a tumor consuming ATP at a rate of A_{cancer} (mol ATP/day), where

$$A_{cancer} = A_{aerobic} + A_{anaerobic} \qquad (2)$$

Then,

$$Glucose_{cost} = A_{aerobic}/30 + A_{Cori}/30 \qquad (3)$$
$$= A_{aerobic}/30 + 6(A_{anaerobic}/2)/30 \qquad (4)$$
$$= (A_{aerobic} + 3 A_{anaerobic}) / 30 \qquad (5)$$
$$= (A_{cancer} + 2 A_{anaerobic}) / 30 \qquad (6)$$
$$= (A_{cancer}/30)(1+2X_{anaerobic}) \qquad (7)$$

$Glucose_{cost}$ is the rate glucose is consumed as a direct result of the tumor, in (mol glucose/day). A_{Cori} is the rate of ATP consumed by the Cori cycle to reconvert the lactate to glucose. The first term in equation (3) is the glucose used by the aerobic portion of the tumor, and the second term refers to the glucose needed to generate the ATP in the liver to convert the lactate generated by the anaerobic portion of the tumor, using the fact that a

glucose yields 30 ATP [1]. Equation (4) uses the fact that 6 ATP are required to convert lactate back to glucose, and $A_{anaerobic}/2$ is the amount of glucose used anaerobically by the tumor, as glycolysis in a cell generates 2 ATP. Equation (6) uses

$$A_{cancer} = A_{aerobic} + A_{anaerobic} \tag{8}$$

Equation (7) uses

$$X_{anaerobic} = A_{anaerobic} / A_{cancer} \tag{9}$$

The aerobic component of the tumor metabolism includes glucose and all other fuels consumed aerobically.

If $X_{anaerobic}=1$, we see from equation (7) that the glucose cost is three times as much as if $X_{anaerobic}=0$. Thus, we say that an anaerobic tumor costs three times as much as an aerobic tumor. This is graphically illustrated in Figure 2.

As ATP is the currency of energy in the cell, equation (7) can be rewritten as:

$$P_{cost} = P_{cancer}(1 + 2 X_{anaerobic}) \tag{10}$$

which is equation (5-6) in the main text.

B.2 Table B.1

Table B.1. Percent of increased measured tumor energy expenditure, $P_{cost} = P_{Cori} + P_{aerobic}$, due to different metabolic pathways, according to our model, at various percentages of ATP supplied by glycolysis, $X_{anaerobic}$.

Percentage glycolysis $X_{anaerobic}$ (%)	% of P_{cost} due to Cori cycle (P_{Cori}/P_{cost}) (%)	% of P_{cost} due to aerobic portion of tumor ($P_{aerobic}/P_{cost}$) (%)
0	0	100
5	14	86
10	25	75
20	43	57
25	50	50
50	75	25
60	82	18
85	94	6
100	100	0

In effect, the anaerobic tumor due to the Cori cycle costs 3 times an aerobic tumor (see Additional file 1).
So:

$$P_{Cori} / P_{aerobic} = 3 \, X_{anaerobic} / (1 - X_{anaerobic})) \qquad (1)$$

As in equation (5) in the main text:

$$P_{cost} = P_{aerobic} + P_{Cori} \qquad (2)$$

So:

$$P_{Cori}/P_{cost} = 3 \, X_{anaerobic} / (3 \, X_{anaerobic} + (1 - X_{anaerobic})) \qquad (3)$$
$$= 3 \, X_{anaerobic} / (2 \, X_{anaerobic} + 1) \qquad (4)$$

Likewise:

$$P_{aerobic}/P_{cost} = (1 - X_{anaerobic}) / (3 \, X_{anaerobic} + (1 - X_{anaerobic})) \qquad (5)$$
$$= (1 - X_{anaerobic}) / (2 \, X_{anaerobic} + 1) \qquad (6)$$

These values are shown in Table S1 in columns 2 and 3.

B.3 Tumor cost from oxygen consumption increase

In Koea and Shaw [2], oxygen consumption (µmol / kg min) as a function of tumor bulk (g) is given. The slope is 41 µmol / kg tumor/ min/kg patient (r^2=0.79). To convert this into the cost of cancer as a function of tumor bulk in kcal/kg tumor/day/kg patient, the oxygen consumption per tumor bulk (µmol / kg tumor/ min/kg patient) is converted to ml oxygen/kg tumor/min/kg patient) using the conversion 0.022391 ml = µmol O_2. This is converted to kJ/kg tumor/min/kg patient by the conversion 21.1 kJ/ O_2 [3]. This is converted to kcal/kg tumor/day/kg patient using standard conversions. As patient mass was not given in this study, converting this value precisely to kcal/kg tumor/day was not possible; however we assume average patient weight was between 60 and 70 kg [4] to offer a range of values of tumor cost in kcal/kg tumor/day.

B.4 Calculations of cost of tumor based on glucose utilization

p_{cancer} is calculated using equation (21) in the main text.

To calculate the estimated cost of the tumor based on glucose turnover and glucose recycling, $P_{cost\_glucose}$, equations (22) in the main text are used to calculate $p_{anaerobic}$. This assumes that the increased glucose turnover enters the cancer, and that the increased Cori cycling is due to glucose being recycled as a result of the glucose being metabolized anaerobically by the tumor. $p_{anaerobic}$ is equivalent to $X_{anaerobic}$ using the following formula (assuming glucose is used for either aerobic or anaerobic energy)

$$X_{anaerobic} = p_{anaerobic} / (p_{anaerobic} + 15(1 - p_{anaerobic})) \qquad (11)$$

The increased glucose turnover in g/kg patient/day is converted to increased mol glucose/kg patient/day using the molecular mass of glucose, 180.16 g/mol, to get mol glucose/kg patient/day increase. Based on $X_{anaerobic}$, the amount of glucose used anaerobically by the tumor is calculated. This leads to mol glucose/kg patient/day recycled in the Cori cycle. 6 mol ATP is needed per mol glucose/kg/day recycled, leading to mol ATP/kg/day Cori cycling cost. Assuming the liver generated its energy aerobically, we use 30 mol ATP/mol glucose consumed by the liver, to get a mol glucose consumed by liver/kg/day Cori cycle cost. We convert this to g glucose consumed by liver/kg/day for Cori cycle, using again 180.16 g/mol molecular weight of glucose. Then we convert this value to kcal/kg/day using the conversion parameter of 4.2 kcal/g used by Hall [5] to get the Cori cycle cost in kcal/kg/day. As seen in Table S1, the value of $X_{anaerobic}$ leads to the percentage the Cori cycle cost is of the total cost of the cancer. The total cost of the cancer is then calculated in kcal/kg patient/day. In Table 2, the cost, $P_{cost\_glucose}$, is then displayed for a 70kg patient.

In study B, where an estimate of the tumor burden is available, we are able to use the same method to calculate the specific cost of cancer, K_{cost}, for a 70kg patient, with the assumption of $X_{anaerobic}$=25%.

B.5　Recurrence relation $g(p_{cancer}, p_{anaerobic})$

$g(p_{cancer}, p_{anaerobic})$, the expected ATP generated for the body per glucose entering the bloodstream (energetic payout of a glucose), is described by a recurrence relation:

$$g_{(t+1)}(p_{cancer}, p_{anaerobic}) = (1- p_{cancer})30 + p_{cancer}(p_{anaerobic}(-6 + g_{(t)}(p_{cancer}, p_{anaerobic}))) \quad (1)$$

This recurrence relation describes roughly what may happen to a glucose in the bloodstream. In the first case (the first term of equation 1), the glucose is consumed by the body, with probability $(1- p_{cancer})$, and generate 30 ATP for the body.

In the second case (the second term of equation 1), the cancer consumes the glucose, with probability p_{cancer}. In this case, with probability $p_{anaerobic}$, the cancer metabolizes the glucose anaerobically, which leads to lactate being produced. For the body, this costs 6 ATP in the Cori cycle to recycle the glucose. Since the glucose is recycled, it leads to the term $g_{(t)}(p_{cancer}, p_{anaerobic})$) in equation 1 which signifies that $g(p_{cancer}, p_{anaerobic})$ has to be recalculated for that glucose because it is back in the bloodstream at the next time point $(t+1)$. If the cancer uses the glucose aerobically, the body does not get any ATP from this glucose, and so its value is 0 to the body, and so it is omitted from equation 1. t in equation 1 signifies time, starting at $t=0$. Because every time the glucose entering the bloodstream has a chance of being used by the tumor anaerobically and being recycled, it leads to an increase in time t, and the recurrence relation continues. As t increases, there is less and less chance of the original glucose not being consumed either by the body or aerobically by the tumor. $g_{(t)}$ converges to an expected payout of ATP per glucose as t (time) goes to infinity. If no glucose was lost to the cancer, $g_{(t)}$ would be 30 ATP. The initial condition $g_{(0)}$ is given to be 30 ATP, although this does not affect the final solution of $g_{(t)}$ as t goes to infinity. The value of $g(p_{cancer}, p_{anaerobic})$ is the value of $g(p_{cancer}, p_{anaerobic})$ as t goes to infinity.

p_{lost} , the percentage of energy lost to the body per glucose entering the bloodstream, is calculated as follows:

$$p_{lost}(p_{cancer}, p_{anaerobic}) = (30 - g(p_{cancer}, p_{anaerobic})) / 30 \quad (2)$$

Because the tumor consumes glucose, the body will not get the full 30 ATP that would be normally expected in a healthy body. For example, if the probability that glucose enters the cancer is 25%, and the probability that the cancer consumes the glucose anaerobically is 75%, then p_{cancer} is 0.25, $p_{anaerobic}$ is 0.75, $g(0.25, 0.75)$ is 26.3, and so p_{lost} is 12%. In effect, The expected amount of ATP generated for the body in this case is 26.3 ATP, when in a healthy body it would be 30 ATP. So the percentage of energy lost is 12%.

References

1.　Rich PR: **The molecular machinery of Keilin's respiratory chain.** *Biochem Soc Trans* 2003, **31:**1095-1105.
2.　Koea JB, Shaw JH: **The effect of tumor bulk on the metabolic response to cancer.** *Ann Surg* 1992, **215:**282-288.

3.   Scott CB: **Contribution of anaerobic energy expenditure to whole body thermogenesis.** *Nutr Metab* 2005, **2:**14.

4.   Xu WP, Cao DX, Lin ZM, Wu GH, Chen L, Zhang JP, Zhang B, Yang ZA, Jiang Y, Han YS, et al: **Analysis of energy utilization and body composition in kidney, bladder, and adrenal cancer patients.** *Urologic Oncology* 2012, **30:**711-718.

5.   Hall KD: **Computational model of in vivo human energy metabolism during semistarvation and refeeding.** *Am J Physiol Endocrinol Metab* 2006, **291:**E23-E37.

Appendix C

Matlab Code to generate nanofabricated devices for microtubule electrical characterization.

C.1 Flow cell design code

The following code interfaces with the Raith GDSII Matlab Toolbox v1.1 to implement the flow cell electrode design. The code is written in Matlab using Matlab R2012B.

```
% ff1
% Copyright Douglas Friesen, 2015
% Simply device to just involve photolithography electrodes
% Include alignment marks for subsequent EBL alignment if needed
% 100mm x 100mm wafer
% We use just step 3 for now
% Photolithography: Step 0 (layer 1), 3 (layer 3), 4 (layer 4)
% EBL: Step 1 (layer 0), 2 (layer 0)
% Coverslip: Step 5
%

clf;
clear;
% showall: 0 for correct output files, 1 to show all parts of device
together
showall=1;
% show: part of the device to show (0-4). If using showall=1, use
show=0.
% Until we can show particular layers, Optical layers will be cumulative
from 0 to 5
show=0;

% Device width (millimeters)
dwidth_m=30;
dheight_m=30;
dcentrex_m=dwidth_m/2;
dcentrey_m=dheight_m/2;
gridn=3; % Number of row
gridm=3; % Number of columns

nanochannelShiftV_m=0;

% writefield
writefield_u=200;
hwritefield_u=writefield_u/2;

% 4" wafer settings
w_street=0.0;
centredchip=1;
```

```
showplot=0;
w_EBR_m=3;
%[uv_c,uv_s]=waferlayout('circ',w_EBR_m,[dwidth_m
dheight_m],w_street,centredchip,showplot);


% Total wafer width
waferw_m=100;
waferc_m=waferw_m/2;
% electrical pad indent from edges
edge_m=7;

%
% Step 0: Alignment marks
% 3 x 3 grid centred at 0,0. 66x66mm
%

step0Layer=1;

gridw_m=dwidth_m*gridm;
gridh_m=dheight_m*gridn;
linesize_u=50;

bottomleftx_m=waferc_m-gridw_m/2;
bottomlefty_m=waferc_m-gridh_m/2;
centres=centrexyonwafer(gridw_m,gridh_m,gridn,gridm,bottomleftx_m,bottom
lefty_m);
% Instead, manually set the centres
%centres = [50, 25; 50, 50; 50, 75];
fprintf(1,'Centres: %d ', centres);
S(1)=gridlines(gridn,gridm,gridw_m,gridh_m,linesize_u,step0Layer,1);

plusw = [5000, 1000, 350, 120, 60, 20, 15, 9, 6, 3]
plusy = [0, -8800, -11500, -12800, -13800, -14100, -14180, -14250, -
14310, -14350 ]

plusw2 = [1000, 350, 120, 60, 20, 15, 9, 6, 3]
plusy2 = [-8800, -11500, -12800, -13800, -14100, -14180, -14250, -14310,
-14350 ]

% Where optical alignment marks are
plusx_u = 43000;
plusx2_u = 40000;

% Full length of plus mark and width of plus mark lines for raith
alignment
plusraithlw_u=[12, 2;
              16, 4;
              20, 6;
              40, 10;
              60, 16]

% Location of raith alignment marks (reservoir step)
rplusraithuv = zeros(10,4,2);
rplusraithuv(1,:,:) = [-40000, -26000; 40000, -26000; 40000 26000; -
40000 26000];
rplusraithuv(2,:,:) = [-40000, -26100; 40000, -26100; 40000 26100; -
40000 26100];
```

```
rplusraithuv(3,:,:) = [-40000, -26200; 40000, -26200; 40000 26200; -
40000 26200];
rplusraithuv(4,:,:) = [-40000, -26300; 40000, -26300; 40000 26300; -
40000 26300];
rplusraithuv(5,:,:) = [-40000, -26400; 40000, -26400; 40000 26400; -
40000 26400];
rplusraithuv(6,:,:) = [-40000, -20000; 40000, -20000; 40000 20000; -
40000 20000];
rplusraithuv(7,:,:) = [-40000, -20100; 40000, -20100; 40000 20100; -
40000 20100];
rplusraithuv(8,:,:) = [-40000, -20200; 40000, -20200; 40000 20200; -
40000 20200];
rplusraithuv(9,:,:) = [-40000, -20300; 40000, -20300; 40000 20300; -
40000 20300];
rplusraithuv(10,:,:) =[-40000, -20400; 40000, -20400; 40000 20400; -
40000 20400];

% Location of raith alignment marks (wire step)
wplusraithuv = zeros(10,4,2);
wplusraithuv(1,:,:) = [-40000, -23000; 40000, -23000; 40000 23000; -
40000 23000];
wplusraithuv(2,:,:) = [-40000, -23100; 40000, -23100; 40000 23100; -
40000 23100];
wplusraithuv(3,:,:) = [-40000, -23200; 40000, -23200; 40000 23200; -
40000 23200];
wplusraithuv(4,:,:) = [-40000, -23300; 40000, -23300; 40000 23300; -
40000 23300];
wplusraithuv(5,:,:) = [-40000, -23400; 40000, -23400; 40000 23400; -
40000 23400];
wplusraithuv(6,:,:) = [-40000, -17000; 40000, -17000; 40000 17000; -
40000 17000];
wplusraithuv(7,:,:) = [-40000, -17100; 40000, -17100; 40000 17100; -
40000 17100];
wplusraithuv(8,:,:) = [-40000, -17200; 40000, -17200; 40000 17200; -
40000 17200];
wplusraithuv(9,:,:) = [-40000, -17300; 40000, -17300; 40000 17300; -
40000 17300];
wplusraithuv(10,:,:) =[-40000, -17400; 40000, -17400; 40000 17400; -
40000 17400];

% Assert: length(rplusraithuv) == length(plusraithlw_u)

% Optical alignment marks
for i=1:length(plusw)
    S(end+1)=plusalignment(plusw(i),step0Layer,1);
    S(end+1)=inverseplusalignment(plusw(i),step0Layer,1);
    S(end+1)=bigbox(plusw(i),plusw(i),step0Layer,1);
end

%for i=1:length(plusw2)
    %S(end+1)=plusalignment(plusw2(i),step0Layer,1);
    %S(end+1)=inverseplusalignment(plusw2(i),step0Layer,1);
    %S(end+1)=bigbox(plusw2(i),plusw2(i),step0Layer,1);
%end

% For step 3
step3Layer=3;
for i=1:length(plusw)
```

```
    S(end+1)=plussquarealignment(plusw(i),step3Layer,1);
end

for i=1:length(plusw2)
    S(end+1)=bigbox(plusw2(i),plusw2(i),step3Layer,1);
end

% Raith alignmment marks for EBL nanochannels (now done in wire optical
step)
for i=1:length(plusraithlw_u)

S(end+1)=plusraithalignment(plusraithlw_u(i,1),plusraithlw_u(i,2),step3L
ayer,1);
end


% For step 5 (Coverslip)
step5Layer=5;

% Coverslip outline
S(end+1)=bigbox(18000,18000,step5Layer,1);

% number of electrodes put on device
numElectrodes=5;
% Side viewing port
S(end+1)=bigbox(4000,15000,step3Layer,1);

% Bottom viewing port
S(end+1)=bigbox(15000,4000,step3Layer,1);

% Optical wires component

nbottomSideIndent_u=17;
nbottomSpacingWithSides_u= writefield_u - (nbottomSideIndent_u*2);
w_microelectrode_u=3;
nBottomSpace_u=nbottomSpacingWithSides_u - w_microelectrode_u;
%bottomNSpacing_u=nBottomSpace_u/(numElectrodes-1);
microelectrode_spacing_u=4;
%bottomNSpacing_u=nBottomSpace_u/(numElectrodes-1);
bottomNSpacing_u=microelectrode_spacing_u+w_microelectrode_u;
left_bottom_u=-nBottomSpace_u/2;
left_top_u=left_bottom_u;
top_spacing_u=bottomNSpacing_u;
%bottom_space_with_pads_u=(dwidth_m-(2*edge_m))*1000;
%pad_w_u=bottom_space_with_pads_u/((numElectrodes*2)-1);
pad_w_u=2000;
fprintf(1,'\nPad width: %d',pad_w_u);
%bottom_space_u=bottom_space_with_pads_u - pad_w_u;
left_bottom_u=-((dwidth_m/2)-edge_m)*1000;
right_bottom_u=-left_bottom_u;
%bottomSpacing_u=bottom_space_u/(numElectrodes-1);
bottomSpacing_u=4000;
fprintf(1,'\nBottom spacing: %d',bottomSpacing_u);
bottomWidth_u=300;
bottomv_u=(-dcentrey_m-nanochannelShiftV_m+1)*1000;

basetop_u=-1070;
basem1_u=-1570;
```

```
basem2_u=-3070;
basem3_u=-6070;
basem4_u=-9070;
m1left_u=-3650;
m1spacing_u=2000;
pad_h_u = 3000;
vspacing1_u = 200;
vspacing2_u = 1000;


fprintf(1,'\nPad height: %d',pad_h_u);
% 3, 4 spacing, 5 electrodes
bort=0;
S(end+1)=meprobe(w_microelectrode_u,numElectrodes,left_top_u,top_spacing
_u,left_bottom_u,right_bottom_u,bottomSpacing_u,bottomWidth_u,bottomv_u,
basetop_u,basem1_u,basem2_u,basem3_u,basem4_u,m1left_u,m1spacing_u,vspac
ing1_u,vspacing2_u,pad_w_u,pad_h_u,bort,step3Layer,1);
bort=1;
S(end+1)=meprobe(w_microelectrode_u,numElectrodes,left_top_u,top_spacing
_u,left_bottom_u,right_bottom_u,bottomSpacing_u,bottomWidth_u,bottomv_u,
basetop_u,basem1_u,basem2_u,basem3_u,basem4_u,m1left_u,m1spacing_u,vspac
ing1_u,vspacing2_u,pad_w_u,pad_h_u,bort,step3Layer,1);

% 3, 4 spacing, 5 electrodes; longer
bort=0;
S(end+1)=meprobe(w_microelectrode_u,numElectrodes,left_top_u,top_spacing
_u,left_bottom_u,right_bottom_u,bottomSpacing_u,bottomWidth_u,bottomv_u,
-
70,basem1_u,basem2_u,basem3_u,basem4_u,m1left_u,m1spacing_u,vspacing1_u,
vspacing2_u,pad_w_u,pad_h_u,bort,step3Layer,1);
bort=1;
S(end+1)=meprobe(w_microelectrode_u,numElectrodes,left_top_u,top_spacing
_u,left_bottom_u,right_bottom_u,bottomSpacing_u,bottomWidth_u,bottomv_u,
-
70,basem1_u,basem2_u,basem3_u,basem4_u,m1left_u,m1spacing_u,vspacing1_u,
vspacing2_u,pad_w_u,pad_h_u,bort,step3Layer,1);

%4, 6 spacing, 5 electrodes
bort=0;
S(end+1)=meprobe(4,numElectrodes,left_top_u,10,left_bottom_u,right_botto
m_u,bottomSpacing_u,bottomWidth_u,bottomv_u,basetop_u,basem1_u,basem2_u,
basem3_u,basem4_u,m1left_u,m1spacing_u,vspacing1_u,vspacing2_u,pad_w_u,p
ad_h_u,bort,step3Layer,1);
bort=1;
S(end+1)=meprobe(4,numElectrodes,left_top_u,10,left_bottom_u,right_botto
m_u,bottomSpacing_u,bottomWidth_u,bottomv_u,basetop_u,basem1_u,basem2_u,
basem3_u,basem4_u,m1left_u,m1spacing_u,vspacing1_u,vspacing2_u,pad_w_u,p
ad_h_u,bort,step3Layer,1);

%2, 4 spacing, 5 electrodes
bort=0;
S(end+1)=meprobe(2,numElectrodes,left_top_u,6,left_bottom_u,right_bottom
_u,bottomSpacing_u,bottomWidth_u,bottomv_u,basetop_u,basem1_u,basem2_u,b
asem3_u,basem4_u,m1left_u,m1spacing_u,vspacing1_u,vspacing2_u,pad_w_u,pa
d_h_u,bort,step3Layer,1);
bort=1;
S(end+1)=meprobe(2,numElectrodes,left_top_u,6,left_bottom_u,right_bottom
_u,bottomSpacing_u,bottomWidth_u,bottomv_u,basetop_u,basem1_u,basem2_u,b
```

```
asem3_u,basem4_u,m1left_u,m1spacing_u,vspacing1_u,vspacing2_u,pad_w_u,pa
d_h_u,bort,step3Layer,1);


% Alignment
SiLayer=0;
AlignLayer=1;
windowDF=1;
dotdose=1;

% Nano Small alignment marks
a_crossN=7.5;
w_thickN=1;
w_thinN=0.1;
L_thickN=2;
a_manualN=a_crossN*1.2;
L_autoN=a_crossN-2*L_thickN;
w_autoN=L_thickN/6;
S(end+1)=Raith_alignment_mark(['AlignmentMark-' num2str(SiLayer)],[0
0],SiLayer,windowDF,a_crossN,w_thickN,w_thinN,L_thickN,a_manualN,L_autoN
,w_autoN,dotdose);
S(end+1)=Raith_alignment_mark(['AlignmentMark-' num2str(AlignLayer)],[0
0],AlignLayer,windowDF,a_crossN,w_thickN,w_thinN,L_thickN,a_manualN,L_au
toN,w_autoN,dotdose);

% Nano Big alignment marks (for 3-pt alignment)
a_crossBN=75;
w_thickBN=10;
w_thinBN=10;
L_thickBN=20;
a_manualBN=a_crossBN*1.2;
L_autoBN=a_crossBN-2*L_thickBN;
w_autoBN=L_thickBN/6;
S(end+1)=Raith_alignment_mark(['BigAlignmentMark-' num2str(SiLayer)],[0
0],SiLayer,windowDF,a_crossBN,w_thickBN,w_thinBN,L_thickBN,a_manualBN,L_
autoBN,w_autoBN,dotdose);
S(end).elements(end+1)=Raith_element('aref',['AlignmentMark-'
num2str(SiLayer)],[-45 -45],[2 2],[90 90]);
S(end+1)=Raith_alignment_mark(['BigAlignmentMark-'
num2str(AlignLayer)],[0
0],AlignLayer,windowDF,a_crossBN,w_thickBN,w_thinBN,L_thickBN,a_manualBN
,L_autoBN,w_autoBN,dotdose);
S(end).elements(end+1)=Raith_element('aref',['AlignmentMark-'
num2str(AlignLayer)],[-45 -45],[2 2],[90 90]);

%
% End of Basic structures
%

% Step 3: Optical Litho: Electrodes and contact pads
name3a=['bigbox-4000-15000-' num2str(step3Layer)];
EO(1)=Raith_element('sref',name3a,[48000 0]);
EO(end+1)=Raith_element('sref',name3a,[-48000 0]);
name3a=['bigbox-15000-4000-' num2str(step3Layer)];
EO(end+1)=Raith_element('sref',name3a,[0 -48000]);
EO(end+1)=Raith_element('sref',name3a,[0 48000]);

% Align step 3 with step 4
```

```matlab
for i=1:length(plusw)
    name3b=['plussquare-' num2str(plusw(i)) '-' num2str(step3Layer)];
    EO(end+1)=Raith_element('sref',name3b,[-plusx_u plusy(i)]);
    EO(end+1)=Raith_element('sref',name3b,[plusx_u plusy(i)]);
end

% Set alignment marks for step 4
for i=1:length(plusw2)
    name3b=['bigbox-' num2str(plusw2(i)) '-' num2str(plusw2(i)) '-'
num2str(step3Layer)];
    EO(end+1)=Raith_element('sref',name3b,[-plusx2_u plusy2(i)]);
    EO(end+1)=Raith_element('sref',name3b,[plusx2_u plusy2(i)]);
end

% regular
name3j=[num2str(w_microelectrode_u) '-um-melctrd-5-7-500-'
num2str(step3Layer)];
% large
name3k=['4-um-melctrd-5-10-500-' num2str(step3Layer)];
% small
name3l=['2-um-melctrd-5-6-500-' num2str(step3Layer)];
% longer
name3m=[num2str(w_microelectrode_u) '-um-melctrd-5-7-1500-'
num2str(step3Layer)];
for i=1:length(centres)
    if i > 7
        % small
        EO(end+1)=Raith_element('sref',name3l,[centres(i,1)*1000-50000
(centres(i,2)+nanochannelShiftV_m)*1000-50000]);
    elseif i > 5
        % big
        EO(end+1)=Raith_element('sref',name3k,[centres(i,1)*1000-50000
(centres(i,2)+nanochannelShiftV_m)*1000-50000]);
    elseif i > 3
        % longer
        EO(end+1)=Raith_element('sref',name3m,[centres(i,1)*1000-50000
(centres(i,2)+nanochannelShiftV_m)*1000-50000]);
    else
        % regular
        EO(end+1)=Raith_element('sref',name3j,[centres(i,1)*1000-50000
(centres(i,2)+nanochannelShiftV_m)*1000-50000]);
    end
end
% standardize all top electrodes to 3, 4; 5
name3j=[num2str(w_microelectrode_u) '-um-melctrd-t-5-7-500-'
num2str(step3Layer)];
for i=1:length(centres)
    EO(end+1)=Raith_element('sref',name3j,[centres(i,1)*1000-50000
(centres(i,2)-nanochannelShiftV_m)*1000-50000]);
end

% Make EBL alignment marks for whole structure on Wire step
[m n o]=size(wplusraithuv);
for i=1:m
    name3k=['plusraith-' num2str(plusraithlw_u(mod(i-1,5)+1 ,1)) '-'
num2str(plusraithlw_u(mod(i-1,5)+1,2)) '-' num2str(step3Layer)];
    for j=1:n
```

```matlab
        EO(end+1)=Raith_element('sref',name3k,[wplusraithuv(i,j,1)
wplusraithuv(i,j,2)]);
    end
end

% Step 5: Coverslip: Reservoirs.

% Optical component
name5l=['bigbox-18000-18000-' num2str(step5Layer)];
for i=1:length(centres)
    %EO(end+1)=Raith_element('sref',name5l,[centres(i,1)*1000-50000
(centres(i,2))*1000-50000]);
end


% Step 0 on Layer 1
% Step 3 on Layer 3
% Step 4 on Layer 4
% Step 5 on Layer 5

nameO='OpticalStruct';
S(end+1)=Raith_structure(nameO,EO);

%axis equal;
L=Raith_library('ff1',S);
L.writegds('plain');

%
% Step 3: Wires and contact pads
%

%
% Step 4: Microchannels
%


%
% Step 5: Reservoirs
%

%
% All Optical Layers
%

%if showall == 1
    %Pf=Pa;
%else
    Pf=Raith_positionlist(L,'C:\RAITH150-
TWO\User\defriesen\GDSII\ff1.csf',[writefield_u writefield_u], ...
    [waferw_m waferw_m]);
%end

Pf.append(nameO,[waferc_m waferc_m],1,[-hwritefield_u -hwritefield_u
hwritefield_u hwritefield_u]);

Pf.writepls('./ff1f.pls'); % Write pls to current directory

% Plot
```

```
if show==1
    Pa.plotedges; % Plot structures and chip boundaries
    Pa.plotWF; % Plot writefield as green, dotted line
elseif show==2
    Pb.plotedges; % Plot structures and chip boundaries
    Pb.plotWF; % Plot writefield as green, dotted line
elseif show==3
    %Pc.plot; % Plot structures and chip boundaries
    Pf.plotedges; % Plot structures and chip boundaries
    Pf.plotWF; % Plot writefield as green, dotted line
elseif show==4
    Pf.plotedges; % Plot structures and chip boundaries
    Pf.plotWF; % Plot writefield as green, dotted line
elseif show==5
    Pf.plotedges; % Plot structures and chip boundaries
    Pf.plotWF; % Plot writefield as green, dotted line
elseif show==0
    Pf.plotedges; % Plot structures and chip boundaries
    Pf.plotWF; % Plot writefield as green, dotted line
end


% Plot wafer outline
th=linspace(0,2*pi,100);
r=50000;
plot(r*cos(th)+r,r*sin(th)+r,'b-');
```

C.2   Nanofluidic channel design code

The following code interfaces with the Raith GDSII Matlab Toolbox v1.1 to implement the nanofluidic channel design. This code can be run to generate photolithography mask designs for the alignment marks, microchannels, and contact pads and wires. It also generates a design for the Raith-two EBL machine at the Nanofab at the University of Alberta. The code is written in Matlab using Matlab R2012B.

```
% dd5
% Copyright Douglas Friesen, 2015
% Change reservoir mask, so that there is enough space for Nanoport
assemblies
% from dd5. Make EBL alignment marks in reservoir making step and
electrode step
% Remove initial alignment step
% Make it so we can start with either electrodes or reservoirs
% After consultation with Aaron
% 100mm x 100mm wafer
% Nine 22 mm x 22 mm devices
% bottom left is at 17mmx17mm
% top right is at 83mmx83mm
% Photolithography: Step 0 (layer 1), 3 (layer 3), 4 (layer 4)
% EBL: Step 1 (layer 0), 2 (layer 0)
```

```
% Coverslip: Step 5
%

clf;
clear;
% showall: 0 for correct output files, 1 to show all parts of device
together
showall=1;
% show: part of the device to show (0-4). If using showall=1, use
show=0.
% Until we can show particular layers, Optical layers will be cumulative
from 0 to 5
show=0;

% Device width (millimeters)
dwidth_m=74;
dheight_m=20;
dcentrex_m=dwidth_m/2;
dcentrey_m=dheight_m/2;
gridn=3; % Number of row
gridm=1; % Number of columns

nanochannelShiftV_m=4.5;

% writefield
writefield_u=200;
hwritefield_u=writefield_u/2;

% 4" wafer settings
w_street=0.0;
centredchip=1;
showplot=0;
w_EBR_m=3;
[uv_c,uv_s]=waferlayout('circ',w_EBR_m,[dwidth_m
dheight_m],w_street,centredchip,showplot);

% Total wafer width
waferw_m=100;
waferc_m=waferw_m/2;
% electrical pad indent from edges
edge_m=5;

%
% Step 0: Alignment marks
% 3 x 3 grid centred at 0,0. 66x66mm
%

step0Layer=1;

gridw_m=dwidth_m*gridm;
gridh_m=dheight_m*gridn;
linesize_u=50;

bottomleftx_m=waferc_m-gridw_m/2;
bottomlefty_m=waferc_m-gridh_m/2;
%centres=centrexyonwafer(gridw_m,gridh_m,gridn,gridm,bottomleftx_m,botto
mlefty_m);
% Instead, manually set the centres
```

238

```
centres = [50, 25; 50, 50; 50, 75];
%fprintf(1,'Centres: %d ', centres);
S(1)=gridlines(gridn,gridm,gridw_m,gridh_m,linesize_u,step0Layer,1);

plusw = [5000, 1000, 350, 120, 60, 20, 15, 9, 6, 3]
plusy = [0, -8800, -11500, -12800, -13800, -14100, -14180, -14250, -
14310, -14350 ]

plusw2 = [1000, 350, 120, 60, 20, 15, 9, 6, 3]
plusy2 = [-8800, -11500, -12800, -13800, -14100, -14180, -14250, -14310,
-14350 ]

% Where optical alignment marks are
plusx_u = 43000;
plusx2_u = 40000;

% Full length of plus mark and width of plus mark lines for raith
alignment
plusraithlw_u=[12, 2;
               16, 4;
               20, 6;
               40, 10;
               60, 16]

% Location of raith alignment marks (reservoir step)
rplusraithuv = zeros(10,4,2);
rplusraithuv(1,:,:) = [-38000, -26000; 38000, -26000; 38000 26000; -
38000 26000];
rplusraithuv(2,:,:) = [-38000, -26100; 38000, -26100; 38000 26100; -
38000 26100];
rplusraithuv(3,:,:) = [-38000, -26200; 38000, -26200; 38000 26200; -
38000 26200];
rplusraithuv(4,:,:) = [-38000, -26300; 38000, -26300; 38000 26300; -
38000 26300];
rplusraithuv(5,:,:) = [-38000, -26400; 38000, -26400; 38000 26400; -
38000 26400];
rplusraithuv(6,:,:) = [-38000, -20000; 38000, -20000; 38000 20000; -
38000 20000];
rplusraithuv(7,:,:) = [-38000, -20100; 38000, -20100; 38000 20100; -
38000 20100];
rplusraithuv(8,:,:) = [-38000, -20200; 38000, -20200; 38000 20200; -
38000 20200];
rplusraithuv(9,:,:) = [-38000, -20300; 38000, -20300; 38000 20300; -
38000 20300];
rplusraithuv(10,:,:) =[-38000, -20400; 38000, -20400; 38000 20400; -
38000 20400];

% Location of raith alignment marks (wire step)
wplusraithuv = zeros(10,4,2);
wplusraithuv(1,:,:) = [-38000, -23000; 38000, -23000; 38000 23000; -
38000 23000];
wplusraithuv(2,:,:) = [-38000, -23100; 38000, -23100; 38000 23100; -
38000 23100];
wplusraithuv(3,:,:) = [-38000, -23200; 38000, -23200; 38000 23200; -
38000 23200];
wplusraithuv(4,:,:) = [-38000, -23300; 38000, -23300; 38000 23300; -
38000 23300];
```

```
wplusraithuv(5,:,:) = [-38000, -23400; 38000, -23400; 38000 23400; -
38000 23400];
wplusraithuv(6,:,:) = [-38000, -17000; 38000, -17000; 38000 17000; -
38000 17000];
wplusraithuv(7,:,:) = [-38000, -17100; 38000, -17100; 38000 17100; -
38000 17100];
wplusraithuv(8,:,:) = [-38000, -17200; 38000, -17200; 38000 17200; -
38000 17200];
wplusraithuv(9,:,:) = [-38000, -17300; 38000, -17300; 38000 17300; -
38000 17300];
wplusraithuv(10,:,:) =[-38000, -17400; 38000, -17400; 38000 17400; -
38000 17400];

% Assert: length(rplusraithuv) == length(plusraithlw_u)

% Optical alignment marks
for i=1:length(plusw)
    S(end+1)=plusalignment(plusw(i),step0Layer,1);
    S(end+1)=inverseplusalignment(plusw(i),step0Layer,1);
    S(end+1)=bigbox(plusw(i),plusw(i),step0Layer,1);
end

%for i=1:length(plusw2)
    %S(end+1)=plusalignment(plusw2(i),step0Layer,1);
    %S(end+1)=inverseplusalignment(plusw2(i),step0Layer,1);
    %S(end+1)=bigbox(plusw2(i),plusw2(i),step0Layer,1);
%end

% For step 3
step3Layer=3;
for i=1:length(plusw)
    S(end+1)=plussquarealignment(plusw(i),step3Layer,1);
end

for i=1:length(plusw2)
    S(end+1)=bigbox(plusw2(i),plusw2(i),step3Layer,1);
end

% Raith alignmment marks for EBL nanochannels (now done in wire optical
step)
for i=1:length(plusraithlw_u)

S(end+1)=plusraithalignment(plusraithlw_u(i,1),plusraithlw_u(i,2),step3L
ayer,1);
end

% For step 4
step4Layer=4;
for i=1:length(plusw)
    %S(end+1)=inverseplussquarealignment(plusw(i),step4Layer,1);
    S(end+1)=bigbox(plusw(i),plusw(i),step4Layer,1);
end

for i=1:length(plusw2)
    S(end+1)=plussquarealignment(plusw2(i),step4Layer,1);
end
```

```matlab
% Raith alignmment marks for EBL nanochannels (now done in reservoir
optical step)
for i=1:length(plusraithlw_u)

S(end+1)=plusraithalignment(plusraithlw_u(i,1),plusraithlw_u(i,2),step4L
ayer,1);
end


% width of microchannel (microns)
w_microchannel_u = 700;
h_microchannel_u = 1000;
corridorx_u = 19500;
corridortopy_u = 3000;
corridorbottomy_u = -6000;

% diameter of reservoir (microns)
reservoirStep4d_u = 3000;
reservoirStep5d_u = 2000;
reservoirStep6d_u = 8600;

% left == 1
S(end+1)=microchannel(w_microchannel_u,h_microchannel_u,corridorx_u,corr
idortopy_u,corridorbottomy_u,1,step4Layer,1);
% right == 2
S(end+1)=microchannel(w_microchannel_u,h_microchannel_u,corridorx_u,corr
idortopy_u,corridorbottomy_u,2,step4Layer,1);

% left == 1
S(end+1)=reservoir(reservoirStep4d_u,w_microchannel_u,h_microchannel_u,c
orridorx_u,corridortopy_u,corridorbottomy_u,1,step4Layer,1);
% right == 2
S(end+1)=reservoir(reservoirStep4d_u,w_microchannel_u,h_microchannel_u,c
orridorx_u,corridortopy_u,corridorbottomy_u,2,step4Layer,1);


% For step 5 (Coverslip)
step5Layer=5;
% left == 1
S(end+1)=reservoir(reservoirStep5d_u,w_microchannel_u,h_microchannel_u,c
orridorx_u,corridortopy_u,corridorbottomy_u,1,step5Layer,1);
% right == 2
S(end+1)=reservoir(reservoirStep5d_u,w_microchannel_u,h_microchannel_u,c
orridorx_u,corridortopy_u,corridorbottomy_u,2,step5Layer,1);

% Coverslip outline
S(end+1)=bigbox(60000,22000,step5Layer,1);

% For step 6 (Nanoports)
step6Layer=6;
% left == 1
S(end+1)=reservoir(reservoirStep6d_u,w_microchannel_u,h_microchannel_u,c
orridorx_u,corridortopy_u,corridorbottomy_u,1,step6Layer,1);
% right == 2
S(end+1)=reservoir(reservoirStep6d_u,w_microchannel_u,h_microchannel_u,c
orridorx_u,corridortopy_u,corridorbottomy_u,2,step6Layer,1);
```

```
% width of nanochannel
nanochannelwidths = [800, 600, 400];
% how many nanometers above bottom of channel that electrode goes
indents_n =         [200, 200, 200];

w_nanoe_n=300;
w_nanoeBottom_n=1000;
% number of electrodes put on device
numElectrodes=7;
% how many microns on either side of channel before electrodes appear
sidegap_u=5;
S(end+1)=bigbox(5000,1000,step0Layer,1);

% Side viewing port
S(end+1)=bigbox(4000,15000,step3Layer,1);
S(end+1)=bigbox(4000,15000,step4Layer,1);

% Bottom viewing port
S(end+1)=bigbox(15000,4000,step3Layer,1);
S(end+1)=bigbox(15000,4000,step4Layer,1);

% height of funnel in microns
funnel_height_u=20;
funnel_length_u=200;

label=1;
for j=1:length(nanochannelwidths)

S(end+1)=l_funnel(nanochannelwidths(j),funnel_height_u,funnel_length_u,l
abel,1);
end

% Spacing between nanoelectrodes in microns
spacing_u = 2;
%S(end+1)=mininanoelectrodes(w_nanochannel_n,indent_n,numElectrodes,side
gap_u,1);
% spacing between the edge of the writefield and the edge of the
microelectrode wire
nbottomSideIndent_u=17;
nbottomSpacingWithSides_u= writefield_u - (nbottomSideIndent_u*2);
% Width of the microelectrode wire near the nanochannel
w_microelectrode_u=10;
nBottomSpace_u=nbottomSpacingWithSides_u - w_microelectrode_u;
bottomNSpacing_u=nBottomSpace_u/(numElectrodes-1);
left_bottom_u=-nBottomSpace_u/2;
for j=1:length(nanochannelwidths)

S(end+1)=nanoelectrodes2optical(nanochannelwidths(j),indents_n(j),w_nano
e_n,w_nanoeBottom_n,numElectrodes,sidegap_u,spacing_u,left_bottom_u,bott
omNSpacing_u,label,1);
end

% Optical wires component

left_top_u=left_bottom_u;
top_spacing_u=bottomNSpacing_u;
%bottom_space_with_pads_u=(dwidth_m-(2*edge_m))*1000;
%pad_w_u=bottom_space_with_pads_u/((numElectrodes*2)-1);
```

```
pad_w_u=3000;
fprintf(1,'\nPad width: %d',pad_w_u);
%bottom_space_u=bottom_space_with_pads_u - pad_w_u;
left_bottom_u=-((dwidth_m/2)-edge_m)*1000;
right_bottom_u=-left_bottom_u;
%bottomSpacing_u=bottom_space_u/(numElectrodes-1);
bottomSpacing_u=5000;
fprintf(1,'\nBottom spacing: %d',bottomSpacing_u);
bottomWidth_u=100;
bottomv_u=(-dcentrey_m-nanochannelShiftV_m)*1000;

basem1_u=-1570;
basem2_u=-9070;
m1left_u=-650;
m1spacing_u=200;
pad_h_u = 3000;

fprintf(1,'\nPad height: %d',pad_h_u);
S(end+1)=microelectrodes(w_microelectrode_u,numElectrodes,left_top_u,top
_spacing_u,left_bottom_u,right_bottom_u,bottomSpacing_u,bottomWidth_u,bo
ttomv_u,basem1_u,basem2_u,m1left_u,m1spacing_u,pad_w_u,pad_h_u,step3Laye
r,1);

% Alignment
SiLayer=0;
AlignLayer=1;
windowDF=1;
dotdose=1;

% Nano Small alignment marks
a_crossN=7.5;
w_thickN=1;
w_thinN=0.1;
L_thickN=2;
a_manualN=a_crossN*1.2;
L_autoN=a_crossN-2*L_thickN;
w_autoN=L_thickN/6;
S(end+1)=Raith_alignment_mark(['AlignmentMark-' num2str(SiLayer)],[0
0],SiLayer,windowDF,a_crossN,w_thickN,w_thinN,L_thickN,a_manualN,L_autoN
,w_autoN,dotdose);
S(end+1)=Raith_alignment_mark(['AlignmentMark-' num2str(AlignLayer)],[0
0],AlignLayer,windowDF,a_crossN,w_thickN,w_thinN,L_thickN,a_manualN,L_au
toN,w_autoN,dotdose);

% Nano Big alignment marks (for 3-pt alignment)
a_crossBN=75;
w_thickBN=10;
w_thinBN=10;
L_thickBN=20;
a_manualBN=a_crossBN*1.2;
L_autoBN=a_crossBN-2*L_thickBN;
w_autoBN=L_thickBN/6;
S(end+1)=Raith_alignment_mark(['BigAlignmentMark-' num2str(SiLayer)],[0
0],SiLayer,windowDF,a_crossBN,w_thickBN,w_thinBN,L_thickBN,a_manualBN,L_
autoBN,w_autoBN,dotdose);
S(end).elements(end+1)=Raith_element('aref',['AlignmentMark-'
num2str(SiLayer)],[-45 -45],[2 2],[90 90]);
```

243

```
S(end+1)=Raith_alignment_mark(['BigAlignmentMark-'
num2str(AlignLayer)],[0
0],AlignLayer,windowDF,a_crossBN,w_thickBN,w_thinBN,L_thickBN,a_manualBN
,L_autoBN,w_autoBN,dotdose);
S(end).elements(end+1)=Raith_element('aref',['AlignmentMark-'
num2str(AlignLayer)],[-45 -45],[2 2],[90 90]);


%
% End of Basic structures
%


%
% Step 0 Master structure creation
%

name0a=['gridlines-' num2str(gridw_m) '-' num2str(gridh_m) '-'
num2str(step0Layer)];
%EO=Raith_element('sref',name0a,[0 0]);

for i=1:length(plusw)
    name0b=['bigbox-' num2str(plusw(i)) '-' num2str(plusw(i)) '-'
num2str(step0Layer)];
    %EO(end+1)=Raith_element('sref',name0b,[-plusx_u plusy(i)]);
    %EO(end+1)=Raith_element('sref',name0b,[plusx_u plusy(i)]);
end

for i=1:length(plusw2)
    name0b=['bigbox-' num2str(plusw2(i)) '-' num2str(plusw2(i)) '-'
num2str(step0Layer)];
    %EO(end+1)=Raith_element('sref',name0b,[-plusx2_u plusy2(i)]);
    %EO(end+1)=Raith_element('sref',name0b,[plusx2_u plusy2(i)]);
end

name0j=['bigbox-5000-1000-' num2str(step0Layer)];
EO=Raith_element('sref',name0j,[0 -40000]);


% Step 1: EBL: Combine funnel and alignment marks into one structure
step1Layer=0;

name11a=[num2str(nanochannelwidths(1)) '-nm-funnel-'
num2str(funnel_height_u) '-um-height-1'];
E1=Raith_element('sref',name11a,[0 0]);
E1(end+1)=Raith_element('sref',['AlignmentMark-' num2str(SiLayer)],[-50
25]);
E1(end+1)=Raith_element('sref',['AlignmentMark-' num2str(SiLayer)],[50
25]);
E1(end+1)=Raith_element('sref',['AlignmentMark-' num2str(SiLayer)],[-50
-25]);
E1(end+1)=Raith_element('sref',['AlignmentMark-' num2str(SiLayer)],[50 -
25]);

name11=[name11a '-and-marks'];
S(end+1)=Raith_structure(name11,E1);

name12a=[num2str(nanochannelwidths(2)) '-nm-funnel-'
num2str(funnel_height_u) '-um-height-1'];
```

```
E1=Raith_element('sref',name12a,[0 0]);
E1(end+1)=Raith_element('sref',['AlignmentMark-' num2str(SiLayer)],[-50
25]);
E1(end+1)=Raith_element('sref',['AlignmentMark-' num2str(SiLayer)],[50
25]);
E1(end+1)=Raith_element('sref',['AlignmentMark-' num2str(SiLayer)],[-50
-25]);
E1(end+1)=Raith_element('sref',['AlignmentMark-' num2str(SiLayer)],[50 -
25]);

name12=[name12a '-and-marks'];
S(end+1)=Raith_structure(name12,E1);

name13a=[num2str(nanochannelwidths(3)) '-nm-funnel-'
num2str(funnel_height_u) '-um-height-1'];
E1=Raith_element('sref',name13a,[0 0]);
E1(end+1)=Raith_element('sref',['AlignmentMark-' num2str(SiLayer)],[-50
25]);
E1(end+1)=Raith_element('sref',['AlignmentMark-' num2str(SiLayer)],[50
25]);
E1(end+1)=Raith_element('sref',['AlignmentMark-' num2str(SiLayer)],[-50
-25]);
E1(end+1)=Raith_element('sref',['AlignmentMark-' num2str(SiLayer)],[50 -
25]);

name13=[name13a '-and-marks'];
S(end+1)=Raith_structure(name13,E1);

S(end+1)=bigbox(50,50,step1Layer,1);

% Step 2: EBL: Combine nanoelectrodes and alignment marks into one
structure
step2Layer=0;
name21a=[num2str(nanochannelwidths(1)) '-nm-elctrd2o-'
num2str(indents_n(1)) '-nm-indent-1' ];
E2=Raith_element('sref',name21a,[0 0]);
E2(end+1)=Raith_element('sref',['AlignmentMark-' num2str(AlignLayer)],[-
50 25]);
E2(end+1)=Raith_element('sref',['AlignmentMark-'
num2str(AlignLayer)],[50 25]);
E2(end+1)=Raith_element('sref',['AlignmentMark-' num2str(AlignLayer)],[-
50 -25]);
E2(end+1)=Raith_element('sref',['AlignmentMark-'
num2str(AlignLayer)],[50 -25]);

name21=[name21a '-and-marks'];
S(end+1)=Raith_structure(name21,E2);

name22a=[num2str(nanochannelwidths(2)) '-nm-elctrd2o-'
num2str(indents_n(2)) '-nm-indent-1' ];
E2=Raith_element('sref',name22a,[0 0]);
E2(end+1)=Raith_element('sref',['AlignmentMark-' num2str(AlignLayer)],[-
50 25]);
E2(end+1)=Raith_element('sref',['AlignmentMark-'
num2str(AlignLayer)],[50 25]);
E2(end+1)=Raith_element('sref',['AlignmentMark-' num2str(AlignLayer)],[-
50 -25]);
```

```
E2(end+1)=Raith_element('sref',['AlignmentMark-'
num2str(AlignLayer)],[50 -25]);

name22=[name22a '-and-marks'];
S(end+1)=Raith_structure(name22,E2);

name23a=[num2str(nanochannelwidths(3)) '-nm-elctrd2o-'
num2str(indents_n(3)) '-nm-indent-1' ];
E2=Raith_element('sref',name23a,[0 0]);
E2(end+1)=Raith_element('sref',['AlignmentMark-' num2str(AlignLayer)],[-
50 25]);
E2(end+1)=Raith_element('sref',['AlignmentMark-'
num2str(AlignLayer)],[50 25]);
E2(end+1)=Raith_element('sref',['AlignmentMark-' num2str(AlignLayer)],[-
50 -25]);
E2(end+1)=Raith_element('sref',['AlignmentMark-'
num2str(AlignLayer)],[50 -25]);

name23=[name23a '-and-marks'];
S(end+1)=Raith_structure(name23,E2);

if step2Layer ~= step1Layer
    S(end+1)=bigbox(50,50,step2Layer,1);
end

% Step 3: Optical Litho: Electrodes and contact pads
name3a=['bigbox-4000-15000-' num2str(step3Layer)];
EO(end+1)=Raith_element('sref',name3a,[48000 0]);
EO(end+1)=Raith_element('sref',name3a,[-48000 0]);
name3a=['bigbox-15000-4000-' num2str(step3Layer)];
EO(end+1)=Raith_element('sref',name3a,[0 -48000]);
EO(end+1)=Raith_element('sref',name3a,[0 48000]);

% Align step 3 with step 4
for i=1:length(plusw)
    name3b=['plussquare-' num2str(plusw(i)) '-' num2str(step3Layer)];
    EO(end+1)=Raith_element('sref',name3b,[-plusx_u plusy(i)]);
    EO(end+1)=Raith_element('sref',name3b,[plusx_u plusy(i)]);
end

% Set alignment marks for step 4
for i=1:length(plusw2)
    name3b=['bigbox-' num2str(plusw2(i)) '-' num2str(plusw2(i)) '-'
num2str(step3Layer)];
    EO(end+1)=Raith_element('sref',name3b,[-plusx2_u plusy2(i)]);
    EO(end+1)=Raith_element('sref',name3b,[plusx2_u plusy2(i)]);
end

name3j=[num2str(w_microelectrode_u) '-um-melctrd-' num2str(step3Layer)];
for i=1:length(centres)
    EO(end+1)=Raith_element('sref',name3j,[centres(i,1)*1000-50000
(centres(i,2)+nanochannelShiftV_m)*1000-50000]);
end

% Make EBL alignment marks for whole structure on Wire step
[m n o]=size(wplusraithuv);
for i=1:m
```

```matlab
    name3k=['plusraith-' num2str(plusraithlw_u(mod(i-1,5)+1 ,1)) '-'
num2str(plusraithlw_u(mod(i-1,5)+1,2)) '-' num2str(step3Layer)];
    for j=1:n
        EO(end+1)=Raith_element('sref',name3k,[wplusraithuv(i,j,1)
wplusraithuv(i,j,2)]);
    end
end


% Step 4: Optical Litho: Microchannels.

% Viewing ports
name4a=['bigbox-4000-15000-' num2str(step4Layer)];
EO(end+1)=Raith_element('sref',name4a,[48000 0]);
EO(end+1)=Raith_element('sref',name4a,[-48000 0]);
name4a=['bigbox-15000-4000-' num2str(step4Layer)];
EO(end+1)=Raith_element('sref',name4a,[0 -48000]);
EO(end+1)=Raith_element('sref',name4a,[0 48000]);

% Set alignment marks for step 3
for i=1:length(plusw)
    name4b=['bigbox-' num2str(plusw(i)) '-' num2str(plusw(i)) '-'
num2str(step4Layer)];
    EO(end+1)=Raith_element('sref',name4b,[-plusx_u plusy(i)]);
    EO(end+1)=Raith_element('sref',name4b,[plusx_u plusy(i)]);
end

% Align step 4 with step 3
for i=1:length(plusw2)
    name4b=['plussquare-' num2str(plusw2(i)) '-' num2str(step4Layer)];
    EO(end+1)=Raith_element('sref',name4b,[-plusx2_u plusy2(i)]);
    EO(end+1)=Raith_element('sref',name4b,[plusx2_u plusy2(i)]);
end

% New change: Make EBL alignment marks for whole structure on Optical
reservoir step
[m n o]=size(rplusraithuv);
for i=1:m
    name4k=['plusraith-' num2str(plusraithlw_u(mod(i-1,5)+1 ,1)) '-'
num2str(plusraithlw_u(mod(i-1,5)+1,2)) '-' num2str(step4Layer)];
    for j=1:n
        EO(end+1)=Raith_element('sref',name4k,[rplusraithuv(i,j,1)
rplusraithuv(i,j,2)]);
    end
end
% Optical component
% Overlap: 5 microns
overlap_m = 0.005;
%left_res_x = (12-.025)-((w_microchannel_u/1000)/2)+overlap_m;
left_res=centres;
left_res(:,1) = left_res(:,1)-(funnel_length_u/1000/2)-
((w_microchannel_u/1000)/2)+overlap_m;
%right_res_x = (12+.025)+((w_microchannel_u/1000)/2)-overlap_m;
right_res=centres;
right_res(:,1) =
right_res(:,1)+(funnel_length_u/1000/2)+((w_microchannel_u/1000)/2)-
overlap_m;
```

```matlab
name4j=['lmicrochannel-' num2str(w_microchannel_u) '-'
num2str(h_microchannel_u) '-' num2str(step4Layer)];
for i=1:length(centres)
    EO(end+1)=Raith_element('sref',name4j,[left_res(i,1)*1000-50000
(left_res(i,2)+nanochannelShiftV_m)*1000-50000]);
end

name4k=['rmicrochannel-' num2str(w_microchannel_u) '-'
num2str(h_microchannel_u) '-' num2str(step4Layer)];
for i=1:length(centres)
    EO(end+1)=Raith_element('sref',name4k,[right_res(i,1)*1000-50000
(right_res(i,2)+nanochannelShiftV_m)*1000-50000]);
end

name4l=['lreservoir-' num2str(reservoirStep4d_u) '-'
num2str(step4Layer)];
for i=1:length(centres)
    EO(end+1)=Raith_element('sref',name4l,[left_res(i,1)*1000-50000
(left_res(i,2)+nanochannelShiftV_m)*1000-50000]);
end

name4m=['rreservoir-' num2str(reservoirStep4d_u) '-'
num2str(step4Layer)];
for i=1:length(centres)
    EO(end+1)=Raith_element('sref',name4m,[right_res(i,1)*1000-50000
(right_res(i,2)+nanochannelShiftV_m)*1000-50000]);
end

% Step 5: Coverslip: Reservoirs.

% Optical component
% Overlap: 5 microns
overlap_m = 0.005;
%left_res_x = (12-.025)-((w_microchannel_u/1000)/2)+overlap_m;
left_res=centres;
left_res(:,1) = left_res(:,1)-(funnel_length_u/1000/2)-
((w_microchannel_u/1000)/2)+overlap_m;
%right_res_x = (12+.025)+((w_microchannel_u/1000)/2)-overlap_m;
right_res=centres;
right_res(:,1) =
right_res(:,1)+(funnel_length_u/1000/2)+((w_microchannel_u/1000)/2)-
overlap_m;

name5j=['lreservoir-' num2str(reservoirStep5d_u) '-'
num2str(step5Layer)];
for i=1:length(centres)
    EO(end+1)=Raith_element('sref',name5j,[left_res(i,1)*1000-50000
(left_res(i,2)+nanochannelShiftV_m)*1000-50000]);
end

name5k=['rreservoir-' num2str(reservoirStep5d_u) '-'
num2str(step5Layer)];
for i=1:length(centres)
    EO(end+1)=Raith_element('sref',name5k,[right_res(i,1)*1000-50000
(right_res(i,2)+nanochannelShiftV_m)*1000-50000]);
end

coverslipshift_u = (corridortopy_u+corridorbottomy_u)/2;
```

```
name5l=['bigbox-60000-22000-' num2str(step5Layer)];
for i=1:length(centres)
    EO(end+1)=Raith_element('sref',name5l,[centres(i,1)*1000-50000
(centres(i,2)+nanochannelShiftV_m)*1000-50000+coverslipshift_u]);
end

% Step 6: Nanoport: Reservoirs.

% Optical component
% Overlap: 5 microns
overlap_m = 0.005;
%left_res_x = (12-.025)-((w_microchannel_u/1000)/2)+overlap_m;
left_res=centres;
left_res(:,1) = left_res(:,1)-(funnel_length_u/1000/2)-
((w_microchannel_u/1000)/2)+overlap_m;
%right_res_x = (12+.025)+((w_microchannel_u/1000)/2)-overlap_m;
right_res=centres;
right_res(:,1) =
right_res(:,1)+(funnel_length_u/1000/2)+((w_microchannel_u/1000)/2)-
overlap_m;

name6j=['lreservoir-' num2str(reservoirStep6d_u) '-'
num2str(step6Layer)];
for i=1:length(centres)
    EO(end+1)=Raith_element('sref',name6j,[left_res(i,1)*1000-50000
(left_res(i,2)+nanochannelShiftV_m)*1000-50000]);
end

name6k=['rreservoir-' num2str(reservoirStep6d_u) '-'
num2str(step6Layer)];
for i=1:length(centres)
    EO(end+1)=Raith_element('sref',name6k,[right_res(i,1)*1000-50000
(right_res(i,2)+nanochannelShiftV_m)*1000-50000]);
end

% Step 0 on Layer 1
% Step 3 on Layer 3
% Step 4 on Layer 4
% Step 5 on Layer 5
nameO='OpticalStruct';
S(end+1)=Raith_structure(nameO,EO);

%axis equal;
L=Raith_library('dd5',S);
L.writegds('plain');

%
% Step 0: Alignment lines
%

%
% Step 1: Nanochannel
%

% obj=Raith_positionlist(library,csf_path,WF,chipUV)
Pa=Raith_positionlist(L,'C:\RAITH150-
TWO\User\defriesen\GDSII\dd5.csf',[writefield_u writefield_u], ...
    [waferw_m waferw_m]);
```

```
% Append a structure to the positionlist using
% P.append(structname,uv_c,DF,WA,[layers]). WA defines the
% working area, WA=[u_min v_min u_max v_max], in um. Argument
% layers is optional, and defaults to exposing all layers
% present in structure.

% big boxes for profileometer

profileometerShift_m=3;
name=['bigbox-50-50-' num2str(step1Layer)];
Pa.append(name,[centres(1,1)
centres(1,2)+nanochannelShiftV_m+profileometerShift_m],1,[-hwritefield_u
-hwritefield_u hwritefield_u hwritefield_u],0);

name=['bigbox-50-50-' num2str(step1Layer)];
Pa.append(name,[centres(1,1)+1
centres(1,2)+nanochannelShiftV_m+profileometerShift_m],1,[-hwritefield_u
-hwritefield_u hwritefield_u hwritefield_u]);

% Main structure for step1
Pa.append(name11,[centres(1,1) centres(1,2)+nanochannelShiftV_m],1,[-
hwritefield_u -hwritefield_u hwritefield_u hwritefield_u],0);
Pa.append(name12,[centres(2,1) centres(2,2)+nanochannelShiftV_m],1,[-
hwritefield_u -hwritefield_u hwritefield_u hwritefield_u],0);
Pa.append(name13,[centres(3,1) centres(3,2)+nanochannelShiftV_m],1,[-
hwritefield_u -hwritefield_u hwritefield_u hwritefield_u],0);


Pa.writepls('./dd5a.pls'); % Write pls to current directory


%
% Step 2: nanoelectrodes
%

if showall == 1
    Pb=Pa;
else
    Pb=Raith_positionlist(L,'C:\RAITH150-
TWO\User\defriesen\GDSII\dd5.csf',[writefield_u writefield_u], ...
    [waferw_m waferw_m]);
end

metalProfileometerShift_m=profileometerShift_m-1;
% big box for measuring metal thickness
name=['bigbox-50-50-' num2str(step2Layer)];
for i=1:length(centres)
    Pb.append(name,[centres(i,1)
centres(i,2)+nanochannelShiftV_m+metalProfileometerShift_m],1,[-
hwritefield_u -hwritefield_u hwritefield_u hwritefield_u],0);
end

Pb.append(name21,[centres(1,1) centres(1,2)+nanochannelShiftV_m],1,[-
hwritefield_u -hwritefield_u hwritefield_u hwritefield_u],0);
Pb.append(name22,[centres(2,1) centres(2,2)+nanochannelShiftV_m],1,[-
hwritefield_u -hwritefield_u hwritefield_u hwritefield_u],0);
```

```matlab
Pb.append(name23,[centres(3,1) centres(3,2)+nanochannelShiftV_m],1,[-
hwritefield_u -hwritefield_u hwritefield_u hwritefield_u],0);

Pb.writepls('./dd5b.pls'); % Write pls to current directory

%
% Step 3: Wires and contact pads
%

%
% Step 4: Microchannels
%


%
% Step 5: Reservoirs
%

%
% All Optical Layers
%

if showall == 1
    Pf=Pa;
else
    Pf=Raith_positionlist(L,'C:\RAITH150-
TWO\User\defriesen\GDSII\dd5.csf',[writefield_u writefield_u], ...
    [waferw_m waferw_m]);
end

Pf.append(nameO,[waferc_m waferc_m],1,[-hwritefield_u -hwritefield_u
hwritefield_u hwritefield_u]);

Pf.writepls('./dd5f.pls'); % Write pls to current directory

% Plot

if show==1
    Pa.plotedges; % Plot structures and chip boundaries
    Pa.plotWF; % Plot writefield as green, dotted line
elseif show==2
    Pb.plotedges; % Plot structures and chip boundaries
    Pb.plotWF; % Plot writefield as green, dotted line
elseif show==3
    %Pc.plot; % Plot structures and chip boundaries
    Pf.plotedges; % Plot structures and chip boundaries
    Pf.plotWF; % Plot writefield as green, dotted line
elseif show==4
    Pf.plotedges; % Plot structures and chip boundaries
    Pf.plotWF; % Plot writefield as green, dotted line
elseif show==5
    Pf.plotedges; % Plot structures and chip boundaries
    Pf.plotWF; % Plot writefield as green, dotted line
elseif show==0
    Pf.plotedges; % Plot structures and chip boundaries
    Pf.plotWF; % Plot writefield as green, dotted line
end
```

```
% Plot wafer outline
th=linspace(0,2*pi,100);
r=50000;
plot(r*cos(th)+r,r*sin(th)+r,'b-');
```

C.3 Dose test design code

The following code interfaces with the Raith GDSII Matlab Toolbox v1.1 to implement a dose test design for the Raith-two EBL machine at the Nanofab at the University of Alberta. The code is written in Matlab using Matlab R2012B.

```
% edosetestna
% Copyright Douglas Friesen, 2015
% Test 200um writefield on circular borofloat wafer
% dose test for channels, electrodes
% centres: [50 50]
% na changed from n9: Simulate real alignment marks: in first write,
write EBL alignment marks
% Fix alignment marks for precise writefield alignment for
nanoelectrodes
% n9 changed from n8 due to only big alignment mark being visible after
dual PMMA layer and aquasave being added subsequent to edosetestn8a
write and etch.
%
% EBL: Step 1 (layer 0), 2 (layer 0)
%

clf;
clear;
axis equal;
% showall: 0 for correct output files, 1 to show all parts of device
together
showall=1;
% show: part of the device to show (0-4). If using showall=1, use
show=0.
% Until we can show particular layers, Optical layers will be cumulative
from 0 to 5
show=1;

% Device width (millimeters)
dwidth_m=74;
dheight_m=20;
dcentrex_m=dwidth_m/2;
dcentrey_m=dheight_m/2;

nanochannelShiftV_m=0;

% writefield
writefield_u=200;
hwritefield_u=writefield_u/2;

waferw_m=100;
waferc_m=waferw_m/2;
```

```
centres = [50 50]; % mm

% width of nanochannel
w_nanochannel_n=200;

% how many nanometers above bottom of channel that electrode goes
indent_n=w_nanochannel_n;
w_nanoe_n=100;
w_nanoeBottom_n=300;
% number of electrodes put on device
numElectrodes=7;
% how many microns on either side of channel before electrodes appear
sidegap_u=5;

% height of funnel in microns
funnel_height_u=20;
funnel_length_u=200;

label=1;
S(1)=l_nanochannel2(w_nanochannel_n,label,0.25);
%S(1)=l_funnel(w_nanochannel_n,funnel_height_u,funnel_length_u,label,0.2
5);

nanochannelwidths = [50,100,200,400];
indents_n =        [50,100,200,200];
df= [1,1.17,1.33]; % of 150
df2= [1,1.17,1.33]; % of 150
for j=1:length(nanochannelwidths)
    for k=1:length(df)
        S(end+1)=l_nanochannel2(nanochannelwidths(j),label,df(k));

%S(end+1)=l_funnel(nanochannelwidths(j),funnel_height_u,funnel_length_u,
label,df(k));
    end
end

% Spacing between nanoelectrodes in microns
spacing_u = 4;
%S(end+1)=mininanoelectrodes(w_nanochannel_n,indent_n,numElectrodes,side
gap_u,1);
% spacing between the edge of the writefield and the edge of the
microelectrode wire
nbottomSideIndent_u=17;
nbottomSpacingWithSides_u= writefield_u - (nbottomSideIndent_u*2);
% Width of the microelectrode wire near the nanochannel
w_microelectrode_u=10;
nBottomSpace_u=nbottomSpacingWithSides_u - w_microelectrode_u;
bottomNSpacing_u=nBottomSpace_u/(numElectrodes-1);
left_bottom_u=-nBottomSpace_u/2;
for j=1:length(nanochannelwidths)
    for k=1:length(df2)

S(end+1)=nanoelectrodes2optical(nanochannelwidths(j),indents_n(j),w_nano
e_n,w_nanoeBottom_n,numElectrodes,sidegap_u,spacing_u,left_bottom_u,bott
omNSpacing_u,label,df2(k));
    end
end
```

```
% Alignment
SiLayer=0;
AlignLayer=1;
windowDF=1;
dotdose=1;

% Nano Small alignment marks
a_crossN=7.5; % um
w_thickN=1; % um
w_thinN=0.1; % um
L_thickN=2; % um
a_manualN=a_crossN*1.2;
L_autoN=a_crossN-2*L_thickN;
w_autoN=L_thickN/6;
S(end+1)=Raith_alignment_mark(['AlignmentMark-' num2str(SiLayer)],[0
0],SiLayer,windowDF,a_crossN,w_thickN,w_thinN,L_thickN,a_manualN,L_autoN
,w_autoN,dotdose);
S(end+1)=Raith_alignment_mark(['AlignmentMark-' num2str(AlignLayer)],[0
0],AlignLayer,windowDF,a_crossN,w_thickN,w_thinN,L_thickN,a_manualN,L_au
toN,w_autoN,dotdose);

% Big alignment marks (for 3-pt alignment)
a_crossB=75;
w_thickB=10;
w_thinB=10;
L_thickB=20;
a_manualB=a_crossB*1.2;
L_autoB=a_crossB-2*L_thickB;
w_autoB=L_thickB/6;
S(end+1)=Raith_alignment_mark(['BigAlignmentMark-' num2str(SiLayer)],[0
0],SiLayer,windowDF,a_crossB,w_thickB,w_thinB,L_thickB,a_manualB,L_autoB
,w_autoB,dotdose);
S(end).elements(end+1)=Raith_element('aref',['AlignmentMark-'
num2str(SiLayer)],[-45 -45],[2 2],[90 90]);
S(end+1)=Raith_alignment_mark(['BigAlignmentMark-'
num2str(AlignLayer)],[0
0],SiLayer,windowDF,a_crossB,w_thickB,w_thinB,L_thickB,a_manualB,L_autoB
,w_autoB,dotdose);
S(end).elements(end+1)=Raith_element('aref',['AlignmentMark-'
num2str(AlignLayer)],[-45 -45],[2 2],[90 90]);


% Full length of plus mark and width of plus mark lines for raith
alignment
plusraithlw_u=[12, 2;
              16, 4;
              20, 6;
              40, 10;
              60, 16]

% Location of raith alignment marks
%plusraithuv = zeros(5,4,2);
%plusraithuv(1,:,:) = [-38000, -26000; 38000, -26000; 38000 26000; -
38000 26000];
%plusraithuv(2,:,:) = [-38000, -26100; 38000, -26100; 38000 26100; -
38000 26100];
```

```
%plusraithuv(3,:,:) = [-38000, -26200; 38000, -26200; 38000 26200; -
38000 26200];
%plusraithuv(4,:,:) = [-38000, -26300; 38000, -26300; 38000 26300; -
38000 26300];
%plusraithuv(5,:,:) = [-38000, -26400; 38000, -26400; 38000 26400; -
38000 26400];
%

plusraithuv = zeros(5,4,2);
plusraithuv(1,:,:) = [-38000, -26000; 38000, -26000; 38000 26000; -38000
26000];
plusraithuv(2,:,:) = [-38000, -26100; 38000, -26100; 38000 26100; -38000
26100];
plusraithuv(3,:,:) = [-38000, -26200; 38000, -26200; 38000 26200; -38000
26200];
plusraithuv(4,:,:) = [-38000, -26300; 38000, -26300; 38000 26300; -38000
26300];
plusraithuv(5,:,:) = [-38000, -26400; 38000, -26400; 38000 26400; -38000
26400];

alignmentraithuv = zeros(4,2);
alignmentraithuv(:,:) = [ -10000, -10000; 10000, -10000; 10000 10000; -
10000 10000];

% Raith alignmment marks
for i=1:length(plusraithlw_u)

S(end+1)=plusraithalignment(plusraithlw_u(i,1),plusraithlw_u(i,2),0,1);
end


%
% End of Basic structures
%


% Step 1: EBL: Combine nanochannel and alignment marks into one
structure
step1Layer=0;
names1index=1;
for j=1:length(nanochannelwidths)
    for k=1:length(df)
        name1a=[num2str(nanochannelwidths(j)) '-nm-nanochannel-'
num2str(df(k))];
        %name1a=[num2str(nanochannelwidths(j)) '-nm-funnel-'
num2str(funnel_height_u) '-um-height-' num2str(df(k))];
        E1=Raith_element('sref',name1a,[0 0]);
        E1(end+1)=Raith_element('sref',['AlignmentMark-'
num2str(SiLayer)],[-50 25]);
        E1(end+1)=Raith_element('sref',['AlignmentMark-'
num2str(SiLayer)],[50 25]);
        E1(end+1)=Raith_element('sref',['AlignmentMark-'
num2str(SiLayer)],[-50 -25]);
        E1(end+1)=Raith_element('sref',['AlignmentMark-'
num2str(SiLayer)],[50 -25]);
        name1=[name1a '-and-marks'];
        names1{names1index}=name1;
        S(end+1)=Raith_structure(name1,E1);
        names1index=names1index+1;
```

```
    end
end

S(end+1)=bigbox(50,50,step1Layer,1.33);
S(end+1)=bigbox(60,60,step1Layer,2.0);

% Step 2: EBL: Combine nanoelectrodes and alignment marks into one
structure
step2Layer=0;
names2index=1;
for j=1:length(nanochannelwidths)
    for l=1:length(df2)
        name2a=[num2str(nanochannelwidths(j)) '-nm-elctrd2o-'
num2str(indents_n(j)) '-nm-indent-' num2str(df2(l)) ];
        E2=Raith_element('sref',name2a,[0 0]);
        E2(end+1)=Raith_element('sref',['AlignmentMark-'
num2str(AlignLayer)],[-50 25]);
        E2(end+1)=Raith_element('sref',['AlignmentMark-'
num2str(AlignLayer)],[50 25]);
        E2(end+1)=Raith_element('sref',['AlignmentMark-'
num2str(AlignLayer)],[-50 -25]);
        E2(end+1)=Raith_element('sref',['AlignmentMark-'
num2str(AlignLayer)],[50 -25]);
        name2=[name2a '-and-marks'];
        names2{names2index,l}=name2;
        S(end+1)=Raith_structure(name2,E2);
    end
    names2index=names2index+1;
end

if step2Layer ~= step1Layer
    S(end+1)=bigbox(50,50,step2Layer,1.33);
end

%axis equal;
L=Raith_library('edosetestna',S);
L.writegds('plain');

%
% Step 0: Alignment lines
%


%
% Step 1: Nanochannel
%

% obj=Raith_positionlist(library,csf_path,WF,chipUV)
Pa=Raith_positionlist(L,'C:\RAITH150-
TWO\User\defriesen\GDSII\edosetestna.csf',[writefield_u writefield_u],
...
    [waferw_m waferw_m]);

% Append a structure to the positionlist using
% P.append(structname,uv_c,DF,WA,[layers]). WA defines the
% working area, WA=[u_min v_min u_max v_max], in um. Argument
% layers is optional, and defaults to exposing all layers
% present in structure.
```

```matlab
% big boxes for profileometer

profileometerShift_m=4;
name=['bigbox-50-50-' num2str(step1Layer)];
Pa.append(name,[centres(1)
centres(2)+nanochannelShiftV_m+profileometerShift_m],1,[-hwritefield_u -
hwritefield_u hwritefield_u hwritefield_u],0);

name=['bigbox-50-50-' num2str(step1Layer)];
Pa.append(name,[centres(1)+1
centres(2)+nanochannelShiftV_m+profileometerShift_m],1,[-hwritefield_u -
hwritefield_u hwritefield_u hwritefield_u]);

name=['bigbox-60-60-' num2str(step1Layer)];
%Pa.append(name,[centres(1)+2
centres(2)+nanochannelShiftV_m+profileometerShift_m],1,[-hwritefield_u -
hwritefield_u hwritefield_u hwritefield_u]);

% Write chrome alignment marks for raith since they won't be there yet
[m n o]=size(plusraithuv);
for i=1:length(plusraithlw_u)
    name1k=['plusraith-' num2str(plusraithlw_u(i,1)) '-'
num2str(plusraithlw_u(i,2)) '-' num2str(0)];
    for j=1:n
        Pa.append(name1k,[centres(1)+plusraithuv(i,j,1)/1000
centres(2)+plusraithuv(i,j,2)/1000],1,[-hwritefield_u -hwritefield_u
hwritefield_u hwritefield_u]);
    end
end

% Write alignment marks surrounding write field, closer than chrome
alignment marks
[m n]=size(alignmentraithuv);
for i=1:m
    Pa.append(['BigAlignmentMark-'
num2str(SiLayer)],[centres(1)+alignmentraithuv(i,1)/1000
centres(2)+alignmentraithuv(i,2)/1000],1,[-hwritefield_u -hwritefield_u
hwritefield_u hwritefield_u]);
end

Dv = 0.20; % 100 micron separation
% Main structure for step1
for l=1:names1index-1
    for m=1:length(df2)
        Pa.append(names1{l},[centres(1)+(m-1)*Dv centres(2)+(l-
1)*Dv],1,[-hwritefield_u -hwritefield_u hwritefield_u hwritefield_u],0);
    end
end

Pa.writepls('./edosetestnaa.pls'); % Write pls to current directory


%
% Step 2: nanoelectrodes
%

if showall == 1
    Pb=Pa;
```

```
else
    Pb=Raith_positionlist(L,'C:\RAITH150-
TWO\User\defriesen\GDSII\edosetestna.csf',[writefield_u writefield_u],
...
    [waferw_m waferw_m]);
end

metalProfileometerShift_m=profileometerShift_m+1;
% big box for measuring metal thickness
name=['bigbox-50-50-' num2str(step2Layer)];
Pb.append(name,[centres(1)
centres(2)+nanochannelShiftV_m+metalProfileometerShift_m],1,[-
hwritefield_u -hwritefield_u hwritefield_u hwritefield_u],0);

% Main structure for step2
for l=1:names2index-1
    for m=1:length(df)
        for n=1:length(df2)
            Pb.append(names2{l,n},[centres(1)+(n-1)*Dv centres(2)+((l-
1)*length(df)+(m-1))*Dv],1,[-hwritefield_u -hwritefield_u hwritefield_u
hwritefield_u],0);
        end
    end
end

Pb.writepls('./edosetestnab.pls'); % Write pls to current directory


% Plot

if show==1
    Pa.plotedges; % Plot structures and chip boundaries
    Pa.plotWF; % Plot writefield as green, dotted line
elseif show==2
    Pb.plotedges; % Plot structures and chip boundaries
    Pb.plotWF; % Plot writefield as green, dotted line
end


% Plot wafer outline
th=linspace(0,2*pi,100);
r=50000;
plot(r*cos(th)+r,r*sin(th)+r,'b-');
```

C.4 Supporting functions

The following code interfaces with the Raith GDSII Matlab Toolbox v1.1 to implement
the supporting methods for the previous code. The code is written in Matlab using Matlab
R2012B.

```
function S=bigbox(w_u,h_u,layer,DF)
% Create a box with width w_u um, highet h_u in um, DF
% layer

% box
```

```
u=[0 w_u w_u 0 0]-w_u/2;
v=[0 0 h_u h_u 0]-h_u/2;
E=Raith_element('polygon',layer,[u;v],DF);

name=['bigbox-' num2str(w_u) '-' num2str(h_u) '-' num2str(layer)];
S=Raith_structure(name,E);
end

function S=bigboxA(w_u,h_u,DF)
% Create a box with width w_u um, highet h_u in um, DF
% on layer 0

% box
u=[0 w_u w_u 0 0]-w_u/2;
v=[0 0 h_u h_u 0]-h_u/2;
E=Raith_element('polygon',0,[u;v],DF);

name=['bigbox-' num2str(w_u) '-' num2str(h_u)];
S=Raith_structure(name,E);
end

function
coords=centrexyonwafer(gridw_m,gridh_m,gridn,gridm,bottomleftx_m,bottoml
efty_m)
% Create gridlines
% gridw_m (grid width in mm)
% gridh_m (grid height in mm)
% gridn (number of rows)
% gridm (number of columns)
% bottomleftx_m (xcoord of bottom left of grid in mm)
% bottomlefty_m (ycoord of bottom left of grid in mm)
% DF
% on layer 0

boxw = gridw_m/gridm;
boxh = gridh_m/gridn;
centreleft=bottomleftx_m+boxw/2;
centrebottom=bottomlefty_m+boxh/2;
i = 1;

for n = 1:gridn
    for m=1:gridm
        coords(i,1:2)=[centreleft+(m-1)*boxw,centrebottom+(n-1)*boxh];
        i = i+1;
    end
end

end

function S=electrode(w_n,DF)
% Create a nanochannel with length 50 (in um), w_n (in nanometers), DF
% on layer 0
w1=w_n/1000;

u=[0 w1 w1 0 0];
v=[0 0 50 50 0];
E=Raith_element('polygon',0,[u;v],DF);
name=[num2str(w_n) '-nm-electrode'];
```

```matlab
S=Raith_structure(name,E);
end

function S=gridlines(gridn,gridm,gridw_m,gridh_m,linesize_u,layer,DF)
% Create gridlines
% gridn (number of rows)
% gridm (number of columns)
% gridw_m (width of entire grid in mm)
% gridh_m (height of entire grid in mm)
% linesize_u (width of lines made in microns)
% layer
% DF

boxw = gridw_m/gridm;
boxh = gridh_m/gridn;
farleft=-gridw_m/2;
fartop=gridh_m/2;
centreleft=farleft+boxw/2;
centretop=fartop-boxh/2;
centrex=centreleft;
centrey=centretop;
i = 1;

for n = 1:gridn
    for m=1:gridm
        E(i)=gridsquare(centrex+(m-1)*boxw,centrey-(n-
1)*boxh,boxw,boxh,linesize_u,layer,DF);
        i = i+1;
    end
end

name=['gridlines-' num2str(gridw_m) '-' num2str(gridh_m) '-'
num2str(layer)];
S=Raith_structure(name,E);
end

function
E=gridsquare(centrex_m,centrey_m,boxw_m,boxh_m,linesize_u,layer,DF)
% Create gridsquare
% centrex_m (centre x coordinate mm)
% centrey_m (centre y coordinate mm)
% boxw_m (width of box mm)
% boxh_m (height of box mm)
% linesize_u (width of lines made in microns)
% layer
% DF

hw_u=boxw_m/2*1000;
hh_u=boxh_m/2*1000;
centrex_u=centrex_m*1000;
centrey_u=centrey_m*1000;

u=[centrex_u-hw_u centrex_u+hw_u centrex_u+hw_u centrex_u-hw_u
centrex_u-hw_u];
v=[centrey_u-hh_u centrey_u-hh_u centrey_u+hh_u centrey_u+hh_u
centrey_u-hh_u];
E=Raith_element('path',layer,[u;v],linesize_u,DF);
end
```

```matlab
function S=inverseplusalignment(plusw_u,layer,DF)
% Create plus alignment mark
% plusw_u (Width of entire plus mark, um)
% label 1 if label, no label otherwise
% layer
% DF

hlw_u=plusw_u/6;
htw_u=plusw_u/2;

u=[-htw_u -hlw_u -hlw_u -htw_u -htw_u];
v=[htw_u htw_u hlw_u hlw_u htw_u];
E(1)=Raith_element('polygon',layer,[u;v],DF);
u=[hlw_u htw_u htw_u hlw_u hlw_u];
v=[htw_u htw_u hlw_u hlw_u htw_u];
E(2)=Raith_element('polygon',layer,[u;v],DF);
u=[-htw_u -hlw_u -hlw_u -htw_u -htw_u];
v=[-hlw_u -hlw_u -htw_u -htw_u -hlw_u];
E(3)=Raith_element('polygon',layer,[u;v],DF);
u=[hlw_u htw_u htw_u hlw_u hlw_u];
v=[-hlw_u -hlw_u -htw_u -htw_u -hlw_u];
E(4)=Raith_element('polygon',layer,[u;v],DF);

name=['inverseplus-' num2str(plusw_u) '-' num2str(layer)];
S=Raith_structure(name,E);
end


function S=inverseplussquarealignment(plusw_u,layer,DF)
% Create inverse plus square alignment mark
% plusw_u (Width of entire plus mark, um)
% layer
% DF

hlw_u=plusw_u/6;
htw_u=plusw_u/2;
hs_u=plusw_u;

% top left square
u=[-hs_u -hlw_u -hlw_u -hs_u -hs_u];
v=[hs_u hs_u hlw_u hlw_u hs_u];
E(1)=Raith_element('polygon',layer,[u;v],DF);
% bottom left square
u=[-hs_u -hlw_u -hlw_u -hs_u -hs_u];
v=[-hs_u -hs_u -hlw_u -hlw_u -hs_u];
E(end+1)=Raith_element('polygon',layer,[u;v],DF);
% top right square
u=[hs_u hlw_u hlw_u hs_u hs_u];
v=[hs_u hs_u hlw_u hlw_u hs_u];
E(end+1)=Raith_element('polygon',layer,[u;v],DF);
% bottom right square
u=[hs_u hlw_u hlw_u hs_u hs_u];
v=[-hs_u -hs_u -hlw_u -hlw_u -hs_u];
E(end+1)=Raith_element('polygon',layer,[u;v],DF);

name=['inverseplussquare-' num2str(plusw_u) '-' num2str(layer)];
S=Raith_structure(name,E);
end
```

```matlab
function S=l_channel(w_n,l_u,label,DF)
% Create a nanochannel with length 50 um,
% w_n (width of nanochannel in nanometers),
% l_u in um (length of channel),
% label 1 if label, no label otherwise
% DF
% on layer 0

w0=w_n/1000;

hw=w0/2;

hl=l_u/2;

% nanochannel v coords
w1=-hw;
w2=hw;

% nanochannel
u=[-hl hl hl -hl -hl];
v=[w1 w1 w2 w2 w1];
E=Raith_element('polygon',0,[u;v],DF);

if label == 1
    E(1)=Raith_element('text',0,[0 20],5,0,[1 2],[num2str(w_n) 'nm x '
num2str(l_u) 'um'],1);
end

name=[num2str(w_n) '-nm-channel-' num2str(l_u) '-um-length-'
num2str(DF)];
S=Raith_structure(name,E);
end

function S=l_funnel(w_n,funnel_height_u,funnel_length_u,label,DF)
% Create a nanochannel with length 50 um,
% w_n (width of nanochannel in nanometers),
% funnel_height_u in um (height of funnel),
% funnel_length_u in um (length of funnel),
% label 1 if label, no label otherwise
% DF
% on layer 0

w0=w_n/1000;


hw=w0/2;

hl=funnel_length_u/2;

% nanochannel v coords
w1=-hw;
w2=hw;

% funnel v coords
hz=funnel_height_u/2;
z1=-hz;
z2=+hz;
```

```
% nanochannel
u=[-25 25 25 -25 -25];
v=[w1 w1 w2 w2 w1];
E=Raith_element('polygon',0,[u;v],DF);

% left funnel
u2=[-hl -23 -23 -hl -hl];
v2=[z1 w1 w2 z2 z1];
E(2)=Raith_element('polygon',0,[u2;v2],DF);

% right funnel
u3=[23 23 hl hl 23];
v3=[w1 w2 z2 z1 w1];
E(3)=Raith_element('polygon',0,[u3;v3],DF);

if label == 1
    E(4)=Raith_element('text',0,[0 20],5,0,[1 2],[num2str(w_n) 'nm x
50um'],1);
end

name=[num2str(w_n) '-nm-funnel-' num2str(funnel_height_u) '-um-height-'
num2str(DF)];
S=Raith_structure(name,E);
end

function S=l_funnel2(w_n,z_u,DF)
% Create a nanochannel with length 50 um, w_n (in nanometers), z_u in um
(height of funnel), DF
% on layer 0
w0=w_n/1000;


hw=w0/2;

% nanochannel v coords
w1=50-hw;
w2=50+hw;

% funnel v coords
hz=z_u/2;
z1=50-hz;
z2=50+hz;

% nanochannel
u=[25 75 75 25 25];
v=[w1 w1 w2 w2 w1];
E=Raith_element('polygon',0,[u;v],DF);

% left funnel
u2=[0 25 25 0 0];
v2=[z1 w1 w2 z2 z1];
E(2)=Raith_element('polygon',0,[u2;v2],DF);

% right funnel
u3=[75 75 99 99 75];
v3=[w1 w2 z2 z1 w1];
E(3)=Raith_element('polygon',0,[u3;v3],DF);
```

```matlab
E(4)=Raith_element('text',0,[50 70],5,0,[1 2],[num2str(w_n) 'nm x
50um'],1.5);
name=[num2str(w_n) '-nm-funnel-' num2str(z_u) '-um-height'];
S=Raith_structure(name,E);
end

function S=l_funnelA(w_n,z_u,DF)
% Create a nanochannel with length 50 um, w_n (in nanometers), z_u in um
(height of funnel), DF
% on layer 0
w0=w_n/1000;


hw=w0/2;

% nanochannel v coords
w1=-hw;
w2=hw;

% funnel v coords
hz=z_u/2;
z1=-hz;
z2=+hz;

% nanochannel
u=[25 75 75 25 25]-50;
v=[w1 w1 w2 w2 w1];
E=Raith_element('polygon',0,[u;v],DF);

% left funnel
u2=[0 25 25 0 0]-50;
v2=[z1 w1 w2 z2 z1];
E(2)=Raith_element('polygon',0,[u2;v2],DF);

% right funnel
u3=[75 75 100 100 75]-50;
v3=[w1 w2 z2 z1 w1];
E(3)=Raith_element('polygon',0,[u3;v3],DF);

E(4)=Raith_element('text',0,[0 20],5,0,[1 2],[num2str(w_n) 'nm x
50um'],1.5);
name=[num2str(w_n) '-nm-funnel-' num2str(z_u) '-um-height'];
S=Raith_structure(name,E);
end

function S=l_funnelblock(w_n,funnel_height_u,funnel_length_u,label,DF)
% Create a nanochannel with length 50 um,
% w_n (width of nanochannel in nanometers),
% funnel_height_u in um (height of funnel),
% funnel_length_u in um (length of funnel),
% label 1 if label, no label otherwise
% DF
% on layer 0

w0=w_n/1000;
```

```matlab
    hw=w0/2;

    hl=funnel_length_u/2;

    % nanochannel v coords
    w1=-hw;
    w2=hw;

    % funnel v coords
    hz=funnel_height_u/2;
    z1=-hz;
    z2=+hz;

    % nanochannel
    u=[-25 0 0 5 5 25 25 15 15 10 10 -15 -15 -20 -20 -25 -25];
    v=[w1 w1 0 0 w1 w1 w2 w2 0 0 w2 w2 0 0 w2 w2 w1];
    E=Raith_element('polygon',0,[u;v],DF);

    % left funnel
    u2=[-hl -23 -23 -hl -hl];
    v2=[z1 w1 w2 z2 z1];
    E(2)=Raith_element('polygon',0,[u2;v2],DF);

    % right funnel
    u3=[23 23 hl hl 23];
    v3=[w1 w2 z2 z1 w1];
    E(3)=Raith_element('polygon',0,[u3;v3],DF);

    if label == 1
        E(4)=Raith_element('text',0,[0 20],5,0,[1 2],[num2str(w_n) 'nm x
    50um'],1);
    end

    name=[num2str(w_n) '-nm-funnelblock-' num2str(funnel_height_u) '-um-
    height-' num2str(DF)];
    S=Raith_structure(name,E);
    end

    function S=l_nanochannel(L_u,w_n,DF)
    % Create a nanochannel with L_u (in um), w_n (in nanometers), DF
    % on layer 0
    w1=w_n/1000;
    u1 = L_u;

    u=[0 u1 u1 0 0]-u1/2;
    v=[0 0 w1 w1 0]-w1/2;
    E(1)=Raith_element('polygon',0,[u;v],DF);
    E(2)=Raith_element('text',0,[0 5],2,0,[1 1],[num2str(w_n) 'nmx50um DF='
    num2str(DF)],1);
    name=[num2str(w_n) '-nm-nanochannel-' num2str(DF) '-DF'];
    S=Raith_structure(name,E);
    end

    function S=l_nanochannel2(w_n,label,DF)
    % Create a nanochannel with length 50 um,
    % w_n (width of nanochannel in nanometers),
    % funnel_height_u in um (height of funnel),
    % funnel_length_u in um (length of funnel),
```

```matlab
% label 1 if label, no label otherwise
% DF
% on layer 0

w0=w_n/1000;


hw=w0/2;

% nanochannel v coords
w1=-hw;
w2=hw;

% nanochannel
u=[-25 25 25 -25 -25];
v=[w1 w1 w2 w2 w1];
E(1)=Raith_element('polygon',0,[u;v],DF);

if label == 1
    E(2)=Raith_element('text',0,[0 20],5,0,[1 2],[num2str(w_n) 'nm DF='
num2str(DF)],1);
end

name=[num2str(w_n) '-nm-nanochannel-' num2str(DF)];
S=Raith_structure(name,E);
end

function S=l_nanochannelA(L_u,w_n,DF)
% Create a nanochannel with L_u (in um), w_n (in nanometers), DF
% on layer 0
w1=w_n/1000;
u1 = L_u;

u=[0 u1 u1 0 0]-u1/2;
v=[0 0 w1 w1 0]-w1/2;
E=Raith_element('polygon',0,[u;v],DF);
E(2)=Raith_element('text',0,[0 5],2,0,[1 2],[num2str(w_n) 'nmx50um DF='
num2str(DF)],1.5);
name=[num2str(w_n) '-nm-nanochannel-' num2str(DF) '-DF'];
S=Raith_structure(name,E);
end

function S=lmicrochannel(w_u,d_u,DF)
% Create a microchannel with width w_u um,
% and reservoirs of diameter d_u in um, DF
% on layer 0
h_u = 5000;
hh=h_u/2;
h_bottom=0;
h_top=h_u;
hw=w_u/2;
hd=d_u/2;

% Vertical box
u=[-hw hw hw -hw -hw];
v=[-hh -hh h_top-hh h_top-hh -hh];
E=Raith_element('polygon',0,[u;v],DF);
```

```
% bottom left, counter clockwise
u=[-hw hw (-hd)*1.5+hw (-hd)*1.5-hw -hw];
v=[hh hh hh+(hd)*1.5 hh+(hd)*1.5 hh];
E(2)=Raith_element('polygon',0,[u;v],DF);
topu=(-hd)*1.5;
topv=hh+(hd)*1.5;
E(3)=Raith_element('circle',0,[topu;topv],hd,[],60,DF);


u=[0 w_u -w_u -w_u-w_u 0]-w_u/2;
v=[0 0 -2*w_u -2*w_u 0]-h_u/2;
E(4)=Raith_element('polygon',0,[u;v],DF);
bottomu=-w_u*1.5-w_u/2;
bottomv=-2*w_u-h_u/2;
E(5)=Raith_element('circle',0,[bottomu;bottomv],hd,[],60,DF);


name=['lmicrochannel-' num2str(w_u) '-' num2str(d_u)];
S=Raith_structure(name,E);
end


function S=lreservoir(w_u,h_u,DF)
% Create a box with width w_u um, highet h_u in um, DF
% on layer 0
hh=h_u/2;
h_bottom=hh-20;
h_top=hh+20;


% box
u=[0 w_u w_u 0 0]-w_u/2;
v=[0 h_bottom h_top h_u 0]-h_u/2;
E=Raith_element('polygon',0,[u;v],DF);


name=['lreservoir-' num2str(w_u) '-' num2str(h_u)];
S=Raith_structure(name,E);
end


function
S=meprobe(w_u,numElectrodes,left_top_u,top_spacing_u,left_bottom_u,right
_bottom_u,bottomSpacing_u,bottomWidth_u,bottomv_u,basetop_u,basem1_u,bas
em2_u,basem3_u,basem4_u,m1_left_u,m1spacing_u,vspacing1_u,vspacing2_u,pa
d_w_u,pad_h_u,bort,layer,DF)
% Create microelectrodes that for a basis for 4 point probe electrical
measurements
% w_u (in microns), width of wires at overlap with nanoelectrodes
% numElectrodes (number of electrodes)
% left_top_u (left x coord) of left nanoelectrode,
% top_spacing_u (microns between nanoelectrodes)
% left_bottom_u (x coord of leftmost wire at bottom),
% right_bottom_u (x coord of rightmost wire at bottom),
% bottomSpacing_u (spacing between wires at bottom)
% bottomWidth_u (Width of wire at bottom (third line))
% basetop_u (y coord of where electrodes begin, um)
% basem1_u (y coord of first split, um)
% basem2_u (y coord of second split, um)
% basem3_u (y coord of third split, um)
% basem4_u (y coord of fourth split, um)
% m1_left_u (x coord of first split, um)
% m1spacing_u (spacing between wires at first split, um)
% vspacing1_u (horizontal spacing at first wire
```

```
% vspacing2_u (horizontal spacing at first wire
% pad_w_u (width of contact pad at bottom)
% pad_h_u (height of contact pad at bottom)
% layer
%

hw=w_u/2;

hnumElectrodes = numElectrodes/2;
uElectrodeLength = basetop_u-basem1_u;

% electrodes
leftmin=left_top_u;
left=leftmin;

horizontalspacing=200;
middle_width_u=bottomWidth_u;

basetop= basetop_u;
if bort == 1
    basetop=-basetop;
end

if bort == 0
    totalbottom=bottomv_u;
else
    totalbottom=-bottomv_u;
end


% Five lines
% First is top
% Second is connecting
% Third is middle
% Fourth is connecting
% Fifth is bottom
for i=1:numElectrodes
    u=[left-hw,left+hw,left+hw,left-hw,left-hw];
    if i<hnumElectrodes
        if bort == 0
            vbottom=basem1_u-horizontalspacing*(i-1);
        else
            vbottom=-(basem1_u-horizontalspacing*(i-1));
        end
    else
        if bort == 0
            vbottom=basem1_u-horizontalspacing*(numElectrodes-i);
        else
            vbottom=-(basem1_u-horizontalspacing*(numElectrodes-i));
        end
    end
    v=[vbottom,vbottom,basetop,basetop,vbottom]
    E(i)=Raith_element('polygon',layer,[u;v],DF);
    ucoord1(i)=left;
    if bort == 0
    vcoord1(i)=vbottom;
    else
        vcoord1(i)=-vbottom;
```

```
        end

    left=left+top_spacing_u;
end

% Second line

left=m1_left_u;
%moffset_u=0;
moffset_u=500;
moverlap_u=30;
mwidth_u=300;
mwidth_uh=mwidth_u/2;
find=200;

for i=1:numElectrodes
    if i<hnumElectrodes
        %bl,cw
        u=[left+mwidth_uh,left-
mwidth_uh,ucoord1(i),ucoord1(i),left+mwidth_uh];
        if bort == 0

v=[basem2_u,basem2_u,vcoord1(i)+moverlap_u,vcoord1(i),basem2_u];
        else
            v=-
[basem2_u,basem2_u,vcoord1(i)+moverlap_u,vcoord1(i),basem2_u];
        end
    else
        u=[left+mwidth_uh,left-
mwidth_uh,ucoord1(i),ucoord1(i),left+mwidth_uh];
        if bort == 0

v=[basem2_u,basem2_u,vcoord1(i),vcoord1(i)+moverlap_u,basem2_u];
        else
            v=-
[basem2_u,basem2_u,vcoord1(i),vcoord1(i)+moverlap_u,basem2_u];
        end
    end

    ucoord2(i)=left;
    %vcoord2(i)=vcoord1(i);
    E(end+1)=Raith_element('polygon',layer,[u;v],DF);
    left=left+m1spacing_u;
end

% Third line

hbw= mwidth_u/2;
safe_overlap_u=5;

for i=1:numElectrodes
    u=[ucoord2(i)-hbw,ucoord2(i)+hbw,ucoord2(i)+hbw,ucoord2(i)-
hbw,ucoord2(i)-hbw];
    if i<hnumElectrodes
        vbottom=basem3_u-vspacing2_u*(i-1);
    else
        vbottom=basem3_u-vspacing2_u*(numElectrodes-i);
    end
```

269

```matlab
    if bort == 0

v=[basem2_u+safe_overlap_u,basem2_u+safe_overlap_u,vbottom,vbottom,basem2_u+safe_overlap_u]
    else
        v=-[basem2_u+safe_overlap_u,basem2_u+safe_overlap_u,vbottom,vbottom,basem2_u+safe_overlap_u]
    end
    E(end+1)=Raith_element('polygon',layer,[u;v],DF);
    ucoord3(i)=ucoord2(i);
    %if bort == 0
        vcoord3(i)=vbottom;
    %else
        %vcoord3(i)=-vbottom;
    %end
end

% Fourth line

hbw= bottomWidth_u/2;
left=left_bottom_u;
middle=round(numElectrodes/2);
fprintf(1,'\nround:%d',middle);

for i=1:middle-1
    fprintf(1,'\ni:%d',i);
    u=[left,left,ucoord3(i),ucoord3(i),left];

v=[basem4_u,basem4_u+bottomWidth_u,vcoord3(i)+bottomWidth_u,vcoord3(i),basem4_u];
    if bort == 1
        v=-v;
    end
    ucoord4(i)=left;
    %if bort == 0
        vcoord4(i)=basem4_u;
    %else
        %vcoord4(i)=-vcoord3(i);
    %end
    E(end+1)=Raith_element('polygon',layer,[u;v],DF);
    left=left+bottomSpacing_u;
end

for i=middle:middle
    fprintf(1,'\ni:%d',i);
    u=[left+hbw,left-hbw,ucoord3(i)-hbw,ucoord3(i)+hbw,left+hbw];
    v=[basem4_u-hbw,basem4_u-hbw,vcoord3(i)+bottomWidth_u,vcoord3(i)+bottomWidth_u,basem4_u-hbw];
    if bort == 1
        v=-v;
    end
    ucoord4(i)=left;
    %if bort == 0
        vcoord4(i)=basem4_u;
    %else
        %vcoord4(i)=-vcoord3(i);
    %end
```

```
        E(end+1)=Raith_element('polygon',layer,[u;v],DF);
        left=left+bottomSpacing_u;
end

left=right_bottom_u-(numElectrodes-middle-1)*bottomSpacing_u;
for i=middle+1:numElectrodes
        fprintf(1,'\ni:%d',i);
        u=[left,left,ucoord3(i),ucoord3(i),left];

v=[basem4_u,basem4_u+bottomWidth_u,vcoord3(i)+bottomWidth_u,vcoord3(i),b
asem4_u];
        if bort == 1
                v=-v;
        end
        ucoord4(i)=left;
        %if bort == 0
                vcoord4(i)=basem4_u;
        %else
                %vcoord4(i)=-vcoord3(i);
        %end
        E(end+1)=Raith_element('polygon',layer,[u;v],DF);
        left=left+bottomSpacing_u;
end


% Fifth line


for i=1:numElectrodes
        u=[ucoord4(i)-hbw,ucoord4(i)+hbw,ucoord4(i)+hbw,ucoord4(i)-
hbw,ucoord4(i)-hbw];
        if bort == 0

v=[vcoord4(i)+middle_width_u,vcoord4(i)+middle_width_u,totalbottom,total
bottom,vcoord4(i)+middle_width_u]
        else
                v=-[vcoord4(i)+middle_width_u,vcoord4(i)+middle_width_u,-
totalbottom,-totalbottom,vcoord4(i)+middle_width_u]
        end
        E(end+1)=Raith_element('polygon',layer,[u;v],DF);
end

% Contact pads
hpadu = pad_w_u/2;


for i=1:numElectrodes
        u=[ucoord4(i)-hpadu,ucoord4(i)+hpadu,ucoord4(i)+hpadu,ucoord4(i)-
hpadu,ucoord4(i)-hpadu];
        if bort == 0

v=[totalbottom+pad_h_u,totalbottom+pad_h_u,totalbottom,totalbottom,total
bottom+pad_h_u]
        else
                v=[totalbottom-pad_h_u,totalbottom-
pad_h_u,totalbottom,totalbottom,totalbottom-pad_h_u]
        end
        E(end+1)=Raith_element('polygon',layer,[u;v],DF);
```

```
end

%{
%}

if bort == 0
    name=[num2str(w_u) '-um-melctrd-' num2str(numElectrodes) '-'
num2str(top_spacing_u) '-' num2str( uElectrodeLength ) '-'
num2str(layer)];
    fprintf('%s',name);
else
    name=[num2str(w_u) '-um-melctrd-t-' num2str(numElectrodes) '-'
num2str(top_spacing_u) '-' num2str( uElectrodeLength ) '-'
num2str(layer)];
end
S=Raith_structure(name,E);
end

function
S=microchannel(w_u,l_u,corridorx_u,corridortopy_u,corridorbottomy_u,left
,layer,DF)
% Create a microchannel with width w_u um,
% l_u (length of microchannel, um)
% corridorx_u: width of corridor
% corridortopy_u: height of top corridor
% corridorbottomy_u: height of bottom corridor
% left = 1, left. ow right
% DF
% on layer 0
h_u = l_u;
hh=h_u/2;
h_bottom=0;
h_top=h_u;
hw=w_u/2;

% Vertical box
u=[-hw hw hw -hw -hw];
v=[-hh -hh h_top-hh h_top-hh -hh];
E=Raith_element('polygon',layer,[u;v],DF);

% points bottom left, counter clockwise
if left == 1
    u=[-hw+5 -hw+5 -corridorx_u -corridorx_u -hw+5];
else
    u=[hw-5 hw-5 corridorx_u corridorx_u hw-5];
end
v=[hh hh-hw hh-hw+corridortopy_u hh+hw+corridortopy_u hh];
E(end+1)=Raith_element('polygon',layer,[u;v],DF);

if left == 1
    u=[-hw+5 -hw+5 -corridorx_u -corridorx_u -hw+5];
else
    u=[hw-5 hw-5 corridorx_u corridorx_u hw-5];
end
v=[-hh -hh+hw -hh+hw+corridorbottomy_u -hh-hw+corridorbottomy_u -hh];
E(end+1)=Raith_element('polygon',layer,[u;v],DF);

if left == 1
```

```
        name=['lmicrochannel-' num2str(w_u) '-' num2str(l_u) '-'
num2str(layer)];
    else
        name=['rmicrochannel-' num2str(w_u) '-' num2str(l_u) '-'
num2str(layer)];
    end


    S=Raith_structure(name,E);
end



funtion S=mininanoelectrodes(w_n,indent_n,numElectrodes,sidegap_u,DF)
% Create mininanoelectrodes for nanochannel with length 50 um, w_n (in
nanometers), indent_n (height of indent from bottom), sidegap_u (gap
between side of nanochannel and first and last electrode in microns), DF
% on layer 0
% These electrodes only go 5 nm down, and are for testing our electrode
shadow evaporation process

w0=w_n/1000;
indent=indent_n/1000;



hw=w0/2;

% nanochannel v coords
w1=-hw;
w2=hw;

% electrodes
leftmin=-25+sidegap_u;
rightmax=25-sidegap_u;
left=leftmin;
nanoelectrode_width_u=50/1000;
hnewu=nanoelectrode_width_u/2;
gap=((rightmax-leftmin) / (numElectrodes-1));
bottom=-2.5;
for i=1:numElectrodes
    u=[left-hnewu,left+hnewu,left+hnewu,left-hnewu,left-hnewu];
    v=[bottom,bottom,w1+indent,w1+indent,bottom]
    E(i)=Raith_element('polygon',0,[u;v],DF);
    left=left+gap;
end


%E(end+1)=Raith_element('text',0,[0 40],5,0,[1
2],[num2str(numElectrodes) 'me ' num2str(w_n) 'nm ' num2str(indent_n)
'nm in'],1);
name=[num2str(w_n) '-nm-melectrd-' num2str(indent_n) '-nm-indent'];
S=Raith_structure(name,E);
end

funtion S=mininanoelectrodesdt(w_n,indent_n,numElectrodes,sidegap_u)
% Create mininanoelectrodes for nanochannel with length 50 um,
% w_n (width of nanochannel in nanometers),
% indent_n (height of indent from bottom),
% sidegap_u (gap between side of nanochannel and first and last
electrode in microns),
```

```
% DF
% on layer 0
% Nanoelectrodes are 50nm wide
% These electrodes only go 5 nm down, and are for testing our electrode
shadow evaporation process
% Goes from df 0.5 to 0.5 + (numElectrods-1)*0.25

w0=w_n/1000;
indent=indent_n/1000;


hw=w0/2;

% nanochannel v coords
w1=-hw;
w2=hw;

% electrodes
leftmin=-25+sidegap_u;
rightmax=25-sidegap_u;
left=leftmin;
nanoelectrode_width_u=50/1000;
hnewu=nanoelectrode_width_u/2;
gap=((rightmax-leftmin) / (numElectrodes-1));
bottom=-2.5;
df = 0.5;
for i=1:numElectrodes
    u=[left-hnewu,left+hnewu,left+hnewu,left-hnewu,left-hnewu];
    v=[bottom,bottom,w1+indent,w1+indent,bottom]
    E(i)=Raith_element('polygon',0,[u;v],df);
    left=left+gap;
    df = df + 0.25;
end


%E(end+1)=Raith_element('text',0,[0 40],5,0,[1
2],[num2str(numElectrodes) 'me ' num2str(w_n) 'nm ' num2str(indent_n)
'nm in'],1);
name=[num2str(w_n) '-nm-melectrddt-' num2str(indent_n) '-nm-indent'];
S=Raith_structure(name,E);
end

funtion S=nanochannel(L_u,w_n,DF)
% Create a nanochannel with L_u (in um), w_n (in nanometers), DF
% on layer 0
w1=w_n/1000;
u1 = L_u;

u=[0 u1 u1 0 0];
v=[0 0 w1 w1 0];
E=Raith_element('polygon',0,[u;v],DF);
name=[num2str(w_n) '-nm-nanochannel'];
S=Raith_structure(name,E);
End

funtion S=nanoelectrodes(w_n,indent_n,numElectrodes,sidegap_u,DF)
```

```
% Create a nanoelectrodes for nanochannel with length 50 um, w_n (in
nanometers), indent_n (height of indent from bottom), sidegap_u (gap
between side of nanochannel and first and last electrode in microns), DF
% on layer 0

w0=w_n/1000;
indent=indent_n/1000;


hw=w0/2;

% nanochannel v coords
w1=-hw;
w2=hw;

% electrodes
leftmin=-25+sidegap_u;
rightmax=25-sidegap_u;
left=leftmin;
nanoelectrode_width_u=50/1000;
hnewu=nanoelectrode_width_u/2;
gap=((rightmax-leftmin) / (numElectrodes-1));
for i=1:numElectrodes
    u=[left-hnewu,left+hnewu,left+hnewu,left-hnewu,left-hnewu];
    v=[-50,-50,w1+indent,w1+indent,-50]
    E(i)=Raith_element('polygon',0,[u;v],DF);
    left=left+gap;
end


E(end+1)=Raith_element('text',0,[0 40],5,0,[1 2],[num2str(numElectrodes)
'e ' num2str(w_n) 'nm ' num2str(indent_n) 'nm in'],1);
name=[num2str(w_n) '-nm-electrd-' num2str(indent_n) '-nm-indent'];
S=Raith_structure(name,E);
end

funtion
S=nanoelectrodes2optical(w_nanochannel_n,indent_n,w_nanoe_n,wbottom_n,nu
mElectrodes,sidegap_u,spacing_u,left_bottom_u,bottomSpacing_u,label,DF)
% Create nanoelectrodes for nanochannel with length 50 um,
% w_nanochannel_n (width of nanochannel in nanometers),
% indent_n (height of indent from bottom),
% w_nanoe_n (width of nanoelectrodes in nanometers),
% sidegap_u (gap between left side of nanochannel and first electrode in
microns),
% spacing_u (spacing between electrodes in microns at top), DF
% left_bottom_u (x coord of leftmost wire at bottom),
% bottomSpacing_u (spacing between wires at bottom)
% on layer 0
%

w_nanochannel_u=w_nanochannel_n/1000;
indent=indent_n/1000;
wbottom=wbottom_n/1000;
w_nanoe_u=w_nanoe_n/1000;

hw_nanochannel=w_nanochannel_u/2;
hwb=wbottom/2;
```

```
hw_nanoe=w_nanoe_u/2;

% nanochannel v coords
w1=-hw_nanochannel;

%
leftbottom = left_bottom_u;
%rightbottom= 40;
%gap = rightbottom-leftbottom;
%bottomspacing=floor(gap/numElectrodes);
bottomspacing = bottomSpacing_u;

hnumElectrodes = numElectrodes/2;


% electrodes
leftmin=-25+sidegap_u;
left=leftmin;

basebottom=-50;
totalbottom=-100;

% Three lines
% First is top
% Second is connecting
% Third is bottom
for i=1:numElectrodes
    u=[left-hw_nanoe,left+hw_nanoe,left+hw_nanoe,left-hw_nanoe,left-
hw_nanoe];
    if i<hnumElectrodes
        vbottom=basebottom-10*(i-1);
    else
        vbottom=basebottom-10*(numElectrodes-i);
    end
    v=[vbottom,vbottom,w1+indent,w1+indent,vbottom]
    E(i)=Raith_element('polygon',0,[u;v],DF);
    ucoord1(i)=left;
    vcoord1(i)=vbottom;
    left=left+spacing_u;
end

% Second line

left=leftbottom;

for i=1:numElectrodes
    u=[left,left,ucoord1(i),ucoord1(i),left];

v=[vcoord1(i),vcoord1(i)+wbottom,vcoord1(i)+wbottom,vcoord1(i),vcoord1(i
)]
    ucoord2(i)=left;
    vcoord2(i)=vcoord1(i);
    E(end+1)=Raith_element('polygon',0,[u;v],DF);
    left=left+bottomspacing;
end

% Third line
```

```
for i=1:numElectrodes
    u=[ucoord2(i)-hwb,ucoord2(i)+hwb,ucoord2(i)+hwb,ucoord2(i)-
hwb,ucoord2(i)-hwb];

v=[vcoord2(i)+wbottom,vcoord2(i)+wbottom,totalbottom,totalbottom,vcoord2
(i)+wbottom]
    E(end+1)=Raith_element('polygon',0,[u;v],DF);
end

if label == 1
    E(end+1)=Raith_element('text',0,[0 40],5,0,[1
2],[num2str(numElectrodes) 'e ' num2str(w_nanochannel_n) 'nm '
num2str(indent_n) 'in-df-' num2str(DF)],1);
end
name=[num2str(w_nanochannel_n) '-nm-elctrd2o-' num2str(indent_n) '-nm-
indent-' num2str(DF)];
S=Raith_structure(name,E);
end


funtion
S=nanoelectrodes2optical2(w_nanochannel_n,indent_n,w_nanoe_n,w_nanoe2_n,
shiftwidth_n,wbottom_n,numElectrodes,sidegap_u,spacing_u,left_bottom_u,b
ottomSpacing_u,label,DF)
% Create nanoelectrodes for nanochannel with length 50 um,
% 2 because this is making the nanowires beside the original ones
% w_nanochannel_n (width of nanochannel in nanometers),
% indent_n (height of indent from bottom),
% w_nanoe_n (width of old nanoelectrodes in nanometers),
% w_nanoe2_n (width of new nanoelectrodes in nanometers),
% shiftwidth_n (width of shift for new nanoelectrodes)
% wbottom_n (width of nanoelectrodes at the bottom)
% sidegap_u (gap between left side of nanochannel and first electrode in
microns),
% spacing_u (spacing between electrodes in microns at top), DF
% left_bottom_u (x coord of leftmost wire at bottom),
% bottomSpacing_u (spacing between wires at bottom)
% on layer 0
%

w_nanochannel_u=w_nanochannel_n/1000;
indent=indent_n/1000;
wbottom=wbottom_n/1000;
w_nanoe_u=w_nanoe_n/1000;
w_nanoe2_u=w_nanoe2_n/1000;
shiftwidth_u=shiftwidth_n/1000;

hw_nanochannel=w_nanochannel_u/2;
hwb=wbottom/2;

hw_nanoe=w_nanoe_u/2;
hw_nanoe2=w_nanoe2_u/2;

lowerspacing = 2*wbottom;

% nanochannel v coords
w1=-hw_nanochannel;
```

```
%
leftbottom = left_bottom_u;
%rightbottom= 40;
%gap = rightbottom-leftbottom;
%bottomspacing=floor(gap/numElectrodes);
bottomspacing = bottomSpacing_u;

hnumElectrodes = numElectrodes/2;


% electrodes
leftmin=-25+sidegap_u;
left=leftmin;

basebottom=-50;
totalbottom=-100;

% Three lines
% First is top
% Second is connecting
% Third is bottom

% First line
for i=1:numElectrodes
    u=[left-hw_nanoe,left+hw_nanoe,left+hw_nanoe,left-hw_nanoe,left-
hw_nanoe];
    if i<hnumElectrodes
        vbottom=basebottom-10*(i-1);
    else
        vbottom=basebottom-10*(numElectrodes-i);
    end
    v=[vbottom,vbottom,w1+indent,w1+indent,vbottom]
    %E(i)=Raith_element('polygon',0,[u;v],DF);
    ucoord1(i)=left;
    vcoord1(i)=vbottom;
    left=left+spacing_u;
end

% First line shifted
left=leftmin;
for i=1:numElectrodes
    if i<hnumElectrodes
        u=[left-hw_nanoe2,left+hw_nanoe2,left+hw_nanoe2,left-
hw_nanoe2,left-hw_nanoe2]-shiftwidth_u;
        ucoord12(i)=left-shiftwidth_u;
        vbottom=basebottom-10*(i-1);
    else
        u=[left-hw_nanoe2,left+hw_nanoe2,left+hw_nanoe2,left-
hw_nanoe2,left-hw_nanoe2]+shiftwidth_u;
        ucoord12(i)=left+shiftwidth_u;
        vbottom=basebottom-10*(numElectrodes-i);
    end

v=[vbottom+lowerspacing,vbottom+lowerspacing,w1+indent,w1+indent,vbottom
+lowerspacing]
    E(i)=Raith_element('polygon',0,[u;v],DF);
    vcoord12(i)=vbottom+lowerspacing;
    left=left+spacing_u;
```

```
end

% Second line

left=leftbottom;
for i=1:numElectrodes
    u=[left,left,ucoord1(i),ucoord1(i),left];

v=[vcoord1(i),vcoord1(i)+wbottom,vcoord1(i)+wbottom,vcoord1(i),vcoord1(i
)]
    ucoord2(i)=left;
    vcoord2(i)=vcoord1(i);
    %E(end+1)=Raith_element('polygon',0,[u;v],DF);
    left=left+bottomspacing;
end

% Second line shifted

left=leftbottom-lowerspacing;
for i=1:numElectrodes
    u=[left,left,ucoord12(i),ucoord12(i),left];

v=[vcoord12(i),vcoord12(i)+wbottom,vcoord12(i)+wbottom,vcoord12(i),vcoor
d12(i)]
    ucoord22(i)=left;
    vcoord22(i)=vcoord12(i);
    E(end+1)=Raith_element('polygon',0,[u;v],DF);
    left=left+bottomspacing;
    if i<hnumElectrodes && (i+1)>hnumElectrodes
        left = left + 2*lowerspacing;
    end
end

% Third line

for i=1:numElectrodes
    u=[ucoord2(i)-hwb,ucoord2(i)+hwb,ucoord2(i)+hwb,ucoord2(i)-
hwb,ucoord2(i)-hwb];

v=[vcoord2(i)+wbottom,vcoord2(i)+wbottom,totalbottom,totalbottom,vcoord2
(i)+wbottom]
    %E(end+1)=Raith_element('polygon',0,[u;v],DF);
end

% Third line shifted

for i=1:numElectrodes
    u=[ucoord22(i)-hwb,ucoord22(i)+hwb,ucoord22(i)+hwb,ucoord22(i)-
hwb,ucoord22(i)-hwb];

v=[vcoord22(i)+wbottom,vcoord22(i)+wbottom,totalbottom,totalbottom,vcoor
d22(i)+wbottom]
    E(end+1)=Raith_element('polygon',0,[u;v],DF);
end

if label == 1
```

```
    %E(end+1)=Raith_element('text',0,[0 40],5,0,[1
2],[num2str(numElectrodes) 'e ' num2str(w_nanochannel_n) 'nm '
num2str(indent_n) 'in-df-' num2str(DF)],1);
    E(end+1)=Raith_element('text',0,[0 50],5,0,[1
2],[num2str(numElectrodes) 'e ' num2str(w_nanochannel_n) 'nm '
num2str(indent_n) 'in-shift-df-' num2str(DF)],1);
end
name=[num2str(w_nanochannel_n) '-nm-elctrd2o-' num2str(indent_n) '-nm-
indent-' num2str(DF)];
S=Raith_structure(name,E);
end

funtion S=plusalignment(plusw_u,layer,DF)
% Create plus alignment mark
% plusw_u (Width of entire plus mark, um)
% label 1 if label, no label otherwise
% layer
% DF

hlw_u=plusw_u/6;
htw_u=plusw_u/2;

u=[-hlw_u hlw_u hlw_u -hlw_u -hlw_u];
v=[htw_u htw_u -htw_u -htw_u htw_u];
E(1)=Raith_element('polygon',layer,[u;v],DF);
u=[-htw_u htw_u htw_u -htw_u -htw_u];
v=[hlw_u hlw_u -hlw_u -hlw_u hlw_u];
E(2)=Raith_element('polygon',layer,[u;v],DF);

name=['plus-' num2str(plusw_u) '-' num2str(layer)];
S=Raith_structure(name,E);
end

funtion S=plusraithalignment(plusl_u,plusw_u,layer,DF)
% Create plus alignment mark
% plusl_u (Length of entire plus mark, um)
% plusw_u (Width of each line, um)
% label 1 if label, no label otherwise
% layer
% DF

hlw_u=plusw_u/2;
htw_u=plusl_u/2;

u=[-hlw_u hlw_u hlw_u -hlw_u -hlw_u];
v=[htw_u htw_u -htw_u -htw_u htw_u];
E(1)=Raith_element('polygon',layer,[u;v],DF);
u=[-htw_u htw_u htw_u -htw_u -htw_u];
v=[hlw_u hlw_u -hlw_u -hlw_u hlw_u];
E(2)=Raith_element('polygon',layer,[u;v],DF);

name=['plusraith-' num2str(plusl_u) '-' num2str(plusw_u) '-'
num2str(layer)];
S=Raith_structure(name,E);
end

funtion S=plussquarealignment(plusw_u,layer,DF)
% Create plus alignment mark
```

```
% plusw_u (Width of entire plus mark, um)
% layer
% DF

hlw_u=plusw_u/6;
htw_u=plusw_u/2;
hs_u=plusw_u;

u=[-hlw_u hlw_u hlw_u -hlw_u -hlw_u];
v=[htw_u htw_u -htw_u -htw_u htw_u];
E(1)=Raith_element('polygon',layer,[u;v],DF);
u=[-htw_u htw_u htw_u -htw_u -htw_u];
v=[hlw_u hlw_u -hlw_u -hlw_u hlw_u];
E(end+1)=Raith_element('polygon',layer,[u;v],DF);
% top horizontal
u=[-hs_u hs_u hs_u -hs_u -hs_u];
v=[hs_u hs_u htw_u htw_u hs_u];
E(end+1)=Raith_element('polygon',layer,[u;v],DF);
% bottom horizontal
u=[-hs_u hs_u hs_u -hs_u -hs_u];
v=[-hs_u -hs_u -htw_u -htw_u -hs_u];
E(end+1)=Raith_element('polygon',layer,[u;v],DF);
% left vertical
u=[-hs_u -htw_u -htw_u -hs_u -hs_u];
v=[htw_u htw_u -htw_u -htw_u htw_u];
E(end+1)=Raith_element('polygon',layer,[u;v],DF);
% right vertical
u=[hs_u htw_u htw_u hs_u hs_u];
v=[htw_u htw_u -htw_u -htw_u htw_u];
E(end+1)=Raith_element('polygon',layer,[u;v],DF);

name=['plussquare-' num2str(plusw_u) '-' num2str(layer)];
S=Raith_structure(name,E);
end

funtion
S=reservoir(reservoird_u,w_u,l_u,corridorx_u,corridortopy_u,corridorbott
omy_u,left,layer,DF)
% Create a reservoir for microchannels
% reservoirs of diameter reservoird_u in um,
% microchannels with width w_u um,
% l_u (length of microchannel, um)
% corridorx_u: width of corridor
% corridortopy_u: height of top corridor
% corridorbottomy_u: height of bottom corridor
% left = 1, left. ow right
% layer
% DF
h_u = l_u;
hh=h_u/2;
% hd = radius of reservoir
hd=reservoird_u/2;
hw=w_u/2;

if left == 1
    topu=-corridorx_u;
else
    topu=corridorx_u;
```

```
end
topv=corridortopy_u+hh;
E(1)=Raith_element('circle',layer,[topu;topv],hd,[],60,DF);

if left == 1
    bottomu=-corridorx_u;
else
    bottomu=corridorx_u;
end
bottomv=corridorbottomy_u-hh;
E(end+1)=Raith_element('circle',layer,[bottomu;bottomv],hd,[],60,DF);

if left == 1
    name=['lreservoir-' num2str(reservoird_u) '-' num2str(layer)];
else
    name=['rreservoir-' num2str(reservoird_u) '-' num2str(layer)];
end

S=Raith_structure(name,E);
end

funtion S=rmicrochannel(w_u,d_u,DF)
% Create a microchannel with width w_u um,
% and reservoirs of diameter d_u in um, DF
% on layer 0
h_u = 3000;
hh=h_u/2;
h_bottom=0;
h_top=h_u;

% box
u=[0 w_u w_u 0 0]-w_u/2;
v=[0 0 h_top h_top 0]-h_u/2;
E=Raith_element('polygon',0,[u;v],DF);

u=[0 w_u 3*w_u 2*w_u 0]-w_u/2;
v=[h_top h_top h_top+2*w_u h_top+2*w_u h_top]-h_u/2;
E(2)=Raith_element('polygon',0,[u;v],DF);
topu=w_u*2.5-w_u/2;
topv=h_top+2*w_u-h_u/2;
E(3)=Raith_element('circle',0,[topu;topv],d_u,[],60,DF);

u=[0 w_u 3*w_u 2*w_u 0]-w_u/2;
v=[0 0 -2*w_u -2*w_u 0]-h_u/2;
E(4)=Raith_element('polygon',0,[u;v],DF);
bottomu=w_u*2.5-w_u/2;
bottomv=-2*w_u-h_u/2;
E(5)=Raith_element('circle',0,[bottomu;bottomv],d_u,[],60,DF);

name=['rmicrochannel-' num2str(w_u) '-' num2str(d_u)];
S=Raith_structure(name,E);
end

funtion S=rreservoir(w_u,h_u,DF)
% Create a box with width w_u um, highet h_u in um, DF
% on layer 0
hh=h_u/2;
h_bottom=hh-20;
```

```matlab
h_top=hh+20;

% box
u=[0 w_u w_u 0 0]-w_u/2;
v=[h_bottom 0 h_u h_top h_bottom]-h_u/2;
E=Raith_element('polygon',0,[u;v],DF);

name=['rreservoir-' num2str(w_u) '-' num2str(h_u)];
S=Raith_structure(name,E);
end
```